Thèse de doctorat

NNT : 2025UPASP013

université PARIS-SACLAY

Préparation et caractérisation d'états de spin corrélés avec un simulateur quantique à atomes de Rydberg

Preparation and characterization of correlated spin states using a Rydberg quantum simulator

Thèse de doctorat de l'**Université Paris-Saclay**

École doctorale n°572 Ondes et matières (EDOM)
Spécialité de doctorat: Physique
Graduate school : Physique. Établissement référent : Institut d'Optique Graduate School.

Thèse préparée dans l'unité de recherche **LCF** (Institut d'Optique Graduate School),
sous la direction de **Thierry Lahaye** (Directeur de recherche)
et le co-encadrement d'**Antoine Browaeys** (Directeur de recherche).

Thèse soutenue à Paris-Saclay, le 4 mars 2025, par

Gabriel Emperauger

Composition du Jury

Membres du jury avec voix délibérative

Fabienne Goldfarb Professeure des Universités, Université Paris-Saclay (Gif-sur-Yvette)	Présidente
Michele Filippone Chargé de recherche, CEA (Grenoble)	Rapporteur
Sébastien Gleyzes Chargé de recherche, Laboratoire Kastler Brossel (Paris)	Rapporteur
Jonathan Home Professeur, ETH (Zurich)	Examinateur

Preparation and characterization of correlated spin states using a Rydberg quantum simulator

Gabriel Emperauger

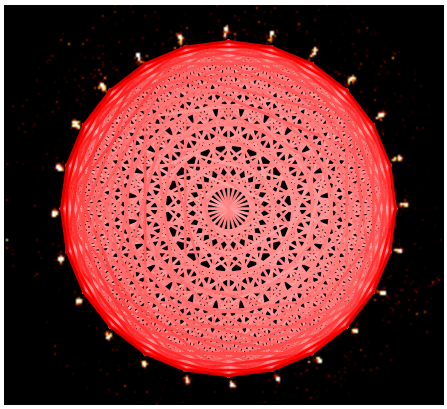

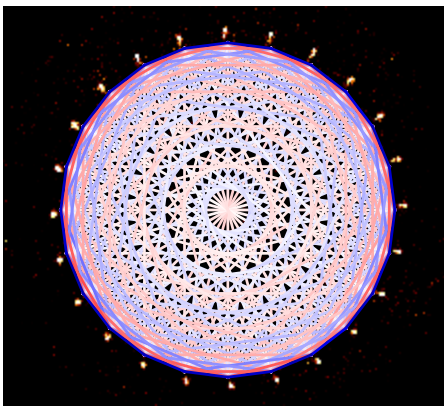

université PARIS-SACLAY | ÉCOLE DOCTORALE Ondes et Matière (EDOM)

Titre: Préparation et caractérisation d'états de spin corrélés avec un simulateur quantique à atomes de Rydberg.

Mots clés: atomes de Rydberg, pinces optiques, interactions dipôle-dipôle, simulation quantique, modèles de spin, magnétisme quantique.

Résumé court: Cette thèse porte sur le développement d'outils et de protocoles expérimentaux pour l'étude de systèmes de spins fortement corrélés, depuis leur préparation jusqu'à leur caractérisation.
Nous utilisons des atomes de Rydberg pour simuler le comportement de spins soumis à des interactions magnétiques. Les atomes sont piégés dans des pinces optiques pour former des réseaux uni- ou bi-dimensionnels, puis excités dans des états de Rydberg où ils échangent de l'énergie suivant l'interaction dipôle-dipôle. Nous mesurons l'état interne des atomes par fluorescence avec une résolution d'atome unique afin d'accéder à la statistique quantique des états préparés.
Ces outils nous permettent d'illustrer divers phénomènes quantiques collectifs, des propriétés d'équilibre à la dynamique d'états excités. En mesurant les corrélations entre spins individuels, nous observons des lois de puissance universelles et étudions la propagation des excitations élémentaires dans le système. Cette caractérisation met en évidence le rôle crucial des interactions dipolaires, qui renforcent l'ordre ferromagnétique et déstabilisent l'ordre antiferromagnétique par frustration géométrique.
Enfin, nous augmentons la complexité du modèle de spin en y incluant des trous mobiles, pouvant sauter d'un site à un autre sur plusieurs sites de distance. L'implémentation expérimentale d'un tel modèle nous permet d'étudier le transport de trous dans des aimants dopés, avec l'objectif de long terme de mieux comprendre les mécanismes complexes régissant le comportement des matériaux supra-conducteurs à haute température.

Title: Preparation and characterization of correlated spin states using a Rydberg quantum simulator.

Keywords: Rydberg atoms, optical tweezers, dipole-dipole interactions, quantum simulation, spin models, quantum magnetism.

Abstract: This thesis focuses on the development of experimental tools and protocols for the study of strongly correlated spin systems, from their preparation to their characterization.
We use Rydberg atoms to simulate the behavior of spins subjected to magnetic interactions. Atoms are trapped in optical tweezers to form one- or two-dimensional arrays, and then excited into Rydberg states where they exchange energy according to the dipole-dipole interaction. We perform fluorescence imaging of the arrays in order to access the quantum statistics of the prepared states with single-atom resolution.
These tools allow us to observe various collective quantum phenomena, from equilibrium properties to the dynamics of excited states. By measuring correlations between individual spins, we uncover universal power laws and study the propagation of elementary excitations within the system. This characterization reveals the crucial role of dipolar interactions, which reinforce ferromagnetic order and destabilize antiferromagnetic order due to geometric frustration.
Finally, we increase the complexity of the spin model by introducing mobile holes, which can hop from one site to another over several sites. The experimental implementation of such a model allows us to study hole transport in doped magnets, with the long-term goal of better understanding the complex mechanisms governing the behavior of high-temperature superconducting materials.

Résumé long: Cette thèse porte sur le développement d'outils et de protocoles expérimentaux pour l'étude de systèmes de spin fortement corrélés, depuis leur préparation jusqu'à leur caractérisation.

Le dispositif expérimental repose sur le piégeage d'atomes de rubidium individuels dans des pinces optiques, selon des structures uni- ou bi-dimensionnelles ordonnées. Une fois excités dans des états de Rydberg, les atomes interagissent deux à deux suivant l'interaction dipôle-dipôle, ce qui peut être décrit de manière effective par un modèle de spin — donnant lieu à des simulations quantiques de ce modèle. L'objectif général est de mieux comprendre les mécanismes à l'œuvre dans les états fortement corrélés de la matière, qui sont notoirement difficiles à simuler numériquement lorsque le nombre de spins devient grand.

La mise en œuvre des modèles de spin nécessite un contrôle précis des degrés de liberté tant internes qu'externes des atomes. Durant ma thèse, j'ai amélioré le montage préexistant, en appliquant une technique de refroidissement Raman pour réduire les fluctuations de position thermiques des atomes dans les pinces optiques. Nous avons également conçu une méthode de transitions locales entre états de Rydberg, permettant la préparation de textures de spin arbitraires et la lecture simultanée de plusieurs spins dans des bases différentes. Enfin, nous avons caractérisé les interactions dites d'*échange de spin* entre deux atomes. Celles-ci peuvent être classées en deux catégories : l'une, dite du premier ordre, varie comme $1/r^3$ avec r la distance moyenne entre les atomes ; l'autre, du deuxième ordre, varie comme $1/r^6$. Nous avons identifié les principales limitations du temps de cohérence des oscillations d'échange, à savoir les fluctuations de position résiduelles et les durées de vie finies des atomes de Rydberg.

Ces outils nous ont permis de mettre en évidence des phénomènes quantiques collectifs dans des systèmes magnétiques avec interactions dipolaires de longue portée. Nous avons étudié plusieurs régimes, depuis les propriétés d'équilibre à basse énergie, jusqu'à la dynamique d'états de haute énergie.

Tout d'abord, la préparation adiabatique des états fondamentaux du modèle de spin dit XY a permis d'observer la formation d'un ordre ferromagnétique ou antiferromagnétique entre spins, mesuré au moyen de leurs corrélations, sur un réseau carré et sur une chaîne unidimensionnelle. Quelle que soit la dimension du système étudié, le caractère dipolaire des interactions s'est traduit par une déstabilisation de la phase antiferromagnétique, et un renforcement de l'ordre ferromagnétique, du fait de la frustration géométrique entre spins deuxièmes voisins. En une dimension, nous avons observé des oscillations de Friedel à proximité d'un défaut localisé et mesuré des profils de corrélations en loi de puissance. L'étude de ces lois de puissance permet d'extraire des exposants critiques universels, caractéristiques d'une phase de la matière appelée liquide de Tomonaga-Luttinger.

Nous avons ensuite mis au point une nouvelle technique de mesure de la relation de dispersion des excitations de basse énergie. Cette méthode, appelée *quench spectroscopy*, consiste à mesurer la propagation des corrélations entre tous les spins à partir d'un état hors-équilibre de basse énergie, et à appliquer une double transformée de Fourier (spatiale et temporelle) pour obtenir l'énergie des excitations élémentaires en fonction de leur vecteur d'onde. Appliquant cette méthode aux cas précédents, nous avons vérifié la linéarité de la relation de dispersion à faible vecteur d'onde, caractéristique des ondes de spin du modèle XY ; à l'exception notable du cas ferromagnétique en deux dimensions, où l'énergie évolue comme la racine carrée du vecteur d'onde du fait des interactions dipolaires.

Enfin, nous avons exploité les interactions de van der Waals non-diagonales pour mettre en œuvre le modèle dit t-J-V, décrivant le mouvement de trous dans un réseau de spins. La réalisation de ce modèle avec des états de Rydberg permet d'accéder à des régimes de paramètres jusqu'à présent inaccessibles avec une résolution à l'échelle de la particule individuelle ; en particulier, les interactions dipolaires équivalent à un effet tunnel de longue portée, autorisant le saut d'une particule entre deux sites distants. En étudiant la dynamique d'un aimant dopé par des trous localisés, nous avons détecté des états liés entre trous, où deux trous se propagent préférentiellement en restant côte à côte. En caractérisant la vitesse de propagation de ces états liés, nous avons trouvé des signatures de l'effet tunnel effectif de longue portée, et mis en évidence l'influence des états de spin sur le transport des trous. L'implémentation expérimentale d'un tel modèle pourrait ouvrir une nouvelle voie à l'étude des phénomènes de transport dans les supra-conducteurs à haute température, un défi majeur de la physique actuelle.

Contents

Remerciements

Contrairement à une tenace idée reçue, faire une thèse ne signifie pas forcément travailler seul dans son coin. Pour ma part, j'ai passé quatre années bien entouré, dans une troupe de joyeux drilles bigarrée au possible mais unie par une passion commune : la physique. À ces super-héros dignes des meilleures bandes dessinées, j'aimerais dire ces quelques mots.

Quand je suis arrivé au labo il y a presque quatre ans, je ne connaissais quasiment rien à la physique atomique et aux lasers : ma formation m'avait donné quelques bases pour résoudre des équations de physique à N corps, mais aligner un miroir et une lentille, ça, j'en étais incapable... Et pourtant, deux personnes m'ont fait confiance pour intégrer cette manip' complexe qu'est CHADOQ[1] : Antoine Browaeys et Thierry Lahaye. Un grand merci à tous les deux pour cela.

Prof. Thierry Mortimer

Thierry, en travaillant à tes côtés on ne tarde pas à se rendre compte de l'immensité de ton savoir, en même temps que ton humilité face à tout ce qui te reste à apprendre ; je suis très admiratif de cette attitude. Au début c'est assez impressionnant, on a peur de poser une question bête ; puis le temps aidant, on ose, et là, la réponse arrive : un exposé limpide, structuré, avec calculs des ordres de grandeur, illustrations, tout ce qu'il faut... (À quand ta chaîne de vidéos Youtube ?) Thierry, j'apprécie aussi ta lucidité et ton ironie mordante. Et quand on en vient à participer à une séance de râlerie collective sur l'état du monde et de la recherche, là on se dit que ça y est, on est vraiment intégré dans l'équipe.

Cpt. Antoine Blake

Antoine, tu es pour moi la source d'énergie de ce groupe, celui qui impulse les projets et motive les troupes. Certes, les carrés de chocolat que tu passes nous distribuer en manip' y sont pour beaucoup, mais pas que : il y a aussi et surtout ton énergie débordante, ta vivacité d'esprit, ton audace, ta curiosité sans faille — et tes doutes, qui te font te remettre en question et toujours chercher à t'améliorer. Tu réussis à garder la flamme de la recherche et à t'émerveiller des dernières avancées, c'est

[1] CHADOQ, c'est le petit nom de notre manip'. Officiellement: "Calculateur Holographique à Atomes pour la Démonstration d'Opérations Quantiques".

vraiment inspirant ! Parfois, ça passe par une crise de collapsologie aïgue, mais on le sait, ça finit par reprendre — et là, chaud devant, ça va vite. Très vite.

Danielix

Et puis, quand on commence sa thèse dans ce groupe, on ne tarde pas à rencontrer Daniel Barredo avec sa question rituelle "Do you like competition ?" et autres phrases fétiches telles que "If one day I kill you, don't be surprised". Le ton est donné... avant de réaliser que ces dehors autoritaires cachent un grand cœur, toujours disponible pour discuter et donner un coup de main. Et avec ça, quel physicien ! Je crois savoir que nombre des avancées dans le groupe n'auraient pas vu le jour sans toi, et l'"esprit CHADOQ" te doit beaucoup.

Guillaume Gaston

Cheng Tchang

J'en arrive à Cheng Chen et Guillaume Bornet, les deux cow-boys avec lesquels j'ai passé la majorité de mes heures de thèse au labo. Travailler à leur côté, c'est s'imprégner d'un véritable état d'esprit : faire corps avec la manip', lutter avec elle contre les éléments, repousser les limites... Presque une religion ! Preuve en est la forte corrélation entre l'humeur de Guillaume et l'état de la manip'. Sans eux, je me demande ce qu'aurait été ma thèse : combien de fois aurais-je renoncé, pris de découragement devant le n$^{\text{ième}}$ alignement de MOT ou la trentième tentative de calibration — mais non, à trois on va y arriver, "we will manage" comme dirait Guillaume ! Et effectivement, ça passait... Cheng, Guillaume, vous resterez pour moi des modèles de ténacité, de pragmatisme et de créativité.

Mu Hauru

Plus récemment, Mu a su prendre le relais avec brio — Mu, une force tranquille à l'efficacité peu commune et à qui rien ne semble impossible. Et la relève n'a pas à rougir : Chew, Bastien, Lukas, Romain, les quelques heures que j'ai pu passer avec vous au labo laissent présager de très belles choses.

Chew Pazu

Super Bastien

Lukas Groot

Lucky Romain

Lucas Fantasio

Je souhaite également tirer mon chapeau aux théoriciens avec lesquels nous avons eu la chance de collaborer pendant ma thèse, à savoir l'équipe de Tommaso Roscilde à Lyon, celle de Norman Yao à Harvard, et celle de Fabian Grusdt et Annabelle Bohrdt à Munich. Un grand merci en particulier à Marcus Bintz, Lukas Homeier et Saverio Boccini qui m'ont aidé à rédiger quelques parties de cette thèse. Et aussi et surtout au plus expérimentateur de nos théoriciens, maître du benchmarking, improvisateur de théâtre et photographe à ses heures perdues, j'ai nommé Lucas Leclerc !

J'ai eu la chance de commencer ma thèse sur une manip' déjà fonctionnelle, grâce aux générations de doctorants et de post-docs qui se sont succédées avant moi pour la construire et l'améliorer. Il me semble important de citer leurs noms ici: Lucas Béguin, Aline Vernier, Sylvain Ravets, Daniel Barredo, Henning Labuhn, Sylvain de Léséleuc, Thomas Boulier, Vincent Lienhard, Pascal Scholl, Hannah Williams et Kai-Niklas Schymik, je suis fier d'avoir pris le relais de votre formidable travail ! Pour m'avoir accueilli au labo à mes débuts et formé le stagiaire ignare que j'étais, je suis particulièrement redevable à Hannah Williams, Pascal Scholl et Florian Wallner.

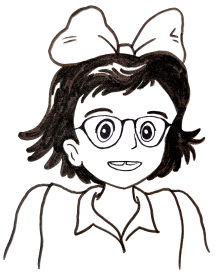

Florence's delivery service

Pour un peu de douceur et de musique dans ce monde de compétition où seul résonne le chant des shutters mécaniques, merci à Florence Nogrette.

Pour la bonne ambiance aux pauses café, pour les footings par tout temps (neige, pluie, et brouillard de préférence), pour les parties passionnées de *Wordle* et de *Mölkky*, pour les séances de *Mario Kart* sur le grand écran de l'auditorium, merci à tout le reste du groupe : Igor, Damien, Britton, Sara, Lucas, Jamie, Sam, Giulio, Guillaume,

Adrien, Nathan, Andrea, Olivia.

Pour leur relecture attentive de ce manuscrit et pour la discussion qui a suivi la soutenance, merci aux membres de mon jury: Michele Filippone, Sébastien Gleizes, Jonathan Home et Fabienne Goldfarb.

Pour rendre possible notre travail de recherche au laboratoire, merci à la partie immergée de l'iceberg, à savoir le staff administratif de l'Institut d'Optique, et plus particulièrement les personnes avec qui j'ai été en contact : son directeur Patrick Georges, Maïké Seychelles au secrétariat, Cynthia Meyns au service "Missions", Christophe Diot et Alioune Toure à l'accueil, Clémentine Bouyé à la communication, Sonia Gamet et Emeline Fort aux ressources humaines...

Pour leur soutien sans faille durant ces années, et pour avoir fait de moi ce que je suis, merci à mes parents.

Pour les moments de bonheur au quotidien, merci à Marie-Charlotte.

Introduction

> Cruc se mâchait nerveusement les lèvres. Il y avait devant lui une feuille de papier couverte de calculs et d'équations du vingt-sixième degré, irrésolues et hésitantes.
>
> Boris Vian, *L'Automne à Pékin*

Contents

The challenge of quantum many-body physics

Proving a fundamental law to be wrong is the dream of many physicists, but fortunately — or unfortunately? — this does not happen often. At the microscopic scale, the quantum theory designed by a few founding fathers during the 20$^{\text{th}}$ century still resists all experimental attempts to challenge it. More precisely, the behavior of microscopic objects can be fully explained by a single equation called the Schrödinger equation, which describes the time evolution of the system in terms of its density matrix ρ (Basdevant and Dalibard, 2006):

$$i\hbar\frac{d\rho}{dt} = [H, \rho],$$

where $\hbar$ is Planck's constant and H is the Hamiltonian. Solving this equation would in principle allow us to predict the time evolution of any microscopic system! But when trying to follow this approach, physicists face two main difficulties.

"Un problème de taille" First, what is the expression of H? Knowing this already requires to have a very good understanding of the elementary ingredients that constitute the system. This is the goal of a whole field of physics, ranging from high-energy physics to high-precision metrology. To this date, the key microscopic ingredients that constitute matter, and the way they can interact together, are gathered in a theory framework called the *standard model* (Griffiths, 2011).

Second, even if we know how to write H, we don't know how to solve the Schrödinger equation when the size of H is too large. And it can be *very* large: it increases exponentially with the number of elementary particles. For example, let us consider the idealized case of N particles, each one with two possible states: $|\uparrow\rangle$ and $|\downarrow\rangle$. Those particles are called *spins*, or equivalently *qubits* when they are denoted by $|0\rangle$ and $|1\rangle$. According to the quantum principle of superposition, the ensemble of particles lives in a space which is composed of 2^N states, meaning that both ρ and H are matrices with 2^{2N} coefficients. With as little as $N = 136$ spins, the number of coefficients exceeds the estimated number of atoms in the universe ($\sim 10^{82}$)! That argument shows not only that an analytical solution is hard, but also that an exact, brute-force numerical simulation for more than a few tens of particles is out of reach.

Fight for precision, fight for complexity Several approaches exist to challenge the limits of our understanding. In one approach, one considers "simple" systems where H is known with a good accuracy, and one tries to measure its properties with the highest possible precision. For example, in an object as "simple" as a hydrogen atom, made of one proton and one electron, placed in a quantum vacuum, measuring the frequency difference between the discrete energy levels of the electron constitutes one of the most accurate tests of the standard model, as it enables the precise measurement of its fundamental constants (Hänsch, 2006).

Another approach consists in increasing the number N of particles, and thus the *complexity* of the system. What happens when N changes? Two extreme regimes are known (Fig. 1). On the one side, for a small number of well-controlled particles ($N \gtrsim 2$), the quantum nature of the system can manifest through entanglement, a property stating that the state of the system cannot be described by independent particles. This implies that measuring one particle in a given state immediately constraints the state of the other particles, whatever the distance between them. It was experimentally demonstrated in the 1980's in the case of two photons (Aspect et al., 1982), and is now routinely observed in many laboratories around the world with photons, atoms, ions, superconducting circuits (Georgescu et al., 2014)...

On the other side, in the thermodynamic limit ($N \to \infty$), the state of the system at equilibrium can generally be described by an equation of state governed by a few macroscopic parameters (temperature, pressure, etc.), forgetting about all the microstates and their potential entanglement. This miraculous description, in which an enormous complexity boils down to a few parameters, allows us to explain the behavior of most materials: phase transitions of water, emission spectrum of stars,

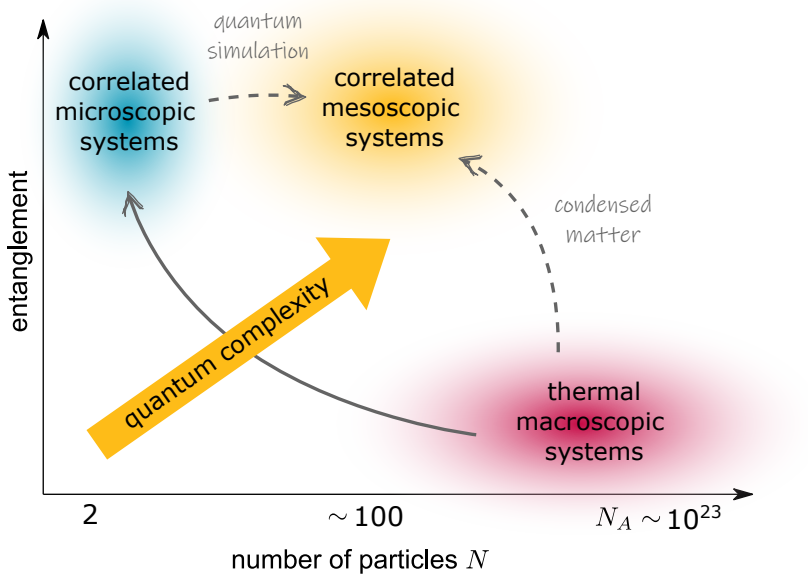

Figure 1: The quest for entangled many-body systems. Position of three fields of physics in a two-dimensional sketch representing the number of particles N in a system, and the entanglement between them (it can be thought of as, for instance, entanglement entropy). Complexity, in a quantum sense, increases with entanglement and with N (orange arrow). On the one side, most macroscopic systems are well-described by thermal equilibrium, with a number of particles on the order of the Avogadro number N_A (red region). On the other side, experimental progress during the last decades made it possible to isolate and control a few particles (solid grey arrow), opening the way for the creation of few-body correlated systems (blue region). Quantum simulation aims at studying entangled systems made of many particles (orange region), at the edge of our understanding in terms of quantum complexity. It requires scaling up the number of particles, without losing the level of control obtained in quantum physics (left dashed grey arrow). Another approach for studying many-body physics is to use condensed matter samples in well-controlled environments (right dashed grey arrow).

electric current in metallic wires, thermal expansion of materials... This description is effective for both open systems connected to a thermal bath, and isolated systems under the so-called *eigenstate thermalization hypothesis* (D'Alessio et al., 2016; Mori et al., 2018).

But what happens in the intermediate regime of correlated mesoscopic systems? In what cases do we need or not entanglement to describe the system? Is there a limit to the number of particles for which entanglement can be observed? What collective effects can emerge from the interactions? The field of physics that studies those questions is called *quantum many-body physics*.

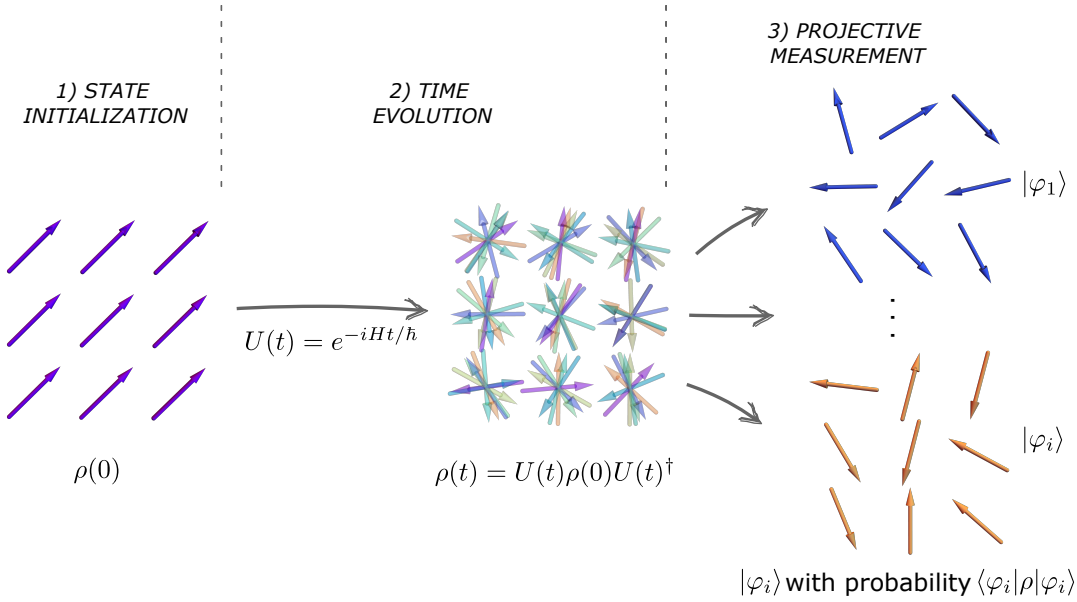

Figure 2: Typical experimental sequence in a quantum simulator, illustrated in the case of a spin system. Each arrow stands for one spin, and each color represents a configuration for a system of 3×3 spins. First, the system is initialized in a state $\rho(0)$; then, it evolves for a time t under the Hamiltonian H, which in general creates the superposition of many possible spin configurations; finally, during the measurement it is projected into one of the states from the measurement basis, $\{|\varphi_i\rangle\}$.

The idea of quantum simulation for studying many-body physics Since a numerical resolution of quantum many-body problems by classical computers is so hard, Richard Feynman proposed in 1982 (Feynman, 1982): "*how can we simulate the quantum mechanics? [...] Let the computer itself be built of quantum mechanical elements which obey quantum mechanical laws.*"

The idea is simple: to simulate the Schrödinger equation with a given Hamiltonian H, let us chose a physical system that is governed by this Hamiltonian —if such as system does not exist, we can create it artificially—, and let us measure its time evolution. The output of the simulation is simply the result of the measurement. This scheme has the advantage of transferring the mathematical complexity of the problem into an experimental complexity[2]: one has to design a system with the desired Hamiltonian H, and find experimentally-accessible observables to measure.

[2] A possible criticism is that measuring the full quantum state of the system (the 2^{2N} coefficients of the density matrix ρ) requires a number of measurements which increases exponentially with the number of particles. But we are usually not interested in all 2^{2N} coefficients, rather a few properties of the state corresponding to a few observables $\{A\}$. As explained in the following, a quantum simulator can give access to the average value of such observables, $\mathrm{Tr}(\rho A)$.

How does it work in practice? Generally speaking, a quantum simulator operates in three steps (Blatt and Roos, 2012; Georgescu et al., 2014), which are illustrated in Fig. 2.

1. State initialization. The system is prepared in an initial state $\rho(0)$, which depends on the problem one wants to study. Since it is limited by the available experimental tools, it is usually a simple state (product state, thermal state).

2. Time evolution. The system evolves under the Hamiltonian H: $\rho(t) = U(t)\rho(0)U(t)^\dagger$ with $U(t) = e^{-iHt/\hbar}$ the evolution operator. This is usually where interesting many-body properties begin to appear.

3. Projective measurement. Due to the quantum nature of the system, the measurement makes the system collapse on a single state $|\varphi_i\rangle$ with a probability $P_i(t) = \langle\varphi_i|\,\rho(t)\,|\varphi_i\rangle$.

Those three steps are repeated many times with the same parameters for the same time t, in order to acquire statistics. With a sufficient number of repetitions, the statistical frequency of the measurement outcome $|\varphi_i\rangle$ can be interpreted as the probability of the considered state $P_i(t)$. From the probability distribution, one can infer the average value of any observable A, under the condition that it is diagonal in the measurement basis $\{|\varphi_i\rangle\}$. Mathematically, with $A = \sum_i A_i\,|\varphi_i\rangle\,\langle\varphi_i|$, its average value at time t is given by

$$\langle A\rangle(t) = \mathrm{Tr}\,(A\,\rho(t)) = \sum_i A_i P_i(t). \tag{0.1}$$

In practice, to estimate $\langle A\rangle(t)$, one does not need to resolve the full-counting statistics of the distribution of states (which would require a number of repetitions that grows exponentially with the system size); in this thesis, we will typically sample over a few hundreds or thousands of repetitions.

Ideally, the experimental Hamiltonian H is directly the same as the one of the many-body problem we want to solve. This approach is known as *analog* quantum simulation. In practice, one can already anticipate that the mapping of the experimental system onto the problem of interest will never be perfect, as it will be illustrated throughout this manuscript. But what one can hope to gain with quantum simulation is (i) a better control over the system's parameters (geometry, interactions, initial states, etc.), that allows one to vary the experimental conditions and test their influence; (ii) a direct access to the microscopic behavior of the system, thanks to single-particle resolved measurements.

Another, more ambitious approach makes use of a quantum computer for realizing the time-evolution of the system: this kind of quantum simulator is called a *digital* simulator, by contrast to the analog version (Georgescu et al., 2014).

Take-home message

Quantum many-body physics studies entangled systems composed of many particles, a notoriously hard problem to simulate with classical computers due to the exponentially-large cost of memory and calculation. This challenge can in principle be overcome by using quantum simulators, transferring the difficulty on the experimental side.

But in practice, are quantum simulators fulfilling this ambitious program? Let us see in the following the current status of quantum simulators: their achievements, the opportunities they created, the challenges they are facing, and the perspectives to overcome them.

Quantum simulators: what are they made of?

Atoms, ions, superconducting qubits, photons... Many platforms are being developed in parallel for quantum simulation and other quantum applications. All of them rely on isolating a few energy levels in individually-controlled systems (typically, electronic levels in one atom), and making several of those systems interact. This gives rise to Hamiltonians with a few degrees of freedom per particle, which are often *spin models* such as Ising, XY, Heisenberg (Sandvik, 2010), or bosonic and fermionic *Hubbard models* (Bloch et al., 2008). Since this is a very rich and constantly-evolving field of research, I will not make an exhaustive list of the existing platforms, but let me mention some of them[3].

Ultracold atomic gases are studied both in macroscopic traps and in optical lattices, where they can be imaged with single-site resolution using a quantum gas microscope [Fig. 3(a)]. In optical lattices, atoms can hop from one site to another and interact on-site via a contact potential, implementing fermionic or bosonic versions of the Hubbard model (Bloch et al., 2012).

Atoms can also be cooled and trapped in optical tweezers and excited to *Rydberg states* [Fig. 3(b)], which naturally interact at large distances (~ 10 µm) via their strong electric dipoles (Browaeys and Lahaye, 2020). One crucial advantage of this technology is the possibility to move the atoms and change geometries at will. This is the platform used in this thesis, and it will be described in more details in the following. Similar to Rydberg atoms are *ultracold polar molecules*, which also interact via the dipole-dipole interaction [Fig. 3(d)]. This is a more recent field which is currently producing its first results (Cornish et al., 2024).

Another long-time standing platform makes use of *ions*, which can be trapped using radio-frequency traps where they form crystalline structures (Kiesenhofer et al., 2023; Guo et al., 2024) [Fig. 3(c)]. Interactions between ions can be engineered by mediation of the crystal's vibrational modes (phonons) and lasers, offering a wide tunability of the Hamiltonian (Blatt and Roos, 2012). Ions offer many degrees of freedom to encode the information, from the discrete electronic levels (Clark et al., 2021) to the motional states, which are continuous variables (Flühmann et al., 2019).

All previously-mentioned platforms are made of real individual particles (atoms, ions, molecules). But it is also possible to isolate a few energy levels in samples of matter made of many atoms, at low temperature. A *superconducting qubit* is made of

[3] A good review can be found in Georgescu et al. (2014), although it does not include state-of-the-art experiments.

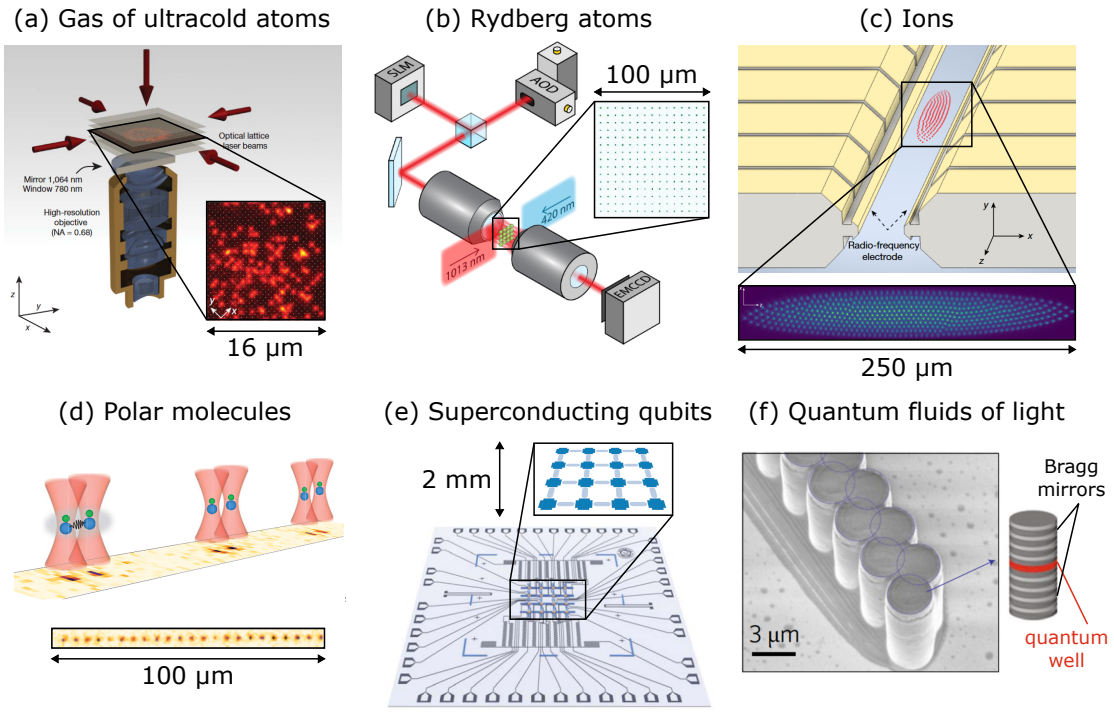

Figure 3: Examples of quantum simulators. (a) Ultracold atoms in an optical lattice, observed in a quantum gas microscope [adapted from Sherson et al. (2010)]. (b) Array of atoms trapped in optical tweezers, and excited to Rydberg states [adapted from Ebadi et al. (2021)]. (c) Array of ions in a two-dimensional radio-frequency Paul trap [adapted from Guo et al. (2024)]. (d) Array of polar molecules trapped in optical tweezers [adapted from Holland et al. (2023)]. (e) Chip hosting an array of superconducting qubits [adapted from Wang et al. (2024)]. (f) Quantum fluid of light made of polaritons in nano-cavities [adapted from St-Jean et al. (2017)].

an LC circuit in parallel with a Josephson junction (Wendin, 2017), and arrays of such qubits can be designed on a chip inside a cryostat [Fig. 3(e)]. They have demonstrated state-of-the-art preparation and detection fidelities, and have the fastest repetition rates of any platforms ($\sim 1-100$ kHz, to be compared with $\sim 0.1-1$ kHz for ions, $\sim 1-10$ Hz for atoms in tweezers and $\sim 0.1-1$ Hz for ultracold gases).

Another example consists of *quantum fluids of light*, which can be emulated by various ways (Carusotto and Ciuti, 2013), including for example semiconductor cavities hosting exciton polaritons [Fig. 3(f)]. This technology provides an easy access to spectral properties of the system, but interactions between the excitons need to be increased.

A few achievements and challenges of quantum simulators

Exemplifying many-body effects Here I give a few examples of successful applications of quantum simulators, in one and two spatial dimensions. I will mainly focus on applications oriented towards condensed-matter, but other applications in high-energy physics and cosmology have also been demonstrated (Georgescu et al., 2014).

Problems where quantum simulation can provide an answer can be classified in two categories: equilibrium problems, where one wants to know the eigenstates of the Hamiltonian (ground state and energy spectrum); and out-of-equilibrium problems, also known as *quench dynamics*, where one initializes the system in a high-energy superposition and monitor its dynamics. Both of them will be studied in part B of this thesis.

Ground state properties A typical problem of the first category consists in preparing the ground state of a Hamiltonian $H(\theta)$, with θ a tunable parameter, and studying the phase diagram of H by tuning θ. The system is initialized in an experimentally-accessible ground state, then θ is varied as a function of time. If the change is slow enough, the system remains in the ground state of $H(\theta)$ all the time: this is called an *adiabatic preparation*. A historical achievement of atomic physics using this technique was the observation of the quantum phase transition between a superfluid and a Mott insulator using a gas of ultracold bosons (Greiner et al., 2002). More recently, a phase of the Fermi-Hubbard model displaying a strong antiferromagnetic order was observed using single-site resolution, with ~ 80 sites (Mazurenko et al., 2017). Using ions, a proof-of-principle of adiabatic preparation was realized in Friedenauer et al. (2008); since then, it was extended to one-dimensional ion chains (Islam et al., 2011) and its performance was carefully studied in Richerme et al. (2013). Adiabatic preparation was also used in two-dimensional square lattices, to prepare an Ising antiferromagnet with ~ 200 Rydberg atoms (Scholl, 2021; Ebadi et al., 2021), and an XY antiferromagnet with 69 superconducting qubits (Google, 2024).

Let me also mention another type of exotic phase that quantum simulators are able to probe: topological phases of matter. Proofs of principle were performed with the realization of the non-interacting Su–Schrieffer–Heeger model using quantum fluids of light (St-Jean et al., 2017), and its interacting version using Rydberg atoms (de Léséleuc et al., 2019). More recently, evidence of a potential spin liquid was measured on a lattice with geometrical frustration (Semeghini et al., 2021); and the fractional quantum Hall effect was observed in an array of superconducting qubits (Wang et al.,

2024). Here, quantum simulators provide new insights on phases of condensed matter with observables that are hardly accessible to real samples of matter (correlations with single-site resolution, string observables, etc.). More generally, showing that quantum simulators have the possibility to probe topological and frustrated phases of matter was an important step, since there are many open questions in this field of research.

Quench dynamics The second class of many-body problems, out-of-equilibrium dynamics, is particularly appealing because it requires the knowledge of the full energy spectrum and its eigenstates, which is usually harder to access than the ground state using classical simulations. For example, a whole field of physics is interested in quantum transport properties beyond the linear regime: how do quantum correlations propagate, and how does it depend on the geometry, the interactions... Here, quantum simulators can offer complementary views to the works performed in condensed matter samples (graphene, carbon nanotubes, etc.). Recent works could observe the emergence of hydrodynamic transport properties, using ions (Joshi et al., 2022) and ultracold atoms (Wienand et al., 2024); and could reveal universal transport properties falling into the Kardar-Parisi-Zhang universality class, using quantum dots (Fontaine et al., 2022) and ultracold atoms (Wei et al., 2022).

Quench dynamics also allow us to test if, and how, a closed system starting in a pure state can evolve to an effective thermal equilibrium — and thus test the eigenstate thermalization hypothesis. Thermalization dynamics was for instance studied using ultracold gases (Zhou et al., 2022), trapped ions (Kranzl et al., 2023) and superconducting qubits Google (2024). Remarkably, the eigenstate thermalization hypothesis can be broken when the system exhibits certain symmetries; this phenomenon, called *quantum scars*, was experimentally observed in Bluvstein et al. (2021).

Quantum simulation or quantum stimulation? The NISQ era The previously-cited results show that quantum simulators can reach regimes where the best classical algorithms and theories struggle to make predictions. But then, how to trust the outcome of the simulator when other theories fail? Of course, the outcome of the simulator is always "true" in the sense that it corresponds to a real physical system; but one is never sure that this system implements exactly the many-body problem that we want to solve.

In fact, there are always experimental imperfections in a quantum simulation, leading to deviations from the ideal solution. A list of general limitations that are common to many quantum simulators is shown in Tab. 1. For example, interactions

Step of the sequence	Typical limitations	Possible strategies
State initialization	Fidelity	- Design new preparation schemes - Postselection of realizations without errors - Computer-assisted optimization - Improved stability, faster repetition rates - Develop higher-performance technologies
Time evolution	Decoherence	- Better isolation from the environment - Use states with longer natural lifetimes - Design shorter sequences (increase interactions, shortcuts to adiabaticity...) - Reduce inhomogeneities and fluctuations of the Hamiltonian - Post-selection using mid-circuit measurements - Quantum error correction
	Finite size effects (edge effects)	- Increase system size - Design systems with periodic boundary conditions (circle in 1D, torus in 2D)
	Limited tunability of the Hamiltonian	- Implement new geometries (various lattices, 3D...) - Design new mappings - Hamiltonian engineering (e.g., Floquet techniques)
Projective measurement	Fidelity	- Design better detection schemes - Find robust observables against experimental noise
	Partial access to the state	- Enhance read-out bases (single particle resolution, multi-bases measurements...) - Design strategies to extract information (randomized benchmarking...) - Non-destructive measurements

Table 1: Typical limitations of quantum simulators and strategies to overcome them.The concepts are quite general to be applied to any quantum simulator, but the main sources of limitation strongly depend on the platform and the type of sequence.

with the environment (decoherence) typically lead to local errors that propagate over the system size, resulting in a proliferation of errors at long times (Shaw et al., 2024). The outcome of the quantum simulator is thus valid only within a given precision range, which gets worse when the simulation time increases.

This regime of quantum simulation is sometimes called the *Noisy Intermediate-Scale Quantum* (NISQ) era (Preskill, 2018). Although some articles are already claiming "quantum advantage" of their quantum simulation over classical algorithms (Google, 2019; Zhong et al., 2020), the future of NISQ simulations is probably more *hand in hand with* classical simulations, rather than *against* them. Being slightly provocative, one could even say that so far, the main achievement of quantum simulators has been to stimulate a field of research, by pushing forward technologies, algorithms and theories, rather than really making ground-breaking discoveries in many-body physics.

Entanglement as a resource Finally, I cannot present applications of quantum simulation without mentioning quantum information. This broad field of research studies how entangled states can be used in practice for computing, optimization, communication and metrology. Since quantum simulators are being designed to produce many-body entangled states, they are natural candidates for the realization of quantum information platforms.

A short-term application of analog quantum simulators is optimization tasks, using for example *quantum annealing* (Yarkoni et al., 2022). The principle of the latter method is that a classical cost function of an optimization problem can be mapped onto the minimization of the energy of a given Hamiltonian. If this Hamiltonian is experimentally realizable, then preparing the ground state of system gives the answer to the optimization problem.

More ambitious, and more powerful, would be a universal quantum simulator, also known as *quantum computer*. Many platforms are concentrating their efforts on the realization of high-fidelity gates in views of this long-term goal. State-of-the-art experiments report 2-qubit gate fidelities of 99.97 % with ions (Löschnauer et al., 2024), $\geq$ 99.9 % with superconducting qubits (DeCross et al., 2024), 99.69 % with photons (Shi et al., 2022) and $\geq$ 99.85 % with Rydberg atoms (Scholl et al., 2023).

As for quantum metrology, it studies how quantum noise, a fundamental limitation of any measurement due to the quantum uncertainty principle, can be reduced by using well-chosen entangled states (Kitagawa and Ueda, 1993; Pezzè et al., 2018). It already has applications in interferometry for the detection of gravitational waves (collaboration LIGO, 2013) and in optical clocks (Robinson et al., 2024). Part of the current research

with quantum simulators focuses on the generation of spin-squeezed states (Gross et al., 2010; Hosten et al., 2016; Bornet et al., 2023; Eckner et al., 2023; Franke et al., 2023). The high-sensitivity of quantum objects to external fields is also used for applications in quantum sensing, for instance to measure radiofrequency electric fields with Rydberg atoms (Simons et al., 2021; Yuan et al., 2023; Trinh et al., 2024), static electric fields with ions (Sägesser et al., 2024) or tiny forces with nanowires (Rossi, 2019).

Current challenges: fidelity, scalability, tunability, detectability Going beyond the NISQ regime is a major challenge (Preskill, 2018). It requires facing those four general limitations:

- fidelity: improving the fidelity of the initial state preparation and its subsequent evolution, mitigating the effects of decoherence, reducing detection errors;
- scalability: increasing the number of particles and/or the number of degrees of freedom per particle (towards more quantum complexity);
- tunability: enhancing the range of accessible Hamiltonians, in views of simulating more physical situations (towards more universality);
- detectability: finding ways to access more information about the prepared states from the repeated projective measurements — or choose problems where simple observables have a large impact.

There are no known fundamental limitations to overcome those challenges; the difficulty seems to be mostly technological. As shown in Tab. 1, many strategies exist, let me emphasize a few of them.

Improving the fidelities requires the detection of errors and mitigation of their effect, to avoid their proliferation. A promising fault-tolerant method for digital simulators consists in replacing the noisy, *physical qubits* of the quantum simulator by error-corrected, *logical qubits* which are made of several physical qubits — the redundancy of the information making the logical state more robust to local errors (Shor, 1996). Then, properties of the logical state are measured via mid-circuit measurements on auxiliary qubits called *ancillas*, to check if errors happened and determine on which physical qubit they occurred. However, introducing more qubits also increases the number of error sources, so the rate of errors must be below a threshold for logical performance to improve with more physical qubits. Recently, a smaller error rate for logical qubits than for physical qubits was demonstrated experimentally, using

superconducting qubits (Google, 2023; Reichardt et al., 2024; Google, 2025) and Rydberg atoms (Bluvstein et al., 2024).

In terms of scalability, many efforts are devoted to increasing the number of isolated particles (physical qubits). In terms of number of individually-imaged particles, platforms with ions and atoms are probably the most advanced: hundreds of ions were imaged in a two-dimensional Paul trap (Guo et al., 2024), more than 6 000 atoms in an array of optical tweezers (Manetsch et al., 2024), and more than 10 000 atoms in an optical lattice (Tao et al., 2024) — with the caveat that the last two were not assembled to form a regular array. Combining those larger numbers of atoms with high many-body fidelities remains a challenge.

Take-home message

Thanks to recent technological progress, quantum simulation is now an experimental reality. In spite of their limitations in terms of state fidelity and number of particles, various experiments are already able to probe interesting effects. Their approach often requires to work hand in hand with classical numerical simulations, to benchmark the system and certify its outcome. Going beyond the NISQ regime is very challenging, and a universal quantum computer will probably not be achieved before a few decades, if ever. Meanwhile, we believe that NISQ analog quantum simulation is an interesting way to explore many-body physics. In the following, I describe in more detail the principle of our setup: arrays of rubidium atoms trapped in optical tweezers.

Our setup: arrays of single rubidium atoms in optical tweezers

In this section, I present the basics of our setup, which are necessary to understand the rest of the thesis. Since the setup started to be built in 2011, several generations of PhD students have succeeded each other[4]. The core setup is mainly their contribution, and in the following I will refer the interested reader to their PhD theses for more details. Part A of this thesis will also be devoted to the experimental upgrades realized during my time in the lab.

Controlling an atom with photons The internal structure of an atom is a collection of discrete energy levels (the electronic orbitals), between which numerous transitions are possible [Fig. 4(a)]. Using lasers, those transitions can be addressed for many purposes (Cohen-Tannoudji, 1998). How to trap an atom? Simply by lowering the energy of the currently-occupied electronic level, using off-resonant light focused at the desired trapping position (Chu et al., 1986; Grimm et al., 2000). How to see it? By sending resonant light and looking at the scattered photons (Schlosser et al., 2001). How to excite it? By absorption of a resonant photon. How to cool it down? By exchanging momentum between the atom and photons, using repeated cycles of absorption, spontaneous and stimulated emission (Chu et al., 1985).

In our case, we use rubidium atoms (^{87}Rb), an alkaline species which is chosen for the simplicity of its structure — like hydrogen, it contains only one valence electron. Moreover, its transition wavelengths lie conveniently in the near-infrared, where many lasers are available. For those reasons, it was one of the first atomic species to be cooled down and trapped in the 1990's, leading for example to the first Bose-Einstein condensate (Anderson et al., 1995). While the early experiments were performed in a gas of many atoms, it was later discovered that a single atom can be isolated and imaged in a micrometer-size optical dipole trap, called an *optical tweezer* (Schlosser et al., 2001)[5].

[4] Eight PhD students to be exact (Lucas Béguin, Sylvain Ravets, Henning Labuhn, Sylvain de Léséleuc, Vincent Lienhard, Pascal Scholl, Kai-Niklas Schymik and Guillaume Bornet). There were also post-docs (Aline Vernier, Daniel Barredo, Thomas Boulier, Hannah Williams, Cheng Chen, Mu Qiao, Yuki Torii Chew) and three permanent members (Florence Nogrette, Thierry Lahaye, Antoine Browaeys).

[5] Antoine Browaeys once told me that this discovery is a good example of serendipity. At the end of their working day, the PhD students in Philippe Grangier's team switched off the atomic flux that was feeding their optical dipole trap with many atoms. After a few minutes, they realized that there was a blinking fluorescence signal at the position of the trap... It was a single atom!

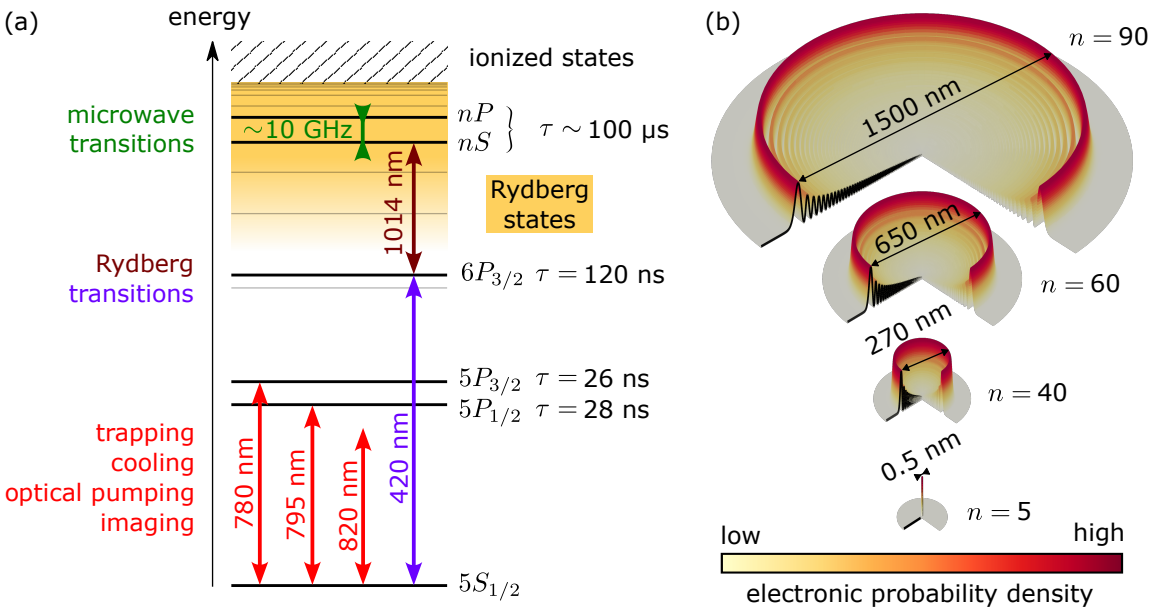

Figure 4: Energy levels of a ^{87}Rb atom, together with the transitions used in this thesis. (a) Energy levels are represented as grey lines (not to scale for clarity), neglecting the hyperfine and Zeeman sublevels. Among all possible energy levels, some are chosen for specific tasks (black lines); associated transitions are indicated by the vertical arrows. An important parameter to take into account for this choice is the lifetime τ of the states: low-excited states with short lifetimes are typically used for cooling and imaging since they can scatter more photons in a given time; whereas states with longer lifetimes (ground state and Rydberg states, indicated by the orange area) are suitable for the quantum simulation itself. (b) Electronic orbitals (radial part) of four states nS with respective principal quantum numbers $n \in \{5, 40, 60, 90\}$. The color code indicates the probability density of the valence electron in arbitrary units, calculated using the software Pairinteraction (Weber et al., 2017).

Three key ingredients allow us to perform quantum simulation with Rydberg atoms:

- creation and detection of arrays of individual atoms with controlled geometries;
- strong, tunable pairwise interactions between Rydberg atoms;
- good-fidelity, versatile manipulations of the Rydberg states.

In the remaining of this introduction, I will briefly go through each of these ingredients, and then present how we use them in a typical experimental sequence.

Arrays of randomly-filled optical tweezers Let me start by presenting the first key ingredient of our setup, its ability to trap and image many atoms in controlled geometries. There are actually two technical challenges: first, how to create arrays of microscopic traps with controlled geometries? Second, how to fill all of them with

individual atoms? During the last decade, those challenges were solved by several technical innovations that involve a combination of static and moving optical tweezers. I briefly review them in the following.

An *optical tweezer* relies on the optical dipole potential, a spatially-dependent lightshift generated by a laser spot whose frequency is red-detuned from an atomic transition [Fig. 5(a)]. Since the trapping potential is proportional to the intensity of the beam, atoms can be trapped at the maximum of intensity of a red-detuned laser spot (Grimm et al., 2000). Due to light-assisted collisions, a regime can be reached where a single atom is trapped in the tweezer (Schlosser et al., 2001). To generate a given geometry of trapped atoms, it is thus sufficient to create an array of laser spots which have their maxima at the desired positions of the atoms. We achieve this experimentally by a holographic method (Nogrette et al., 2014): a laser beam with Gaussian intensity profile and spatially-controlled phase is focused through a high-numerical-aperture ($NA = 0.5$) aspheric lens, leading to a controlled intensity pattern in the focal plane of the lens [Fig. 5(c)]. The phase pattern is imprinted on the laser beam by a spatial-light modulator (SLM); it is calculated using the Gerchberg-Saxton algorithm and a feedback loop is applied to correct for inhomogeneous trapping depths (de Léséleuc, 2018). Although the intensity patterns were already extended to three spatial dimensions in Barredo et al. (2018), the data shown in this thesis will be restricted to two-dimensional geometries which are experimentally easier to handle for quantum simulation[6]. Atoms are loaded into the array from a cloud of atoms in a magneto-optical trap (MOT) which is generated by three pairs of counter-propagating beams at 780 nm. We can then image all atoms at once by globally shining resonant MOT light on the array during 20 ms, and collecting the resulting *fluorescence image* on a camera: this gives us bright spots at the positions where atoms are present in the tweezers, and dark sports everywhere else [Fig. 5(b,c)].

By doing so, we obtain static arrays of optical tweezers where we can trap and image individual atoms. Our tweezers are generated by a laser with a wavelength of 820 nm; they have a typical waist of 1 µm and a trap depth of 1 mK (i.e. 20 MHz). Two tweezers can be brought to any distance above 3 µm. The largest extent of the array is limited by the field of view of the aspheric lens: in practice, we obtain tweezers with satisfactory shapes inside a disk of about 140 µm in diameter. Beyond this limit, geometrical aberrations prevent us from trapping and imaging reliably. For

[6]Due to the intrinsic two-dimensional symmetry of our setup, imaging and assembling atoms in two dimensions is easier than in three dimensions. Another problem is that most Rydberg-Rydberg interactions are not isotropic in three dimensions. But of course, three-dimensional geometries would be of great interest for future prospects!

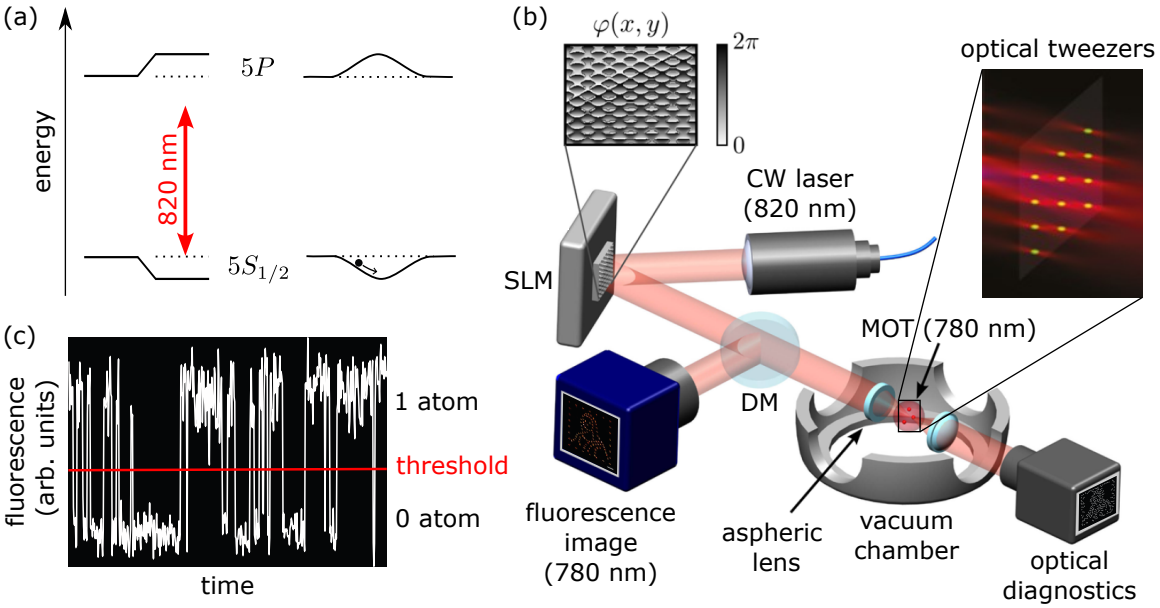

Figure 5: Creation and detection of arrays of optical tweezers with arbitrary geometries. (a) Principle of an optical tweezer: a red-detuned light beam from the $5S_{1/2}$ to $5P$ transition creates a negative lightshift on $5S_{1/2}$ and a positive one on $5P$. A focused Gaussian beam can thus trap an atom in $5S_{1/2}$ at the maximum of light intensity. (b) Experimental setup for trapping individual atoms in optical tweezers [adapted from Nogrette et al. (2014)]. To generate the tweezers, a Gaussian beam at 820 nm is reflected on a spatial-light modulator (SLM) and then focused by an aspheric lens inside the vacuum chamber, resulting in a controlled intensity pattern in the focal plane of the lens (inset). Atoms are loaded in the tweezers from a magneto-optical trap (MOT). A CCD camera at the back of the chamber can be used for optical diagnostics of the tweezer pattern. To image the atoms with single-site resolution, MOT light is shined on the array and the fluorescence at 780 nm is collected through a dichroic mirror (DM) by an EMCCD camera. (c) Example of fluorescence trace showing the presence and absence of a single atom in a tweezer. The red line is an empirical threshold that separates the two cases.

a given lattice spacing, this limits the number of atoms that we can trap in one array. Another limitation is the available laser power, which scales linearly with the number of tweezers: at 820 nm, we need approximately 4 mW per tweezer on the atoms, which means that 250 tweezers can be generated with ~ 1 W. This power is obtained by a titanium-sapphire laser (M-squared SolsTIS). Overall, we can achieve a few hundred of trapped atoms on the array (Scholl, 2021).

A fundamental limit of this arrangement is that the loading of an atom in the tweezers is random: due to the light-assisted collisions, pairs of atoms in the same tweezer are ejected when we shine the imaging light; this projects the number of atoms on either 0 or 1, depending on its initial parity. In the end, each tweezer has a probability of only $\sim 50\%$ to be filled by an individual atom after the imaging. This

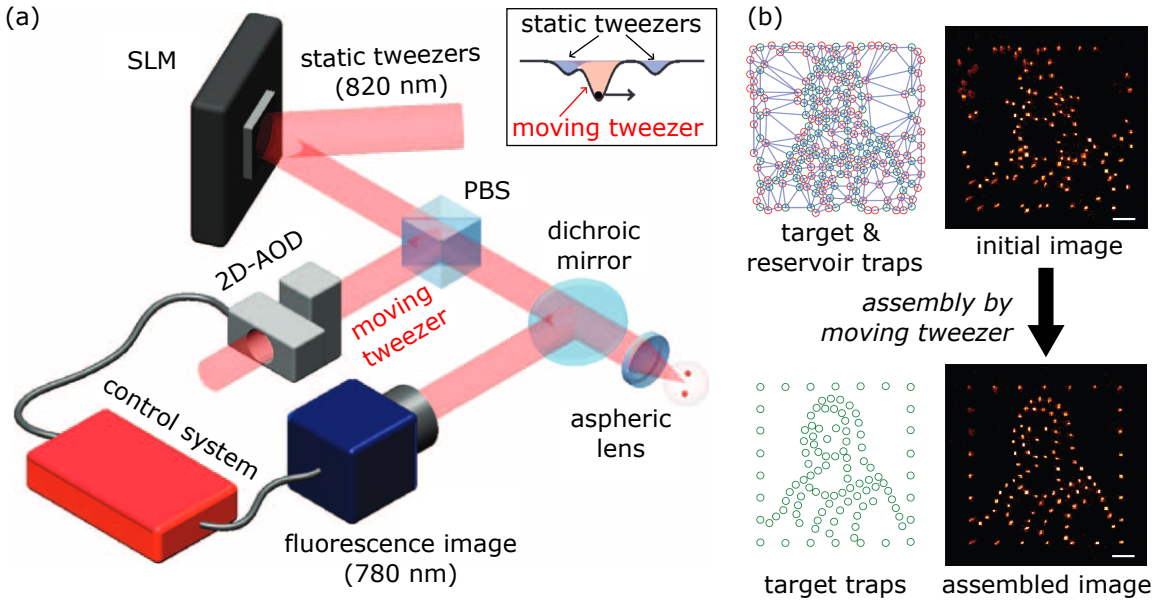

Figure 6: Assembly of defect-free arrays from randomly-filled arrays. (a) Experimental setup for the assembling procedure [adapted from Barredo et al. (2016)]. An additional "moving tweezer" at 820 nm is merged with the static tweezers using a polarized beam splitter (PBS). Its power and its position in the atomic plane can be dynamically tuned using a two dimensional acousto-optic deflector (2d-AOD). The moving tweezer is able to grab an atom in a static tweezer and move it to another tweezer (inset). (b) Example of assembling procedure [adapted from Schymik (2022)]. To fill a target array with individual atoms (bottom-left image), a larger array of static tweezers is generated (top-left), made of both target traps (green circles) and reservoir traps (red circles). When loaded from the MOT, each trap has only ∼50% of chance to be filled due to light-assisted collisions, leading to randomly-filled arrays (top-right fluorescence image). The moving tweezer then rearranges the array by moving atoms one-by-one from the filled reservoir traps to the empty target traps. A final fluorescence image (bottom-right) is performed to check the success of the procedure.

means that an array of N traps has a probability of $\sim 1/2^N$ to be totally filled, which is not acceptable for large arrays. For example, to obtain a defect-free array of $N = 20$ atoms, we would need to wait for one million repetitions of the experiment, which takes approximately 10 days if each repetition takes 0.8 second! To solve this issue, we use an assembling technique which makes use of a moving tweezer to fill each tweezer with one atom.

Assembly of defect-free arrays The basic idea of the assembling procedure is to split the tweezers in two categories: *target traps*, which we want to be filled with one atom, and *reservoir traps*, which we want to be empty [Fig. 6(b)]. An additional tweezer is added on top of the static array, and can be moved in the atomic plane

using a two-dimensional acousto-optic deflector (2d-AOD) [Fig. 6(a)]. This moving tweezer is able to grab an atom in one trap and deposit it in another trap, with a high-probability ($> 99\%$). One assembling cycle works as follows (Barredo et al., 2016): the whole array (targets and reservoirs) is loaded by the MOT, and a first fluorescence image is taken; from this initial image, the positions of the atoms are extracted and given to an algorithm. Next, the algorithm computes on the fly the moves that are required to transfer the atoms from the unwanted filled reservoir traps to the empty target traps; those moves are then performed by the moving tweezer. Once it is done, we also remove atoms in the remaining filled reservoir traps. Finally, a last fluorescence image is taken to check if all atoms have been moved correctly. The whole cycle takes a few tens of ms (between 80 and 150 ms), including the imaging time of twice 20 ms. For large arrays, two or three assembling cycles can be necessary. Crucial to the performance of the assembly is the control setup and the algorithm, which have to be fast and well-synchronized. A detailed description of the setup can be found in de Léséleuc (2018), and recent updates on the algorithm in Schymik et al. (2020) and Schymik (2022).

Strong, tunable interaction Strong interactions between two atoms are achieved by exciting them to Rydberg states, which are highly-excited states located close to the ionization threshold [orange region of Fig. 4(a)]. Rydberg states are characterized by extremely-large electronic orbitals [Fig. 4(b)] which lead to exaggerated properties compared with the ground state: large transition dipole, long lifetimes (compared with the low-excited states), enhanced sensitivity to external fields, strong interactions, etc. (Gallagher, 1994). Interactions strongly depend on the principal quantum number n of the Rydberg states, and on the interatomic distance, allowing us to control their value (Browaeys et al., 2016). A realistic order of magnitude for $n = 60$ is 0.1 to 1 MHz for an interatomic distance of about 10 µm, leading to dynamics that are two orders of magnitude faster than the natural Rydberg lifetimes ($\tau \sim 100$ µs). I won't go into more details on the Rydberg-Rydberg interactions in this introduction, since chapter 3 of this thesis is dedicated to this topic.

Rydberg manipulations Since Rydberg states are highly sensitive to electric and magnetic fields, we need to control them accurately. Different sets of coils allow us to control the magnetic field in the vicinity of the array. Two main pairs of coils in Helmholtz configuration serve for applying a strong, constant magnetic field (up to 50 G) during the Rydberg sequence, in order to lift the degeneracy between the

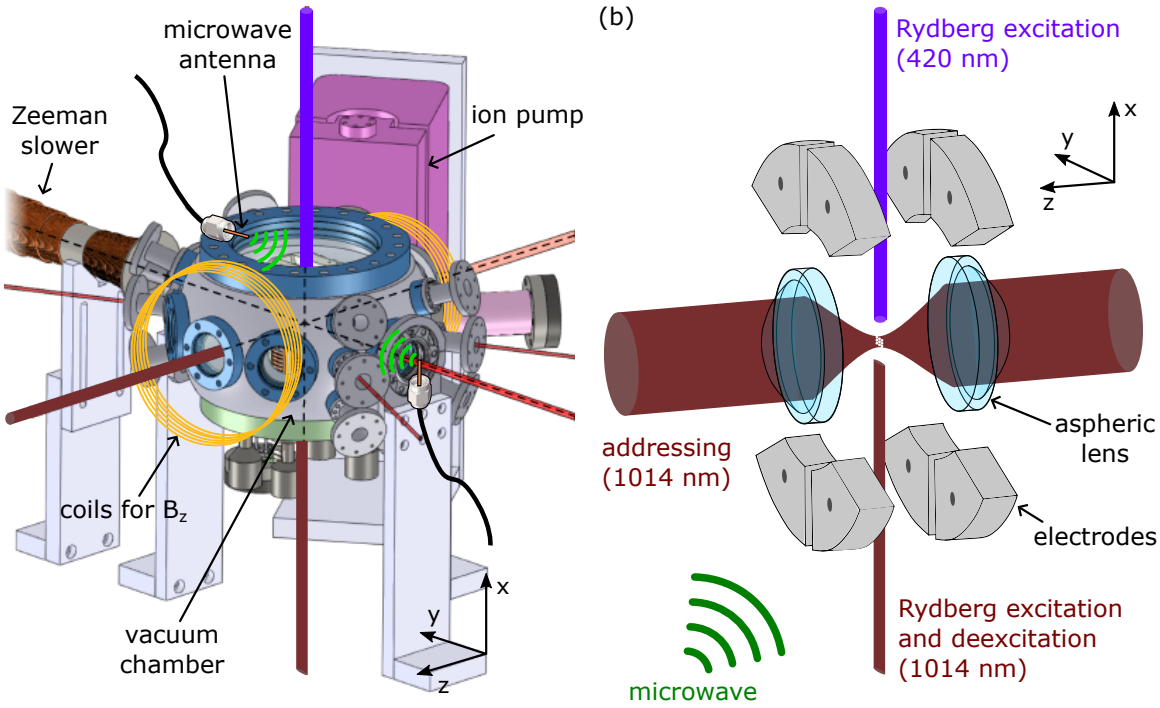

Figure 7: Overview of the experimental tools for Rydberg manipulations. (a) Out-of-vacuum Rydberg control [adapted from Beguin (2013)]. The surroundings of the vacuum chamber contain several pairs of coils, two of which being shown for the generation of the main magnetic field along z (B_z). There are also several microwave antennas for driving Rydberg-Rydberg transitions, which are located close to the windows to maximize the power seen by the atoms. (b) In-vacuum control [adapted from Bornet (2024)]. Six electrodes are used for compensating residual electric fields. Rydberg excitation is performed by two vertical counter-propagating beams at 420 nm and 1014 nm, the 1014-nm beam being more focused along z than along y to maximize its Rabi frequency. An addressing beam goes through the aspheric lenses for local control.

Zeeman sublevels: a pair of coils located inside the chamber can generate a magnetic field along x (in the plane of the atomic array); and another pair located outside the chamber can create a field along z (perpendicularly to the array) [Fig. 7(a)]. Three additional smaller pairs of coils, centered on the three main axes x, y and z, are used to compensate residual magnetic fields of up to 3 G (Beguin, 2013).

To set the electric field, eight electrodes are located in the vacuum chamber, close to the array [Fig. 7(b)]. They are connected to three voltage sources in a way that allows us to tune the electric field along three almost-independent directions (Beguin, 2013). In most cases, we want to work with zero electric field, so we use the electrodes to compensate the residual electric field on the array (Scholl et al., 2021), which, in the absence of compensation potentials, would be around 0.1 V/cm.

Excitation of an array of atoms from the ground-state manifold $5S_{1/2}$ to a chosen

Rydberg state is performed in two steps. First, we optically pump the atom into a stretched state of the ground-state manifold, $\left|5S_{1/2}, F = 2, m_F = 2\right\rangle$. To do so, we shine circularly-polarized laser light at 795 nm on the array, together with a repumper at 780 nm to avoid atoms leaking in the $F = 1$ manifold. Second, we perform a two-photon transition using 420 nm and 1014 nm lasers, via the intermediate state $\left|6P_{3/2}, F' = 3, m_F = 3\right\rangle$ [Fig. 4(a)]. Due to selection rules for dipole transitions, this allows us to target the Rydberg states with orbital quantum number $L = 0$ and $L = 2$, i.e. states nS and nD. In this thesis, we will always excite the atoms to states of the form $\left|nS_{1/2}, m_J = 1/2\right\rangle$ with $60 \leq n \leq 90$. The two-photon transition can either be a π-pulse, when the excitation lasers are far-detuned from the intermediate state, or a stimulated Raman adiabatic passage (STIRAP) with an intermediate detuning close to 0 (de Léséleuc, 2018). The excitation scheme used in this thesis is mostly STIRAP, since it has the advantage to be more robust to intensity variations than a π-pulse, and is thus less sensitive to drifts and spatial inhomogeneities. With the laser setup and parameters described in Bornet (2024), we achieve excitation efficiencies of 98 ± 1 % for $n = 60$[7], homogeneous across the array, using a pulse of total duration ~ 2.5 µs.

Our measurement scheme also requires deexciting atoms from a Rydberg state to the ground-state manifold, where they will be imaged. The deexcitation is performed by shining a pulse of 1014 nm light on the array during 2.5 µs, on resonance with the transition $\left|nS_{1/2}, m_J = 1/2\right\rangle \rightarrow \left|6P_{3/2}, F' = 3, m_F = 3\right\rangle$. Since the intermediate state has a short lifetime $\tau = 120$ ns, it quickly decays to the ground-state manifold $5S_{1/2}$. The efficiency of the deexcitation pulse is 98 ± 1 %.

Finally, two crucial tools allow us to perform rotations and transitions between Rydberg states: a microwave setup, composed of generators and antennas, and an additional laser beam at 1014 nm called the *addressing* beam [Fig. 7(b)]. They will be presented in more details in chapter 2 of this thesis.

A typical experimental sequence Now that I have briefly presented the tools that we need for controlling individual atoms, I will explain how we gather these tools to make an effective quantum simulation. I will go through the typical experimental sequence which is illustrated in Fig. 8.

1. **State initialization** We start by generating a cloud of rubidium atoms in a MOT close to the static array of tweezers. In approximately 200 ms, a sufficient number of atoms is loaded from the cloud into the tweezers. A first fluorescence

[7] Simulations show that this value is mostly limited by the finite lifetime of the intermediate state, and to a smaller extent by non-optimal pulse shape (Leclerc, 2024).

image of the array is taken (during 20 ms), projecting the number of atoms of each tweezer into 0 or 1 with probability $\sim 50\%$. The resulting randomly-filled array is then assembled into a defect-free array using the moving tweezer; a few ms are needed to compute the moves and about 1 ms per individual move to perform them. A second fluorescence image is taken to check the success of the assembly. Next, we perform several cooling steps to minimize the atomic motion inside the tweezers: polarization gradient cooling (PGC) and Raman sideband cooling (RSC, which will be presented in details in chapter 1 of this thesis). On top of that, we adiabatically ramp down the tweezer depth to $\sim 25\%$ of its initial value, in order to reduce the atomic velocity dispersion (see comments in sec. 1.4 for more explanations). Meanwhile, the magnetic field is set to its desired value for the quantum simulation (usually along z). The next step is the Rydberg excitation using optical pumping and STIRAP, followed by potential global and local rotations in the Rydberg manifold (see chapter 2 of this thesis), depending of the many-body problem we are studying. Note that the tweezers have to be switched off before the Rydberg excitation, since Rydberg states are anti-trapped by the ponderomotive force exerted by the tweezers.

2. **Time evolution** Atoms naturally evolve under dipole-dipole interactions: this is the core of the quantum simulation. The duration of this step is typically a few µs, and is limited by Rydberg lifetimes and the motion of the atoms in free flight.

3. **Projective measurement** The exact sequence for the measurement depends on the details of the observable we want to measure. Another set of microwave rotations can be applied to chose the measurement basis. Then, atoms can be deexcited from a specific Rydberg state to the ground-state manifold. Once it is completed, the tweezers are switched on again to their maximal value, such that atoms in the ground state are recaptured, whereas atoms remaining in Rydberg states are ejected and lost. Finally, the magnetic field is set back to its MOT settings and a last fluorescence image is taken. The result of one measurement is a bitstring containing the status of each atom: either present (if recaptured and imaged) or absent (if lost).

This whole sequence is repeated many times to accumulate statistics on the measurement outcomes, and compute the observables we are interested in.

Since measurements are independent from each other, the statistical uncertainty on an observable decreases as $1/\sqrt{N}$ with N the number of measurements. For example,

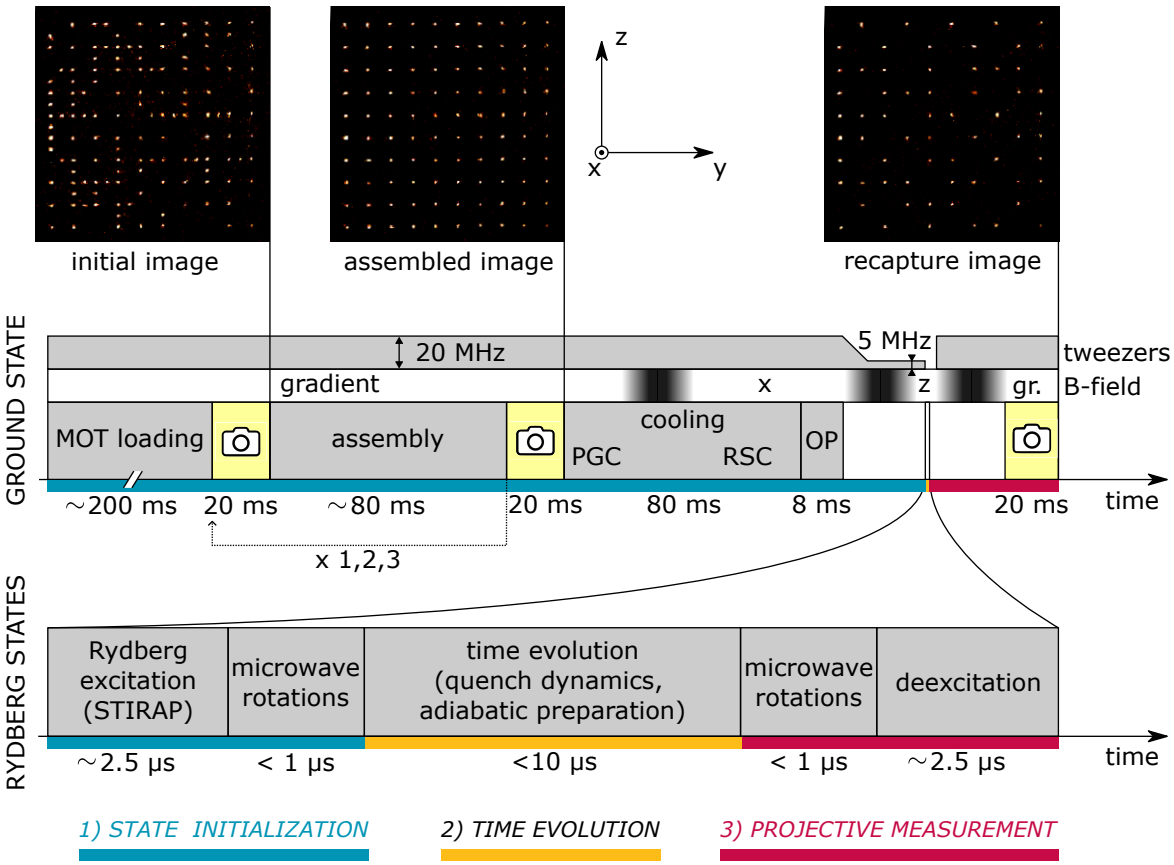

Figure 8: A typical experimental sequence (see text for detailed description). Ground-state manipulations include: depth of the tweezers (indicated in MHz), direction of the magnetic field ("gradient" refers to the anti-Helmholtz configuration, "z" and "x" refer to the Helmholtz configuration for a uniform field along the indicated direction), and various steps including loading, imaging assembling, cooling ("PGC" stands for "polarization gradient cooling" and "RSC" for "Raman sideband cooling") and optical pumping (OP). The assembly can be repeated one to three times. The sequence is classified into the three steps defined in Fig. 2 by the blue, yellow and red color bands.

let us consider a specific atom on the array. The measurement outcomes for this atom are a set of classical bits $\{x_i\}_{1\leq i\leq N}$ where $x_i = 1$ (respectively, $x_i = 0$) means that the atom has been recaptured (resp. lost) at shot i. The statistical frequency of the event "the atom is recaptured" is given by $X(N) = 1/N \sum_{i=1}^{N} x_i$. When $N \to \infty$, it converges to the recapture probability p of the considered atom. The statistical uncertainty on $X(N)$ (also known as *standard error on the mean*) is then given by $\sqrt{p(1-p)/N}$. This reasoning can be extended to any observable A: the standard error on the mean of A will be given by $\sigma_A/\sqrt{N}$ where σ_A is the standard deviation of A. In practice, we typically chose $N \sim 100 - 1000$ which is a trade-off between the statistical uncertainty and the noise due to the drifts of the experimental parameters (laser power, static electric and magnetic fields, etc.).

Take-home message

Our setup can generate arbitrary geometries of micro-traps for ^{87}Rb atoms, called arrays of *optical tweezers*. A subset of the array can be totally filled with individual atoms, by an assembling technique which makes use of a moving tweezer to grab the atoms one by one. This versatile technology is combined with a set of tools to manipulate atoms into highly-excited states called *Rydberg states*, which are characterized by strong electric dipoles and long lifetimes. We can thus expect two atoms located in different tweezers to interact via the dipole-dipole interaction with long coherence times, which makes this platform suitable for quantum simulation.

Outline of this thesis

Most of my time as a PhD student was spent on an already-working experiment[8], from my first day of internship in April 2021 to the beginning of writing of this manuscript in July 2024. For this, I am grateful to all the previous PhD students, post-docs, engineers and researchers who designed and built the setup before my arrival. I take the opportunity to thank them all again. My first role was to run the machine and take data for studying many-body effects; and my second job was, from time to time, to implement improvements on the existing setup — without, if possible, breaking the already-working part! In this thesis, I will talk about both roles: Part A is dedicated to upgrades of the setup; and part B to many-body effects. I would also like to emphasize that all the results presented in the manuscript were obtained within our team and in collaboration with theoreticians; credit for this should go to all members.

Chapter 1 presents a cooling method (Raman sideband cooling) that we added on the setup for reducing the atomic motion close to its quantum limit.

In chapter 2, I will show methods for driving transitions between Rydberg states, globally on the full array (section 2.1) or with local control (section 2.2).

Chapter 3 dives into the details of dipole-dipole interactions between two atoms in Rydberg states. After reminding their various contributions and their usual mappings on spin models (section 3.1), I will focus on the off-diagonal terms (sometimes called "spin exchanges") in sections 3.2, 3.4 and 3.3.

In chapter 4, I will discuss our results on equilibrium properties of the dipolar XY

[8] If we except all the inevitable disasters that experimentalists experience regularly: AC failures, power cuts, water leaks, lasers dying...

spin model in various geometries: a one-dimensional spin chain (section 4.2) and a two-dimensional square array (section 4.1).

Chapter 5 introduces a method that we developed for measuring the dispersion relation of low-energy states of the XY spin model. After presenting the principle of the method (section 5.1), I will show how we apply it to the case of a one-dimensional chain (section 5.2) and a two-dimensional square array (section 5.3).

Finally, chapter 6 reports the implementation of a new interacting model, which makes use of three Rydberg states instead of two, to generate a spin-hole model: the so-called bosonic t-J-V model.

Part A:
Upgraded toolbox for quantum simulation with arrays of Rydberg atoms

L'homme se découvre quand il se mesure avec l'obstacle.
Mais, pour l'atteindre, il lui faut un outil.

Antoine de Saint-Exupéry, *Terre des Hommes*

Chapter 1

Reducing the atomic motion close to its quantum limit

> His memory was a lens, an illuminating searchlight which picked out fragments, isolating them, but forever failing to stop the ceaseless motion and modification which surged into his view.
>
> Frank Herbert, *Children of Dune*

An atom trapped in an optical tweezer is never perfectly localized, it "moves" due to both thermal and quantum fluctuations. This residual motion is a limitation for quantum simulation because the interactions between two atoms depend of their distance r: as we will see in more details in chapter 2, dipole-dipole interactions lead to power-law interactions of the form $J(r) \propto 1/r^\alpha$ with $\alpha \in \{3, 6\}$. If the interatomic distance fluctuates by Δr, then the interaction will fluctuate by a relative amount $\frac{\Delta J}{J} = \alpha \frac{\Delta r}{r}$. With $\frac{\Delta r}{r} \sim 1$ %, we see that the relative fluctuations $\frac{\Delta J}{J}$ can easily reach ~ 10 % of unwanted disorder, which can prevent us from preparing some fragile states of matter. For example, frustrated lattices are especially sensitive to positional disorder.

To mitigate the atomic motion, we need to cool down each atom in its tweezer to cancel its thermal fluctuations. This is why we implemented a cooling scheme called *Raman sideband cooling* (RSC), an adaption of *resolved sideband cooling* where coherent transitions and optical pumping are performed between motional levels of a particle trapped in a harmonic potential, in order to lower the average occupation number (Leibfried et al., 2003; Dalibard, 2014). RSC was first implemented with ions in radiofrequency traps (Monroe et al., 1995), then with atoms in optical lattices (Kerman, 2002) and more recently in optical tweezers (Kaufman et al., 2012; Thompson et al., 2013).

Our ambition for this project was to implement a simple version of RSC for practical improvement of the setup, with the constraints that the cooling should be robust to experimental drifts (to avoid recalibrating it every day) and to trap heterogeneities (such that all atoms of a potentially large array can be cooled down). For a more

careful study of the cooling procedure, I refer the interested reader to the following PhD theses: Kerman (2002), Kaufman (2009) and Thompson (2014).

Contents

Contributors

The implementation of RSC was the project of my master internship in the group, before the official start of my PhD thesis. Florian Wallner supervised me for the design and building of the cooling setup, under the management of Thierry Lahaye and Antoine Browaeys; we then integrated it on the main experimental setup with the rest of the experimental team. Most of the data shown in this chapter were taken by Guillaume Bornet and me.

1.1 Atomic motion in an optical tweezer

Motional eigenstates in a tweezer A tweezer is generated by a Gaussian beam which leads to the following trapping potential in the directions $\{x, y, z\}$:

$$V(x,y,z) = -U \exp\left(-2\,\frac{x^2+y^2}{w^2}\right)\frac{1}{1+(z/z_R)^2} \tag{1.1}$$

where $U \approx h \times 20$ MHz $\approx k_\mathrm{B} \times 1$ mK is the trap depth, $w \approx 1$ µm is the waist and $z_R \approx 4$ µm is the Rayleigh length. Since the typical atomic temperature in the tweezer ($T \sim 10\mu$K) is much smaller than U, the atom only explores the very bottom of the tweezer [Fig. 1.1(a)]. Close to its minimum, V can be approximated by a harmonic potential which reads (up to a constant term)

$$V(x,y,z) \approx V_\mathrm{harmonic}(x,y,z) = \sum_{\mu\in\{x,y,z\}} \frac{1}{2} m\omega_\mu^2 \mu^2 \tag{1.2}$$

with m the mass of our ^{87}Rb atoms and ω_μ is the trapping frequency along μ. The latter are related to the beam parameters by the relations: $\omega_x = \omega_y = \sqrt{\frac{4U}{mw^2}} \approx 2\pi \times 100$ kHz

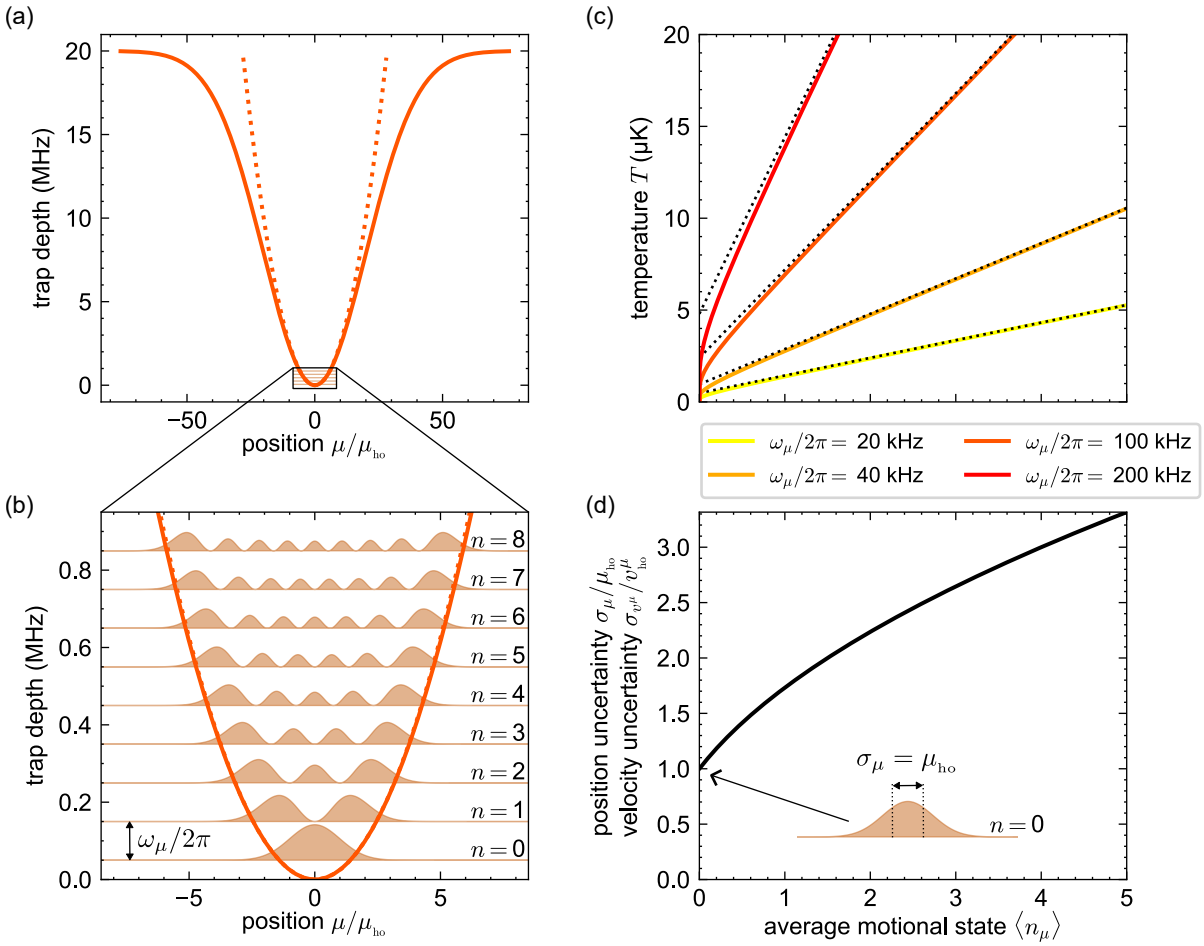

Figure 1.1: Motional eigenstates and thermal states in an optical tweezer. (a) Typical radial trapping profile of a tweezer (in MHz). The profile is Gaussian (solid line) and can be approximated by a harmonic potential (dotted line). The radial position $\mu \in \{x, y\}$ is rescaled by the characteristic length of the harmonic oscillator, $\mu_{\rm ho}$. (b) Zoom on the previous curve, at the bottom of the tweezer, with a representation of the first 9 motional eigenstates of an atom in the tweezer. For each eigenstate, the spatial density probability is shown, with a vertical offset corresponding to its energy. Energy levels form a regular ladder separated by the trapping frequency $\omega_\mu/2\pi$ which equals 100 kHz in this example. (c) Relation between temperature T and average motional state $\langle n_\mu\rangle$, in a thermal state, for various trapping frequencies ω_μ. The colored solid lines correspond to a bosonic thermal statistics (see Tab. 1.1), and the dotted black lines to the classical asymptotic behavior at high temperature. (d) Relation between position uncertainty σ_μ (rescaled by $\mu_{\rm ho}$) and average motional state $\langle n_\mu\rangle$, in a thermal state (see Tab. 1.1). This relation is independent of the trapping frequency. The ground state (at $\langle n_\mu\rangle = 0$) corresponds to the standard quantum limit, where thermal fluctuations are canceled and only quantum fluctuations remain. The same interpretation can be done for the velocity σ_{v^μ}.

in the radial directions and $\omega_z = \sqrt{\frac{2U}{mz_R^2}} \approx 2\pi \times 20$ kHz in the axial direction. As a result, the atomic motion in a tweezer is described by three independent harmonic oscillators. The motional eigenstates are given by the tensor products $\{|n_x\rangle \otimes |n_y\rangle \otimes |n_z\rangle\}_{(n_x,n_,n_z)\in\mathbb{N}^3}$ where n_μ is the n^{th} eigenstate of the harmonic oscillator along μ. The associated spatial wavefunctions are illustrated in Fig. 1.1(b) in one dimension, and their spectrum form a regular ladder with spacing $\hbar\omega_\mu$ along μ.

Reminders about thermal states in a harmonic oscillator When loaded into a tweezer, an atom is not in a motional eigenstate but rather in a thermal state. Its density matrix can be written $\rho = \rho_x \otimes \rho_y \otimes \rho_z$ where

$$\rho_\mu = \sum_{n\in\mathbb{N}} P_n^\mu \, |n\rangle \langle n| \, . \tag{1.3}$$

Here, $P_n^\mu = \left(1 - e^{-\hbar\omega_\mu/k_\mathrm{B}T}\right) e^{-\hbar\omega_\mu n/k_\mathrm{B}T}$ is the probability that the atom occupies the motional state $|n\rangle$ at temperature T. Basic mathematical properties of thermal states are reminded in Tab. 1.1. Two properties are noteworthy. First, the average occupation number follows a bosonic statistics that depends on the trapping frequency: the smaller ω_μ, the higher the average motional state for the same temperature [Fig. 1.1(c)]. For a typical temperature $T = 15$ µK before RSC, we obtain $\langle n_x\rangle \approx \langle n_y\rangle \approx 3$ radially and $\langle n_z\rangle \approx 15$ axially. Second, the position uncertainty σ_μ depends very simply on the average quantum number, when rescaled by a characteristic length scale $\mu_\mathrm{ho} = \sqrt{\frac{\hbar}{2m\omega_\mu}}$:

$$\sigma_\mu = \sqrt{2\langle n_\mu\rangle + 1}\, \mu_\mathrm{ho} \tag{1.4}$$

This dependence [which is illustrated in Fig. 1.1(d)] quantifies the crossover between thermal fluctuations, which dominate at high $\langle n_\mu\rangle$, and quantum fluctuations which dominate at low $\langle n_\mu\rangle$ — reaching $\sigma_\mu = \mu_\mathrm{ho}$ in the motional ground state. Before RSC, we estimate $\sigma_{x,y} \approx 70$ nm radially and $\sigma_z \approx 280$ nm axially. Let us now see how we can decrease those fluctuations.

1.2 Principle of Raman sideband cooling in one dimension

Basic schemes for RSC Let me first explain the principle of RSC for an atom in a one-dimensional harmonic trap with trapping frequency ω_μ. RSC makes use of transitions between internal states of the atom to reduce the average occupation number of its motional state. The basic scheme includes three internal states: two

	Fock state	Thermal state
Density matrix	$\rho_\mu = \lvert n\rangle\langle n\rvert$	$\rho_\mu = \sum_n P_n^\mu \lvert n\rangle\langle n\rvert$ with $P_n^\mu = \left(1 - e^{-\hbar\omega_\mu/k_\mathrm{B}T}\right) e^{-\hbar\omega_\mu n/k_\mathrm{B}T}$
Average occupation number	$\langle n_\mu\rangle = n$	$\langle n_\mu\rangle = 1 \,/\, \left(e^{\hbar\omega_\mu/k_\mathrm{B}T} - 1\right)$ Classical limit: $\langle n_\mu\rangle \sim \frac{k_\mathrm{B}T}{\hbar\omega_\mu}$ when $k_\mathrm{B}T \gg \hbar\omega_\mu$
Standard deviation in position σ_μ	$\sigma_\mu = \sqrt{2n+1}\,\mu_\mathrm{ho}$ where $\mu_\mathrm{ho} = \sqrt{\frac{\hbar}{2m\omega_\mu}}$	$\sigma_\mu = \sqrt{2\langle n_\mu\rangle + 1}\,\mu_\mathrm{ho}$ Classical limit: $\sigma_\mu \sim \sqrt{\frac{k_\mathrm{B}T}{m\omega_\mu^2}}$ when $k_\mathrm{B}T \gg \hbar\omega_\mu$
Standard deviation in velocity σ_{v^μ}	$\sigma_{v^\mu} = \sqrt{2n+1}\,v^\mu_\mathrm{ho}$ where $v^\mu_\mathrm{ho} = \sqrt{\frac{\hbar\omega_\mu}{2m}}$	$\sigma_{v^\mu} = \sqrt{2\langle n_\mu\rangle + 1}\,v^\mu_\mathrm{ho}$ Classical limit: $\sigma_{v^\mu} \sim \sqrt{\frac{k_\mathrm{B}T}{m}}$ when $k_\mathrm{B}T \gg \hbar\omega_\mu$

Table 1.1: A few properties of Fock and thermal states in a harmonic oscillator with trapping frequency ω_μ along a direction $\mu \in \{x, y, z\}$.

long-lived states $|g\rangle$ and $|f\rangle$ which can be coherently coupled via a Raman transition; and one short-lived state $|e\rangle$ which is coupled to $|g\rangle$ via an optical pumping beam. The situation is illustrated in Fig. 1.2(a). RSC can be conceptually understood in three steps. Suppose that the atom initially occupies the state $|f, n_\mu\rangle \equiv |f\rangle \otimes |n_\mu\rangle$. First, a Raman transition transfers the atom from $|f, n_\mu\rangle$ to $|g, n_\mu - 1\rangle$. This can be achieved by detuning the Raman transition by an amount equal to the trapping frequency [green arrows from Fig. 1.2(a)]. After this, we want the atom to be back to $|f\rangle$, without changing its motional state. To do so, a solution is to transfer the atom to the third level $|e\rangle$ with the optical pumping beam [red arrow from Fig. 1.2(a)], which quickly decays back to $|f\rangle$ by spontaneous emission [wavy blue line in Fig. 1.2(a)]. Performing the optical pumping without changing the motional state requires to be in the Lamb-Dicke regime, which will be described more precisely in the following.

There are two ways to carry out RSC:

- *Pulsed cooling*: the beams are switched on successively. First, a π-pulse is performed on the Raman transition to transfer the atomic population from $|f, n_\mu\rangle$ to $|g, n_\mu - 1\rangle$, and then the optical pumping is switched on to go from $|g, n_\mu - 1\rangle$ to $|e, n_\mu - 1\rangle$. This procedure is repeated many times until the atom ends up in $|f, n_\mu = 0\rangle$.

- *Continuous cooling*: all beams are switched on simultaneously until reaching a steady state. The atomic system is then governed by rate equations, which depend on the optical power in each beam. If the parameters are chosen correctly, the atom is optically pumped into $|f, n_\mu = 0\rangle$, the only state that is dark to the detuned Raman transition.

Even if it is slower (Kaufman, 2009), we chose the second method, which is rather straightforward to implement.

Lamb-Dicke regime An important condition for RSC is the preservation of the motional state during optical pumping. To understand how this can be achieved, let us look at the Hamiltonian of the light-matter interaction for our three-level system. We also define $\Omega_{1,2,\mathrm{op}}$ the Rabi frequency of the Raman beams and the optical pumping beam, and $k_{1,2,\mathrm{op}} \equiv \mathbf{k}_{1,2,\mathrm{op}} \cdot \mathbf{e}_\mu$ the projection of their respective wavevectors on the cooling direction defined by the unit vector $\mathbf{e}_\mu$. In the basis $\{|g\rangle, |f\rangle, |e\rangle\}$, the Hamiltonian reads

$$H_{\mathrm{RSC}} = \frac{\hbar}{2} \begin{pmatrix} \Delta_{\mathrm{R}} & \Omega_{\mathrm{R}}^* \, e^{-i\Delta k \, \mu} & \Omega_{\mathrm{op}}^* \, e^{-ik_{\mathrm{op}}\mu} \\ \Omega_{\mathrm{R}} \, e^{i\Delta k \, \mu} & -\Delta_{\mathrm{R}} & 0 \\ \Omega_{\mathrm{op}} \, e^{ik_{\mathrm{op}}\mu} & 0 & 0 \end{pmatrix} \tag{1.5}$$

Here, $\Delta k = k_1 - k_2$ is the momentum transfer from the Raman beams to the atom, $\Omega_{\mathrm{R}} \equiv \frac{\Omega_1 \Omega_2^*}{2\Delta}$ is the effective two-photon Rabi frequency, and $\Delta_{\mathrm{R}} \equiv \delta + \frac{|\Omega_1|^2 - |\Omega_2|^2}{4\Delta}$ is the effective detuning, including the lightshifts induced by the Raman beams [Fig. 1.2(b)].

In a harmonic trap, the position operator μ can be written $\mu = \mu_{\mathrm{ho}} \, (a + a^\dagger)$ where $\mu_{\mathrm{ho}} = \sqrt{\frac{\hbar}{2m\omega_\mu}}$ is the characteristic length of the harmonic oscillator and $a, a^\dagger$ are the creation and annihilation operators of motional states. This allows us to define dimensionless coefficients for each transition, which are called the Lamb-Dicke parameters[1]:

$$\eta_{\mathrm{op}}^{\mu} \equiv \mu_{\mathrm{ho}} \, k_{\mathrm{op}} \tag{1.6}$$

$$\eta_{\mathrm{R}}^{\mu} \equiv \mu_{\mathrm{ho}} \, \Delta k. \tag{1.7}$$

An interesting interpretation can be made in the so-called Lamb-Dicke regime, defined by $\left(\eta_{\mathrm{R,op}}^{\mu}\right)^2 \, (2\langle n_\mu \rangle + 1) \ll 1$. In this case, a Taylor expansion of the exponential terms

[1] An equivalent definition of the Lamb-Dicke parameters is the ratio of the recoil energy and the trapping energy: $\eta_{\mathrm{R,op}}^{\mu} = \sqrt{\omega_{\mathrm{rec}}/\omega_\mu}$ with $\omega_{\mathrm{rec}} \equiv \hbar \, k_{\mathrm{op}}^2 / 2\, m$ for the optical pumping and $\omega_{\mathrm{rec}} \equiv \hbar \, \Delta k^2 / 2\, m$ for the Raman transition. The larger $\eta_{\mathrm{R,op}}$, the larger the recoil energy given to the atom by the photons.

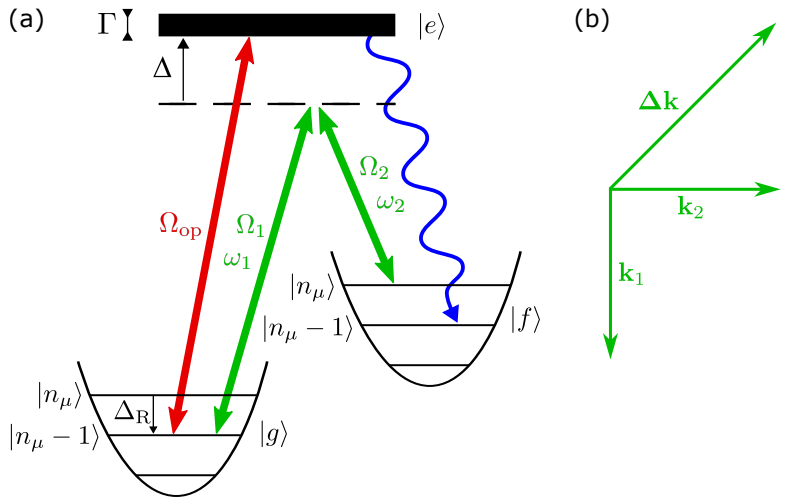

Figure 1.2: Principle of Raman sideband cooling. (a) The two internal states $|g\rangle$ and $|f\rangle$ are coherently coupled through a Raman process (in green) which is detuned by one trapping frequency, thus reducing the number of motional quanta by one unit (from $|f, n_\mu\rangle$ to $|g, n_\mu - 1\rangle$). Then the atom is transferred to the state $|f, n_\mu - 1\rangle$ thanks to an optical pumping beam (in red) followed by fast decay from the short-lived state $|e\rangle$ to the intermediate state $|f\rangle$ (in blue). Repeating this procedure, either iteratively ("pulsed cooling") or continuously ("continuous cooling") leads in principle to pump the atom in its motional ground state $|f, n_\mu = 0\rangle$, which is the only state unaffected by the process. (b) The transfer of momentum during the Raman transition happens in a direction $\mathbf{\Delta k}$ which is the difference between the wavevectors of the individual Raman beams: $\mathbf{\Delta k} = \mathbf{k}_2 - \mathbf{k}_1$.

can be made in Eq. (1.5):

$$H_{\mathrm{RSC}} = \frac{\hbar}{2}\begin{pmatrix} \Delta_{\mathrm{R}} & \Omega_{\mathrm{R}}^* & \Omega_{\mathrm{op}}^* \\ \Omega_{\mathrm{R}} & -\Delta_{\mathrm{R}} & 0 \\ \Omega_{\mathrm{op}} & 0 & 0 \end{pmatrix} + i\,\frac{\hbar}{2}\left(a + a^\dagger\right)\begin{pmatrix} 0 & -\eta_{\mathrm{R}}^\mu\,\Omega_{\mathrm{R}}^* & -\eta_{\mathrm{op}}^\mu\,\Omega_{\mathrm{op}}^* \\ \eta_{\mathrm{R}}^\mu\,\Omega_{\mathrm{R}} & 0 & 0 \\ \eta_{\mathrm{op}}^\mu\,\Omega_{\mathrm{op}} & 0 & 0 \end{pmatrix} + O\left[(\eta_{\mathrm{R,op}}^\mu)^2\right]. \tag{1.8}$$

The first matrix represents the couplings between the internal levels $|g\rangle$, $|f\rangle$ and $|e\rangle$ with the same motional state ($\Delta n = 0$). The second matrix corresponds to the couplings between internal states with a gain or a loss of one motional quanta ($\Delta n = \pm 1$). Since the coefficients of the second matrix are directly proportional to the Lamb-Dicke parameters, the latter can be interpreted as the ability of a laser to transfer momentum to the atom: the larger the Lamb-Dicke parameter, the more the atom receives momentum kicks from the photons, and the easier it is to change the motional state of the atom.

For RSC, we want the Raman couplings between different motional states to be

non-zero. From Eq. (1.8), the Rabi frequency of the Raman transition between states $|f, n_\mu\rangle$ and $|g, n_\mu - 1\rangle$ is

$$\begin{aligned}\Omega_{\mathrm{R}}^{(n,n-1)} &\equiv \frac{2}{\hbar} \langle f, n_\mu | H_{\mathrm{RSC}} | g, n_\mu - 1 \rangle \\ &= i\, \eta_{\mathrm{R}}^{\mu}\, \Omega_{\mathrm{R}}\, \sqrt{n} + O\left[(\eta_{\mathrm{R}}^{\mu})^2\right]. \end{aligned} \tag{1.9}$$

So we want η_{R}^{μ} to be non-negligible. With the setup presented in the following, we compute $\eta_{\mathrm{R}}^{x,y} \approx 0.27$ in the radial directions of the tweezers (using $\omega_{x,y} = 2\pi \times 100$ kHz); in the axial direction, $\eta_{\mathrm{R}}^{z} \approx 0.60$ (using $\omega_z = 2\pi \times 20$ kHz). Note that the interest of the Raman transition is to provide a high wave vector, compared with that of a microwave transition. This makes the Raman transition possible from $|f, n_\mu\rangle$ to $|g, n_\mu - 1\rangle$, if the detuning is chosen to match the resonance condition: $\Delta_{\mathrm{R}} = \omega_\mu$. However, the optical pumping should preserve the motional state, so the optical pumping transition should be in the Lamb-Dicke regime. With the setup presented in the following, we have $\eta_{\mathrm{op}}^{x,y} \approx 0.19$ and $\eta_{\mathrm{op}}^{z} \approx 0.43$, which is not negligible but sufficient for cooling, as we will see in the following.

1.3 A practical implementation of Raman sideband cooling

Experimental setup In the previous section, I explained that one pair of Raman beams can cool down the motional states along one given direction μ, as long as the Raman momentum transfer $\mathbf{\Delta k} = \mathbf{k}_1 - \mathbf{k}_2$ has an overlap with the cooling direction. In a practical implementation of RSC, we want to cool in several directions (ideally, all three directions), and the question of the number of Raman beams arises. There is not a single answer to this question, and several approaches exist in the literature. My understanding is that it depends on the isotropy of the potential. In the extreme case of a fully isotropic trapping potential, there are no predefined quantization axes for the motional states, so the cooling direction of a pair of Raman beams is defined by its momentum transfer $\mathbf{\Delta k}$. For three-dimensional cooling, we need three directions $\{\mathbf{\Delta k}\}$, so at least four pairs of Raman beams are required. In the other extreme case of a fully anisotropic trapping potential, the directions of the motional states are fixed by the anisotropy; one pair of Raman beams is theoretically sufficient to cool along all three directions[2], as long as each of them has an overlap with $\mathbf{\Delta k}$. In our case, we

[2]However, an additional difficulty of strongly anisotropic traps is that the trapping frequency depends on the direction. Consequently, the resonance condition of the Raman transition for removing one motional quanta is different along each direction.

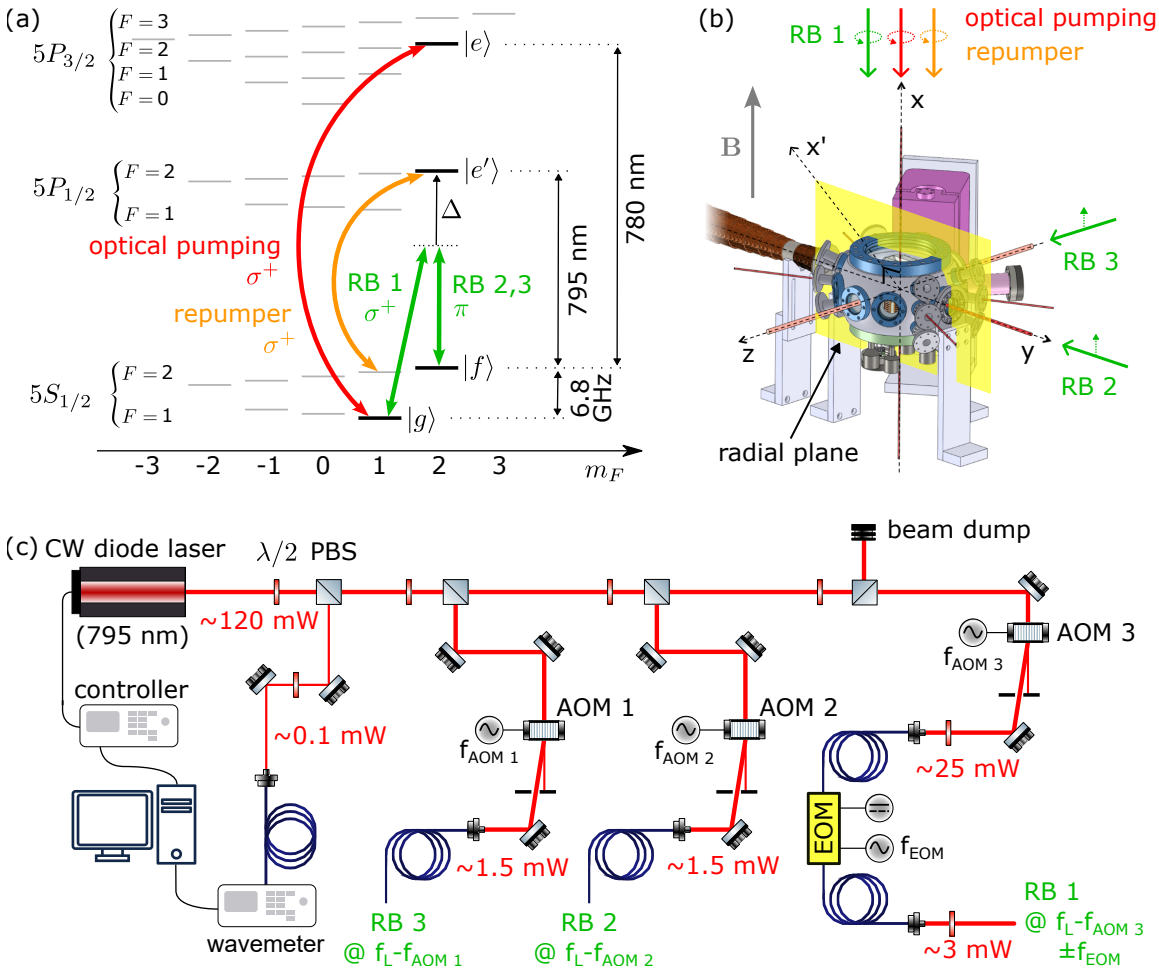

Figure 1.3: Experimental setup for Raman sideband cooling. (a) Internal atomic states of ^{87}Rb used in our Raman cooling procedure (see text for details). (b) Position and polarization of the laser beams used in the Raman scheme. Large colored arrows indicate the direction of propagation, and small colored dotted arrows the polarization. The radial plane (atomic plane) is the xy plane, indicated by a yellow rectangle. The magnetic field $\mathbf{B}$ is along x. x' is the direction addressed by the Raman pair {RB 1, RB 2}. (c) Optical setup used for the generation of the three Raman beams from a single laser. The laser is a grating-stabilized diode laser at 795 nm (DL Pro by Toptica Photonics). A small amount of light is first used for monitoring the wavelength, allowing us to perform a slow compensation of the drifts via the laser controller. Then the light is divided into three beams, one for each Raman beam, by a combination of a half-wave plate ($\lambda/2$) and a Polarized Beam Splitter (PBS). Each of them goes through an acousto-optic modulator (AOM) which controls the optical power and can fine-tune the frequency by an amount $f_{\mathrm{AOM1}} \approx f_{\mathrm{AOM2}} \approx f_{\mathrm{AOM3}} \sim 110$ MHz. Finally, one of the Raman beams (RB 1) goes through an electro-optic modulator (EOM) to detune it by $f_{\mathrm{EOM}} \sim 6.8$ GHz from the other beams. The resulting frequency of each beam is indicated in green, with f_{L} the bare laser frequency.

have two approximately isotropic radial directions and one axial direction, and the number of beams is limited by the optical access. Following Thompson et al. (2013), we decided to use three orthogonal Raman beams, allowing us to make two Raman transitions.

We use two hyperfine states of our ^{87}Rb atoms: $|g\rangle = \left|5S_{1/2}, F = 1, m_F = 1\right\rangle$ and $|f\rangle = \left|5S_{1/2}, F = 2, m_F = 2\right\rangle$ which are separated by 6.8 GHz [Fig. 1.3(a)]. The degeneracy between Zeeman levels is lifted by a magnetic field $B_x \approx 7$ G, which defines the quantization axis. Two Raman beams at 795 nm, denoted by RB 1 and RB 2, are used for radial cooling, and a third Raman beam can be used for both radial and axial cooling [Fig. 1.3(b)]. They are far-detuned from the excited state $|e'\rangle = \left|5P_{1/2}, F = 2, m_F = 2\right\rangle$, by an amount $\Delta \approx 2\pi \times 5$ GHz. Since the magnetic quantum number m_F is changed by one unit, one of the Raman beams (RB 1) needs to be circularly polarized (σ^+) and the other ones (RB 2 and 3) linearly polarized (π). An optical pumping beam [red arrow in Fig. 1.3(a)] connects $|g\rangle$ to $|e\rangle = \left|5P_{3/2}, F = 2, m_F = 2\right\rangle$ which then decays back to $|f\rangle$ by spontaneous emission with a lifetime of 26 ns. An additional repumper beam [orange arrow in Fig. 1.3(a)] is necessary to avoid the atoms accumulating in the $F = 2$ manifold of $5S_{1/2}$[3].

To generate the three Raman beams, we use a single diode laser and an electro-optic modulator (fiber EOM NIR-MX800-LN-10 by iXblue) to shift the frequency of RB 1 by 6.8 GHz compared with RB 2 and RB 3. The EOM is a Mach-Zehnder interferometer which allows us to create two sidebands at the modulation frequency $f_{\mathrm{EOM}} \sim 6.8$ GHz, while canceling the carrier with a DC bias voltage. The detailed optical setup is illustrated in Fig. 1.3(c). The resulting frequency of RB 1 is $f_{\mathrm{RB1}} = f_{\mathrm{RB2,3}} \pm f_{\mathrm{EOM}}$, and we use the +1 sideband for driving the Raman transition[4]. To keep the Raman detuning fixed within a few ~ 10 MHz, we use a home-made feedback system that reads the laser frequency with a wavemeter, and applies corrections on the laser piezoelectric actuator.

Two-photon Rabi oscillation To test the coherence of our Raman setup, we acquire a two-photon oscillation between the states $|f\rangle$ and $|g\rangle$, with $\Delta_{\mathrm{R}} = 0$ resonant with the carrier transition $|f, n_{x'}\rangle \leftrightarrow |g, n_{x'}\rangle$. Here, x' is the radial direction probed by the

[3] The names for the repumper and the optical pumping can be misleading, due to the fact that they have opposite roles for MOT cooling and for RSC. Indeed, the "optical pumping" for the MOT is the "repumper" for RSC and vice-versa. The names given in Fig. 1.3(a,b) correspond to the naming convention of RSC.

[4] The -1 sideband also leads to a resonant transition $|f\rangle \leftrightarrow |g\rangle$ which makes use of a π-polarized RB2 at f_{RB2} and a σ^--polarized RB1 at $f_{\mathrm{RB1}} = f_{\mathrm{RB2}} - f_{\mathrm{EOM}}$. But this contribution can be canceled by setting the polarization of RB 1 to be perfectly σ^+.

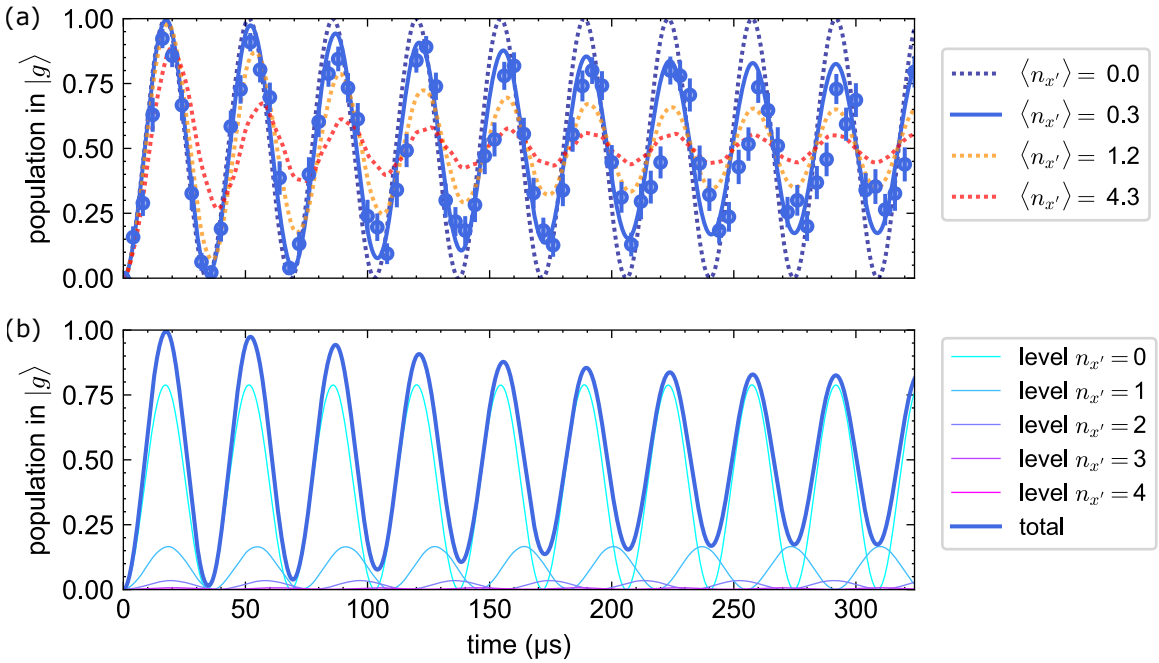

Figure 1.4: Two-photon Rabi oscillation using RB 1 and RB 2. (a) Blue points: population of the internal state $|g\rangle$ as a function of the Raman pulse duration, for a single atom. The coherent oscillation is compared with simulations including the motional states, with the effective Rabi frequency Ω_R as the only free parameter. The damping can be fully explained by thermal average with a motional state $\langle n_{x'}\rangle = 0.3$ (solid blue line), corresponding to a temperature $T = 4$ μK with a trapping frequency $\omega_{x'} = 2\pi \times 130$ kHz [those values were independently measured using a Raman spectrum, see Fig. 1.7(e)]. Other values of the average motional state $\langle n_{x'}\rangle$ are shown in dotted lines to show the effect of temperature. (b) Simulation of the decomposition of the atomic population in $|g\rangle$ in the five first motional states $n_{x'}$, for $\langle n_{x'}\rangle = 0.3$. I checked that the result matches the theory formula given by Eq. (1.10). The different oscillation frequencies for each value of $n_{x'}$ explain the damping of the total population.

Raman transition which involves RB 1 along x and RB 2 along y [see geometry of the beams in Fig. 1.3(b)]. After shining the Raman beams on the atoms for the desired duration, we measure the atomic population in $|g\rangle$ by removing the population in $|f\rangle$ with a push-out beam, and acquiring a fluorescence image of the remaining atoms. The obtained oscillation for a single atom is shown in Fig. 1.4(a): we achieve an effective two-photon Rabi frequency of $\Omega_R = 2\pi \times 30$ kHz with a detuning $\Delta = 2\pi \times 5$ GHz, and a damping rate of a few hundred μs that is fully explained by a thermal ensemble with $\langle n_{x'}\rangle = 0.3$. Note that this low occupation number was obtained after RSC.

The damping can be easily understood by solving the dynamics of an atom in a thermal state (as defined in Tab. 1.1) under the two-photon Hamiltonian of Eq. (1.5)

(with $\Omega_{\mathrm{op}} = 0$). The predicted population in state $|g\rangle$ obeys

$$\begin{aligned} P_{|g\rangle}(t) &\equiv \langle g|\, \rho(t)\, |g\rangle \\ &= \sum_{n=0}^{+\infty} P_n^{x'}\, \frac{1-\cos\left(\Omega_{\mathrm{R}}^{(n,n)} t\right)}{2}, \end{aligned} \tag{1.10}$$

where $P_n^{x'}$ is the Boltzmann probability of occupation of the motional state n along x' (defined in Tab. 1.1) and $\Omega_{\mathrm{R}}(n)$ is the two-photon coupling between internal states with the same motional state:

$$\begin{aligned} \Omega_{\mathrm{R}}^{(n,n)} &\equiv \frac{2}{\hbar}\, \langle f, n_{x'}|\, H_{\mathrm{RSC}}\, |g, n_{x'}\rangle \\ &= \Omega_{\mathrm{R}}\, \langle n_{x'}|\, e^{i\,\eta_{\mathrm{R}}^{x'}\,(a+a^\dagger)}\, |n_{x'}\rangle \\ &= \Omega_{\mathrm{R}} \left[1 - \left(\eta_{\mathrm{R}}^{x'}\right)^2 \left(n+\frac{1}{2}\right)\right] + O\left[\left(\eta_{\mathrm{R}}^{x'}\right)^4 n^2\right] \end{aligned} \tag{1.11}$$

The damping is thus caused by the thermal average of many oscillations with different frequencies, depending on the motional state. This is illustrated in Fig. 1.4(b) with the experimental parameters.

However, note that we have to select the data from a single atom to get such a good level of agreement with the ideal simulation. If the data is averaged over all atoms from the array, small inhomogeneities of various parameters between the atoms (temperature, trapping frequency, effective Rabi frequency, effective detuning) lead to a faster damping.

A crucial requirement for the coherence of the two-photon Rabi oscillation on a resolved motional carrier transition is the polarization of the tweezer light. If the latter has a finite ellipticity, it induces a differential vectorial light shift on the states $|g\rangle$ and $|f\rangle$, that can be seen as an effective magnetic field (Dalibard, 2012). Since a tweezer is made of a tightly focused laser beam, its polarization deviates from perfect linearity close to the focal point. The resulting position-dependent ellipticity creates an inhomogeneous effective magnetic field B_{eff} inside the tweezer, with a gradient that reaches ~ 2 G/µm, for rubidium atoms with a ~ 1 mK trap depth, using a numerical aperture of 0.5 (Thompson et al., 2013). This corresponds to a gradient of differential light shift on the order of ~ 4 MHz/µm for the transition $|g\rangle \leftrightarrow |f\rangle$, which is enough to prevent the resolution of the motional states ($\omega_x/2\pi \sim 0.1$ MHz) for positional uncertainties as small as $\sigma_x \sim 25$ nm! A solution to mitigate this effect is to set a large bias magnetic field B_x which is perpendicular to the effective magnetic

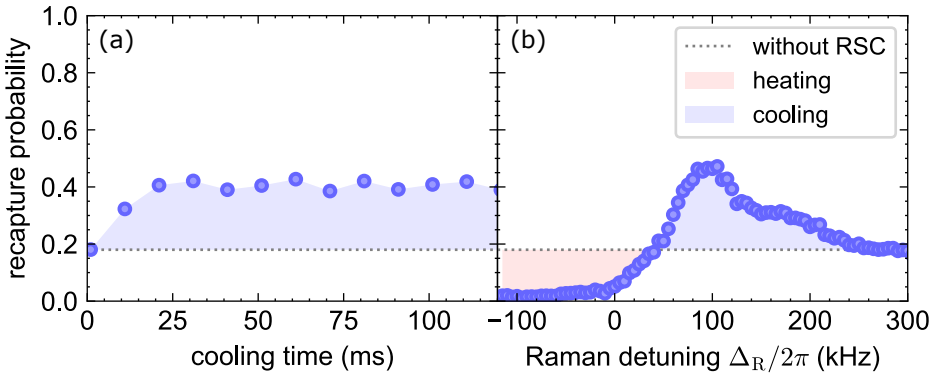

Figure 1.5: Practical optimization of Raman sideband cooling using a release and recapture experiment with 40 µs of release time. The recapture probability was measured as a function of cooling time (a) and as a function of Raman detuning (b). The dotted line indicates the value of the recapture probability in the absence of RSC, i.e. with only MOT and polarization gradient cooling. Since the value of the resonance $\Delta_R = 0$ was not measured in the presence of the optical pumping and repumper beams, the x-axis in (b) has an unknown offset, but the optimal cooling is obtained for $\Delta_R \sim \omega_{x,y} \sim 2\pi \times 100$ kHz.

field (Thompson et al., 2013). If $|B_x| \gg |B_{\text{eff}}|$, the total length of the magnetic field is $\sqrt{B_x^2 + B_{\text{eff}}^2} \approx B_x + \frac{B_{\text{eff}}^2}{2B_x}$, whereas it would be $|B_x \pm B_{\text{eff}}|$ if the two magnetic fields were parallel. In our case, the bias magnetic field is the quantization one ($B_x \approx 7$ G); the polarization of the tweezers is optimized when it is along x before the lens, such that the effective magnetic field is along y.

Measuring the cooling efficiency We now want to apply the RSC procedure. To this end, we first apply the usual cooling mechanisms (MOT and PGC), and we turn on all Raman beams simultaneously, together with the optical pumping and repumper. We optimized empirically the following parameters: power of the beams, single-photon detuning Δ, Raman detuning Δ_R, and duration of cooling, to maximize the recapture probability after a release and recapture experiment. We found that the recapture probability improves and then saturates after roughly 40 ms of continuous cooling [Fig. 1.5(a)]. The value of the Raman detuning Δ_R is particularly important, since it allows us to cool or heat the atoms depending on the motional sideband that we drive [Fig. 1.5(b)].

To quantify the occupation number before and after cooling, we can use several independent methods, that are summarized in Fig. 1.6. I will quickly go through three of them, since they have different interests and, in our case, show some unexplained discrepancies.

The first method is a Raman spectrum with resolved sidebands: starting from atoms

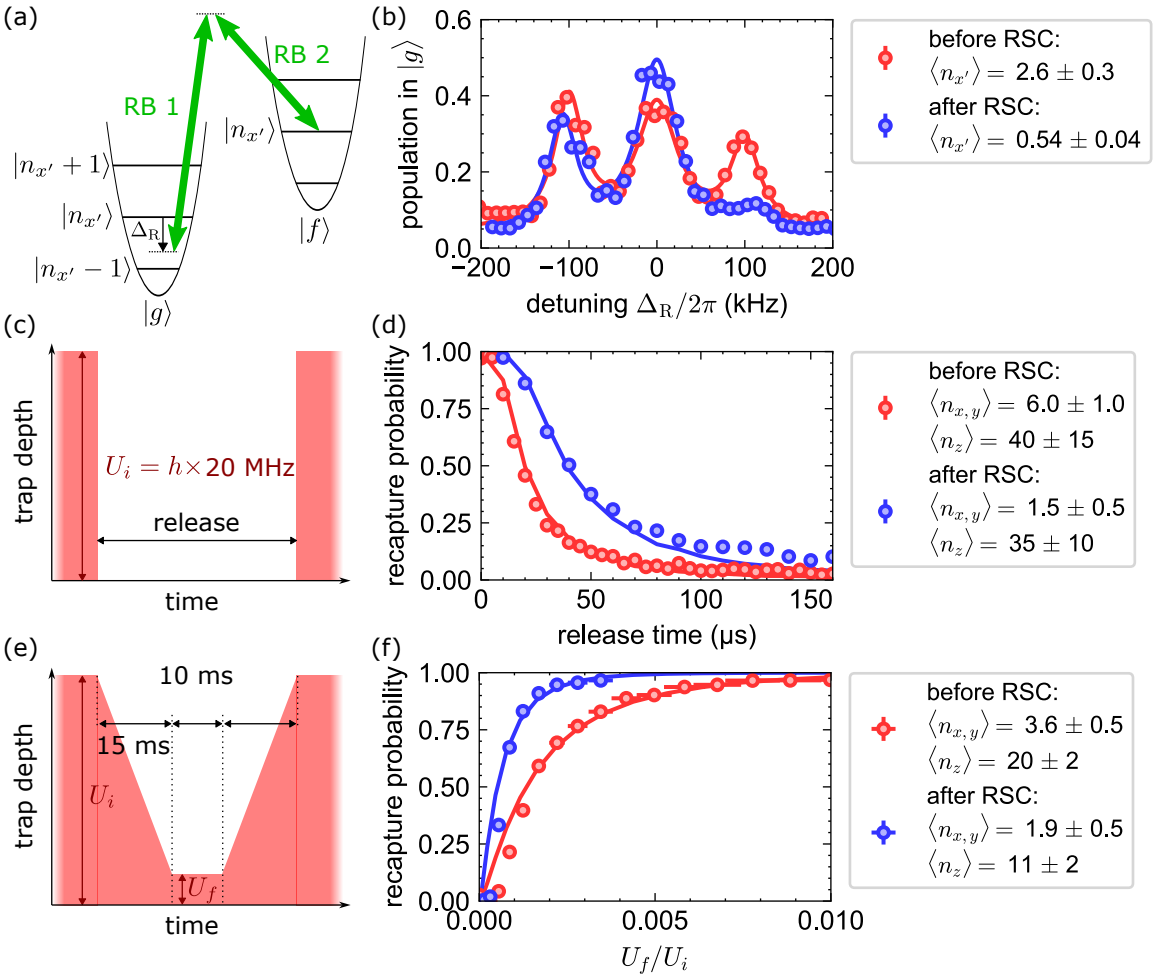

Figure 1.6: Three methods to measure the average occupation number in an array of tweezers. Although similar, the experimental conditions (such as tweezer parameters and cooling efficiency) may vary between the data sets. The data is averaged over all atoms in the array. (a) Principle of sideband-resolved Raman spectrum. (b) Raman spectrum using RB 1 and RB 2, before RSC (red points) and after 40 ms of RSC (blue points). Parameters: exposure time of 50 μs, Rabi frequency $\Omega_R \approx 2\pi \times 24$ kHz on the motional carrier transition. The data points are fitted by three Lorentzian functions (solid lines); the ratio between the $+1$ and -1 sidebands give the average occupation number along the Raman direction (here x'). (c) Experimental sequence for a release and recapture experiment. (d) Recapture probability as a function of the release time, before and after RSC. Data points are fitted by Monte-Carlo simulations (solid lines) to get values of the average occupation number in each spatial direction. (e) Sequence for an adiabatic recapture experiment. (f) Recapture probability as a function of the trap depth, before and after RSC. The data points are fitted assuming a Boltzmann distribution with a uniform temperature, following the procedure explained in Tuchendler et al. (2008).

optically pumped in $|f\rangle$, we carry out a Raman transition with a fixed pulse duration, and scan the frequency of one Raman beam. Depending on the value of the detuning Δ_R, the Raman pulse is resonant with the motional-carrier transition $|f, n_{x'}\rangle \leftrightarrow |g, n_{x'}\rangle$ (for $\Delta_R = 0$), with the +1-sideband transition $|f, n_{x'}\rangle \leftrightarrow |g, n_{x'} + 1\rangle$ (for $\Delta_R = -\omega_{x'}$) or with the −1-sideband transition $|f, n_{x'}\rangle \leftrightarrow |g, n_{x'} - 1\rangle$ (for $\Delta_R = \omega_{x'}$). This is illustrated in Fig. 1.6(a). We then measure the population in $|g\rangle$ by applying a push-out beam that ejects the atoms in $|f\rangle$. Examples of spectra before and after RSC are shown in Fig. 1.6(b). The asymmetry of the spectrum around $\Delta_R = 0$ depends on the occupation of the motional states: typically, the −1-sideband vanishes when the atom is in the motional ground state $|n_{x'} = 0\rangle$. Following Kaufman et al. (2012), the average occupation number $\langle n_{x'}\rangle$ can be extracted from the ratio of the probabilities of the ±1-sidebands ($P_{\Delta n=\pm 1}$):

$$\frac{\langle n_{x'}\rangle}{\langle n_{x'}\rangle + 1} \approx \frac{P_{\Delta n=-1}}{P_{\Delta n=+1}}. \tag{1.12}$$

Fitting the three peaks of the spectrum by Lorentzian functions, we obtain the values of $P_{\Delta n=\pm 1}$ from which we compute $\langle n_{x'}\rangle$. We find that RSC improves $\langle n_{x'}\rangle$ from 2.6 ± 0.3 to 0.54 ± 0.04, reducing the radial temperature in the tweezer to approximately 5 µK.

The second method is the already-mentioned *release and recapture* method, illustrated in Fig. 1.6(c): the tweezer power is abruptly switched off during a given release time. Atoms in free flight have a probability to escape from the trapping region that increases with the release time. Measuring the recapture probability as a function of the release time allows us to quantify their initial position and velocity by comparing them to a classical Monte-Carlo simulation (Tuchendler et al., 2008). To do the fit, we assume that RSC works in the radial direction but not in the axial direction: there are thus two fitting parameters, the radial average occupation, $\langle n_x\rangle = \langle n_y\rangle$, and the axial one, $\langle n_z\rangle$. However simulations show that the recapture probability after a release is not very sensitive to the axial temperature, which will translate into large error bars for the value of $\langle n_z\rangle$. As shown in Fig. 1.6(d), we find a clear improvement of the recapture probability due to RSC, but the obtained values of the radial average occupation ($\langle n_{x,y}\rangle = 1.5 \pm 0.5$) are higher than the one measured with the Raman spectrum ($\langle n_{x'}\rangle = 0.54 \pm 0.04$). There are two possibilities to explain this mismatch: either the assumption of homogeneous radial cooling is wrong, and RSC only cools one radial direction efficiently (x'); or the release and recapture method is biased. We do not have strong evidence for one of those hypotheses. The first one would be in contradiction with the measurements of Kaufman et al. (2012) who found that a single

pair of Raman beams is sufficient to cool down two directions with similar trapping frequencies, due to slight anisotropy of the tweezers that couple the radial modes. The second hypothesis could be explained by several factors: imperfect shape of the tweezers reducing the recapture probability, decreased imaging fidelity for atoms with a high energy...

A final method was proposed in Alt et al. (2003) for optical lattices and realized in Tuchendler et al. (2008) in an optical tweezer. It consists in truncating the energy distribution of an atom in the tweezer, by adiabatically ramping down the tweezer depth its initial value $U_i = h \times 20$ MHz to a final value U_f. We wait for 10 ms with this low trap depth, to let the untrapped atoms escape, we ramp up adiabatically the tweezer depth back to U_i, and we image the remaining atoms [Fig. 1.6(e)]. We measure the survival probability as a function of the ratio U_f/U_i, and plot the result in Fig. 1.6(f). We follow the procedure of Tuchendler et al. (2008) to extract a temperature from the recapture curve. Note, however, that this temperature is the same in all trapping directions, which is probably not the case experimentally. The obtained values of the average occupation are also larger than in the Raman spectrum, and are closer to the ones of the release and recapture.

Overall, all three measurement methods show a clear reduction of the temperature with RSC, but they do not agree quantitatively. Raman spectra are more precise and probably less biased, but only give access to the motional state along one direction. The two methods based on trap depth modulation probe all directions at the same time, but are less accurate and could be subject to biases. Still, they are very useful for fast calibrations of the temperature.

Homogeneity of cooling Previous assessments of the cooling efficiency were global, in the sense that the probabilities were averaged on the whole array. But we can also probe the cooling efficiency with single-atom resolution, thanks to Raman spectra for example. On top of the value of $\langle n_{x'} \rangle$ for each atom, Raman spectra also give us access to the trapping frequency $\omega_{x'}$ of their tweezer. The results are plotted in Fig. 1.7 for two different arrays, together with numerical simulations of the Raman spectra that show a quasi-perfect agreement with only the two-photon Rabi frequency Ω_{R} as a free parameter.

Although the spectra from the two arrays cannot be directly compared (since they were not taken in the same experimental conditions), a general picture emerges from this analysis: the first array, which has a large dispersion of trapping frequencies (relative standard deviation of 14%), also has a large dispersion of $\langle n_{x'} \rangle$ (standard

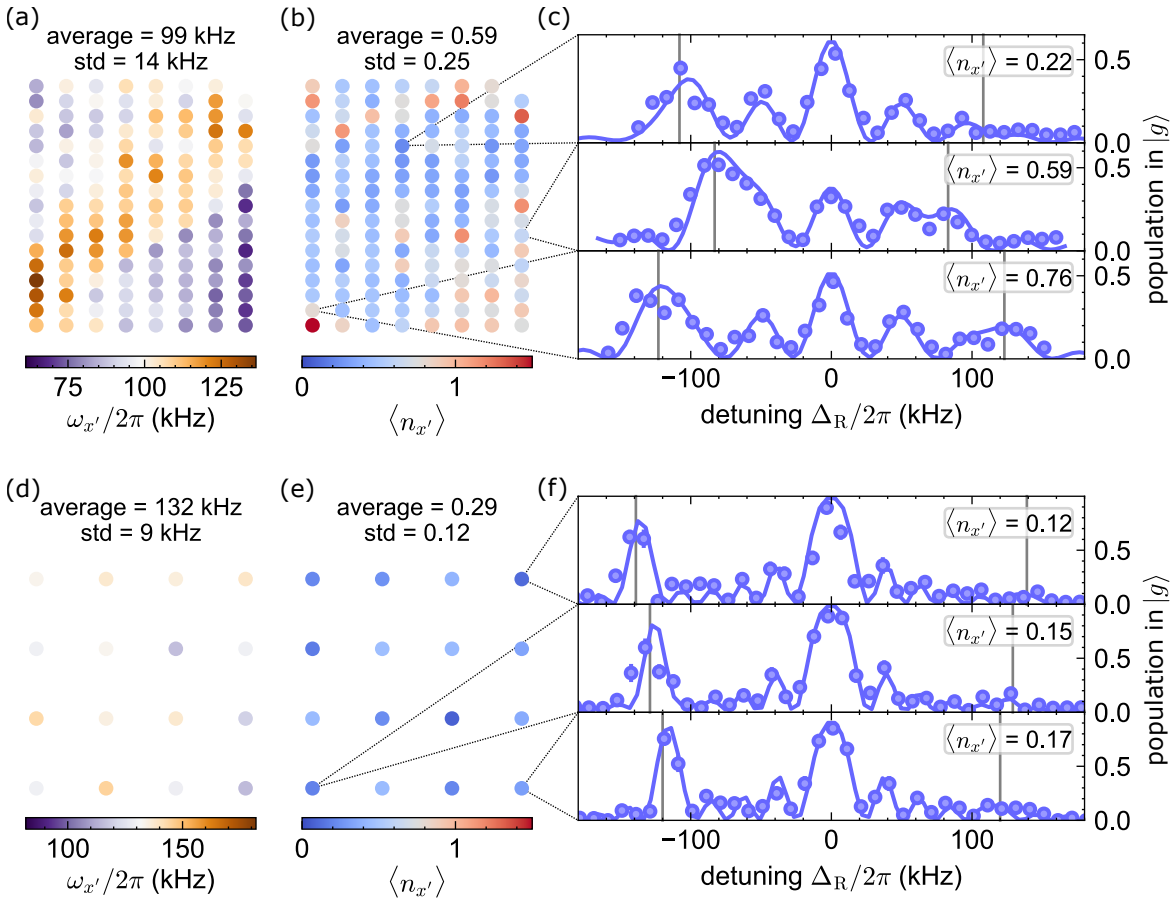

Figure 1.7: Assessment of the homogeneity of Raman sideband cooling from Raman spectra on two different arrays (top and bottom), using RB 1 and RB 2. Parameters of the spectra: effective Rabi frequency of $\Omega_R/2\pi \approx 30$ kHz, pulse duration of respectively 25 µs and 50 µs for the top (a,b,c) and bottom (d,e,f) spectra. The spectra were taken after 20 ms of continuous RSC in the top case, and 40 ms in the bottom case. (a,d) Map of trapping frequency $\omega_{x'}/2\pi$ for each tweezer, extracted by fitting the motional carrier and sidebands of the Raman spectrum of the corresponding atom. (b,e) Map of average occupation number $\langle n_{x'} \rangle$, extracted from the Raman spectrum using Eq. (1.12). (c,f) Examples of spectra for three atoms in the array. Solid lines are simulations of the Raman spectrum taking into account internal and motional degrees of freedom along the Raman direction x'. The parameters of the simulation are within error bars of the fitted values of $\omega_{x'}/2\pi$ and $\langle n_{x'} \rangle$, and the effective Raman frequency is the only free parameter (which we allow to vary by a few percents across the array). The vertical grey lines indicate the position of the motional sidebands $\Delta n = \pm 1$. The intermediate peaks between the carrier and the sidebands are revivals due to the fact that we use square pulses.

deviation of 0.25), whereas the second array is more homogeneous for both the trapping frequency (7%) and $\langle n_{x'} \rangle$ (0.12). In the absence of a more evolved cooling scheme[5], we believe that RSC is limited by inhomogeneities in the array.

Several ways exist to mitigate this effect: in the case of continuous cooling, the Raman detuning Δ_R can be scanned during the cooling sequence to successively cool all atoms; in the case of pulsed cooling, adiabatic Raman transitions can be designed to be insensitive to such inhomogeneities (de Léséleuc and Chew, 2022; Garwood and DelaBarre, 2001). Another strategy is to improve the homogeneity of the trapping frequencies across the array. In our case, we homogenize the tweezers based on their loading rate, which is more or less equivalent to equalizing their trap depth (Schymik, 2022). But equal trap depths do not mean equal trapping frequencies, since the trapping frequency also depends on the tweezer waist. If we wanted to be more accurate, feedback techniques were recently demonstrated to improve the homogeneity of both the trap depth and the trapping frequency (Chew et al., 2024).

What about the axial direction? In spite of a few attempts, we did not manage to show an improvement in the occupation number of the axial direction. As shown in Fig. 1.8, we can resolve the motional sidebands along z. From Raman spectra, we extract a trapping frequency $\omega_z \approx 2\pi \times 20$ kHz and $\langle n_z \rangle = 10 \pm 5$. But Raman spectra do not show a clear improvement before and after RSC using RB 3.

Two main difficulties probably explain why we did not manage to cool axially. First, the Lamb-Dicke regime is not achieved in the axial direction, since $\left(\eta^z_{\mathrm{op}}\right)^2 (2\langle n_z \rangle + 1) \approx 4 > 1$. This leads to additional heating due to the optical pumping. Second, the Raman transition gets broadened in the presence of the optical pumping and the repumper: indeed, the state $|g\rangle$ gets resonantly coupled by the optical pumping and repumper to $|e\rangle$ and $|e'\rangle$ which have a large linewidth $\Gamma/2\pi \approx 6$ MHz, so its effective linewidth gets larger by an amount $\Omega^2_{\mathrm{op}}/\Gamma$. As a result, it is harder to resolve the motional states axially during continuous RSC.

An obvious solution to circumvent these problems is to implement pulsed cooling, as done for example in Kaufman et al. (2012); Thompson et al. (2013); Yu et al. (2018). However, we did not have time to do it during my PhD thesis.

[5] With pulsed cooling, the shape of Raman pulses can be optimized to be robust to inhomogeneities of the resonance condition.

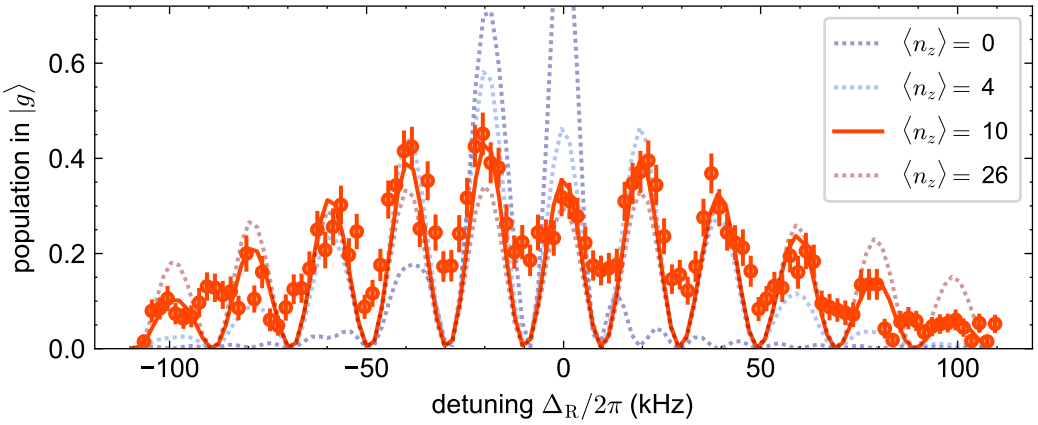

Figure 1.8: Axial Raman spectrum with resolved motional states, using RB 1 and RB 3. Parameters of the spectrum: exposure time of 100 µs, Rabi frequency $\Omega_R = 2\pi \times 6.5$ kHz. Data points are for a single atom. Colored lines correspond to simulations for various temperatures, with the Rabi frequency as a free parameter (up to 35 motional states are taken into account in the simulation). From the simulations, we extract $\langle n_z\rangle = 10 \pm 5$ which corresponds to a temperature of 10 µK.

1.4 Discussion of the results

Practical improvement in terms of interatomic distance Now that I have presented our results in terms of occupation number, let us come back to the original motivation of Raman sideband cooling: reducing the position fluctuations. Going from $\langle n_{x'}\rangle \approx 2.5$ before RSC to $\langle n_{x'}\rangle \approx 0.3$ at best after RSC, we decreased the radial position uncertainty from $\sigma_{x'} \approx 60$ nm to $\sigma_{x'} \approx 32$ nm. Axially, we have $\langle n_z\rangle \approx 10$ before and after RSC, leading to $\sigma_z \approx 230$ nm.

Naively, it seems a shame that the dominating source of position fluctuations occurs along the direction that we do not cool with RSC. But for the purpose of quantum simulation, the real figure of merit is in fact not the position fluctuations, but the fluctuations of interaction energies, which depend on the interatomic distance. To get a feeling of how the interatomic distance is affected by positional disorder, let us consider two atoms separated by an average distance d along the x axis, each atom having a position uncertainty σ_μ along μ. Let us now consider the interatomic distance $r = \sqrt{(d + x_2 - x_1)^2 + (z_2 - z_1)^2}$. Due to the position fluctuations, $\mu_2 - \mu_1$ will fluctuate by an amount $\sqrt{2}\,\sigma_\mu$, so the distance fluctuations Δr are given by

$$\Delta r \sim \sqrt{2}\,\sigma_x + \frac{\sigma_z^2}{d} \tag{1.13}$$

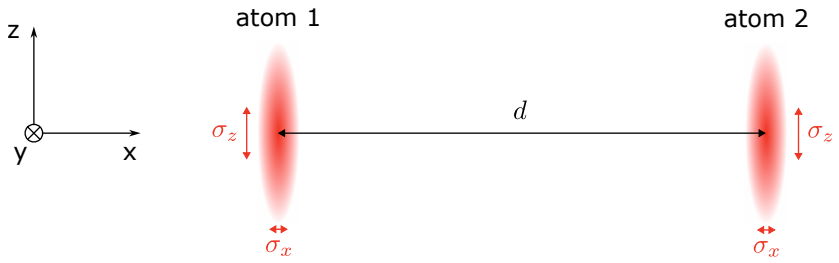

Figure 1.9: Distance fluctuations between two atoms.

where we have neglected third-order terms according to the following hierarchy of distances: $d \gg \sigma_z \gg \sigma_{x,y}$. The first term is the contribution of the radial fluctuations in the direction of the interatomic axis, and the second term corresponds to axial fluctuations. Note however that the perturbative estimate given by Eq. (1.13) can fail, especially when the spatial disorder σ_z gets on the same order of magnitude as d — in which case Eq. (1.13) tends to overestimate Δr. The radial contribution equals the axial one for a critical distance

$$d_c \equiv \sigma_z^2/\sqrt{2}\sigma_x \tag{1.14}$$

The axial contribution will dominate for shorter distances ($d < d_c$) and the radial contribution for larger distance ($d > d_c$). After RSC we have $d_c \sim 1.2$ µm. As we will see in chapter 2, dipole-dipole interactions between Rydberg states can be large enough to work at distances $d \sim 10$ µm, where the radial contribution is ten times larger than the axial one.

What about velocities? In our experiment, velocities are indirectly a limitation due to their effect on the positions[6]: when the traps are switched off for the Rydberg sequence (see Fig. 8 of the Introduction), the atoms move due to their initial velocity. If an atom is in free flight during a time t, its total position uncertainty σ_μ^{tot} along direction μ will increase with time according to

$$\sigma_\mu^{\text{tot}} = \sqrt{\sigma_\mu^2 + (\sigma_{v^\mu} t)^2}. \tag{1.15}$$

[6]We are not affected by Doppler broadening of the atomic transitions, because it is negligible compared with the typical Rabi frequencies in use.

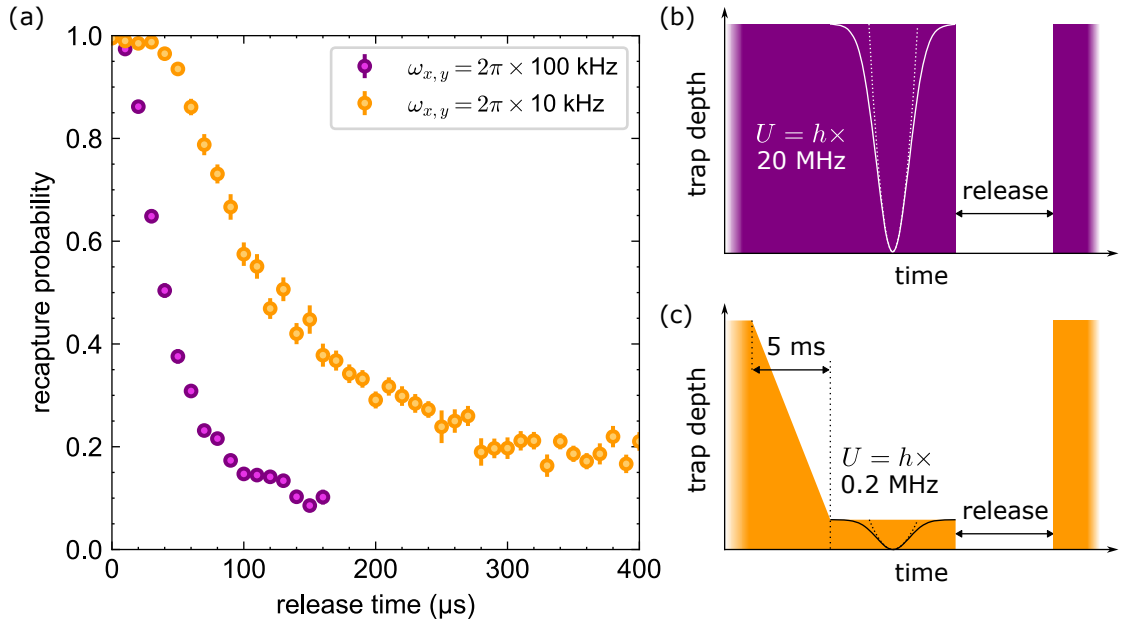

Figure 1.10: Effect of adiabatic ramp-down of the tweezer power on a release and recapture experiment. (a) Release and recapture with two experimental conditions: with the usual trapping frequencies $\omega_{x,y} = 2\pi \times 100$ kHz (purple points) and with adiabatic reduction to 10 kHz (orange points). The corresponding sequences are indicated in (b) and (c), with illustrations of the shape of the optical tweezer. To get a reduction of the velocities by a factor 10, we need to reduce the tweezer power and the trap depth by a factor 100. As a consequence, the velocity dispersion is reduced by a factor ~ 3, and the initial position dispersion is increased by the same amount. The ramp down in (c) takes 5 ms.

We can define a critical time t_c^μ for which the initial position dispersion has the same contribution as the initial velocity dispersion:

$$\begin{aligned} t_c^\mu &\equiv \sigma_\mu / \sigma_{v^\mu} \\ &= 1/\omega_\mu \quad \text{for a thermal state (see Tab. 1.1)} \end{aligned} \tag{1.16}$$

For tweezers with larger trapping frequencies (i.e. very steep harmonic potential), the critical time happens sooner due to the large initial velocity dispersion. With our typical radial trapping frequencies $\omega_{x,y} = 2\pi \times 100$ kHz, we obtain $t_c^{x,y} \approx 1.6$ µs. This means that after 1.6 µs, we start to be limited by velocity fluctuations more than by initial position fluctuations.

What if we want to conduct an experiment lasting longer than 1.6 µs (which is almost always the case for our typical interaction energies)? Is there anything we can do to reduce the velocity dispersion? The answer is given by Eq. (1.16): we just have to reduce the trapping frequency to increase $t_c^{x,y}$. The only condition for this to work is

Quantity	Scaling	Typical value (after RSC)	
Trap depth	$U' = \alpha\, U$	$U/h \sim 20$ MHz	
Average occupation number	$\langle n_\mu \rangle' = \langle n_\mu \rangle$	$\langle n_{x,y} \rangle \sim 0.5$	$\langle n_z \rangle \sim 10$
Trapping frequency	$\omega'_\mu = \alpha^{1/2}\, \omega_\mu$	$\omega_{x,y} \sim 2\pi\times$100 kHz	$\omega_z \sim 2\pi\times$20 kHz
Harmonic oscillator length	$\mu'_{\mathrm{ho}} = \alpha^{-1/4}\, \mu_{\mathrm{ho}}$	$x_{\mathrm{ho}}, y_{\mathrm{ho}} \sim 25$ nm	$z_{\mathrm{ho}} \sim 50$ nm
Position uncertainty (Tab. 1.1)	$\sigma'_\mu = \alpha^{-1/4}\, \sigma_\mu$	$\sigma_{x,y} \sim 35$ nm	$\sigma_z \sim 230$ nm
Harmonic oscillator velocity	$v^{\mu\,\prime}_{\mathrm{ho}} = \alpha^{1/4}\, v^\mu_{\mathrm{ho}}$	$v^x_{\mathrm{ho}}, v^y_{\mathrm{ho}} \sim 11$ nm/µs	$v^z_{\mathrm{ho}} \sim 5$ nm/µs
Velocity uncertainty (Tab. 1.1)	$\sigma'_{v^\mu} = \alpha^{1/4}\, \sigma_{v^\mu}$	$\sigma_{v^{x,y}} \sim 15$ nm/µs	$\sigma_{v^z} \sim 7$ nm/µs
Critical time [Eq. (1.16)]	$t^{\mu\prime}_{\mathrm{c}} = \alpha^{-1/2}\, t^\mu_{\mathrm{c}}$	$t^{x,y}_{\mathrm{c}} \sim 1.6$ µs	$t^z_{\mathrm{c}} \sim 8$ µs
Critical distance [Eq. (1.14)]	$d'_{\mathrm{c}} = \alpha^{-1/4}\, d_{\mathrm{c}}$	$d_{\mathrm{c}} \sim 1.2$ µm	

Table 1.2: Scalings of some quantities related to motion with the adiabatic ramp-down factor α. Here, α is defined as the ratio of the tweezer power after and before the adiabatic ramp-down. The quantities labeled by " $'$ " are the rescaled ones after the ramp down.

that the distribution of motional states remains the same, i.e. that $\langle n_\mu \rangle$ is not changed through the procedure. This can be achieved by adiabatically ramping down the trap power, as explained in Tuchendler et al. (2008). The effect of adiabatic ramp-down is to reduce the velocity dispersion as $\sigma_{v^\mu} \propto \omega_\mu^{1/2} \propto U^{1/4}$, with U the trap depth of the tweezers; conversely, the atomic wavefunctions will expand, leading to an increase of the initial position dispersion as $\sigma_\mu \propto \omega_\mu^{-1/2} \propto U^{-1/4}$. Those effects can be tested experimentally with a release and recapture experiment. As seen from Fig. 1.10, the reduction of velocity dispersion allows us to recapture the atoms for a longer release time, typically a few 10 µs.

The final value of the tweezer depth can be chosen depending on the desired duration of the experiment. For practical use, Table 1.2 recaps the scalings with the trap depth U of some quantities related to motion. For example, to carry out an experiment during $t = 4$ µs, we need to decrease to radial trapping frequency from $\omega_{x,y} = 2\pi \times 100$ kHz to 40 kHz, which can be achieved by changing the tweezer power by a factor $\alpha = (40/100)^2 = 0.16$. Note that the critical distance introduced in the previous paragraph increases when the trap depth is reduced, thus increasing the relative contribution of the axial position uncertainty.

Take-home message

One atom in an optical tweezer has a residual motion due to thermal and quantum fluctuations. To reduce the thermal contribution, we implemented a cooling scheme called *Raman sideband cooling* that makes use of three beams for coherent Raman transitions that lower the occupation number of the motional states, and two optical pumping beams to close the cooling cycle. This allows us to achieve $\langle n_{x'} \rangle \sim 0.3$ in the radial direction, corresponding to around 75 % of occupation in the motional ground state. The thermal contribution to position and velocity dispersions is thus reduced to 30 % of the quantum contribution. The axial direction is however not cooled, but it has a smaller contribution than the radial direction to the fluctuations of interatomic distance, for the typical distances used in this thesis. The velocity dispersion also participates to increase the position dispersion during the Rydberg sequence, but this effect can be mitigated by adiabatically lowering the trap depth. We will see in details in chapter 3 how the residual motion affects the interactions between the atoms.

Chapter 2

Global and local transitions between Rydberg states

> There are no two-level atoms,
> and [rubidium] isn't one of them.
>
> Bill Phillips

In this chapter, I present methods and technical improvements for driving high-fidelity transitions between Rydberg levels on large atomic arrays. In the context of quantum simulation, this is motivated by achieving better preparation fidelities, increasing the range of accessible initial states, and increasing the accessible measurement bases. I will try to identify the limitations for the fidelities, by sometimes showing calibration curves that are usually not shown in articles, because considered too technical. This part is thus mostly addressed to experimentalists who are interested in the gory details of real atoms, far away from ideal two-level objects.

Since the transitions that we target are in the microwave domain (between 1 and 30 GHz, broadly speaking), they correspond to wavelengths ranging from 1 cm to 30 cm, which are much larger than the largest size of the array (140 µm in diameter). As a consequence, the microwave fields alone cannot address the atoms locally, they are naturally global. For this reason, this chapter is split into two sections: first, I present the typical performance of global microwave transitions, with one or two microwave photons (sec. 2.1); second, I show how we can make local transitions with the help of an addressing beam (sec. 2.2).

Contents

Contributors

The methods presented in this chapter were developed throughout my PhD thesis by the experimental team at Institut d'Optique: Guillaume Bornet, Cheng Chen, Bastien Gély, Yuki Torii Chew, Mu Qiao, Romain Martin, Pascal Scholl, Jamie Boyd, Daniel Barredo, Thierry Lahaye and Antoine Browaeys. I will show a small selection of the numerous sets of data that we have been taking for calibrations, in the view of the many-body projects that are presented in part B. Some helpful simulations of our experimental system were performed by Lucas Leclerc from Pasqal.

2.1 Global transitions

2.1.1 Coherent microwave transitions for global rotations

Here, I present our methods to isolate two Rydberg states and drive global coherent microwave transitions between those states. In the context of quantum simulation, coherent transitions correspond to spin/qubit rotations, which are a crucial step in state preparation and detection. We mainly perform three types of calibration experiments:

- Microwave spectra for identifying the states that we want to isolate, and measuring the energy difference with other states.
- Rabi oscillations on the targeted transition for measuring the Rabi frequency.
- Ramsey oscillations for measuring accurately the resonance frequency.

In the following, I describe the experimental setup that allows us to perform those calibrations; then, I will go through each of the calibration, to present the performance and limitations of the setup.

Microwave setup Coherent microwave transitions require full control over the microwave field's phase and amplitude. In Fig. 2.1, I show two typical setups that allow us to perform phase and amplitude modulation. In the first setup, a microwave carrier at frequency f_0 (generated by SMB 100A by Rohde&Schwarz) is mixed with a radio-frequency field $V_{\mathrm{RF}}(t)$ produced by an arbitrary waveform generator (AWG SDG6000X Series Pulse by Siglent). Writing the AWG voltage as an RF sine wave

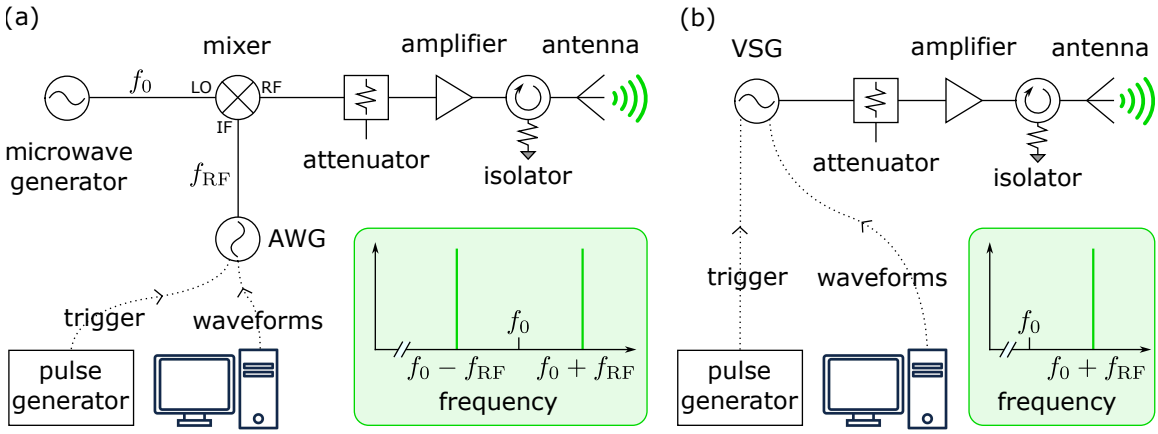

Figure 2.1: Two typical microwave setups used in this thesis. Both setups are composed of a microwave source on the one end, and an antenna close to the chamber on the other end (see Fig. 7 of the Introduction to see the position of the antennas). In between the source and the antenna, we can use attenuators and amplifiers to tune the microwave power. The isolator (for example, DBIS2012001800A by Qotana Technologies) prevents strong reflections due to imperfect impedance matching of the antenna. The two setups differ by their microwave source: in (a), we use a microwave generator at a fixed frequency $f_0 \sim 10$ GHz that is mixed with the signal from an arbitrary waveform generator (AWG) in the radio-frequency range ($f_{\mathrm{RF}} < 300$ MHz). A typical mixer is ZX05-24MH-S+ by Mini-Circuits. In (b), we use a vector signal generator (VSG) which directly performs IQ modulation with $f_{\mathrm{RF}} \leq 500$ MHz. The devices are used in burst mode and are triggered by a pulse generator (Pulse Streamer 8/2 by Swabian Instruments) which is synchronized with the experimental sequence. Waveforms are preloaded on the devices' internal memories. Green insets: spectrum of the output microwave field, assuming perfect modulation with a simple sine wave [see Eq. (2.1,2.2)].

modulated by a time-dependent envelope $V_{\mathrm{RF}}(t) = A_{\mathrm{RF}}(t)\,\cos(2\pi f_{\mathrm{RF}} t + \varphi_{\mathrm{RF}})$, the output microwave signal has two sidebands

$$\begin{aligned} V(t) &= V_{\mathrm{RF}}(t)\,\cos(2\pi f_0 t) \\ &= \frac{A_{\mathrm{RF}}(t)}{2}\left[\cos\left(2\pi(f_0 + f_{\mathrm{RF}})t + \varphi_{\mathrm{RF}}\right) + \cos\left(2\pi(f_0 - f_{\mathrm{RF}})t - \varphi_{\mathrm{RF}}\right)\right]. \end{aligned} \tag{2.1}$$

We use one of the sidebands to drive the targeted transition, the other one being chosen to be far-detuned[1]. This setup has the advantage of being easy to build experimentally, at a reasonable price.

A more powerful — and more expensive — solution makes use of a vector signal generator (SMM100A by Rohde&Schwarz). This device contains a microwave generator

[1] We also have to avoid resonances with the carrier at f_0, which is never perfectly canceled in real devices. For example, with a typical mixer from our setup (ZX05-24MH-S+), the extinction ratio of the carrier (L-R isolation) is about 26dB at 16 GHz.

with a built-in quadrature amplitude modulation (IQ modulation) in the radio-frequency domain. The output voltage writes $V(t) = I(t)\cos(2\pi f_0 t) + Q(t)\sin(2\pi f_0 t)$ where f_0 is the microwave carrier, and $I(t)$ and $Q(t)$ are the field quadratures. In particular, the most simple use of the device is to choose $I(t) = A_{\mathrm{RF}}(t)\cos(2\pi f_{\mathrm{RF}} t + \varphi_{\mathrm{RF}})$ and $Q(t) = -A_{\mathrm{RF}}(t)\sin(2\pi f_{\mathrm{RF}} t + \varphi_{\mathrm{RF}})$, in which case the output field contains only one sideband:

$$V(t) = A_{\mathrm{RF}}(t)\cos\left(2\pi(f_0 + f_{\mathrm{RF}})t + \varphi_{\mathrm{RF}}\right). \tag{2.2}$$

This voltage then leads to a free-space electric field $E(t) \propto V(t)$ after the antenna. Note that the polarization of the resulting field is not controlled, due to the complicated boundary conditions of our metallic chamber (see Fig. 7 of the Introduction). Typical powers required for driving resonant single-photon transitions are around -5 dBm before the antenna, corresponding to Rabi frequencies of $\Omega/2\pi \sim 10$ MHz for $n = 60$; but we can achieve much larger powers (~ 30 dBm) using amplifiers such as ZVE-3W-83+ by Mini-Circuits. All devices for the Rydberg sequence, including the microwave setup, are triggered by the same pulse generator to minimize the jitter from shot to shot. We measured jitter times on the order of 3 ns, on a fast oscilloscope.

Microwave spectra To identify the Rydberg levels, we excite all atoms to the same Rydberg state $\left|nS_{1/2}, m_J = 1/2\right\rangle$ using STIRAP (see Introduction); then, we send a microwave pulse with a well-defined duration and frequency ; finally, we measure the population remaining in $\left|nS_{1/2}, m_J = 1/2\right\rangle$. For this sequence and all sequences of this chapter, the measurement is done by deexciting the atoms from $\left|nS_{1/2}, m_J = 1/2\right\rangle$ to the ground state manifold $5S_{1/2}$ using a resonant pulse of 1014 nm light, and imaging the atoms in the ground state. Imaged atoms are interpreted as being in the state $\left|nS_{1/2}, m_J = 1/2\right\rangle$, whereas lost atoms are considered as being in other Rydberg states. The sequence is repeated a few tens of times to compute the probability of being in $\left|nS_{1/2}, m_J = 1/2\right\rangle$. Performing the measurement for different microwave frequencies allows us to acquire a spectrum of the accessible microwave transitions. An example of such spectrum with resolved Zeeman sublevels is shown in Fig. 2.2 for $n = 60$.

For a given transition between two Rydberg states $|r\rangle$ and $|r'\rangle$, the coupling between the atom and the microwave field is given by the Rabi frequency: $\Omega_{r,r'} \equiv -\langle r|\,\mathbf{d}\cdot\mathbf{E}_{\mu\mathrm{w}}\,|r'\rangle/\hbar$ where $\mathbf{d}$ is the electric dipole operator and $\mathbf{E}_{\mu\mathrm{w}}$ is the amplitude of the microwave electric field. It scales as n^2 with n the principal quantum number. For efficient pulses, we want the highest possible Rabi frequency, in order to be able to neglect Rydberg interactions during the pulse. However, we cannot increase it too

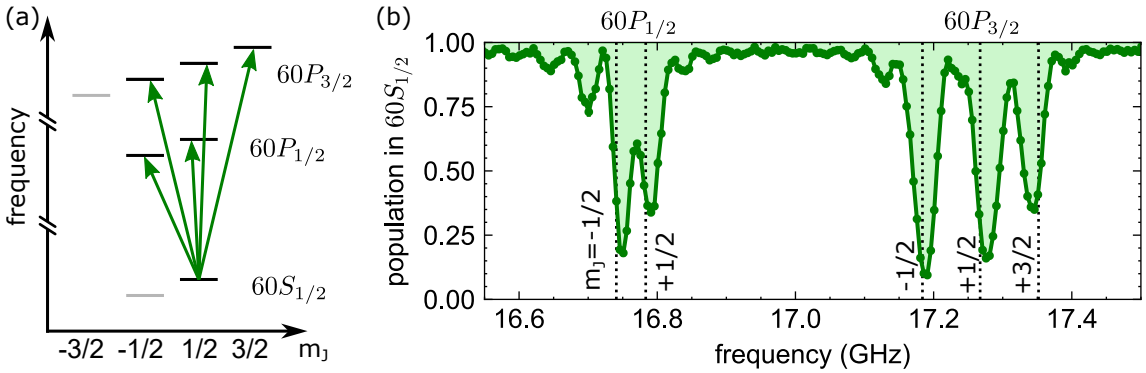

Figure 2.2: Microwave spectroscopy of the $60P$ manifold. (a) Energy levels involved in the sequence. Green arrows point from the initial state $|i\rangle = |60S_{1/2}, m_J = 1/2\rangle$ to accessible states via dipole coupling. (b) Spectrum of the transition, with a 24-ns square pulse. The sequence is the following: we excite atoms to $|i\rangle$ via STIRAP, then we perform the microwave pulse, deexcite them from $|i\rangle$ and image them in the ground state. The vertical dotted lines indicate the simulated resonance frequencies using Weber et al. (2017), with a magnetic field $B = 45$ G. Discrepancies from the theoretical resonance are about a few MHz, we attribute them to microwave shifts due to the other Zeeman levels [see simulation in Bornet (2024)].

much, otherwise neighboring Zeeman sublevels will be populated. A solution would be to tune the microwave polarization, but we are not able to control it well enough with the current experimental design. As a result, we cannot tune the ratio of Rabi frequencies between transitions $\sigma-$, π and $\sigma+$; we can only rescale them by a common proportionality factor, by changing the microwave power $|\mathbf{E}_{\mu\mathrm{w}}|^2$, as $\Omega_{r,r'} \propto |\mathbf{E}_{\mu\mathrm{w}}|$.

The accessible Rabi frequencies are not limited by microwave power, but by the Zeeman splittings due to the finite values of the magnetic field ($B \lesssim 50$ G). With a magnetic field of $B \approx 45$ G, we obtain frequency differences of 40 to 90 MHz between the different Zeeman sublevels (Fig. 2.2), which mean that the typical Rabi frequencies that we can achieve are $\Omega_{r,r'}/2\pi \lesssim 30$ MHz. For a fixed peak Rabi frequency, we can better isolate a transition from neighboring states by playing with the shape of the pulse. In Fig. 2.3, I compare the performances of two common shapes, square pulses and Gaussian pulses. We define the parameters of a Gaussian pulse by $\Omega(t) = \Omega_0 \exp\left(-\pi \frac{t^2}{\Delta t^2}\right)$, such that the angle of rotation on resonance (area under the curve) is $\Omega_0 \Delta t$, like for a square pulse with duration Δt. A clear advantage of the Gaussian pulses is the so-called phenomenon of *apodization*. Indeed, the spectrum of a square pulse with duration Δt shows revivals of the excitation probability with the detuning δ, which for a two-level system follows the Rabi formula (Basdevant and

Dalibard, 2006):

$$P_{\text{square}}(\delta, \Delta t) = \frac{\Omega_0^2}{\Omega_0^2 + \delta^2} \sin^2\left(\frac{\sqrt{\Omega_0^2 + \delta^2}}{2}\Delta t\right) \tag{2.3}$$

with Ω_0 the Rabi frequency. A clear revival can be seen in Fig. 2.3(a) around -60 MHz, effectively broadening the spectrum. On the contrary, a Gaussian pulse with the same peak amplitude has a Gaussian-like spectrum which does not have any revival: this is called apodization. It has the cost of a slightly longer pulse, for the same peak Rabi frequency. We find that for a π-pulse, the excitation probability in a two-level system is well approximated by a Gaussian:

$$P_{\text{Gaussian}}\left(\delta, \Delta t = \frac{\pi}{\Omega_0}\right) \approx \exp\left(-1.8\,\frac{\delta^2}{\Omega_0^2}\right). \tag{2.4}$$

We then perform a Rabi oscillation on resonance, using the same parameters as Fig. 2.3(a). We do not see a clear effect of the Gaussian pulse compared with the square pulses [Fig. 2.3(b)]. However simulations with a larger Rabi frequency show a clear reduction of the contrast after a 2π-pulse with a square pulse [Fig. 2.3(c)]; this is due to the presence of the closest Zeeman state, which gets populated because of the revival. In the case of the Gaussian pulse, this effect would appear for an even larger Rabi frequency.

Time coherence and homogeneity of microwave transitions The previous curves were measured on arrays with many atoms, in the presence of Rydberg interactions. Even if the typical Rydberg interaction $J/2\pi \sim 0.1$ to 1 MHz is small compared to the typical Rabi frequencies at play, it typically leads to damping at long times $\Delta t \gg 1/J$. Inhomogeneous broadening of the Rabi frequencies can also create damping. To check the coherence of a Rabi oscillation without the effect of the interactions and inhomogeneities, we acquire a measurement on a single atom (Fig. 2.4). The obtained coherence time is of a few tens of µs, possibly due to neighboring states and Rydberg lifetimes; it will not be a limiting factor for the typical durations of our Rydberg sequences (< 10 µs).

The fidelity of a π-pulse can be estimated by the recapture probability, after removing the effect of detection errors [see Bornet (2024) for a detailed description of the detection errors on our setup]. For non-interacting atoms, the π-pulse efficiency typically reaches > 99 %.

Repeating the same measurement on different atoms reveals slight inhomogeneities of

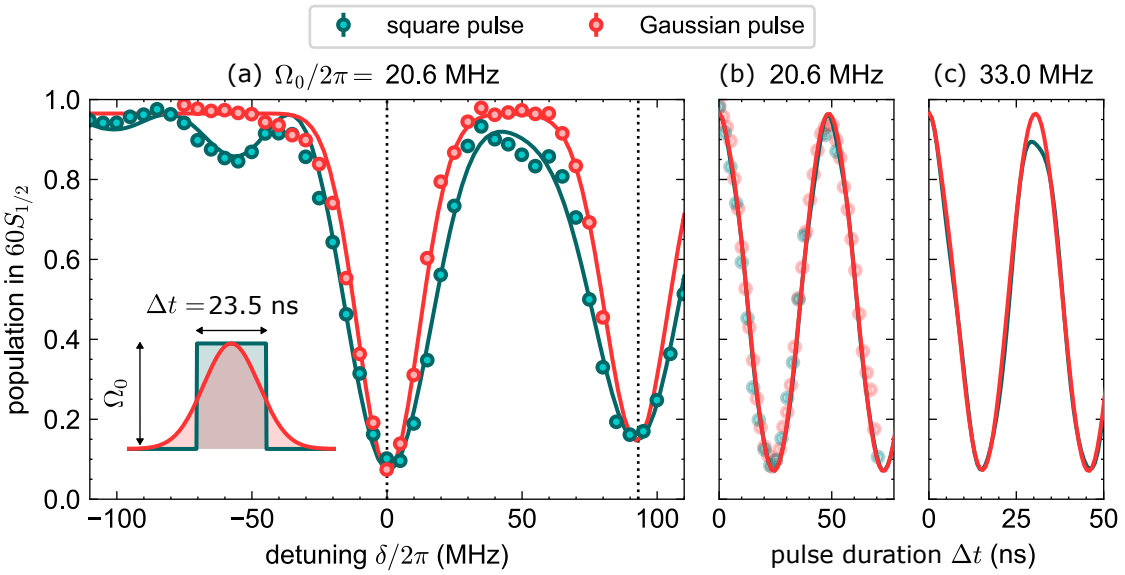

Figure 2.3: Influence of the microwave pulse shape. (a) Comparison of two microwave spectra of the $60P_{3/2}$ manifold, respectively taken with a square pulse and a Gaussian pulse. Inset: parameters of the pulses. The peak Rabi frequency is $\Omega_0/2\pi = 20.5$ MHz, and the pulse duration is $\Delta t = 23.5$ ns. Solid lines are numerical simulations taking into account three Rydberg levels ($\left|60S_{1/2}, m_J = 1/2\right\rangle$, $\left|60P_{3/2}, m_J = -1/2\right\rangle$ and $\left|60P_{1/2}, m_J = 1/2\right\rangle$), with two free parameters: the Zeeman splitting between $m_J = -1/2$ and $m_J = +1/2$, and the ratio of the corresponding Rabi frequencies. Typical experimental detection errors are added to the simulation, reducing the contrast. (b) Rabi oscillation at $\delta = 0$, with Rabi frequency $\Omega_0/2\pi = 20.5$ MHz. Solid lines are numerical simulations with the same parameters as in (a). (c) Numerical simulation of a Rabi oscillation with increased Rabi frequency $\Omega_0/2\pi = 33$ MHz, showing a reduction of the 2π-pulse efficiency in the case of the square pulse, due to unwanted population in the neighboring $60P_{3/2}$ state ($m_J = +1/2$).

the microwave Rabi frequency, with a standard deviation of $\delta\Omega/\Omega \sim 1$ %. This will lead to inhomogeneities in the angles of rotation $\theta \equiv \Delta t\,\Omega$, such that $\delta\theta/\theta = \delta\Omega/\Omega \sim 1$ %. This level of inhomogeneity will not affect significantly the efficiency of the microwave pulses, as long as we perform a small number of rotations: for example, for a π-pulse, $\theta = 180°$ so $\delta\theta \sim 2°$, which decreases the fidelity by a factor $\cos^2(\delta\theta) \sim 99.9$ %. If necessary, the shape of the pulses can be optimized to mitigate the effect of these inhomogeneities; but in practice the main limitation for the fidelities of the microwave rotations are the interatomic interactions, which we cannot switch off during the pulse.

Ramsey interferometry Another possible source of decoherence are the fluctuations of the resonance frequencies of the Rydberg transitions in the absence of microwave field. To quantify those fluctuations spatially and in time, we perform a Ramsey

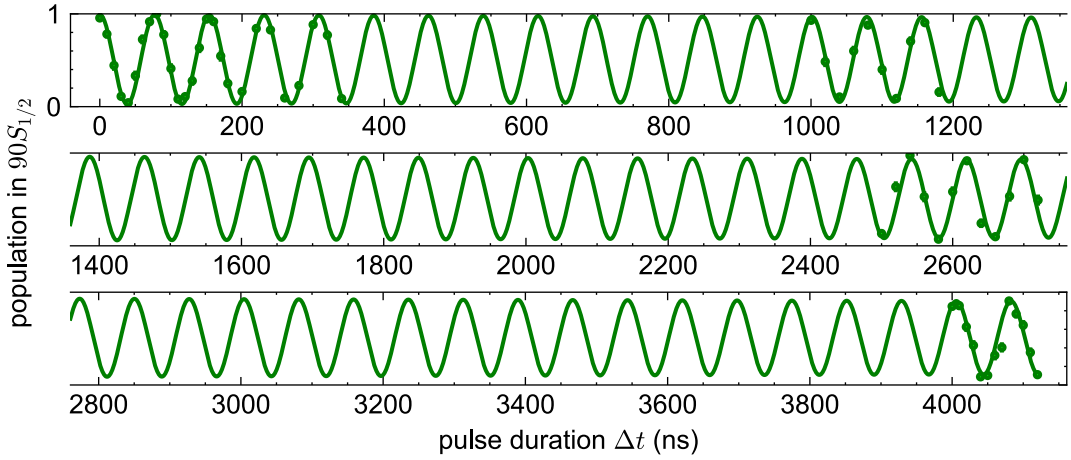

Figure 2.4: Long-time coherence of a Rabi oscillation acquired on a single atom between the states $|90S_{1/2}, m_J = 1/2\rangle$ and $|90P_{3/2}, m_J = 1/2\rangle$, using square pulses. The solid line is a fit with a Rabi frequency of $\Omega_0/2\pi = 12.98 \pm 0.002$ MHz and an exponential $1/e$ decay constant of 20 ± 4 µs.

interferometry measurement, composed of two $\pi/2$ pulses separated by a gap time Δt. The resulting population in the initial Rydberg state nS oscillates at a frequency given by the microwave detuning δ:

$$P_{nS} = \frac{1 - \cos(\Delta t\, \delta)}{2}. \tag{2.5}$$

up to a finite contrast which is mostly due to detection errors, and a slow damping due to decoherence. Typical Ramsey oscillations on the transition $nS \leftrightarrow nP$ are shown in Fig. 2.5(a) for four non-interacting atoms located at the corners of a square (~ 100 µm away from each other). They allow us to measure accurately the detuning $|\delta|$ of each atom and thus the value of the resonance frequency for the considered transition. Ideally, it should be the same for all atoms on the array, but in practice the value can change due to spatial inhomogeneities of the electro-magnetic environment: typically, in the presence of a static electric field $\mathbf{E}$, the DC Stark effect leads to a shift δ_{Stark} which adds up to the microwave detuning δ:

$$\delta_{\text{Stark}} = \frac{1}{2}(\alpha_{nS} - \alpha_{nP})\,|\mathbf{E}|^2 \tag{2.6}$$

with α_r the electric polarizability of the Rydberg state $|r\rangle$. A small variation δE of the electric field amplitude will lead to a change of the Stark shift by an amount $(\alpha_{nS} - \alpha_{nP})\,|\mathbf{E}|\delta E$. To minimize the fluctuations of the detuning, we thus want to minimize $|\mathbf{E}|$ at all atomic positions. To do that, we sit at a fixed value of Δt and

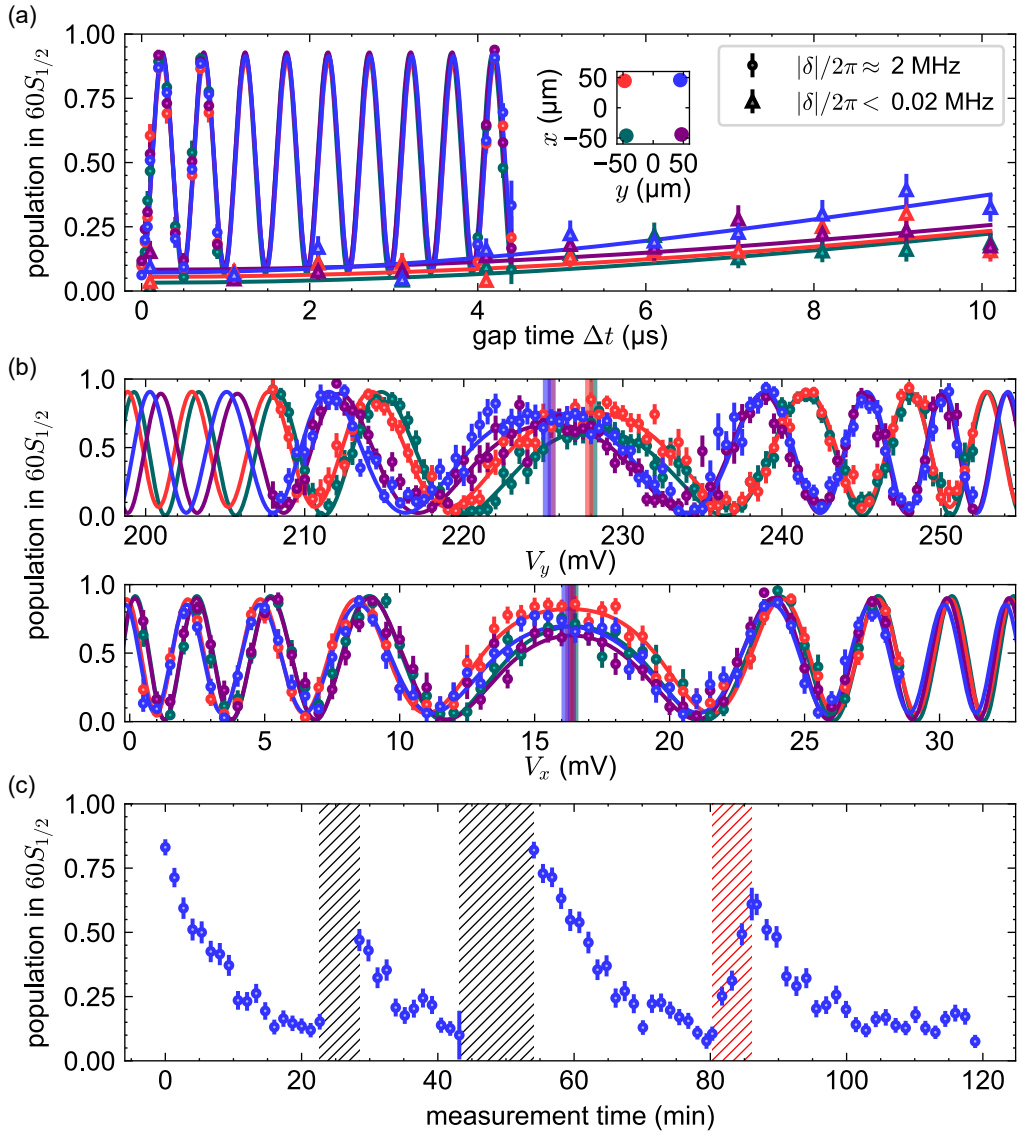

Figure 2.5: Quantifying the inhomogeneities and drifts of the resonance frequencies of several $60S \leftrightarrow 60P$ transitions, using Ramsey interferometry. Data was taken on four atoms far away from each other, such that interactions are negligible during the sequence. (a) Examples of Ramsey oscillations, for two different detunings δ. Inset: position of the four atoms of interest. (b) Calibration of the compensation electric field based on Ramsey interferometry. We sit at a gap time $\Delta t = 4$ μs between the two $\pi/2$-pulses, and change the electric field by scanning the voltage V_μ applied on the compensation electrodes in direction μ. For each atom, the colored vertical line indicate the voltage V_μ^0 which sets the electric field component E_μ to zero. A left-right gradient is visible along the y direction. (c) Stability test of the resonance frequency, using a gap time of $\Delta t = 8$ μs. The same measurement is repeated many times with identical experimental parameters, with dead times (black hatched regions) and a change of the rising time for the z-magnetic field (red hatched region).

change $\mathbf{E}$ by scanning the voltages on the compensation electrodes (see Fig. 7 of the Introduction). Injecting the Stark shift given by Eq. (2.6) into the Ramsey formula [Eq. (2.5)], we expect the population in nS to oscillate in a symmetric way around the zero of the electric field. Experimentally, we are able to change each component E_μ of the electric field for $\mu \in \{x, y, z\}$ in an almost independent way, by scanning three voltages V_μ. Experimental results are shown in Fig. 2.5(b) along x and y. For each atom, we identify the voltage V_μ^0 which sets E_μ to zero, by fitting the probability with the functional form $A\cos\left[\Delta t\,\alpha\left(V_\mu - V_\mu^0\right)^2\right] + B$, where A, B, α and V_μ^0 are free parameters. While the probabilities of the four considered atoms overlap well with respect to V_x, indicating a homogeneous electric field, they are dephased along y, revealing a residual left-right gradient with unexplained origin so far. Using the conversion $E_y = V_y/l_y$ with $l_y \sim 1.5$ cm, we estimate the gradient to be 2 mV/cm in 100 µm. This leads to inhomogeneities of δ_{Stark}, which can be minimized by fixing the voltage to the average value of all V_y^0 — resulting in a trade-off between homogeneity and perfect cancellation of the electric field. After calibration of the electric field, we achieve inhomogeneities that are less than 20 kHz for $n = 60$.

A crucial aspect of the calibration of the detuning is its stability in time. I would like to mention an example of thermal effect affecting the stability, even if it is probably quite specific to our setup. As shown in Fig. 2.5(c), an interruption of the experiment during a few minutes can change the detuning by as much as ~ 50 kHz (here for $n = 60$), before it goes back to its initial value in about 10 minutes. We identified that this drift is due to the heating of the coils that produce the magnetic field along z, since the phenomenon can be reproduced by changing the coil turn-on duration: a drift of the magnetic field of 40 mG (0.1% of the set value of 45 G) is sufficient to explain the observed frequency shift of ~ 50 kHz. An obvious solution to this problem would be to continuously trigger the coils, even when the experiment is not running.

Two-photon microwave transitions The microwave transitions that I have shown so far are single-photon transitions, and they are thus limited to dipole-coupled states. To go beyond, we need to apply multi-photon transitions. For instance, to produce a $\pi/2$-pulse between two S states or two P states, we need two-photon microwave transitions. This was set up during my PhD, as shown in Fig. 2.6 where we performed two-photon transitions between two S states: $\left|nS_{1/2}, m_J = 1/2\right\rangle$ and $\left|(n+1)S_{1/2}, m_J = 1/2\right\rangle$.

We can achieve two-photon Rabi frequencies on the order of 10 MHz with detuning from the intermediate states of ~ 200 MHz. Increasing much further the Rabi frequency

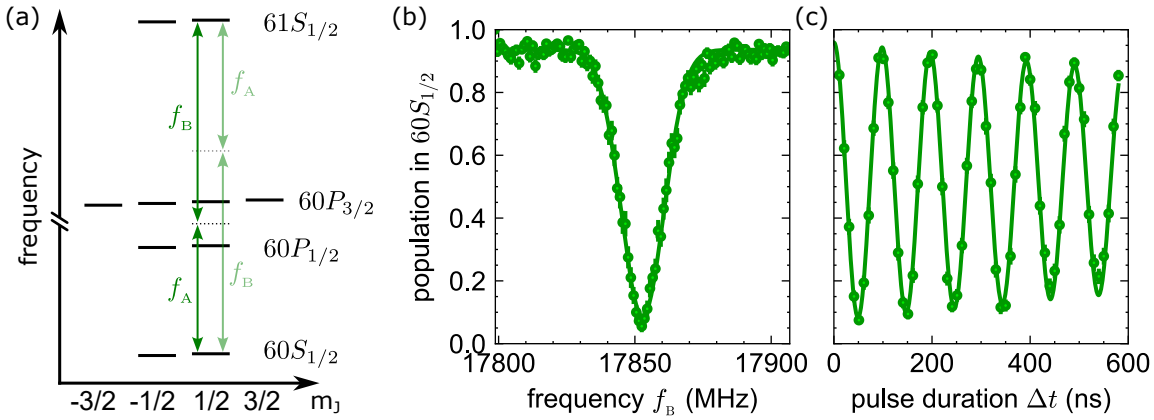

Figure 2.6: Example of a two-photon microwave transition. (a) Relevant atomic levels for the two-photon transition between the states $|nS_{1/2}, m_J = 1/2\rangle$ and $|(n+1)S_{1/2}, m_J = 1/2\rangle$. The green arrows indicates the microwave tones involved in the transition: the main contribution comes from the dark green scheme ($f_A + f_B$) which is detuned by ~ 200 MHz from both $60P_{1/2}$ and $60P_{3/2}$; the light green scheme ($f_B + f_A$) probably also plays a role. (b) Two-photon spectrum versus f_B, with $f_A = 17\,000$ MHz. The pulse shape is Gaussian. (c) Two-photon Rabi oscillation at the resonance ($f_A = 17\,853$ MHz), giving an effective Rabi frequency of 10.2 MHz.

is probably hard, due to the finite detuning that has to be compared with the single-photon Rabi frequency (a few tens of MHz). Still, the fidelity of a π-pulse reaches 99 ± 1 % on non-interacting atoms. A promising, but costly alternative to two-photon microwave transitions is optical Raman transitions, for which we can set larger detunings due to the larger frequency spacings in the low-energy states; on top of that, it would offer local resolution.

Take-home message

Our microwave setup allows us to drive coherent single- and two-photon transitions between Rydberg states, with a percent-level homogeneity across the array and coherence times of several µs in the absence of interatomic interactions. To do so, we need to compensate for several sources of frequency shifts, that originate from the microwave field itself (microwave shifts) and from the static electric field background (Stark shifts). We achieve a stabilization of the Ramsey resonance frequencies of a few tens of kHz, which at the moment is limited by thermal drifts and residual electric field gradients. In the context of quantum simulation, those techniques can be used for precise global rotations of our spins/qubits.

2.1.2 Incoherent transitions for fast removal of atomic population

The previous subsection showed coherent population transfers between two isolated Rydberg states. In some cases, coherence (in the sense that the atom can come back to its initial state) is not needed: one just wants to get rid of the population in an atomic state, by shelving it in a "garbage" state. For example, to switch off the dipole-dipole interactions involving two Rydberg states $|r\rangle$ and $|r'\rangle$ (typically, $|r,r'\rangle$ getting coupled with $|r',r\rangle$), one just has to transfer the population in $|r'\rangle$ to a third Rydberg state $|r''\rangle$ (or an ionized state) which does not interact anymore with $|r\rangle$. The pulse that realizes this atomic transfer has to be fast compared with the typical interaction energies; and it also has to be state-selective, in the sense that it removes only one of the two Rydberg states of interest ($|r'\rangle$ but not $|r\rangle$). We call such pulses *freezing pulses*, since they allow us to stop the interacting dynamics. Another motivation of fast removal is to decrease the detection errors that originate from the finite lifetimes of the Rydberg states (de Léséleuc et al., 2018).

In the following, I will show two methods for removing the atomic population of a given Rydberg state: one is based on a multi-photon transition, and is now routinely used on our setup; the other one consists in using a strong DC electric field. Both of them send the atomic population into one of the close *hydrogenic manifolds*, meaning the set of almost degenerate levels with high orbital momentum $L > 4$.

Multi-photon transitions In Fig. 2.7, I show how a three-photon transition allows us to get rid of the atomic population in the Rydberg state $\left|60P_{1/2}, m_J = 1/2\right\rangle$, by transferring it to $58G$. This is done by using a large microwave power (a few hundred mW), at a frequency three times smaller than the target transition. If the effective Rabi frequency of the three-photon process is much larger than the Zeeman splitting of the state $58G$, we observe that we lose the population in $\left|60P_{1/2}, m_J = 1/2\right\rangle$ over a broad range of frequencies ~ 100 MHz [Fig. 2.7(b)]. We think that we populate many sublevels of $58G$ and from the hydrogenic manifold $n = 58$ (which is located 60 MHz above $58G$), thus preventing the transfer to be reversible. Remarkably, the pulse is state-selective; for example, $\left|60S_{1/2}, m_J = 1/2\right\rangle$ is very weakly affected [Fig. 2.7(c)].

One may argue that this incoherent pulse is actually not needed to remove the population in $\left|60P_{1/2}, m_J = 1/2\right\rangle$. As can be seen from Fig. 2.7(a), a single-photon π-pulse to $59D$ would be sufficient. This protocol also works, with similar efficiencies and pulse durations; however the incoherent pulse has the advantage that it reduces the contribution of Rydberg lifetimes to detection errors. An atom in a Rydberg state,

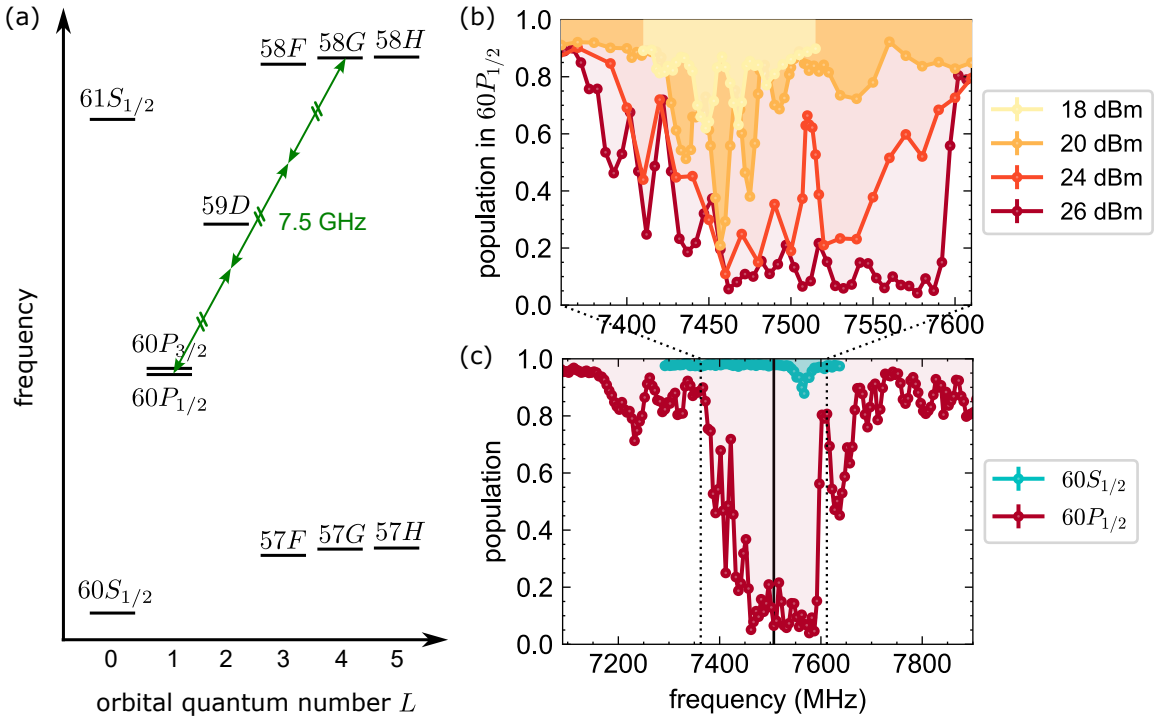

Figure 2.7: Fast, incoherent, state-selective population transfer from the Rydberg state $|60P_{1/2}, m_J = 1/2\rangle$, using a three-photon transition. (a) Accessible energy levels from $60P_{1/2}$ (the Zeeman sublevels are not represented). Green arrows show the three-photon transition to $58G$ which, together wit $58F$, $58H$, etc., is part of the *hydrogenic manifold* of $n = 58$. (b) Microwave spectra of the three photon transition, starting from the state $|60P_{1/2}, m_J = 1/2\rangle$, for various values of the microwave power at the position of the antenna (expressed in dBm). The magnetic field is 45 G. The microwave pulse has a duration $\Delta t \approx 45$ ns, and is produced using an amplifier with gain 34 dB (ZVE-3W-83+ by Mini-Circuits). At low powers, the Zeeman structure of $58G$ is resolved. (c) Microwave spectra with the same experimental parameters, at 26 dBm, starting from either $|60P_{1/2}, m_J = 1/2\rangle$ or from $|60S_{1/2}, m_J = 1/2\rangle$. At the frequency shown by the solid black line, the pulse can remove most of the $60P_{1/2}, m_J = 1/2$ population, without affecting $60S_{1/2}, m_J = 1/2$.

which should be kicked out from its tweezer and lost after the Rydberg sequence, has a finite probability ε' to decay back to the ground state and be imaged, leading to a false positive (de Léséleuc et al., 2018). For $59D$ which has a lifetime $\tau \sim 200$ µs (Beterov et al., 2009), we measure $\varepsilon' = 7 \pm 1$ %, whereas after the incoherent pulse it can reach $\varepsilon' = 1 \pm 1$ %.

Effect of a strong DC electric field Motivated by the perspective of ionizing the Rydberg levels in a state-selective way, we tested an ionization method making use of a DC electric field. Our expectation was the following: when subject to a DC electric field E, the Coulombic potential of the valence electron is linearly shifted; if the

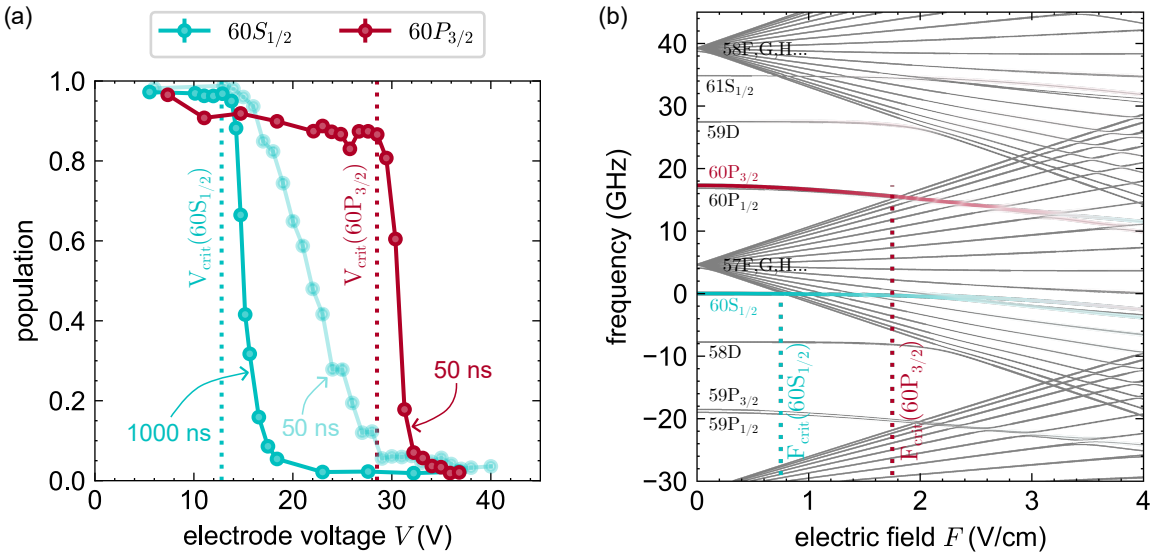

Figure 2.8: Effect of a strong DC electric field on the atomic population of two Rydberg states. (a) Measured population of two Rydberg states $\left|60S_{1/2}, m_J = 1/2\right\rangle$ and $\left|60P_{3/2}, m_J = -1/2\right\rangle$ as a function of the applied voltage on one of the the eight electrodes. The experimental sequence consists of the Rydberg excitation to the target state (using STIRAP and an additional microwave π-pulse for $60P_{3/2}, m_J = -1/2$), a pulse of high-voltage DC electric field with one compensation electrode, and state detection in the target state. For the red and light blue curves, the pulse duration is $\Delta t = 50$ ns; since the population in $60S_{1/2}, m_J = 1/2$ takes a longer time to be transferred, we also applied a longer pulse $\Delta t = 1000$ ns (dark blue curve). For each state, we infer a critical value of the electrode voltage V_{crit} for which the population is lost. (b) Energy spectrum of ^{87}Rb versus DC electric field F (Stark map), simulated using Šibalić et al. (2017). The overlap with the state $60S_{1/2}, m_J = 1/2$ (resp. $60P_{3/2}, m_J = -1/2$) is shown by the strength of the blue (resp. red) color. We identify two critical fields F_{crit} for which the state of interest merges with the hydrogenic manifold $57F, G, H...$

electric field is strong enough, the electron can tunnel out of the Coulombic trapping potential and escape. The ionization probability depends on the energy of the Rydberg state: the higher the energy, the smaller the electric field needed for ionization. A semi-classical formula states that the ionizing electric field $F_{\text{ionization}}$ for an alkaline Rydberg atom with principal quantum number n is (Gallagher, 1994; Littman et al., 1978):

$$F_{\text{ionization}} = \frac{F_0}{16\, n^4} \tag{2.7}$$

where $F_0 = \frac{e}{4\pi\epsilon_0 a_0^2} \approx 5 \cdot 10^9$ V/cm is the electric field felt by an electron, at a distance from the nucleus equal to the Bohr radius a_0. To ionize the state $n = 60$, we need to apply a strong DC electric field $F_{\text{ionization}} \approx 24$ V/cm according to Eq. (2.7).

To test this hypothesis, we slightly modified the existing setup: we disconnected one compensation electrode — checking that the effect on the background electric

field was weak enough to maintain efficient Rydberg excitation and deexcitation —, and connected the free electrode to a high-voltage pulse generator (LINOS LIV 20) which is generally used to drive a free space EOM. We initialized a few atoms in a given Rydberg state, either $\left|60S_{1/2}, m_J = 1/2\right\rangle$ or $\left|60P_{3/2}, m_J = -1/2\right\rangle$, switched on the electric field with a voltage V for a duration Δt and measured the remaining population in the initial state. Results are shown in Fig. 2.8(a). Scanning the voltage V, we observe two regimes: under a critical voltage V_{crit}, the atomic population is almost not affected; above this voltage, atom losses start, with a dynamics that strongly depend on the state. For $\left|60P_{3/2}, m_J = -1/2\right\rangle$, a pulse duration $\Delta t = 50$ ns is sufficient to remove all the population for $V > V_{\text{crit}}$, whereas for $\left|60S_{1/2}, m_J = 1/2\right\rangle$ the losses are much slower, and we need a long pulse duration $\Delta t \sim 1$ µs to define a sharp transition between the two regimes.

However, two observations are not in agreement with the hypothesis of DC ionization. First, the critical voltage V_{crit} for which atoms start to be lost is a lot smaller than our expectations[2]: $V_{\text{crit}}(60S_{1/2}) \approx 12.8$ V and $V_{\text{crit}}(60P_{3/2}) \approx 28.5$ V. Second, the measured critical field for $60S_{1/2}$ is smaller than the one for $60P_{3/2}$, whereas $60P_{3/2}$ is closer to the ionization threshold. For those reasons, we think that we actually do not ionize the Rydberg atoms, but transfer them to the hydrogenic manifold $n = 57$. Figure 2.8(b) shows the energy dependence of a few Rydberg states with the applied electric field F. As F increases, the state energies are shifted (Stark shift), and they start to mix with other neighboring states. For each of the two states of interest, we can define a critical field E_{crit} for which the state merges into the hydrogenic manifold $57F, G, H...$ The ratio of the two theoretical critical fields $F_{\text{crit}}(60P_{3/2})/F_{\text{crit}}(60S_{1/2}) \approx 2.3$ is in good agreement with the ratio of the two experimental critical voltages $V_{\text{crit}}(60P_{3/2})/V_{\text{crit}}(60S_{1/2}) \approx 2.2$[3]. In the end, our interpretation of the losses is that the pulse of high-electric field acts like a violent change of the atomic Hamiltonian (a "quench") that redefines the eigenstates; the initial state population gets projected on many new eigenstates within the hydrogenic manifold, leading to a complex out-of-equilibrium dynamics during which the overlap with the initial state decreases irreversibly.

Now, can this process be useful for a practical removal of the atomic population? From Fig. 2.8(a), the range of voltages that we can use for a state-selective removal is

[2] Our intern Jamie Boyd performed simulations using finite element method, to estimate the amplitude of the electric field when applying a DC voltage on one electrode, and obtained a conversion factor: $F = V/l$ with $l = 13$ cm. To create the estimated ionization field of $F \sim 24$ V/cm for $n = 60$, we expect a voltage $V \sim 300$ V.

[3] The absolute values of the critical voltages are also in reasonable agreement with the effective length l extracted from finite-element-method simulations (within a factor 1.5).

very narrow: for a pulse duration $\Delta t = 50$ ns, working close to the critical voltage $V_{\text{crit}}(60P_{3/2})$ might be an option, to remove the population in $60S_{1/2}$ without affecting much the one in $60P_{3/2}$, but the fidelity of the process looks limited. Using longer pulses $\Delta t \sim 1$ µs is not an option if we want the freezing pulse to be fast compared with the typical interaction time scales. Finally, repetitive applications of high-voltage on the electrodes could have unknown effects on the stability of the electric field background. For those reasons, we did not use this process in the experiments described in the rest of the manuscript. However, this method could be useful for getting rid of detection errors due to the finite Rydberg lifetimes: for example, one could think of applying a fast removal pulse without state selectivity, after the Rydberg sequence, to remove all the remaining Rydberg population before imaging the ground state atoms. This would be a way to efficiently distinguish between ground and Rydberg atoms, without the bias due to the lifetimes; it will be implemented in the next-generation machine with dedicated electrodes.

Take-home message

Incoherent transitions are an efficient way to get rid of the atomic population in a Rydberg state, in a fast and state-selective way. It also has the advantage of decreasing the detection errors due to the finite lifetimes. To this end, we use multi-photon transitions to the hydrogenic manifold. Another option consists of applying a pulse of high-voltage DC electric field, although our current setup does not allow to use it in a state-selective way.

2.2 Local transitions

In this section, I describe a new procedure that we designed for coherent local transitions between Rydberg states, in the sense that rotations are spatially resolved. Our results were published in Bornet et al. (2024).

In the quest for full many-body quantum control, various platforms ranging from neutral atoms and trapped ions to polar molecules and superconducting circuits, have developed strategies to combine their native interactions with high-fidelity local rotations. This enhanced level of control has enabled the preparation of broader classes of initial states (Fukuhara et al., 2013; Dumitrescu et al., 2022), the measurement of multi-basis observables (Roushan et al., 2017), and even mid-evolution gates (Zhang et al., 2017). These advances enabled the integration of novel quantum information protocols with quantum simulators (Knill et al., 2008; Gambetta et al., 2012; Gaebler et al., 2012; Pagano et al., 2020; Elben et al., 2023).

In arrays of atoms coupled via Rydberg interactions, local rotations have already been demonstrated, with the combination of ground-state Raman manipulations (Yavuz et al., 2006; Jones et al., 2007) and the ability to address individual atoms (Birkl and Fortágh, 2007; Isenhower et al., 2010; Xia et al., 2015; Labuhn et al., 2014). This is appropriate when the qubit is encoded, for example, in the hyperfine ground states of alkali atoms. However, when the qubit is encoded in a pair of Rydberg states, realizing an analogous procedure would require mapping coherently two Rydberg states on two hyperfine states, which is experimentally challenging (Glaetzle et al., 2015).

Our technique makes use of local lightshifts combined with a global microwave field, to make rotations directly in the Rydberg manifold. I will first describe how we generate local lightshifts with arbitrary spatial amplitude on atomic arrays. Then, I will explain the details of our technique for local rotations and study its performance.

2.2.1 Local lightshifts with improved stability

Local addressing lightshifts Contrary to microwave fields, optical fields have the ability to resolve spatially each atom of the array. More precisely, a 1014-nm beam with spatially-dependent Rabi frequency $\Omega(\mathbf{r})$, detuned by a frequency Δ from the transition $6P_{3/2} \leftrightarrow nS_{1/2}$, creates a lightshift $\delta_{\text{ls}}(\mathbf{r})$ on the Rydberg state $nS_{1/2}$ (Fig. 2.9). In the regime where $|\Delta| \gg |\Omega(\mathbf{r})|$, the lightshift is given by $\delta_{\text{ls}}(\mathbf{r}) \sim \Omega(\mathbf{r})^2/4\Delta$[4]. By tuning

[4]In practice, Ω has contributions from several hyperfine sublevels of the $6P_{3/2}$ manifold.

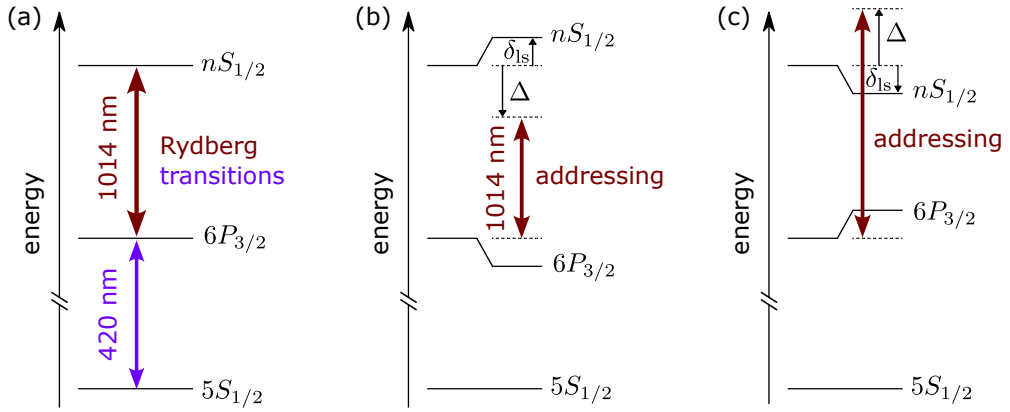

Figure 2.9: Addressing lightshifts. Contrary to the Rydberg excitation (a) which is carried out using a 1014-nm laser beam on resonance with the transition $6P_{3/2} \leftrightarrow nS_{1/2}$, addressing lightshifts are generated using a 1014 nm laser beam detuned by a frequency Δ of a few hundred MHz. By tuning the sign of Δ, we can apply either a positive (b) or a negative (c) lightshift $\delta_{\rm ls}$ on $nS_{1/2}$.

the local power of the addressing beam, we change proportionally $\Omega(\mathbf{r})^2$, so we control the value of the local lightshift. By changing the sign of the detuning, we control the global sign of the lightshift. A proof of principle was already performed in our group in de Léséleuc et al. (2017) by addressing a single atom. During my PhD, we developed tools to extend this ability to large arrays, in a precise and stable way.

Local lightshifts have many applications. At the single-atom level, they enhance our local control of the atoms: they allow us to tune the resonance frequency of a transition at will, allowing us to shield the transition for some atoms and to perform local rotations (as will be explained in the next subsection). At the many-body level, they can be seen as a spatially-dependent magnetic field, that enrich the tunability of the experimentally-accessible Hamiltonians, and allow us to probe new phases (see for example chapter 4).

Addressing setup To generate local lightshifts, we use the optical setup that is shown in Fig. 2.10. As for optical tweezers, a dedicated spatial light modulator (LCOS-SLM X10468 by Hamamatsu) is used for imprinting a spatially-dependent phase pattern on a Gaussian beam at 1014 nm. The addressing beam is merged with the tweezer beam before the vacuum chamber, and focused on the atomic plane through the same aspheric lens as the tweezers. The phase pattern is designed such that the two-dimensional Fourier transform of the beam on the SLM realizes the target intensity pattern $\Omega(\mathbf{r})^2$. In practice, the intensity pattern is an array of diffraction-limited Gaussian spots that overlap with a set of selected tweezers. We use the same algorithm

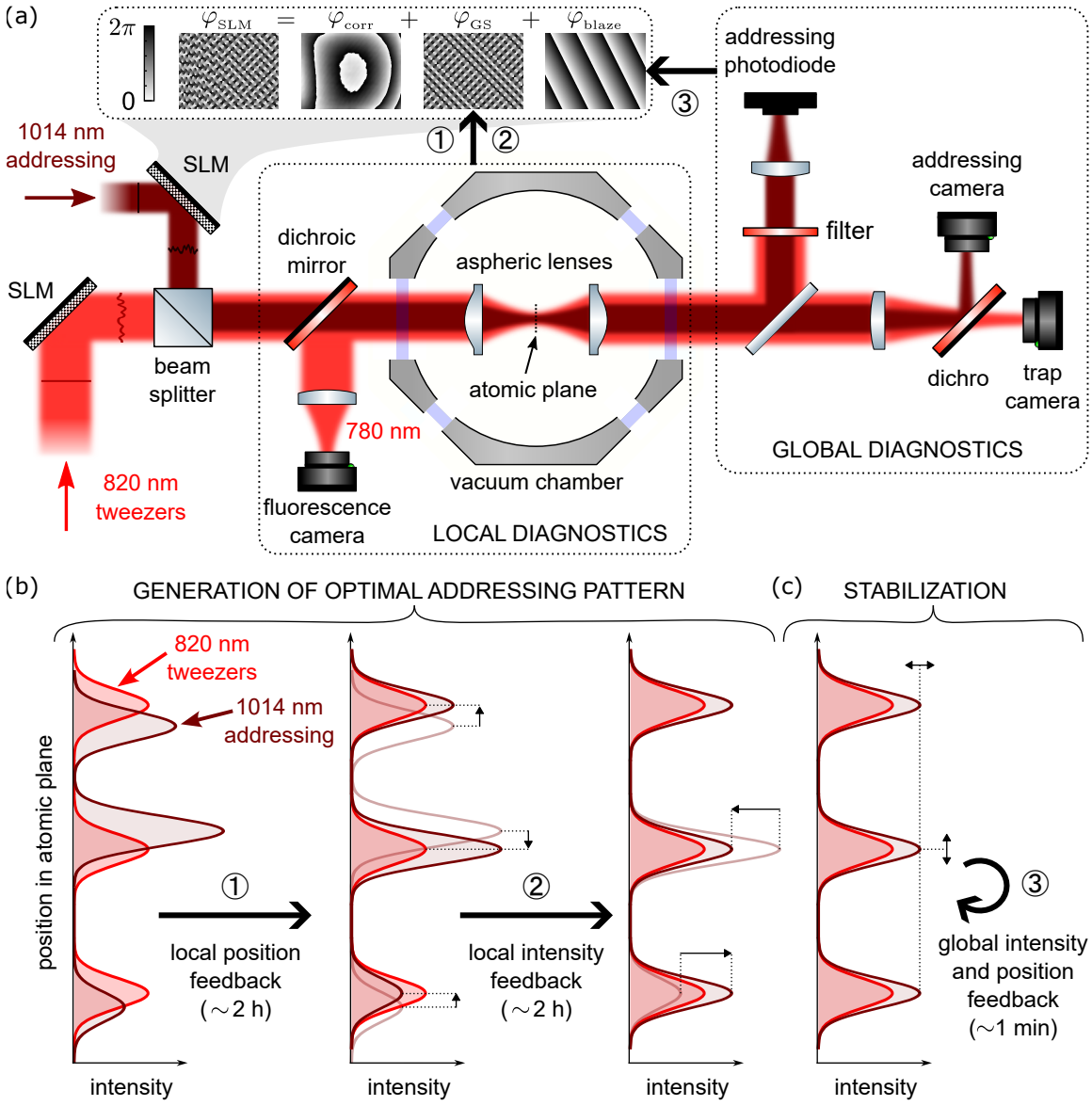

Figure 2.10: Generation and stabilization of addressing patterns. (a) Simplified optical setup. The light beams for optical tweezers and addressing get reflected on two spatial light modulators (SLM) to imprint a spatially-resolved phase pattern φ_{SLM} (inset); then, they are merged on a beam splitter and focused with an aspheric lens inside the vacuum chamber to produce the desired intensity pattern in the atomic plane. A telescope (not shown) is used for pupil conjugation of the SLM plane on the aspheric lens. We carry out two types of diagnostics: local diagnostics using the fluorescence imaging path at 780 nm; or global optical diagnostics using a photodiode and two cameras at the back of the vacuum chamber. Various feedbacks labeled by steps 1 to 3 are performed on the phase pattern of the SLM (see text for details). (b) Typical feedback procedure to generate homogeneous addressing spots, aligned on the tweezers. Starting from a misaligned and inhomogeneous intensity pattern, we first align independently each addressing spot on its associated tweezer (step 1); then we homogenize the intensities with a local intensity feedback (step 2), resulting in an optical phase pattern φ_{GS}. (c) To improve the stability of the relative alignment of the tweezers and the addressing, we regularly (every ~ 7 min) perform a global feedback on the position of each beam in the atomic plane, by tuning the blazing phase on the associated SLM (φ_{blaze}). The feedback takes about 1 min and runs simultaneously to the experiment.

as for the tweezers (weighted Gerchberg-Saxton) to calculate the addressing phase pattern φ_{GS} [see de Léséleuc (2018) for a detailed explanation]. Additionally to this numerically-calculated phase pattern, we apply a fixed phase mask φ_{corr} to correct for various optical aberrations and curvature of the SLM (Nogrette et al., 2014). We also apply a blazed grating φ_{blaze} that controls the global position of the array in the atomic plane. In the end, the total phase mask displayed on the the SLM reads $\varphi_{\mathrm{SLM}} = \varphi_{\mathrm{corr}} + \varphi_{\mathrm{GS}} + \varphi_{\mathrm{blaze}}$.

The amount of available addressing power is a limiting factor for generating lightshifts on many atoms, since the required power scales linearly with the number of addressed atoms. The addressing beam is generated by a 10-W fiber amplifier (ALS-IR-1015-10-A-CP-SF by Azur Light Systems), seeded by a diode laser (DL Pro by Toptica Photonics). A free-space electro-optic modulator (EOM) allows us to switch on and off the power in about 10 ns, and an acousto-optic modulator (AOM) is used for slower intensity modulation (with a typical response time of a few 100 ns). With this setup, we can reach ~ 3 W of optical power before the chamber, which typically allow us to generate lightshifts $|\delta_{\mathrm{ls}}|/2\pi \sim 10 - 60$ MHz on $60S_{1/2}$ with a detuning $|\Delta|/2\pi \sim 400$ MHz, on a few tens of atoms. For a given optical power and detuning, the lightshift scales as n^{-3} with the principal quantum number n.

When the first addressing pattern is generated, the local intensity profile $\Omega(\mathbf{r})^2$ usually deviates from its target. Two correlated imperfections occur: first, the addressing spots in the atomic plane can be misaligned from the tweezers; second, the local intensity felt by the atom (and thus the local light shift) is not homogeneous on the array. We attribute those imperfections to the unavoidable geometrical and chromatic aberrations on the optical path. We designed a procedure to mitigate those two effects, which is summarized in Fig. 2.10(b). It consists of two steps:

1. local position feedback on φ_{GS}, to align each addressing spot on the associated atom position;

2. local intensity feedback on φ_{GS}, to homogenize the addressing lightshifts.

Once it is done, we have an optimal phase pattern φ_{GS}. But in the absence of active stabilization, we still observe global drifts of both the intensity of the addressing (measured by a photodiode) and its relative position with the tweezers (measured by two diagnostic cameras), over the time scale of hours. Those are probably due to slow thermal fluctuations in the laboratory. To correct for those drifts, we added an automatic feedback loop that regularly adjusts the blazed grating φ_{blaze} for both the addressing and the SLM tweezers, to make sure that their position remains the

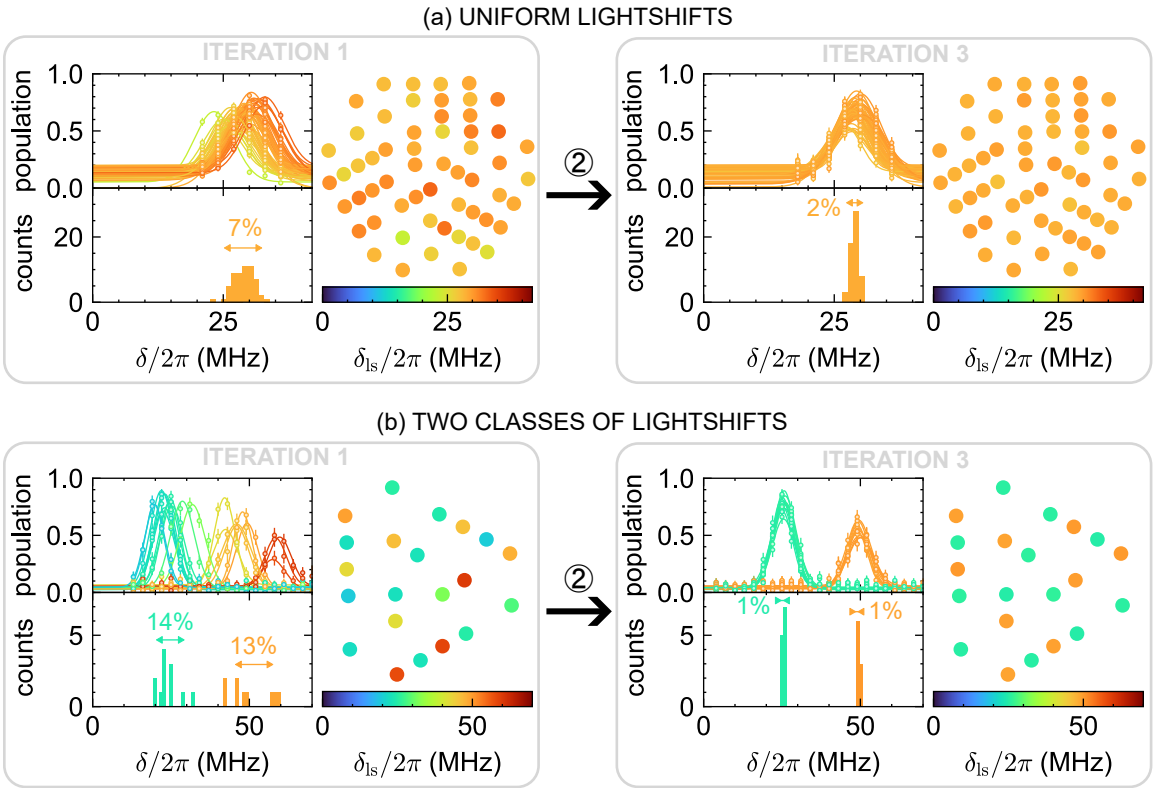

Figure 2.11: Homogenization of the addressing lightshifts, illustrated with two geometries. In the first geometry (a), the target lightshifts are the same for all addressed atoms, whereas in the second geometry (b), there are two classes of addressed atoms, each one with a different value of the target lightshift. For each geometry, the lightshifts are characterized before the feedback on the local intensity (iteration 1) and after (iteration 3). For each iteration, the upper right plot is a microwave spectrum, representing the measured population in $nS_{1/2}$ as a function of the microwave detuning δ ($\delta = 0$ being the resonance in the absence of lightshift). Each spectrum is fitted by a Gaussian function to extract the lightshift δ_{ls}. A histogram of the obtained values of δ_{ls} is shown on the lower left plot. The standard deviation is indicated as a percentage of the average value of δ_{ls}. The right plot is a spatial map of δ_{ls} for the considered geometry.

same as in a reference picture on the diagnostics cameras; we can also stabilize the global addressing intensity to a few percents by a feedback on the addressing AOM [Fig. 2.10(c)].

In the following, let me present in more details the local feedback steps. For a more pedagogical approach, I will start by the homogenization, even if we usually do it after the local alignment.

Homogenization of the addressing lightshifts To measure the local addressing lightshifts on the state $|nS_{1/2}, m_J = 1/2\rangle$, we acquire microwave spectra simultaneously on all addressed atoms. To ensure that dipole-dipole interactions do not affect too

much the spectrum, we apply a fast freezing pulse after the microwave pulse, and use a π-pulse with Rabi frequency $\Omega/2\pi \sim 5 - 10$ MHz which is larger than the typical interaction strength ($J/2\pi \sim 0.1 - 1$ MHz). A spectrum before homogenization is shown on Fig. 2.11(a). From the spectrum of an addressed atom j, we extract the value of the lightshift $\delta_{\mathrm{ls}}^{(j)}$ by a Gaussian fit. We typically obtain standard deviations $\sigma(\delta_{\mathrm{ls}}^{(j)})/\bar{\delta}_{\mathrm{ls}} \sim 10$ % with $\bar{\delta}_{\mathrm{ls}}$ the lightshift averaged on all addressed atoms. The feedback then consists in consists in regenerating a new phase pattern φ_{GS} with a modified target intensity (by re-running the Gerchberg-Saxton algorithm): if the target intensity for atom j at iteration k was $w_k^{(j)}$, then the new target intensity after the feedback will be

$$w_{k+1}^{(j)} = \frac{w_k^{(j)}}{1 - \alpha\left(1 - \delta_{\mathrm{ls}}^{(j)}/\bar{\delta}_{\mathrm{ls}}\right)}, \tag{2.8}$$

where α is a gain that we set to $\alpha \lesssim 1$ to avoid oscillations of the feedback. If $\alpha = 1$, the previous formula simply becomes $w_{k+1}^{(j)} = w_k^{(j)}\bar{\delta}_{\mathrm{ls}}/\delta_{\mathrm{ls}}^{(j)}$. After a few iterations (typically 3 to 5), the standard deviation gets down to $\sigma(\delta_{\mathrm{ls}}^{(j)})/\bar{\delta}_{\mathrm{ls}} \sim 2$ %.

This procedure is not restricted to uniform target lightshift. We can define several classes of addressed atoms, each one having a different target lightshift, and homogenize the lightshifts independently inside each class. For the feedback, we simply adapt the gain from Eq. (2.8) for each class, by redefining $\bar{\delta}_{\mathrm{ls}}$ as the lightshift averaged on atoms from the considered class. An example with two classes of atoms is shown in Fig. 2.11(b). The interest of such a procedure will become clear in section 2.2.2 that deals with local rotations.

Local alignment of the addressing spots Let me now come back to the first step of the feedback. At first sight, if we only want homogeneous addressing light shifts, this step is not essential, since the local intensity feedback will naturally compensate small misalignments of the addressing spots by increasing their intensity. However, this would lead to situations where some atoms lie at the edge of very powerful spots, as illustrated in Fig. 2.12(a).

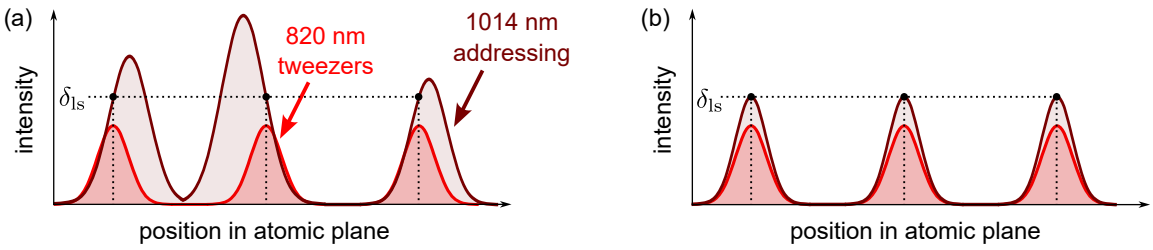

Figure 2.12: Homogeneous lightshifts with misaligned (a) or aligned (b) addressing.

Such a situation is not optimal for three reasons: first, we lose addressing power; second, the lightshifts are more sensitive to any small drift in position; third, the gradient of electric field induces a ponderomotive force on the atoms which will produce unwanted momentum kicks [see Fig. 2.15 for an analysis of the addressing ponderomotive force]. Therefore, we perform an alignment feedback procedure, in addition to the intensity homogenization.

To align the addressing spots on the tweezers, we need to measure the relative displacement $\mathbf{\Delta r}^{(j)}$ of the addressing with respect to the center of the tweezer, for each addressed atom j [as defined in Fig. 2.13(d)]. We apply the following method: we globally move the addressing pattern in the atomic plane along x (resp. along y) by a distance Δx (resp. Δy), by scanning the blazed grating φ_{blaze} on the addressing SLM; for each displacement, we record the population $P^{(j)}(\Delta x, \Delta y)$ in $\left|60S_{1/2}, m_J = 1/2\right\rangle$ after a Gaussian microwave π-pulse with a fixed detuning $|\delta| \gtrsim |\bar{\delta}_{\text{ls}}|$. Our intuition is the following: as we move the addressing in the xy plane, the local lightshift $\delta_{\text{ls}}^{(j)}(\Delta x, \Delta y)$ felt by atom j will vary, which modifies the effective detuning $\delta - \delta_{\text{ls}}^{(j)}(\Delta x, \Delta y)$ of the microwave pulse. More precisely, according to Eq. (2.4), the population for atom j after a Gaussian π-pulse can be approximated by

$$P^{(j)}(\Delta x, \Delta y) \approx \exp\left(-1.8\,\frac{\left(\delta - \delta_{\text{ls}}^{(j)}(\Delta x, \Delta y)\right)^2}{\Omega_0^2}\right). \tag{2.9}$$

with Ω_0 the peak Rabi frequency of the Gaussian pulse. We can fit each population $P^{(j)}(\Delta x, \Delta y)$ to extract the position of the maximum lightshift $\max_{\Delta x, \Delta y}\left[\delta_{\text{ls}}^{(j)}(\Delta x, \Delta y)\right]$[5]. This position, that we will call $\Delta x^{(j)}$ (resp. $\Delta y^{(j)}$) in the following, is simply the projection of the displacement along x (resp. y): $\mathbf{\Delta r}^{(j)} = \Delta x^{(j)}\,\mathbf{e}_x + \Delta y^{(j)}\,\mathbf{e}_y$, with $\mathbf{e}_\alpha$ the unit vector in direction α. An illustration of the method is shown in Fig. 2.13(a) for a circular pattern. With two scans (one along x and one along y), we can extract the displacement $\mathbf{\Delta r}^{(j)}$ for all atoms j in a parallel way. In this particular case, we identify that the addressing pattern is globally rotated with respect to the tweezers.

Once we have measured $\mathbf{\Delta r}^{(j)}$ for all atoms j, we apply a feedback by regenerating a new phase pattern φ_{GS} with redefined positions. If the target position of the addressing

[5] If $|\delta| > \max_{\Delta x, \Delta y}\left[|\delta_{\text{ls}}^{(j)}(\Delta x, \Delta y)|\right]$, the effective detuning does not change sign, so the measured population $P^{(j)}$ is an increasing function of the lightshift. Even if this condition is not satisfied, the population is still symmetric around $\delta = \max_{\Delta x, \Delta y}\left[\delta_{\text{ls}}^{(j)}(\Delta x, \Delta y)\right]$ so we can still extract the position of the maximum lightshift, by identifying the symmetry point. However, this makes the fitting procedure harder, since $P^{(j)}$ can have two peaks.

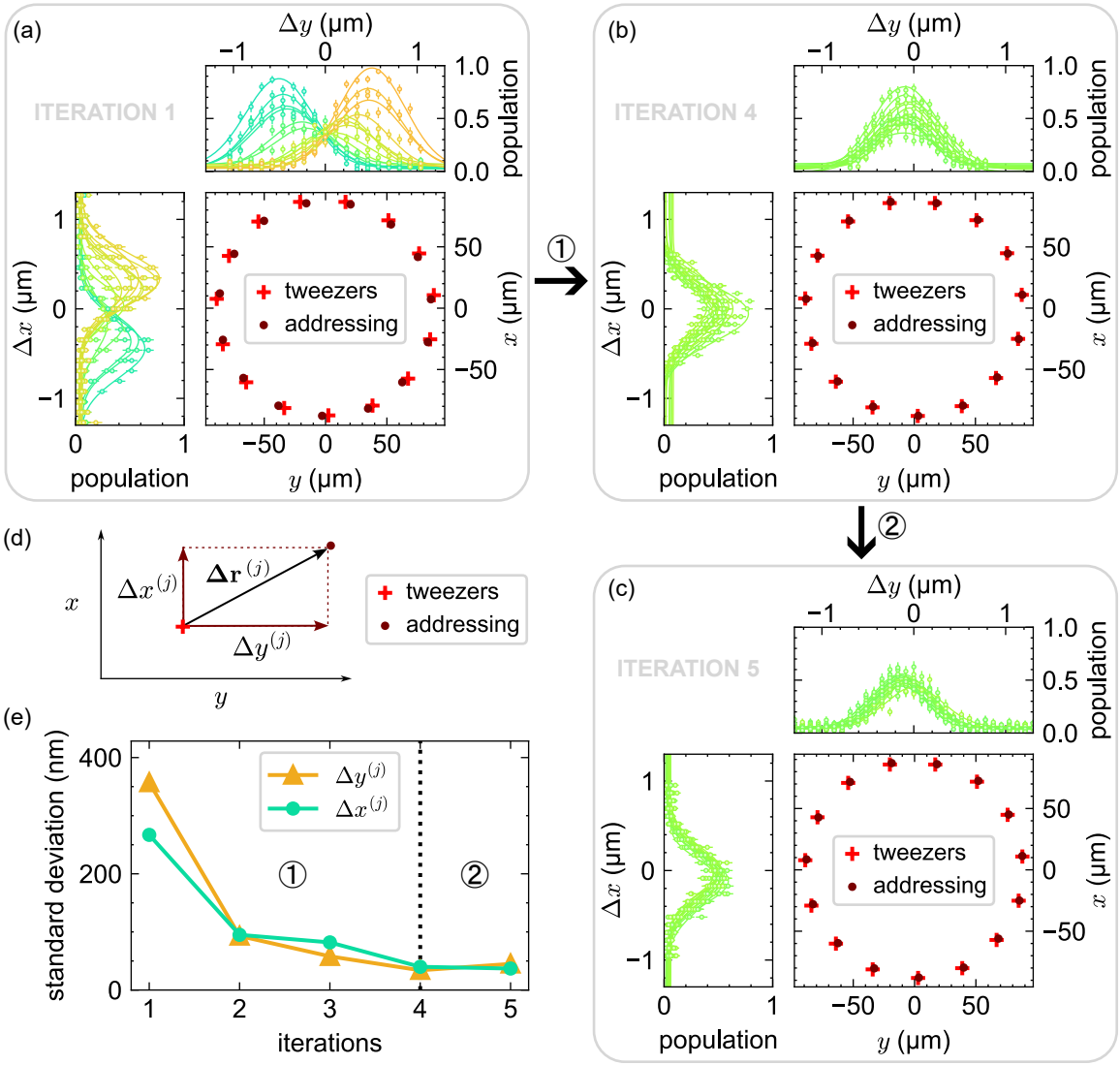

Figure 2.13: Local alignment of the addressing on the tweezers, illustrated for a circular geometry. At each iteration of the feedback [grey frames (a) and (b)], we apply the following procedure to extract the displacement $\mathbf{\Delta r}^{(j)}$ of the addressing with respect to the center of the tweezer [as defined in (d)]: we sit at a fixed microwave detuning $\delta/2\pi = -30$ MHz which is larger than the average lightshift $\bar{\delta}_{\mathrm{ls}}/2\pi \sim -23$ MHz, and we scan the blazed grating φ_{blaze} of the addressing SLM, successively along x and y. We measure the population in $|60S_{1/2}, m_J = 1/2\rangle$ as a function of the global position Δx (resp. Δy) of the addressing, and fit it with a Gaussian probability. The center of the Gaussian for atom j gives us $\Delta x^{(j)}$ (resp. $\Delta y^{(j)}$), the projection of $\mathbf{\Delta r}^{(j)}$ along x (resp. y). The displacements are represented in the xy plane, enhanced by a factor 10 for a better visualization. After four iterations, the standard deviation of the projected displacements $\Delta x^{(j)}$ and $\Delta y^{(j)}$ goes down to ≈ 40 nm. At the end of the local alignment feedback, we apply a local intensity feedback to homogenize the lightshifts, and measure again the local displacements (iteration 5) to check that the intensity feedback has no measurable impact on the displacements.

spot j at iteration k is denoted by $\mathbf{r}_k^{(j)}$, then the new positions are given by

$$\mathbf{r}_{k+1}^{(j)} = \mathbf{r}_k^{(j)} - \beta \boldsymbol{\Delta}\mathbf{r}^{(j)} \tag{2.10}$$

with $\beta \lesssim 1$ a gain to avoid divergence of the feedback. In a few iterations, we converge to an aligned pattern, with a standard deviation of ~ 40 nm for both displacements $\Delta x^{(j)}$ and $\Delta y^{(j)}$ [Fig. 2.13(b,e)]. We also checked that a feedback on the local intensities preserves the alignment [Fig. 2.13(c,e)].

Note that the local position feedback allows us to align the addressing spots on the center of the tweezers, even if the tweezers have a disordered geometry. This is due to the fact that we measure a relative displacement, and not an absolute position. Measuring the absolute position of the tweezers is not straightforward, I refer the interested reader to Bornet (2024) for preliminary works done in our team, and also to Chew et al. (2024).

Atoms as a local probe of the addressing profile The measurement method for local position feedback does not only give access to the maximum lightshift, but to the full intensity profile: in some sense, atoms are a local probe that goes beyond the diffraction limit! To illustrate this, I show in Fig. 2.14 how we can extract the addressing waist for each atom.

Interestingly, we do not find the same waist along the two radial directions. We do not yet understand why, this could be the subject of future investigations.

Undesirable effects of the addressing Before concluding this subsection about the addressing, let me mention a few side effects of the addressing that we try to experimentally mitigate.

- **Depumping** If the Rabi frequency Ω of the addressing is too large compared with the detuning $|\Delta|$, an addressed atom in the addressed state $nS_{1/2}$ can scatter an addressing photon and be transferred to the intermediate state $6P_{3/2}$, from which it decays to the ground state $5S_{1/2}$ within a few hundred ns. This *depumping* effectively reduces the lifetime of $nS_{1/2}$ for addressed atoms. A solution to reduce this effect is to increase the detuning, but this will also reduce the value of the lightshifts as $|\delta_{\text{ls}}(\mathbf{r})| \sim \Omega(\mathbf{r})^2/4|\Delta|$. For this reason, we usually work in trade-off regime where $\Omega \lesssim |\Delta|/2$. The depumping rate can be measured by initializing an atom in $nS_{1/2}$, applying an addressing pulse and recording the population in the ground state (without deexcitation). A typical order of

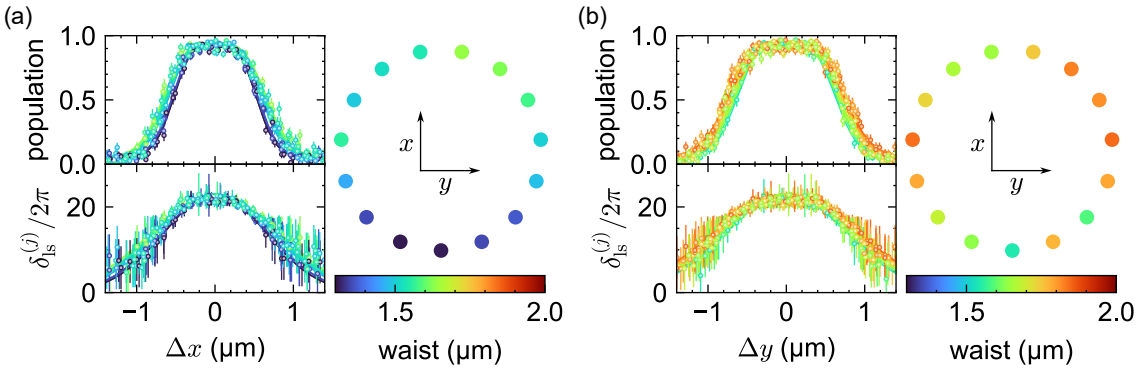

Figure 2.14: Measurement of the addressing waist along x (a) and along y (b). For each direction $\mu \in \{x, y\}$, we measure the population $P^{(j)}$ in $|60S_{1/2}, m_J = 1/2\rangle$ as a function of the displacement $\Delta\mu$ of the addressing (upper left plot). For each atom j, we fit the recapture probability $P^{(j)}(\Delta\mu)$ by Eq. (2.9) using a Gaussian profile for $\delta_{\text{ls}}^{(j)}(\Delta x, \Delta y)$. We can invert Eq. (2.9) to compute the Gaussian profile of the lightshift in MHz (lower left plot); however error bars are large on the wings of the Gaussian. The right plot shows the extracted waist for all addressed atoms j. Here, the waist is defined as the $1/e^2$ radius of the intensity. We find an average waist of 1.5 μm along x and 1.7 μm along y, with standard deviations of 0.1 μm. No pupil was used for this experiment.

magnitude for the above parameters is a lifetime of ~ 0.5 μs instead of the natural Rydberg lifetime ~ 100 μs for $n = 60$. For the purpose of quantum simulation, this means that we have to design sequences which minimize the duration spent by the addressed atoms in the state $nS_{1/2}$.

- **Momentum kicks due to the ponderomotive force** The addressing beam, as an oscillating electric with spatially-dependent amplitude, exerts a ponderomotive force on the addressed atoms. The microscopic origin of this force is the micromotion of the valence electron in the oscillating electric field. Classically, the ponderomotive potential can be expressed as $U_{\text{add}}(\mathbf{r}) = \frac{e^2}{2m_e\omega_{\text{L}}^2\varepsilon_0 c} I_{\text{L}}(\mathbf{r})$ where e is the charge of the electron, m_e its mass, ω_{L} is the laser angular frequency, ε_0 is the vacuum permittivity, c is the speed of light and $I_{\text{L}}(\mathbf{r})$ is the laser intensity at position $\mathbf{r}$ (in W/m^2). It is anti-trapping for all Rydberg states (independently on the orbital quantum number L) and weakly depends on n (Dutta et al., 2000; Barredo et al., 2020). Assuming a Gaussian spot with a waist of 1.5 μm and a power of 100 mW, the peak laser intensity is $I \sim 30$ mW/μm^2, resulting in a height $U_{\text{add}} \sim 3$ mK. This value scales linearly with the addressing power.

  In a typical sequence, we apply the addressing on the atoms for a duration Δt of a few hundred ns, resulting in a momentum kick that tends to expel the atom away from the tweezers. This can increase the position fluctuations of the atoms

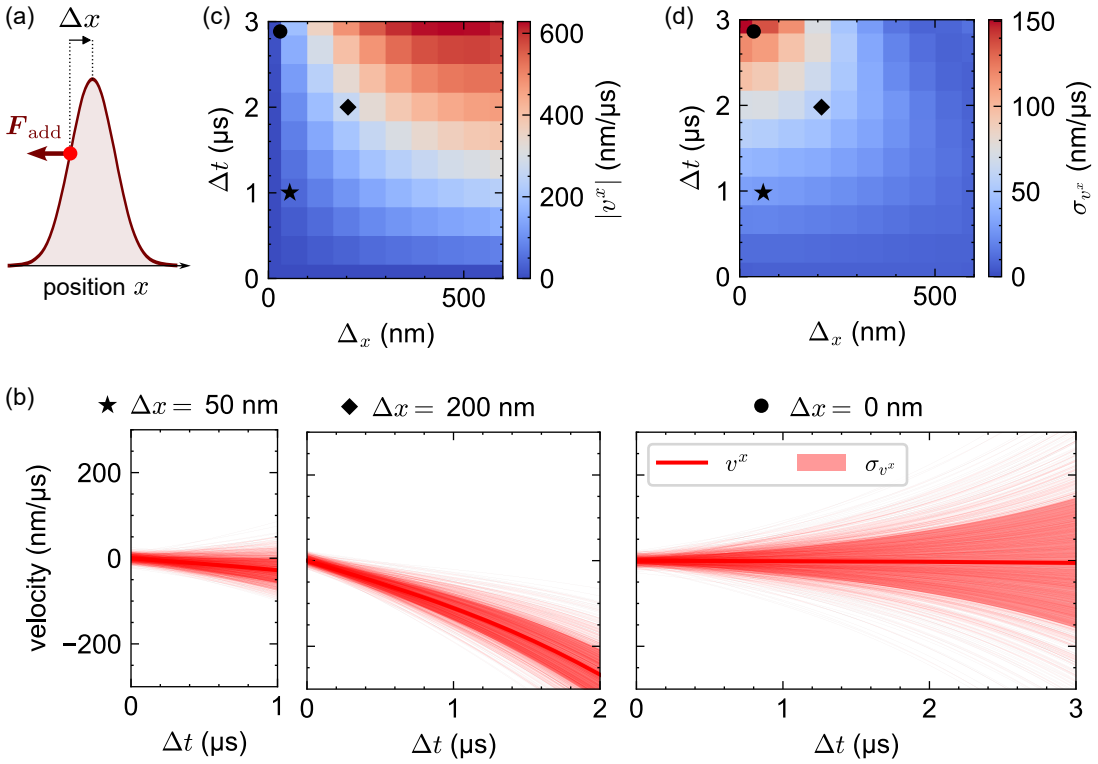

Figure 2.15: Numerical simulations of the momentum kicks due to the addressing ponderomotive force. (a) Sketch of the situation: an atom with initial position dispersion $\sigma_x = 50$ nm and initial velocity dispersion $\sigma_{v^x} = 7$ nm/µs (typical experimental parameters after adiabatic ramp down of the tweezer power) is exposed to the addressing ponderomotive potential U_{add} during an exposure time Δt. The addressing potential is modeled by a Gaussian with waist 1.5 µm and with height 3.2 mK; its center is shifted by a distance Δx from the average atomic position. The resulting force is $\mathbf{F}_{\text{add}} = -\boldsymbol{\nabla} U_{\text{add}}$. (b) Monte-Carlo simulations of the atomic velocity for different values of Δx and Δt. Each thin red line is one simulated trajectory, with a random Gaussian initial position and velocity. The thick red line is the average velocity v^x over all trajectories, and the shaded area is the $\pm\sigma_{v^x}$, with σ_{v^x} the standard deviation of velocity along x. (c) Final value of the average velocity $|v_x|$ as a function of Δx and Δt, simulate using Monte-Carlo. The black symbols refer to the parameters shown in (b). (d) Final value of the standard deviation of the velocity σ_{v^x}.

and induce detection errors due to the higher probability to lose an atom before recapturing it. The value of the kick strongly depends on the addressing power, on the pulse duration Δt and also on the relative alignment of the addressing spots with the tweezers Δx [Fig. 2.15(a,b)]. The larger Δx, the more directional the ponderomotive force, so the larger the average velocity $|v^x|$ after the kick. Consequently, the previously-described local alignment procedure is a way to minimize the average kick [Fig. 2.15(c)]. However, even for $\Delta x = 0$ for which the average kick is zero ($|v^x| = 0$), the standard deviation of velocities σ_{v^x} can still be strongly affected [Fig. 2.15(d)]. For this reason, we try to minimize Δt in the

Rydberg sequence.

To go further, a possible solution would be to use flat-top beams. However, generating an array of flat-top beams without losing a significant amount of optical power is a difficult task, so we did not implement it yet on our experiment.

- **Modification of the microwave Rabi frequency** For addressed atoms, we measure that the microwave Rabi frequency between nP and the lightshifted state $nS_{1/2}$ is reduced. This is actually visible in Fig. 2.11(b), where the height of the peak of a Gaussian spectrum decreases when the lightshift increases. We think it is due to an imperfect control of the polarization of the addressing beam, which couples to many states of the $6P_{3/2}$ manifold; since the addressing Rabi frequency is not negligible compared with its detuning, this can lead to state mixing. However during my PhD we did not have time to investigate this problem in detail. In practice, if we want to drive a transition on resonance with a lightshifted state, we can overcome this problem by simply increasing the microwave power.

2.2.2 Local rotations with Rydberg-encoded qubits

Here, I explain the protocol that we designed for local transitions between two Rydberg states. It makes use of the two tools that have been extensively described in the previous sections of this chapter: global microwave rotations and local addressing lightshifts.

Protocol for local rotations For an easier interpretation of the rotations, it will be useful to define the states involved in the transition as spins 1/2: we use $|\uparrow\rangle \equiv \left|60S_{1/2}, m_J = 1/2\right\rangle$ and $|\downarrow\rangle \equiv \left|60P_{1/2}, m_J = -1/2\right\rangle$. In the absence of lightshift, those states are separated by a frequency $\omega_0/2\pi = 16.7$ GHz. For an experimental demonstration, we want to apply independent rotations on three disjoint classes of atoms. Atoms are classified according to the value of the applied lightshift: atoms from the class 0δ are non-addressed; atoms from the class 1δ receive a lightshift δ; and atoms from the class 2δ receive a lightshift 2δ. We use a geometry composed of six equilateral triangles, each one containing one atom from each class [Fig. 2.16(a)]. The nearest-neighbor distance within a triangle is $a = 12.3$ µm, and the triangles are positioned at large distances $\sim 5a$ from each other to avoid interactions between them. To address each class independently, we generate a microwave field composed of two tones: one tone at angular frequency ω_0, which is resonant with the atoms from 0δ and off-resonant with the other classes; and one tone at $\omega_0 + \delta$, which is resonant with the atoms from 1δ and off-resonant with the other classes. A phase offset can be independently tuned in the two frequency tones, to set the axes of rotation. The microwave field is generated by a single device using IQ modulation (VSG SMM100A by Rohde&Schwarz). The off-resonance criterion can be achieved under the condition that the microwave Rabi frequency Ω is much smaller than the frequency splitting δ between the classes. Another obvious limitation for the rotations is the interactions between the atoms, which are not switched off during the rotation. Defining the typical interaction strength as J, we can summarize the conditions for efficient local rotations as the following hierarchy of quantities:

$$|J| \ll |\Omega| \ll |\delta|. \tag{2.11}$$

Experimentally, we work in a regime where $J = -2\pi \times 0.82$ MHz is the nearest-neighbor XY interaction energy (see chapter 3 for a proper definition). To benefit from apodization, we use Gaussian pulses with peak Rabi frequency $\Omega = 2\pi \times 5.4$ MHz. Lightshifts were set to $\delta = 2\pi \times 23$ MHz, which is a trade-off between the condition

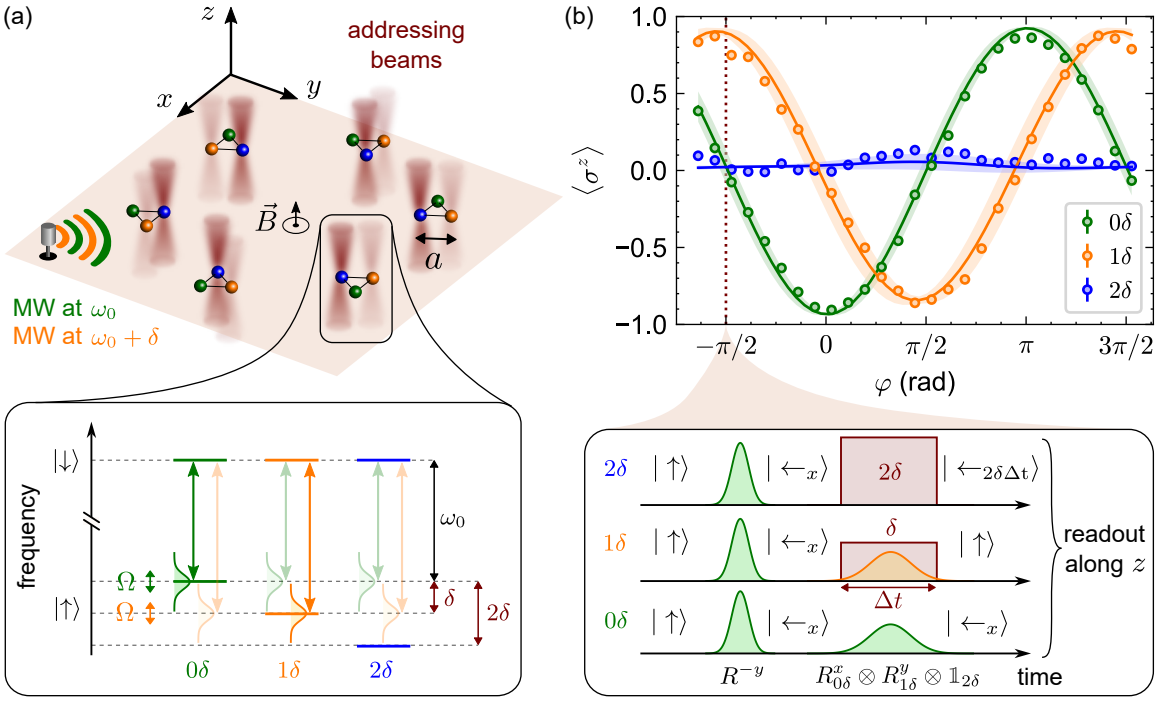

Figure 2.16: Protocol for local rotations. (a) Experimental setup. Atoms are arranged in six equilateral triangles with nearest-neighbor distance $a = 12.3$ µm. The addressing beams generate local lightshifts on three distinct classes of atoms: 0δ (non-addressed atoms), 1δ (atoms with a lightshift $\delta = 2\pi \times 23$ MHz) and 2δ (atoms with a lightshift 2δ). The microwave field (MW) at a frequency $\omega_0 = 2\pi \times 16.7$ GHz (resp. $\omega_0 + \delta$) is on resonance with the resonance of the 0δ (resp. 1δ) atom and off-resonant with the others. (b) z-magnetization averaged over each class of atoms in a Ramsey-experiment, as a function of the phase φ of the first $\pi/2$-pulse. The sequence is made explicit in the lower panel for $\varphi = -\pi/2$. Solid lines are Monte-Carlo simulations taking into account the measured experimental imperfections, with the standard deviation of the simulation indicated as a shaded area.

$|\Omega| \ll |\delta|$ and the various limitations of addressing lightshifts that are described in the previous part (depumping, momentum kicks and modification of the Rabi frequency).

Testing the local rotations with a Ramsey experiment We illustrate and benchmark the protocol above by performing a Ramsey experiment: starting from all atoms in $|\uparrow\rangle$, we apply a first global rotation $R^{x\cos\varphi + y\sin\varphi}\left(\frac{\pi}{2}\right)$, followed by the local rotations $R^x_{0\delta}\left(\frac{\pi}{2}\right) \otimes R^y_{1\delta}\left(\frac{\pi}{2}\right) \otimes \mathbb{1}_{2\delta}$ and finally read-out the states for various φ. Here, $R^\mu_j(\theta)$ is the rotation operator by an angle θ along direction μ for atom j; it writes $R^\mu_j(\theta) = e^{-i\theta/2\,\sigma^\mu_j}$ where σ^μ_j is the Pauli matrix along μ acting on atom j. Each experimental sequence is repeated ~ 500 times to compute the average magnetizations. We expect oscillations of the 0δ and 1δ-atom magnetization that are out of phase by $\pi/2$, whereas the 2δ-atom magnetization should remain constant at 0. Fig. 2.16(b) shows the experimental results.

We obtain the expected oscillations, albeit with a finite contrast (85 to 90%) that we attribute to experimental imperfections. To confirm this, Lucas Lerclerc performed a Monte Carlo simulation including state preparation and measurement errors, finite Rydberg lifetime, interactions between atoms, time jitter of the pulses, depumping and losses induced by the addressing. Taking into account all these experimentally calibrated mechanisms in the numerics yields good agreement with the data. There is no dominant contribution of the imperfections to the loss of contrast.

One may argue that our protocol for local rotations does not take into account the rotations due to the addressing lightshifts themselves. Indeed, a lightshift is equivalent to a frequency detuning, so it induces a rotation along z with an angle $\delta\Delta t$, where Δt is the duration of the addressing pulse. Instead of $R^x_{0\delta}\left(\frac{\pi}{2}\right)\otimes R^y_{1\delta}\left(\frac{\pi}{2}\right)\otimes \mathbb{1}_{2\delta}$, the genuine formula for the local rotation described above should be: $R^x_{0\delta}\left(\frac{\pi}{2}\right)\otimes R^z_{1\delta}(\delta\Delta t)R^y_{1\delta}\left(\frac{\pi}{2}\right)\otimes R^z_{1\delta}(2\delta\Delta t)$. However, since we read out the state in the z-basis, the final rotation along z has no effect on the measurement outcome, and it can be neglected. To get convinced of this statement, let us consider the state $|\psi\rangle$ of a single spin j before the z-rotation. After the z-rotation by an angle θ, the new state is $|\psi'\rangle = R^z_j(\theta)\,|\psi\rangle = e^{-i\theta/2\,\sigma^z_j}\,|\psi\rangle$. The measurement outcome is given by: $\langle\psi'|\,\sigma^z_j\,|\psi'\rangle = \langle\psi|\,e^{i\theta/2\,\sigma^z_j}\sigma^z_j e^{-i\theta/2\,\sigma^z_j}\,|\psi\rangle = \langle\psi|\,\sigma^z_j\,|\psi\rangle$, which shows that the measurement is not affected by the z-rotation. This argument only works if the z-rotation pulse is the last operation before the readout; otherwise, the accumulated phase shift would start to play a role. This is a limitation of our protocol, since it means that the local pulses can only be applied once in a sequence.

Perspectives of the method With a generalization of the Ramsey sequence proposed above to any pulse duration, we can conduct any combination of independent local rotations: the two simultaneous local rotations address the atoms from 0δ and 1δ, and the global rotation addresses the atoms from 2δ. The angle of each pulse can be independently tuned by controlling the durations and phases of each pulse.

To address the three classes, it would be theoretically equivalent to use a single pulse with three tones, instead of this combination of a global pulse and one pulse with two tones. However, driving a microwave rotation on resonance with a lightshifted atom has a lower efficiency than on a non-addressed atom, due to various addressing-induced imperfections such as depumping, state mixing and residual inhomogeneities of the lightshifts. This can be seen on Fig. 2.16(b), where the contrast of the oscillation for 1δ atoms is slightly smaller than the one of 0δ. For this reason, we avoid sending a resonant microwave pulse on the 2δ atoms.

In principle, our method can be generalized to any number N of independent local

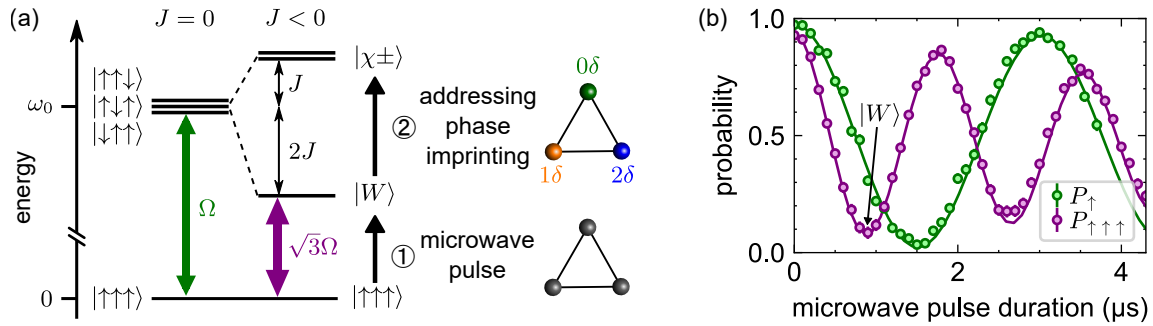

Figure 2.17: Protocol for the preparation of chiral states. (a) Energy spectrum of a triangular plaquette, with and without XY interactions. Colored arrows indicate the matrix element coupling the states of the system, using a microwave Rabi frequency Ω. Black arrows are the preparation steps: starting from $|\uparrow\uparrow\uparrow\rangle$, we drive a microwave π-pulse to $|W\rangle$, followed by an addressing pulse that imprints a different phase on each atom, allowing us to prepare $|\chi(\phi)\rangle$. (b) Rabi oscillations without interactions (green points) and with interactions (purple points), showing an enhancement of the Rabi frequency by a factor $\sqrt{3}$. Solid lines are numerical simulations taking into account experimental imperfections (finite STIRAP fidelity, Rydberg lifetimes and detection errors) without any adjustable parameter.

rotations. To this end, one needs to define N classes of lightshifts and use a microwave field with N tones (or $N-1$ tones and a global pulse before the local pulses). However, as N increases one will face the already-mentioned undesirable effects of the addressing that will decrease the fidelity of the pulses for atoms with the strongest lightshifts. In the rest of this thesis, we will extensively use the case $N = 2$ for the preparation of staggered states on two independent sublattices.

To push the fidelities of local rotations above 90%, optical control could be envisioned for fine-tuning the pulses' shapes (Leclerc, 2024). To go much beyond, I believe that we need to eliminate the constraint of energy scales summarized in Eq. (2.11). To get rid of the condition $|\Omega| \ll |\delta|$, one could consider optical Raman pulses instead of microwave pulses. However, this would only allow us to perform transitions between states with the same parity ($S \leftrightarrow S'$, $S \leftrightarrow D$, etc.) and not the dipole transitions $S \leftrightarrow P$ that we study here.

An application of local rotations: preparation of chiral states In Bornet et al. (2024), we show several applications of local rotations: the preparation of states which break the parity and time-reversal invariance; the measurement of string operators in different spin bases; and quantum state tomography. Here, I will dwell on the first two applications (see Bornet (2024) for more details about quantum state tomography).

To illustrate our ability to prepare new states, we adapted a protocol which was

introduced and realized with superconducting qubits in Roushan et al. (2017). The protocol aims at preparing three-atom entangled states of the form:

$$|\chi(\phi)\rangle \equiv \frac{1}{\sqrt{3}}\left(|\uparrow\uparrow\downarrow\rangle + e^{i\phi}\,|\uparrow\downarrow\uparrow\rangle + e^{i2\phi}\,|\downarrow\uparrow\uparrow\rangle\right) \tag{2.12}$$

which is parametrized by a phase ϕ. In the particular case $\phi = 0$, $|\chi(\phi)\rangle$ is called a *W-state* and will be denoted by $|W\rangle$. For $\phi = \pm 2\pi/3$, we will call it $|\chi^{\pm}\rangle$. More generally, preparing one of the states $|\chi(\phi)\rangle$ with $\phi \neq 0$ requires an ingredient that breaks the time-reversal symmetry in the Hamiltonian (Tsomokos et al., 2008). Our protocol makes use of the fact that $|W\rangle$ and $|\chi^{\pm}\rangle$ are eigenstates of our interacting Hamiltonian of a triangle [Fig. 2.17(a)]. It is composed of two steps, which are realized on independent triangular plaquettes that contain one atom from each class.

1. Starting from all atoms in $|\uparrow\rangle$ inside the plaquettes, we perform a microwave pulse to $|W\rangle$. Tho do so, we detune the microwave frequency by $2J$ and use a small Rabi frequency $\Omega = 2\pi \times 0.33$ MHz $< |J|$, resulting in a spin flip $|\uparrow\rangle \rightarrow |\downarrow\rangle$ which is delocalized over the plaquette. The resulting Rabi oscillation is displayed in Fig. 2.17(b) and shows the expected $\sqrt{3}$ enhancement of the Rabi frequency compared with a non-interacting system.

2. We apply an addressing pulse during a time Δt_{add}, that imprints local phases on the system. More precisely, an atom from the 1δ class accumulates a phase shift $\phi = \delta \Delta t_{\text{add}}$, an atom from the 2δ class accumulates a phase shift 2ϕ, and a non-addressed atom gets no shift. By tuning the duration Δt_{add} of the phase imprinting, we can prepare any state of the form of Eq. (2.12).

In this protocol, the local rotations are performed along z via the addressing pulse: this is the step that breaks the time-reversal symmetry.

Another application of local rotations: multi-basis measurements We now want to characterize the states prepared with the above protocol. A global measurement in the z-basis is not enough to distinguish the various states $|\chi(\phi)\rangle$ since it does not give access to the phase ϕ. Instead, we measure several multi-basis observables that are allowed by our local rotation protocol.

The first multi-basis observable that we will consider is the spin chirality (Tsomokos et al., 2008), which for three spins $\boldsymbol{\sigma}_{i,j,k}$ is defined as the triple product between the

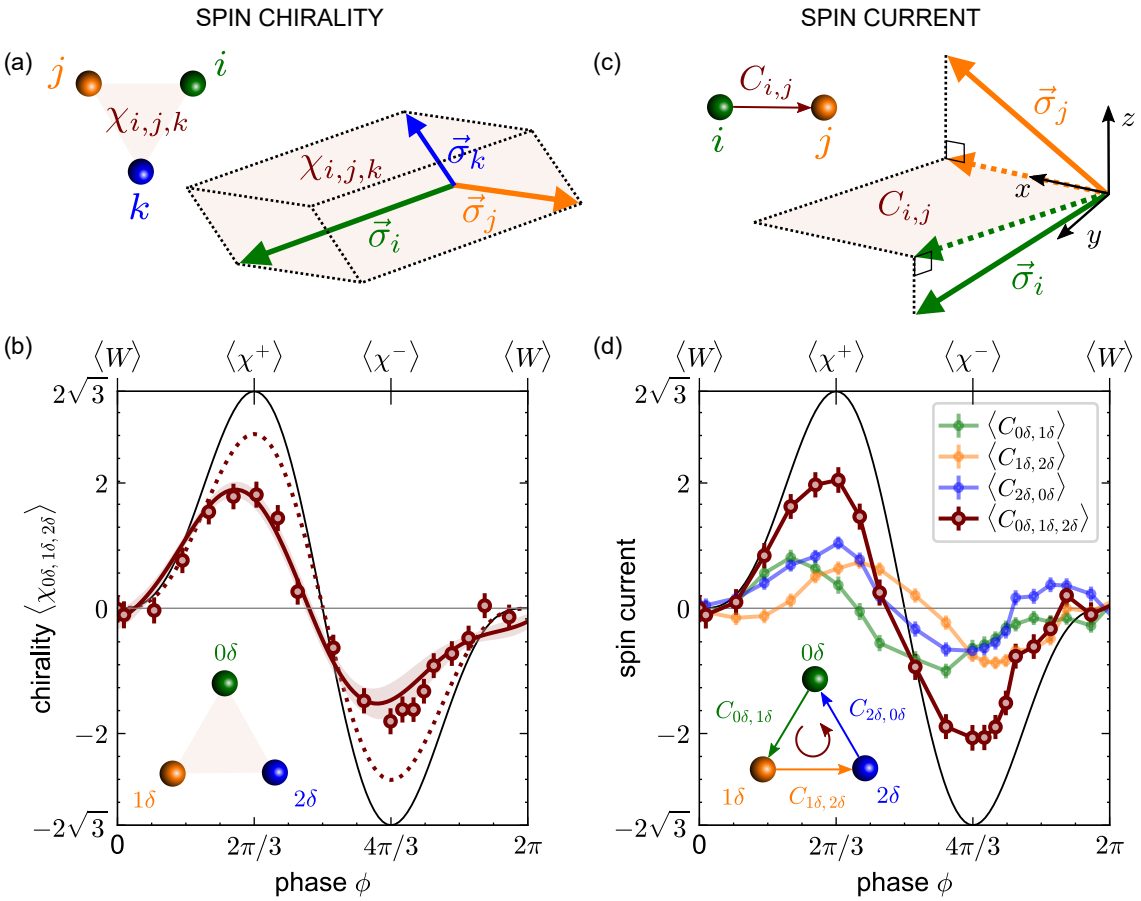

Figure 2.18: Measurement of spin chirality and spin currents. (a) Geometrical representation of the chirality $\chi_{i,j,k}$ for three spins $\boldsymbol{\sigma}_{i,j,k}$. (b) Experimental measurement of the chirality of a triangle composed of three classes 0δ, 1δ and 2δ. The solid black line is the theory expectation $\langle\chi(\phi)|\,\chi_{0\delta,1\delta,2\delta}\,|\chi(\phi)\rangle$ given by Eq. (2.14). The solid brown line is a Monte-Carlo simulation including the measured preparation and detection errors, with the standard deviation indicated as the shaded area. The dotted line corresponds to the same simulation, in the absence of detection errors. (c) Geometrical representation of the spin current $C_{i,j}$ from a spin $\boldsymbol{\sigma}_i$ to a spin $\boldsymbol{\sigma}_j$. (d) Experimental measurement of all pairwise spin currents in the triangle geometry. The total spin current (brown data points) is the sum of the three pairwise spin currents.

spins:

$$\begin{aligned}\chi_{i,j,k} &\equiv \boldsymbol{\sigma}_i \cdot (\boldsymbol{\sigma}_j \times \boldsymbol{\sigma}_k) \\ &= \sigma_i^x\sigma_j^y\sigma_k^z + \sigma_i^y\sigma_j^z\sigma_k^x + \sigma_i^z\sigma_j^x\sigma_k^y - \sigma_i^y\sigma_j^x\sigma_k^z - \sigma_i^x\sigma_j^z\sigma_k^y - \sigma_i^z\sigma_j^y\sigma_k^x.\end{aligned} \tag{2.13}$$

A geometrical interpretation of the chirality is shown is Fig. 2.18(a): it is the algebraic volume spanned by the three spins. Consequently, any product state has a chirality bounded by 1 in absolute value. However, entangled states can exceed

this limit. In particular, the states with the highest chirality are $|\chi^{\pm}\rangle$, which satisfy: $\langle\chi^{\pm}|\,\chi_{i,j,k}\,|\chi^{\pm}\rangle = \pm 2\sqrt{3}$. To measure the six terms of the chirality from Eq. (2.13), we need to carry out six measurements, one in each permutation of the bases $\{\sigma_i^x, \sigma_j^y, \sigma_k^z\}$. The resulting curve is shown in Fig. 2.18(b) as a function of ϕ, together with the theoretical expectation:

$$\langle\chi(\phi)|\,\chi_{i,j,k}\,|\chi(\phi)\rangle = \frac{4}{3}\left[2\sin(\phi) - \sin(2\phi)\right] \tag{2.14}$$

The measured oscillation goes well above 1, signaling an entangled state, but its amplitude is reduced due to experimental imperfections. Simulating each step of the sequence while accounting for these imperfections leads to a better agreement between theory and experiment [solid brown line in Fig. 2.18(b)]. The same simulation with only preparation errors, and no detection errors (dotted brown line), tells us that the main limitations of the chirality measurement are the detection errors. Indeed, the chirality is a three-body observable, so it is particularly sensitive to detection errors: assuming that the single-atom detection fidelity of $\sim 90\%$ is independent from one atom to another, we can estimate that the change of contrast for the chirality is a factor $0.9^3 \sim 70\%$, which roughly corresponds to the mismatch between the dotted line and the solid line.

One interpretation of the chirality involves spin currents (Tsomokos et al., 2008; Roushan et al., 2017). Let us see in more details how different chirality and spin currents are, and how we can measure them using local rotations. The pairwise current flowing from one spin $\boldsymbol{\sigma}_i$ to another spin $\boldsymbol{\sigma}_j$ can be defined as:

$$\begin{aligned} C_{i,j} &\equiv \mathbf{e}_z \cdot (\boldsymbol{\sigma}_i \times \boldsymbol{\sigma}_j) \\ &= \sigma_i^x \sigma_j^y - \sigma_i^y \sigma_j^x \\ &= 2i\left(\sigma_i^+ \sigma_j^- - \sigma_i^- \sigma_j^+\right). \end{aligned} \tag{2.15}$$

As shown in Fig. 2.18(c), it corresponds to the algebraic area spanned by the projections of the spins in the xy plane. From the same data shots as for the chirality, we compute the pairwise current flowing through each of the triangle's bonds, and plot their sum: $C_{i,j,k} \equiv C_{i,j} + C_{j,k} + C_{k,i}$ [Fig. 2.18(d)]. We obtain an oscillation that is very similar to the one of the chirality. This is because the total spin current and the chirality are related by the simple relationship

$$\chi_{i,j,k} = C_{i,j,k} \cdot M^z \tag{2.16}$$

with $M^z = \sigma_i^z + \sigma_j^z + \sigma_k^z$ the total magnetization along z. Since the target states $|\chi(\phi)\rangle$ are eigenstates of the manifold $M^z = 1$, the theory expectation value for the total current is the same as for the chirality: $\langle\chi(\phi)| C_{i,j,k} |\chi(\phi)\rangle = \langle\chi(\phi)| \chi_{i,j,k} |\chi(\phi)\rangle$. The slight experimental deviations are due to the residual measurements that are out of the spin sector $M^z = 1$.

Take-home message

Local rotations between two Rydberg states cannot be achieved with a bare microwave field on distances as small as a few micrometers, but we can create spatially-resolved lightshifts with an addressing beam. After several steps of feedbacks that guarantee their stability, those lightshifts allow us to perform spin rotations along z. For rotations along x and y, we use several microwave tones with detunings that are chosen to match the resonance frequency of lightshifted atoms. Although this method has a reduced rotation fidelity ($\sim 90\%$ for a π-pulse) compared with the global rotations, they allow us to increase our range of experimentally-accessible initial states for quantum simulation (see part B for a direct use of this), and to perform multi-basis measurements of exotic observables such as chirality and spin current.

Chapter 3

Measuring the exchange interactions between two Rydberg atoms

Now flip, flop and fly
I don't care if I die.

Big Joe Turner

In the previous chapter, interatomic interactions were considered as a detrimental effect for the fidelity for single-atom manipulations in Rydberg states. But interactions are also, more than anything else, the key ingredient of our platform for probing many-body physics. What is the physical origin of dipole-dipole interactions between Rydberg atoms? How can we measure and control them? What are the experimental limitations for the control of interactions? In this chapter, I try to answer those questions.

Historically, first signatures of the dipole-dipole interaction between Rydberg atoms were experimentally observed in Raimond et al. (1981) with dense atomic gases, and such disordered many-body systems are still an active area of research Signoles et al. (2021); Delpy et al. (2024). Here, we rather focus on systems composed of only two atoms, and more specifically on the measurement of the off-diagonal dipole-dipole terms, which are known in the literature as *exchange interaction* or *flip-flop interaction*. After a general introduction to the physical origin of dipole-dipole interactions (sec. 3.1), I show two methods that we use to measure its first-order contribution (sec. 3.2). The experimental data are benchmarked against numerical simulations, allowing us to perform thermometry of the atomic motion, in a complementary way to the single-atom methods presented in chapter 1. After that, I present first results on the time-dynamics due to its second-order off-diagonal contribution (sec. 3.3). Finally, I dwell on the effects of the interactions on the atomic motion (sec. 3.4).

Contents

Contributors

As in chapter 2, the sets of data which will be shown in this chapter come from calibrations of various quantum simulation projects, credit for this should go to all members of the experimental team. For the calculation of interactions, we relied on the very good software PairInteraction (Weber et al., 2017). I especially want to thank Johannes Mögerle for helpful discussions about the software.

3.1 Interactions between Rydberg atoms

This section is a review of dipole-dipole interactions between isolated Rydberg atoms. It aims at answering two basic questions:

- what is the physical origin of dipole-dipole interactions?
- how do we use them in practice for quantum simulation?

More detailed reviews can be found in Bijnen (2013) and in Browaeys et al. (2016). A more recent work, complementary to this section, was done in chapter 2 of Geier (2023) in the context of disordered Rydberg gases. For a more historical overview of the dipole-dipole interaction in atomic clouds, I refer the interested reader to Gallagher and Pillet (2008).

In this part, the atomic motion will be neglected, and spins will be considered as fixed particles. This assumption will be challenged in the next sections.

Origin of the dipole-dipole interaction Let us start by a classical vision of the interaction between two electric dipoles, when they are static (in the sense that their value do not evolve in time). The electric field generated by a static dipole $\mathbf{d}$ at a position $\mathbf{r}$ reads (Cohen-Tannoudji et al., 1994):

$$\mathbf{E}_{\mathrm{d}}(\mathbf{r}) = \frac{1}{4\pi\epsilon_0}\frac{3(\mathbf{d}\cdot\mathbf{e}_r)\mathbf{e}_r - \mathbf{d}}{r^3}. \tag{3.1}$$

The interaction energy between the two static dipoles $\mathbf{d}_i$ and $\mathbf{d}_j$ can be thought as the energy of $\mathbf{d}_j$ in the electric field $\mathbf{E}_{d_i}$ created by $\mathbf{d}_i$ (or vice-versa):

$$\begin{aligned} V_{\mathrm{dd}}(\mathbf{r}) &\equiv -\mathbf{E}_{d_i}(\mathbf{r}) \cdot \mathbf{d}_j \quad = -\mathbf{E}_{d_j}(\mathbf{r}) \cdot \mathbf{d}_i \\ &= \frac{1}{4\pi\epsilon_0} \frac{\mathbf{d}_i \cdot \mathbf{d}_j - 3(\mathbf{d}_i \cdot \mathbf{e}_r)(\mathbf{d}_j \cdot \mathbf{e}_r)}{r^3}. \end{aligned} \tag{3.2}$$

This interaction is called the *dipole-dipole interaction* and is represented in Fig. 3.1.

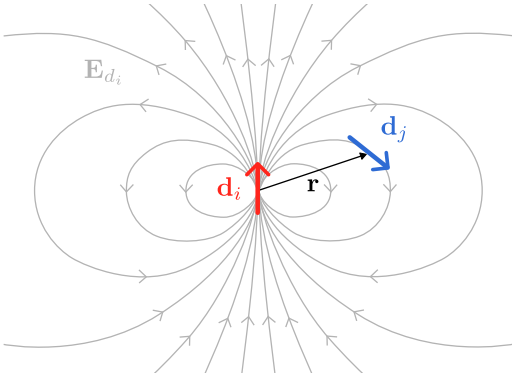

Figure 3.1: Interaction between two electric dipoles $\mathbf{d}_i$ and $\mathbf{d}_j$ separated by a distance $\mathbf{r}$. The interaction energy is minimized when $\mathbf{d}_j$ is aligned with the electric field $\mathbf{E}_{d_i}$ created by $\mathbf{d}_i$.

The electric dipole of atoms, however, is a quantum operator. The classical expression of the dipole-dipole interaction given by Eq. (3.2) remains valid for two interacting atoms, with $\mathbf{d}$ now being the dipole operator (Cohen-Tannoudji et al., 1994). The approximation of static dipoles is only valid in the near-field, when the interatomic distance r is much smaller than the wavelength λ associated to the transition wavelength of the atomic transitions at play; otherwise, other terms due to the radiated field of the oscillating dipoles have to be taken into account, that evolve as $1/r^2$ and $1/r$. In our case, $r \sim 10$ µm and $\lambda \sim 1$ cm for the microwave transitions that were studied in the previous chapter, so we can safely neglect the far-field contributions.

Expression in the atomic basis To calculate the matrix elements of the dipole-dipole interaction, it is convenient to decompose the dipole operator in spherical coordinates, following the procedure in Ravets et al. (2015). Fixing the quantization axis to be along z, the dipole operator of an atom i can be decomposed as $\mathbf{d}_i = \frac{d_i^- - d_i^+}{\sqrt{2}}\mathbf{e}_x + i\frac{d_i^- + d_i^+}{\sqrt{2}}\mathbf{e}_y + d_i^0\mathbf{e}_z$ where the operator d_i^0 couples states with $\Delta m_J = 0$ and $d_i^\pm$ couples states with $\Delta m_J = \pm 1$[1], as shown in Fig. 3.2.

[1]Beware that with this convention, $(d_i^+)^\dagger = -d_i^-$.

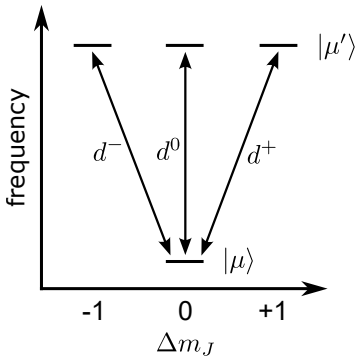

Figure 3.2: Decomposition of the dipole operator $\mathbf{d}_i$ on three components acting on transitions with different Δm_J (π and $\sigma_\pm$ transitions).

Injecting this formula in Eq. (3.2), we obtain a decomposition of the dipole-dipole interaction as the sum of pairwise interactions, each one involving a single atomic transition:

$$V_{\mathrm{dd}}(\mathbf{r}) = \frac{1}{4\pi\epsilon_0 r^3}\left[\frac{1-3\cos^2(\theta)}{2}\left(d_i^+ d_j^- + d_i^- d_j^+ + 2d_i^0 d_j^0\right)\right.$$
$$+\frac{3}{\sqrt{2}}\sin(\theta)\cos(\theta)\left(e^{-i\phi}d_i^+ d_j^0 - e^{i\phi}d_i^- d_j^0 + e^{-i\phi}d_i^0 d_j^+ - e^{i\phi}d_i^0 d_j^-\right)$$
$$\left.-\frac{3}{2}\sin^2(\theta)\left(e^{-2i\phi}d_i^+ d_j^+ + e^{2i\phi}d_i^- d_j^-\right)\right] \tag{3.3}$$

where θ and ϕ are the spherical coordinates of $\mathbf{e}_r = \sin(\theta)\cos(\phi)\mathbf{e}_x + \sin(\theta)\sin(\phi)\mathbf{e}_y + \cos(\theta)\mathbf{e}_z$. In particular, θ is the angle between the interatomic axis and the quantization axis z (usually set by the magnetic field). The various matrix elements contained in Eq. (3.3) are illustrated in Fig. 3.3.

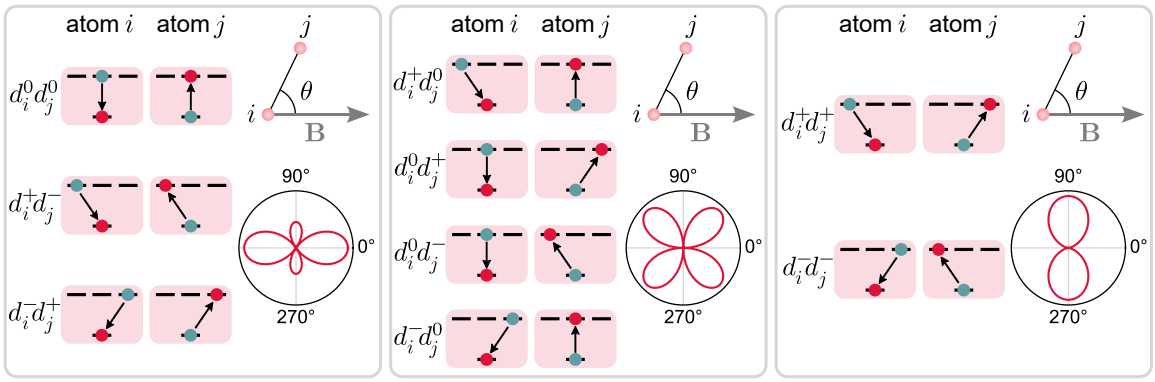

Figure 3.3: Schematic representation of the matrix elements of the dipole-dipole interaction [Eq. (3.3)] and their associated angular dependence with the quantization axis (here a magnetic field $\mathbf{B}$).

Effective Hamiltonian theory The two-atom dipole-dipole Hamiltonian of Eq. (3.3) contains all the couplings between all pairs of atomic levels, which is numerically tractable if we restrict to a few tens of levels, but hard to handle in practice. In the context of quantum simulation, we want to work with few-level atoms, that is to say to isolate a manifold composed of few atomic levels (typically two or three) and forget about the other ones. We also want to neglect the couplings between states that have very different energies, since the associated transitions are off-resonant and extremely unlikely to happen. A convenient framework to do so is called the effective Hamiltonian theory, also known as Schrieffer-Wolff transformation, which is a generalization of the second-order perturbation theory. I will not go through its derivation [see Cohen-Tannoudji et al. (1998) or Bravyi et al. (2011)] but just state its conditions of application and the result for two interactions atoms.

Let us denote by H^0 the Hamiltonian of a single atom. The Hamiltonian for the two interacting atoms is: $H = H_i^0 + H_j^0 + V_{\text{dd}}$. When we restrict the basis of interest to a few atomic levels, we can group the two-atom levels in degenerate manifolds: more specifically, two two-atom levels $|\mu, \mu'\rangle$ and $|\mu'', \mu'''\rangle$ are in the same manifold if their non-interacting energies are the same, that is to say $E_{\mu,\mu'} = E_{\mu'',\mu'''}$ where $E_\mu \equiv \langle\mu| H^0 |\mu\rangle$ is the energy of state $|\mu\rangle$ and $E_{\mu,\mu'} = E_\mu + E_{\mu'}$. The Schrieffer-Wolff transformation allows us to define an effective Hamiltonian H^{eff} for the two atoms, that has the same eigenvalues as H but is block-diagonal with each block corresponding to one manifold (Cohen-Tannoudji et al., 1998). The coupling between two states $|\mu, \mu'\rangle$ and $|\mu', \mu''\rangle$ from the same manifold is given by

$$\begin{aligned}
\langle\mu, \mu'| H^{\text{eff}}(\mathbf{r}) |\mu'', \mu'''\rangle \quad &= \quad (E_\mu + E_{\mu'})\, \delta_{\mu,\mu''}\, \delta_{\mu',\mu'''} \\
&+ \quad \langle\mu, \mu'| V_{\text{dd}}(\mathbf{r}) |\mu'', \mu'''\rangle \\
&+ \quad \sum_{\substack{\alpha,\,\beta \\ E_{\alpha,\beta} \neq E_{\mu,\mu'}}} \frac{\langle\mu, \mu'| V_{\text{dd}}(\mathbf{r}) |\alpha, \beta\rangle \langle\alpha, \beta| V_{\text{dd}}(\mathbf{r}) |\mu'', \mu'''\rangle}{E_{\mu,\mu'} - E_{\alpha,\beta}} \\
&+ \quad O\left(\frac{V_{\text{dd}}(\mathbf{r})^3}{\left(E_{\mu,\mu'} - E_{\alpha,\beta}\right)^2}\right).
\end{aligned} \tag{3.4}$$

The first line of Eq.(3.4) is simply the non-perturbed energy. The second line corresponds to the direct dipole-dipole coupling between $|\mu, \mu'\rangle$ and $|\mu'', \mu'''\rangle$ (first order of perturbation theory) that scales as $1/r^3$; it also strongly depends on the principal quantum number n of the considered transitions, as n^4. The third line is a second-order coupling that involves virtual transitions through all states outside of the considered manifold; it scales as $1/r^6$ and n^{11}. Those processes are illustrated on Fig. 3.4(a).

Calculating the coupling between two states can be done using the following procedure: starting from the diagonalized atomic Hamiltonian with a restricted number of levels (typically around 100), we evaluate Eq. (3.4) using Eq. (3.3) to compute the dipole-dipole coupling for each pair of considered states. We use the software PairInteraction (Weber et al., 2017) which also includes the magnetic and electric fields as input parameters of the atomic Hamiltonian.

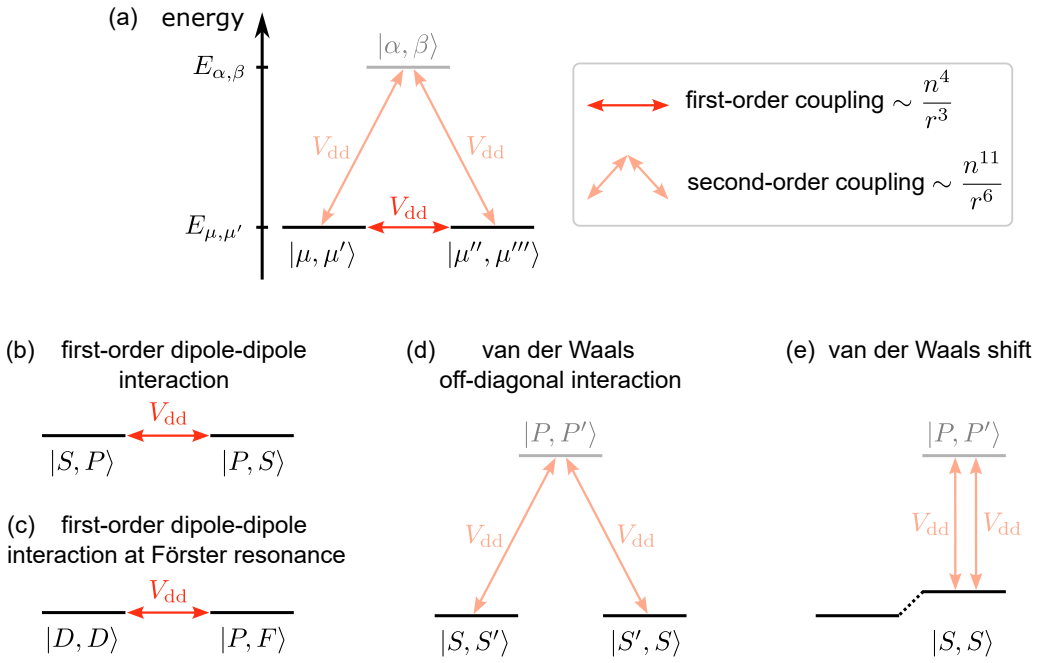

Figure 3.4: First-order and second-order two-body processes due to the dipole-dipole interaction. (a) Couplings between two degenerate states $|\mu,\mu'\rangle$ and $|\mu'',\mu'''\rangle$ are represented by colored arrows:: red arrows are the first-order $1/r^3$ coupling, and the two pink arrows represent the second-order $1/r^6$ coupling, that involves virtual transitions to all possible states $|\alpha,\beta\rangle$. (b,c,d) Examples of processes between specific states, labeled by their orbital quantum number $L \in \{S,P,D,\dots\}$. The prime symbol denotes another state with the same value of L.

Quick overview of possible two-body processes Fig. 3.4(b,c,d) illustrates some of the most common processes with specific states. The *van der Waals shift* is a second-order energy shift in the case $|\mu,\mu'\rangle = |\mu'',\mu'''\rangle$ [Fig. 3.4(d)]. A smoking gun evidence of this process was the observation of the *Rydberg blockade* in the optical excitation of two neighboring atoms (Urban et al., 2009; Gaëtan et al., 2009). Since then, it was carefully characterized: for example, its $1/r^6$ dependence was measured in Béguin et al. (2013), and its angular dependence was measured in Barredo et al. (2014) for different values of L. It is now routinely used as a tool for quantum gates (Evered et al., 2023; Scholl et al., 2023).

In this chapter, we are interested in the off-diagonal parts of the effective Hamiltonian. The most obvious contribution is the *first-order dipole-dipole interaction*, which is also known as the *resonant dipole-dipole interaction*. It can couple any pair states where two dipole-coupled Rydberg levels are exchanged between the two atoms, such as pair states $|S, P\rangle$ and $|P, S\rangle$ [Fig. 3.4(b)]. It was experimentally observed with two Rydberg atoms in Barredo et al. (2015), and more recently with dipolar molecules in Bao et al. (2023); Holland et al. (2023). Section 3.2 will be devoted to a detailed study of this process.

Many first-order couplings involve more than two Rydberg levels (for example, $|D, D\rangle$ gets coupled to $|P, F\rangle$), but most of these terms are off-resonant; typically, the coupling does not play any role as long as it is negligible compared with the energy difference between the two coupled states ($E_P + E_F - 2E_D$ in the previous example). However, the energy difference can be set to zero, for example by tuning the electric field, thus making $|D, D\rangle$ degenerate with $|P, F\rangle$. This is called a Förster resonance and was experimentally demonstrated in Ravets et al. (2014). Its characteristic angular dependence as $1 - 3\cos^2(\theta)$ was later measured in Ravets et al. (2015).

Another off-diagonal term of the effective Hamiltonian originates from second-order perturbation theory, for example between states $|S, S'\rangle$ and $|S', S\rangle$ [Fig. 3.4(c)]: for the rest of this thesis, we will call it *off-diagonal van der Waals interaction*. Contrary to the first-order interaction, it decays with interatomic distance as $1/r^6$. It was already used in Rydberg experiments in disordered ensembles (Signoles et al., 2021; Franz et al., 2024) but to our knowledge, no signature of this interaction with single-atom resolution has been observed yet. Section 3.3 of this manuscript will show first results for coherent dynamics using this interaction.

Mappings of two-level atomic Hamiltonians on spin systems Thanks to the effective interaction model, we managed to restrict the complexity of the dipole-dipole interaction between two many-level atoms, to an effective Hamiltonian between two few-level atoms. In the remainder of this section, let us focus on the simplest possible case: two-level atoms. This is a natural playground for quantum simulation, since the system is equivalent to a pair of spins 1/2. Let us name $|\mu\rangle$ and $|\mu'\rangle$ the two atomic levels of interest, which will later be mapped on spin states. The most general way of

writing the effective Hamiltonian in the basis $\{|\mu,\mu\rangle, |\mu,\mu'\rangle, |\mu',\mu\rangle, |\mu',\mu'\rangle\}$ is

$$H^{\text{eff}}(\mathbf{r}) = \hbar \begin{bmatrix} V_{\mu\mu} & 0 & 0 & 0 \\ 0 & V_{\mu\mu'} & J_{\mu\mu'} & 0 \\ 0 & J_{\mu\mu'} & V_{\mu\mu'} & 0 \\ 0 & 0 & 0 & V_{\mu'\mu'} \end{bmatrix} \tag{3.5}$$

where all diagonal terms are van der Waals shifts that scale as $1/r^6$, and the off-diagonal term is either first-order $(1/r^3)$ if $\langle\mu|\,\mathbf{d}\,|\mu'\rangle \neq 0$ or second-order $(1/r^6)$ otherwise. Equation (3.5) is written in the rotating frame of the transition $|\mu\rangle \leftrightarrow |\mu'\rangle$, such that the energy terms E_μ and $E_{\mu'}$ are dropped.

We define the spin operator $\mathbf{S}_i = S_i^x\mathbf{e}_x + S_i^y\mathbf{e}_y + S_i^z\mathbf{e}_z$ as $S_i^\alpha = \sigma_i^\alpha/2$ with σ_i^α the Pauli matrix in direction α acting on particle i. Now, we consider the following mapping:

$$\begin{cases} |\mu\rangle & \equiv & |\uparrow\rangle \\ |\mu'\rangle & \equiv & |\downarrow\rangle \end{cases} \tag{3.6}$$

where $|\uparrow\rangle$ and $|\downarrow\rangle$ are the two eigenstates of S_i^z with eigenvalues $\pm\frac{1}{2}$. We want to know what is the equivalent of the effective atomic Hamiltonian H^{eff} of Eq. (3.5) in terms of spin language. To this end, we define the so-called *XXZ Hamiltonian* as

$$H_{\text{XXZ}} \equiv \hbar \left[J_\perp \left(S_i^x S_j^x + S_i^y S_j^y \right) + J_z\, S_i^z S_j^z \right], \tag{3.7}$$

which contains two parameters: $J_\perp$ and J_z. This Hamiltonian is a very general and extensively-studied spin model (Sachdev, 2011), with three well-known particular cases: the Ising model ($J_\perp = 0$), the XY model ($J_z = 0$) and the Heisenberg model ($J_\perp = J_z$).

To make an exact mapping on H^{eff} which contains four parameters ($J_{\mu\mu'}$, $V_{\mu\mu}$, $V_{\mu\mu'}$ and $V_{\mu'\mu'}$), we need to add two additional terms which we set to be a magnetic field b_z, and a constant term that is just a global energy shift. Imposing the mapping

$$H^{\text{eff}} = H_{\text{XXZ}} + \hbar b_z (S_i^z + S_j^z) + \text{cst} \tag{3.8}$$

leads to the following constraints:

$$\begin{cases} J_{\mu\mu'} &= \frac{J_\perp}{2} \\ V_{\mu\mu} &= \frac{J_z}{4} + b_z + \text{cst} \\ V_{\mu'\mu'} &= \frac{J_z}{4} + b_z - \text{cst} \\ V_{\mu\mu'} &= -\frac{J_z}{4} + \text{cst}. \end{cases} \tag{3.9}$$

Reciprocally, the spin parameters can be expressed as a function of the atomic interaction energies by inverting Eq. (3.9):

$$\begin{cases} J_\perp &= 2J_{\mu\mu'} \\ J_z &= V_{\mu\mu} + V_{\mu'\mu'} - 2V_{\mu\mu'} \\ b_z &= \left(V_{\mu\mu} - V_{\mu'\mu'}\right)/2 \\ \text{cst} &= \frac{1}{4}\left(V_{\mu\mu} + V_{\mu'\mu'} + 2V_{\mu\mu'}\right). \end{cases} \tag{3.10}$$

We have obtained an exact mapping between the effective Hamiltonian of a two-level atom, to an XXZ spin model placed in a magnetic field. Several terms are worth commenting.

First, setting $J_{\mu\mu'} = 0$ leads to the well-known Ising model with $1/r^6$-decaying interaction strength. This regime can be simply accessed by choosing $|\mu'\rangle = |\downarrow\rangle$ to be the atomic ground state and $|\mu\rangle = |\uparrow\rangle$ to be a Rydberg state. It has already been extensively used for quantum simulations with Rydberg arrays (Browaeys and Lahaye, 2020; Scholl, 2021; Ebadi et al., 2021).

Second, the off-diagonal dipole-dipole interaction $J_{\mu\mu'}$ maps to an XY model, that can also be interpreted as a spin exchange that couples $|\uparrow,\downarrow\rangle$ to $|\downarrow,\uparrow\rangle$. This mapping will be extensively used in part B of this thesis, with a first-order coupling that leads to a dipolar $1/r^3$ interaction energy.

Take-home message

The interactions between two Rydberg atoms originate from the coupling of their strong electric dipoles. When restricted to a few levels per atom, the two-atom system is governed by an effective Hamiltonian that contains first-order dipolar couplings, scaling as n^4/r^3; and second-order couplings scaling as n^{11}/r^6. When mapping two atomic states on a spin 1/2, the effective Hamiltonian becomes equivalent to an XXZ Hamiltonian (up to a constant magnetic field) with interaction parameters that be experimentally tuned with many degrees of freedom: the interatomic distance r, the angle θ with the quantization axis and the choice of the levels (n, m_J).

3.2 Benchmark of the first-order dipole-dipole interaction

In this section, I focus my analysis on the first-order dipole-dipole interaction that couples the pair states $|S,P\rangle$ and $|P,S\rangle$, where $|S\rangle$ stands for $\left|nS_{1/2}, m_J = 1/2\right\rangle$ and $|P\rangle$ stands for one of the states of the nP or $(n-1)P$ manifold. This is the only first-order interaction in the presence of a magnetic field that lifts the degeneracy between the Zeeman sublevels, and in the absence of electric field or local addressing. It corresponds to the left panel in Fig. 3.3. As explained in the previous section, it corresponds to a dipolar spin exchange under the mapping $|S\rangle = |\uparrow\rangle$ and $|P\rangle = |\downarrow\rangle$. We chose $n = 60$ and work at distances $r > 10$ µm, such that the expected spin exchange interaction energy J_{SP} is much larger than the van der Waals contributions. For a spin model, this corresponds to a Hamiltonian close to the ideal XY model.

Sign of the interaction From Eq. (3.3), the value of the first-order dipole-dipole interaction between $|S,P\rangle$ and $|P,S\rangle$ is

$$\begin{aligned} J_{SP} &\equiv \langle S,P|\, V_{\mathrm{dd}}(\mathbf{r})\, |P,S\rangle /\hbar \\ &= \frac{1}{4\pi\epsilon_0\hbar r^3}\frac{1-3\cos^2(\theta)}{2}\, \langle S,P|\left(d_i^+ d_j^- + d_i^- d_j^+ + 2d_i^0 d_j^0\right)|P,S\rangle \\ &= \frac{1}{4\pi\epsilon_0\hbar r^3}\frac{1-3\cos^2(\theta)}{2} \times \begin{cases} 2\,|\langle S|\, d^0\, |P\rangle|^2 > 0 & \text{for a } \pi \text{ transition} \\ -|\langle S|\, d^+\, |P\rangle|^2 < 0 & \text{for a } \sigma^+ \text{ transition} \\ -|\langle S|\, d^-\, |P\rangle|^2 < 0 & \text{for a } \sigma^- \text{ transition} \end{cases} \end{aligned} \tag{3.11}$$

where we have used the fact that $(d^0)^\dagger = d^0$ and $(d^+)^\dagger = -d^-$. Here, π, σ^+ and σ^- are transitions that change the angular momentum along z by a value Δm which

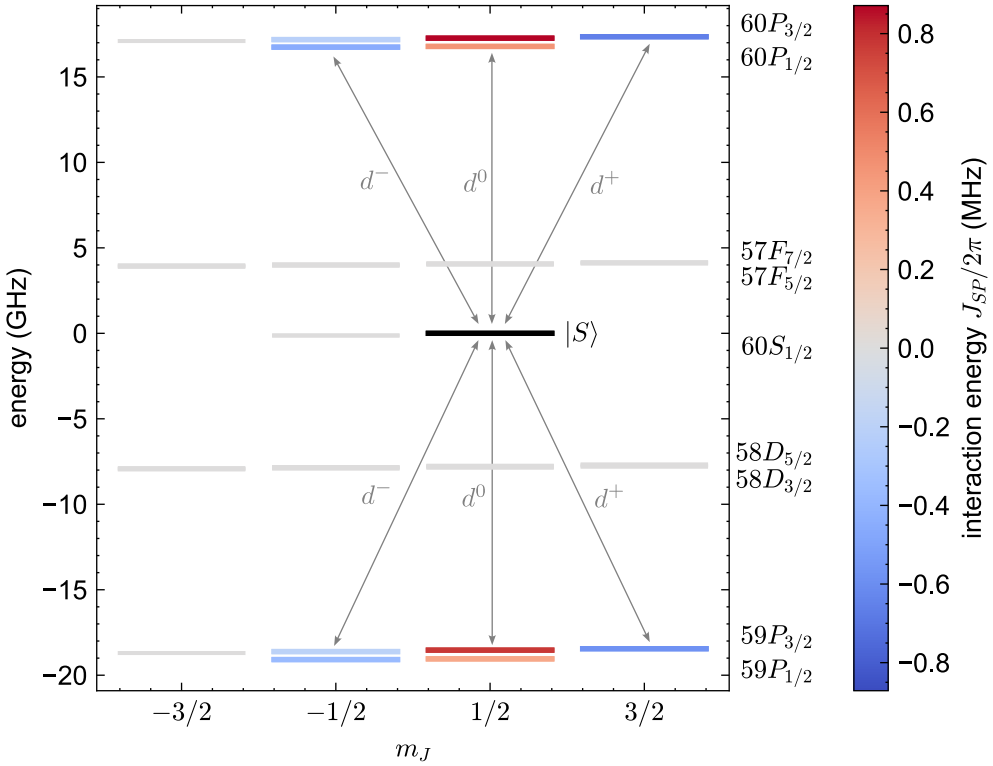

Figure 3.5: Values of the first-order dipole-dipole interaction J_{SP} between $|S,P\rangle$ and $|P,S\rangle$ for a fixed state $|S\rangle = |60S_{1/2}, m_J = 1/2\rangle$ and for various states $|P\rangle$. The colors code for the interaction energy; states with no dipole coupling with $|S\rangle$ are represented by a thin grey line. The interatomic distance is $r = 15$ µm and the magnetic field $B = 45$ G is perpendicular to the interatomic axis ($\theta = \pi/2$).

is respectively 0, +1 and −1. The values of J_{SP} for various $|P\rangle$ states are shown in Fig. 3.5. This shows that the choice of $|P\rangle$ is another degree of freedom for J_{SP}, allowing us to change both its sign and its absolute value in a straightforward way, without having to change the geometry of the array. It also makes it possible to change dynamically the interaction energy during the time evolution by a simple microwave transfer, which has some applications for quantum simulation: for example, changing the sign of the interaction amounts to reversing the unitary dynamics of the Hamiltonian (Geier et al., 2024; Bornet, 2024).

Spin exchange We want to measure the interaction energy J_{SP} and compare the experimental realization with the ideal XY model, for a simple two-atom system where most of the experimental imperfections can be modeled. In this section, I will present two methods for this measurement. Let us start by the one called a *spin exchange* (Barredo et al., 2015).

The method consists simply in preparing the initial state $|P,S\rangle$ and monitoring the

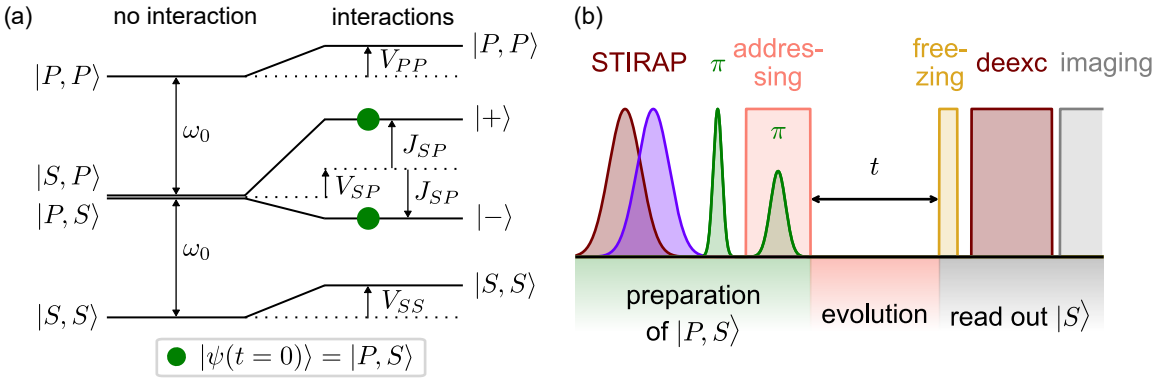

Figure 3.6: Principle of a spin-exchange experiment. (a) Sketch of the energy spectrum of two atoms interacting under H^{eff} given by Eq. (3.12), here for $r(t) = r_0$. For clarity, energy levels are separated by ω_0, which is the frequency difference between $|S\rangle$ and $|P\rangle$ in the absence of interactions (ω_0 does not appear in H^{eff}, which is defined in the atomic rotating frame at ω_0). The green points represent the overlap of the initial state $|\psi(t=0)\rangle = |P,S\rangle$ with the eigenstates. (b) Experimental sequence for a spin exchange: after global Rydberg excitation to $|S,S\rangle$ with STIRAP, a sequence of local microwave rotations (see sec. 2.2 of the previous chapter) prepares $|P,S\rangle$ with the first atom being addressed. We let the system evolve under H^{eff} for a time t, before measuring the population in level $|S\rangle$. The measurement includes an incoherent freezing pulse of ~ 50 ns (see sec. 2.1.2 of the previous chapter) for fast switch off of the interactions, followed by deexcitation of atoms from $|S\rangle$ to the ground state where atoms are imaged.

time dynamics in the natural $|S\rangle$ basis, under the effective Hamiltonian:

$$\begin{aligned} H^{\text{eff}}(t) = \hbar \left(\frac{r_0}{r(t)}\right)^3 J_{SP} \Big(|S,P\rangle\langle P,S| + |P,S\rangle\langle S,P| \Big) \\ + \hbar \left(\frac{r_0}{r(t)}\right)^6 \Big(V_{SS}\,|S,S\rangle\langle S,S| + V_{PP}\,|P,P\rangle\langle P,P| \\ + V_{SP}\,|S,P\rangle\langle S,P| + V_{SP}\,|P,S\rangle\langle P,S| \Big) \end{aligned} \tag{3.12}$$

where r_0 is the average interatomic distance and $r(t)$ is the instantaneous distance. This Hamiltonian is block-diagonal and can be easily diagonalized. Two eigenstates, $|S,S\rangle$ and $|P,P\rangle$, are simply shifted by the energy V_{SS} (respectively V_{PP}), whereas two eigenstates mix $|S,P\rangle$ and $|P,S\rangle$ as $|\pm\rangle \equiv \frac{1}{\sqrt{2}}(|S,P\rangle \pm |P,S\rangle)$, with respective energies $\pm J_{SP} + V_{SP}$. A schematic spectrum is shown in Fig. 3.6(a). The time dynamics for for fixed atoms ($r(t) = r_0$) can be analytically solved. Since the initial state gets decomposed on only two eigenstates, $|\psi(t=0)\rangle = |P,S\rangle = \frac{1}{\sqrt{2}}(|+\rangle - |-\rangle)$, the time

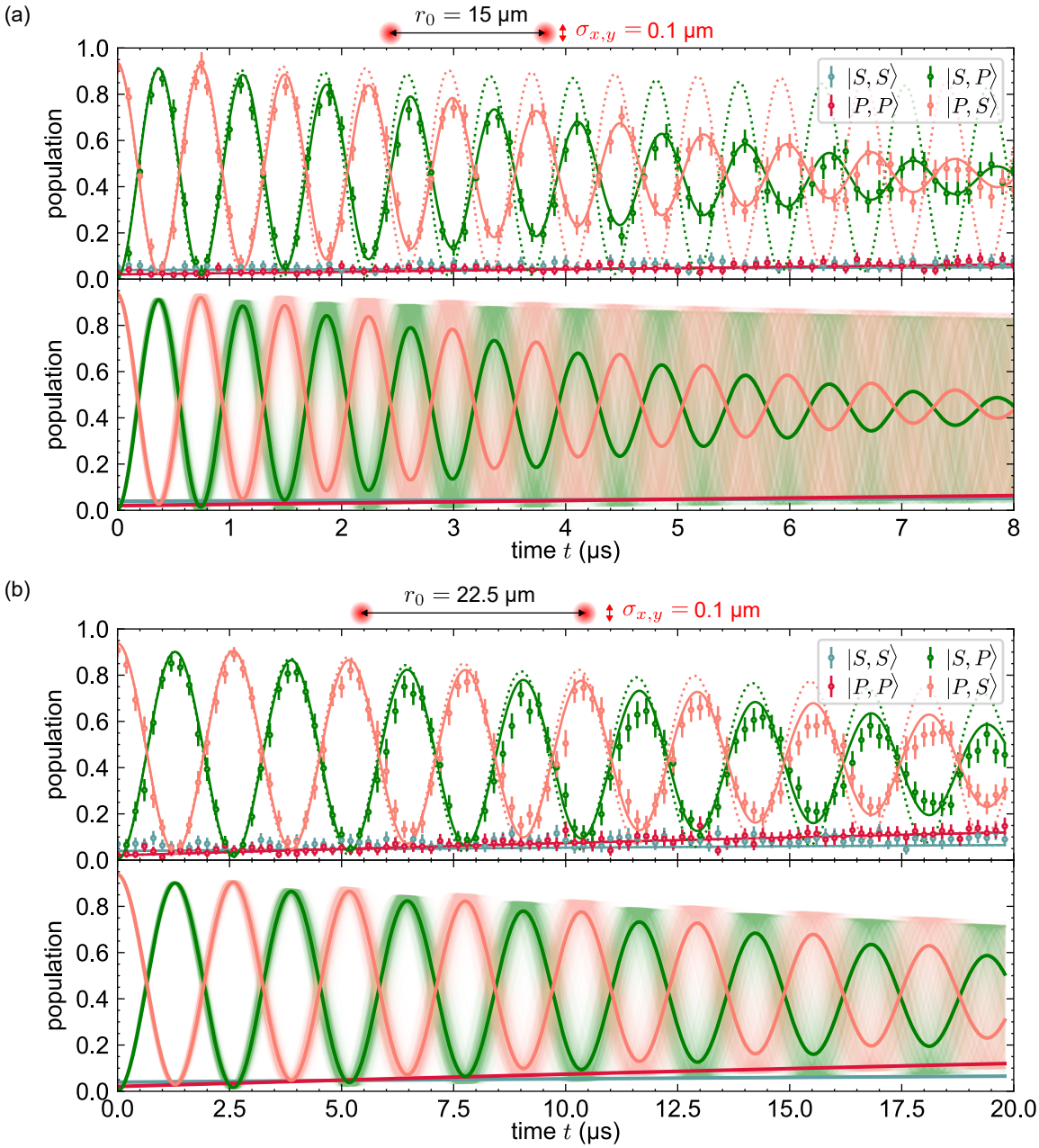

Figure 3.7: Spin exchange and its limitations for $|S\rangle = |60S_{1/2}, m_J = 1/2\rangle$ and $|P\rangle = |60P_{3/2}, m_J = 3/2\rangle$. (a) Top: measurement of the population in the four possible two-atom states, as a function of interacting time t, for an average interatomic distance $r_0 = 15 \pm 1$ µm, after Raman sideband cooling and with an adiabatic ramp down factor of the tweezers of $\alpha \approx 0.01$ (see sec. 1.4 of chapter 1). Solid lines are Monte-Carlo simulations of the dynamics following Eq. (3.14), taking into account positional disorder and detection errors according to Eq. (3.15). Free parameters are the atomic temperature and the exact value of the interaction energy J_{SP}. We obtain $T_{x,y} = 4 \pm 2$ µK, $T_z = 10 \pm 5$ µK and $|J_{SP}|/2\pi = 675$ kHz which would predict $r_0 = 14.9$ µm. Dotted lines are the same simulation in the absence of positional disorder. Bottom: principle of the Monte-Carlo simulation, revealing the main origin of the observed damping. The measured populations (thin solid lines) are averaged over many classical trajectories which are sampled with a random positional disorder (1000 realizations, represented by thin solid lines). (b) Same as (a), for a larger interatomic distance $r_0 = 22.5$ µm. We find the same temperatures and $|J_{SP}|/2\pi = 194$ kHz.

evolution is simply given by

$$|\psi(t)\rangle = \frac{e^{-iV_{SP}t}}{2}\left(e^{-iJ_{SP}t}\,|+\rangle - e^{+iJ_{SP}t}\,|-\rangle\right)$$
$$= e^{-iV_{SP}t}\left[\cos(J_{SP}t)\,|P,S\rangle - i\sin(J_{SP}t)\,|S,P\rangle\right]. \tag{3.13}$$

This results in an oscillation at frequency $2J_{SP}$ between the states $|P,S\rangle$ and $|S,P\rangle$ that can be measured experimentally. The experimental sequence is shown in Fig. 3.6(b). An advantage of this method is that the oscillation frequency is directly the interaction energy (up to a factor 2) and does not depend on the van der Waals terms; however, it does not give access to the sign of J_{SP} but only its absolute value.

Figure 3.7(a) shows an example of spin exchanges for $n = 60$, at an average distance $r_0 = 15$ µm which is the typical order of magnitude used for quantum simulation of many-body physics with our setup. We observe long-lived oscillations that allow us to extract the interaction energy $|J_{SP}|/2\pi = 675$ kHz. In contrast with the ideal case given by Eq. (3.13), the oscillation has a finite contrast of about 90 % and is damped. The fit of the oscillations by a sine wave with a Gaussian envelope $\exp(-t^2/2\tau^2)$ yields a damping time $\tau = 3.8 \pm 0.1$ µs corresponding to a quality factor $Q = \tau|J_{SP}| = 16 \pm 0.3$. To understand better the sources of those imperfections, we built the following error model.

Modeling the two-atom system We restrict the internal degrees of freedom of each atom to four atomic levels: $|S\rangle$ and $|P\rangle$, plus two other levels $|g\rangle$ and $|r\rangle$ that account for leakage, and that stand respectively for the ground state manifold and other Rydberg states. Interactions are described by the Hamiltonian $H^{\text{eff}}(t)$ with interaction energies predicted by the software PairInteraction (Weber et al., 2017), and we neglect interactions with the two other levels $|g\rangle$ and $|r\rangle$.

Several physical effects are expected to create deviations from the ideal XXZ model.

- **Positional disorder** For now, we assume that the motional degrees of freedom are independent of the internal degrees of freedom, and that the two atoms are in free flight during the interaction. We model the initial atomic position by a classical, three-dimensional Gaussian distribution with standard deviation σ_α along direction α; similarly, initial velocities are described by a distribution with standard deviation σ_{v^α}). This allows us to perform a Monte-Carlo simulation of the atomic motion, by averaging the quantum dynamics over many classical trajectories; for each trajectory and for each atom j, we sample a random initial atomic position $r_j^\alpha(0)$ and velocity $v_j^\alpha(0)$ and make it evolve according to:

$r_j^\alpha(t) = r_j^\alpha(0) + v_j^\alpha(0)t$. These assumptions will be checked in sec. 3.4 of this chapter.

- **Rydberg lifetimes** Each of the Rydberg levels $|\mu\rangle$ for $\mu \in \{S, P\}$ has two decay channels: it can decay to the ground state $|g\rangle$ with a rate $\Gamma_{\mu\to g}$ due to spontaneous emission[2]; or it can decay to another Rydberg state $|r\rangle$ with a rate $\Gamma_{\mu\to r}$ due to black-body radiation in our room temperature setup. Those two channels have to be dissociated in the simulation, since atoms in $|g\rangle$ are recaptured and imaged, whereas atoms in $|r\rangle$ are typically lost. To account for those finite lifetimes, we introduce the collapse operators $L_{\mu\to\mu'} \equiv |\mu'\rangle\langle\mu|$ and integrate the Lindblad equation for the dynamics of the density matrix ρ:

$$\frac{d\rho}{dt} = \frac{1}{i\hbar}\left[H^{\text{eff}}, \rho\right] + \sum_{\substack{\mu\in\{S,P\}\\ \mu'\in\{g,r\}}} \Gamma_{\mu\to\mu'}\left(L_{\mu\to\mu'}\rho L_{\mu\to\mu'}^\dagger - \frac{1}{2}\left\{L_{\mu\to\mu'}^\dagger L_{\mu\to\mu'}, \rho\right\}\right). \tag{3.14}$$

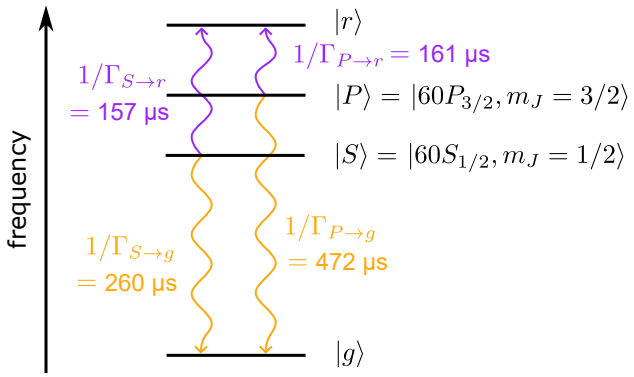

Figure 3.8: Simplified model for taking into account the Rydberg lifetimes.

- **Preparation errors** The global excitation pulse (STIRAP) has a finite fidelity, leading to a small probability η_{st} per atom that it is initialized in the ground state $|g\rangle$ instead of $|S\rangle$. We take this into account by modifying the initial density matrix. If the target initial state for the two atoms is $|\psi_0\rangle$, the initial density matrix is $\rho(t=0) \equiv (1-2\eta_{\text{st}})|\psi_0\rangle\langle\psi_0| + \eta_{\text{st}}\sum_i P_i|\psi_0\rangle\langle\psi_0|P_i^\dagger$, where $P_i \equiv |g\rangle\langle g|_i$ projects the atom i in the ground state. Here, we treat the residual population in $|g\rangle$ as a statistical mixture and we neglect the potential coherence terms of the density matrix, even thought they are probably present in the

[2] Actually, the level $|S\rangle$ does not decay directly to the ground state $|g\rangle = 5S_{1/2}$, but it decays to low-lying P levels that all end up quickly in $|g\rangle$.

experimentally-prepared state. However, for two atoms this does affect the dynamics, since there is no interaction between an atom in level $|g\rangle$ and its neighbor in a Rydberg levels $|S\rangle$ or $|P\rangle$.

$$\begin{cases} |S\rangle\langle S|'_j & \equiv & (1-\varepsilon_\uparrow)\,|S\rangle\langle S|_j + \varepsilon_\downarrow\,|P\rangle\langle P|_j + |g\rangle\langle g|_j \\ |P\rangle\langle P|'_j & \equiv & 1 - |S\rangle\langle S|'_j \end{cases} \tag{3.15}$$

where $|\mu\rangle\langle\mu|'_j$ stands for the projector on state $|\mu\rangle$ of atom j after imperfect readout, and $|\mu\rangle\langle\mu|_j$ before the readout. Detection errors are assumed to be homogeneous and independent on each atom of the array.

The previously-described error model allows us to explain fully the experimentally-measured finite contrast and damping shown in Fig. 3.7(a). While preparation and detection errors contribute to the finite contrast, the damping is mainly due to the positional disorder: as explained in chapter 1, fluctuation of the atomic positions induce fluctuations of the interatomic distance, which lead in turn to fluctuations of the interaction energies, as $\Delta J_{SP}/|J_{SP}| \sim 3\Delta r/r_0$; the resulting oscillation can be interpreted as the average between many oscillations, each one having a different frequency. On top of that, the position fluctuations increase over time due to the initial dispersion of velocities. We obtain perfect agreement with the data by using the temperatures: $T_{x,y} = 4 \pm 2$ µK radially and $T_z = 10 \pm 5$ µK axially, which correspond to average occupation numbers $n_{x,y} \approx 0.3$ and $n_z \approx 10$. Those values are compatible with the ones after Raman sideband cooling, according to the Raman spectra (see Sec. 1.3 of chapter 1).

Of course, we can increase the average distance r_0 between the atoms to reduce the relative fluctuations $\Delta J_{SP}/|J_{SP}|$. Figure 3.7(b) shows a spin exchange in the same conditions as Fig. 3.7(a), but with larger distance $r_0 = 22.5$ µm. Compared with the case $r_0 = 14.9$ µm, the obtained interaction energy $|J_{SP}|/2\pi = 194$ kHz is in good agreement with the expected $1/r_0^3$ scaling which predicts a change by a factor $(14.9/22.5)^3 \approx 0.29$. The damping time $\tau = 13.4 \pm 0.4$ µs is increased by approximately the same factor, resulting in the end in a similar quality factor $Q = \tau|J_{SP}| = 16.1 \pm 0.2$. At long times, Rydberg lifetimes also start to be a major limitation, as can be seen from the slow rise up of probabilities in the states $|S,S\rangle$ and $|P,P\rangle$.

To go further, one would need to use states with larger principal quantum number n, which have two advantages: longer lifetimes, and larger interaction energies, so that one can decrease the fluctuations of ΔJ_{SP} without decreasing $|J_{SP}|$.

Two-atom Ramsey Another method for measuring J_{SP} is an adaptation of a Ramsey sequence to the case of two atoms: we call it a two-atom Ramsey measurement. The experimental sequence is given in Fig. 3.9(b): starting from $|S,S\rangle$ after the global Rydberg excitation, we apply a global microwave $\pi/2$ pulse to prepare the state $|{\rightarrow},{\rightarrow}\rangle$ where $|{\rightarrow}\rangle \equiv (|S\rangle + |P\rangle)/\sqrt{2}$ corresponds to a spin along x in spin language. Similarly, we define $|{\leftarrow}\rangle \equiv (|S\rangle - |P\rangle)/\sqrt{2}$. We let the system evolve for a time t, and apply another global microwave $\pi/2$ pulse that allows us to measure in the x basis for spins.

At first sight, this sequence seems simpler than the spin exchange because there is no need for local addressing. However, contrary to a spin exchange, the initial state gets decomposed over three eigenstates of H^{eff}, each one with a potentially different eigenenergy: $|\psi(t=0)\rangle = |{\rightarrow},{\rightarrow}\rangle = \frac{1}{\sqrt{2}}\left[|+\rangle + \frac{1}{\sqrt{2}}(|S,S\rangle + |P,P\rangle)\right]$. In the absence of careful phase compensation, this would lead to a beating instead of a simple oscillation. I will show that this beating can be compensated by a simple microwave detuning[3]. Let us introduce the single-atom microwave detuning δ as $H^{\text{det}} = \hbar\delta\left(|S\rangle\langle S| - |P\rangle\langle P|\right)/2$. The resulting time evolution under the total Hamiltonian $H^{\text{eff}} + H_i^{\text{det}} + H_j^{\text{det}}$ is given by:

$$|\psi(t)\rangle = \frac{1}{\sqrt{2}}\left[e^{-i(J_{SP}+V_{SP})t}|+\rangle + \frac{1}{\sqrt{2}}\left(e^{-i(V_{SS}+\delta)t}|S,S\rangle + e^{-i(V_{PP}-\delta)t}|P,P\rangle\right)\right]. \tag{3.16}$$

To avoid a beating, we want the accumulated phase to be the same for the two states $|S,S\rangle$ and $|P,P\rangle$ such that the phase factor can be factorized. Solving for $V_{SS}+\delta = V_{PP}-\delta$, we get $\delta = (V_{PP}-V_{SS})/2$[4] and the time evolved state becomes

$$\begin{aligned}|\psi(t)\rangle &= \frac{1}{\sqrt{2}}\left[e^{-i(J_{SP}+V_{SP})t}|+\rangle + e^{-i\frac{V_{SS}+V_{PP}}{2}t}\frac{1}{\sqrt{2}}(|S,S\rangle + |P,P\rangle)\right] \\ &= e^{-i\left(\frac{J_{SP}+V_{SP}}{2}+\frac{V_{SS}+V_{PP}}{4}\right)t}\left[\cos\left(\frac{\tilde{J}_{SP}t}{2}\right)|{\rightarrow},{\rightarrow}\rangle + i\sin\left(\frac{\tilde{J}_{SP}t}{2}\right)|{\leftarrow},{\leftarrow}\rangle\right],\end{aligned} \tag{3.17}$$

where we have defined an effective oscillation energy as $\tilde{J}_{SP} \equiv J_{SP} + V_{SP} - \frac{V_{SS}+V_{PP}}{2}$. Up to a non-important global phase factor, we get an oscillation at angular frequency $\tilde{J}_{SP}$ between the two states $|{\rightarrow},{\rightarrow}\rangle$ and $|{\leftarrow},{\leftarrow}\rangle$. In the simple case where van der

[3] An alternative method would be to use a spin echo technique, such as done in Bao et al. (2023).
[4] In spin language, the compensation of the accumulated phase by the microwave shift is equivalent to canceling out the magnetic field b_z generated by the interactions [see Eq. (6.3)].

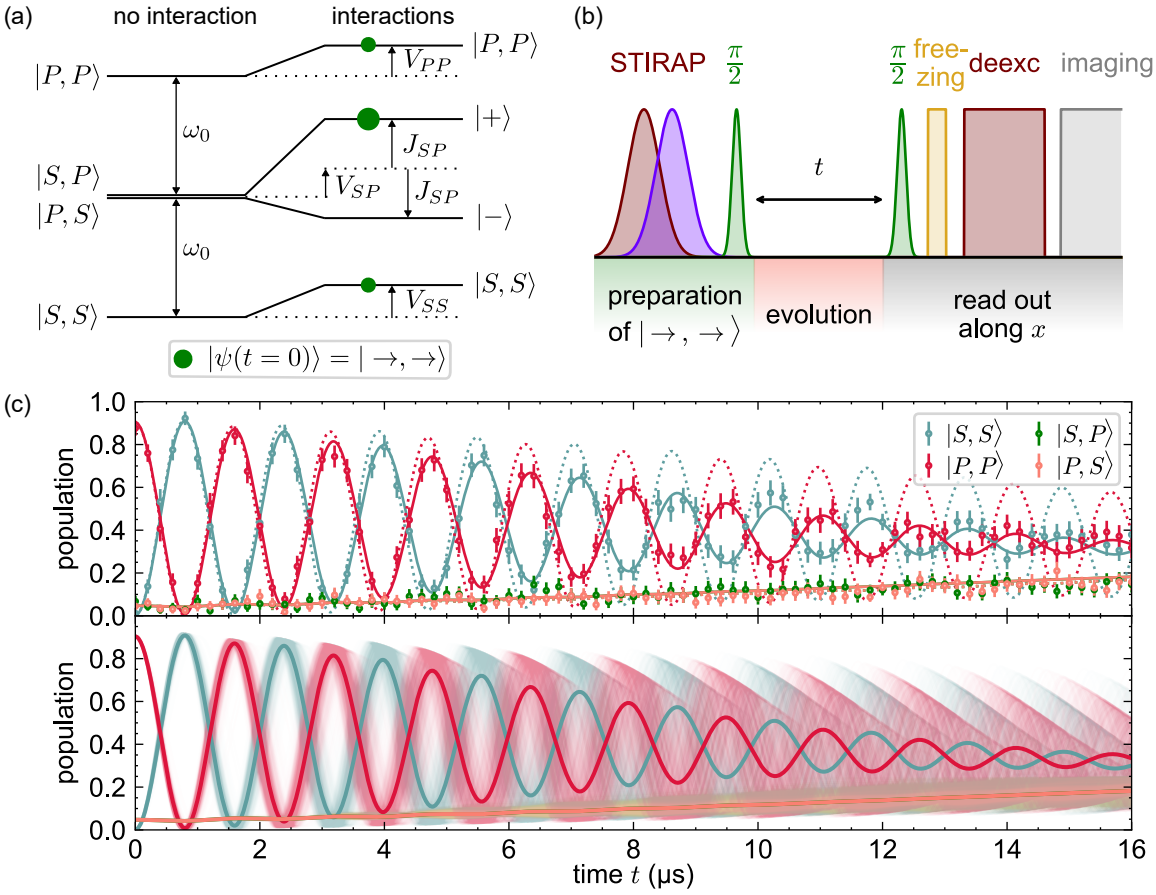

Figure 3.9: Two-atom Ramsey oscillation for $|S\rangle = \left|60S_{1/2}, m_J = 1/2\right\rangle$ and $|P\rangle = \left|60P_{3/2}, m_J = 3/2\right\rangle$. (a) Skecth of the energy spectrum of two atoms interacting under H^{eff}. The green points represent the overlap of the initial state $|\psi(t=0)\rangle = |\rightarrow,\rightarrow\rangle$ with the eigenstates. (b) Experimental sequence for a two-atom Ramsey oscillation. (c) Top: measurement of the population in the four possible two-atom states, as a function of interacting time t, with the same parameters as in Fig. 3.7(a), using a slightly detuned microwave pulse ($\delta/2\pi = -40$ kHz). Solid lines are Monte-Carlo simulations of the dynamics with temperature and the average interatomic distance as free parameters. We obtain $T_{x,y} = 4 \pm 2$ μK, $T_z = 20 \pm 8$ μK and a distance $r_0 = 14.9$ μm which corresponds to the following interaction energies: $J_{SP}/2\pi = -675$ kHz, $V_{SS}/2\pi = 12$ kHz, $V_{PP}/2\pi = 17$ kHz and $V_{SP}/2\pi = -52$ kHz. This leads to an oscillation at the effective frequency $\tilde{J}_{SP}/2\pi = -638$ kHz.

Waals interactions are negligible, the oscillation occurs at frequency $\tilde{J}_{SP} \equiv J_{SP}$ which is the frequency difference between $|+\rangle$ on the one side, and $|S,S\rangle$ and $|P,P\rangle$ on the other side. After the $\pi/2$ measurement pulse, those states are respectively mapped onto $|S,S\rangle$ and $|P,P\rangle$.

Experimentally, we optimize the microwave detuning δ by maximizing the contrast of the oscillation, resulting in the curve shown in Fig. 3.9(c). The initial contrast and the damping of the oscillation are again well explained by simulations with the same experimental imperfections. Here, the damping can be attributed to three effects: positional disorder mainly, Rydberg lifetimes, and also a slight overcompensation of the detuning, which was experimentally set to $\delta/2\pi = -40$ kHz whereas the ideal compensation should happen for $\delta/2\pi = -32$ kHz according to the simulations, leading to a small rise up of the probabilities of the states $|S,P\rangle$ and $|P,S\rangle$ at long times. Note that compared with the case of a spin exchange with the same experimental parameters [Fig. 3.7(a)], the damping time is twice as long, but the oscillation frequency is also twice as small, so the Q-factor is approximately the same.

Spatial and angular dependence Now that I have presented two methods to extract $|J_{SP}|$, let us measure its spatial and angular dependence with respect to the quantization axis. We use the spin-exchange method to avoid possible biases due to the van der Waals interactions. In Fig. 3.10(a), we measure $|J_{SP}|$ for pairs with various distances r_0 and check that it has the expected scaling $1/r_0^3$. The results match very well with theory predictions using the software PairInteraction (Weber et al., 2017).

In Fig. 3.10(b), we measure the angular dependence of $|J_{SP}|$ on the angle θ between the magnetic field and the interatomic axis. For this measurement, we set the magnetic field $\mathbf{B} = B\mathbf{e}_x$ to be in the atomic plane with $B \approx 46$ G, and we design an array with several pairs of atoms, each one with a different angle θ between $\mathbf{B}$ and the interatomic axis. The results are summarized in Fig. 3.10 and show the expected $1 - 3\cos^2(\theta)$ behavior.

An important parameter to consider for the theory prediction to be accurate is the value of the magnetic field, which mixes the fine structure of the $60P$ manifold. In this example, the state $|P\rangle$ in the presence of a magnetic field $B = 46$ G is redefined as $|P\rangle = \alpha\,|P_1\rangle + \beta\,|P_2\rangle$ with $|P_1\rangle \equiv \left|60P_{3/2}, m_J = -1/2\right\rangle$ and $|P_2\rangle \equiv \left|60P_{1/2}, m_J = -1/2\right\rangle$; we compute $\alpha \approx 0.997$ and $\beta \approx -0.073$. As a result, the dipole-dipole coupling becomes $\hbar J_{SP} \equiv \langle S,P|\,V_{\mathrm{dd}}\,|P,S\rangle = |\alpha|^2\,\langle S,P_1|\,V_{\mathrm{dd}}\,|P_1,S\rangle + 2\,\mathrm{Re}(\alpha^*\beta)\,\langle S,P_1|\,V_{\mathrm{dd}}\,|P_2,S\rangle + O\left(|\beta|^2\right)$. As a result, the coupling in the presence of the magnetic field (solid red line) increases by about 20 % compared with the case with

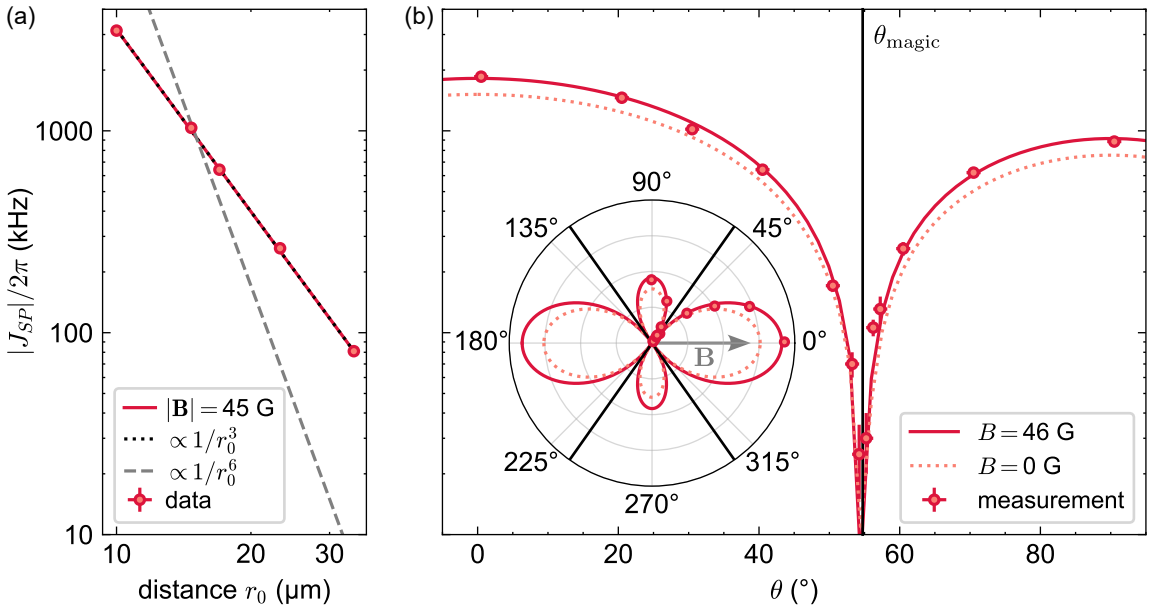

Figure 3.10: Characterization of the first-order dipole-dipole interaction $|J_{SP}|$, for the Rydberg states $|S\rangle = |60S_{1/2}, m_J = 1/2\rangle$ and $|P\rangle = |60P_{3/2}, m_J = 1/2\rangle$ (a) or $|P\rangle = |60P_{3/2}, m_J = -1/2\rangle$ (b). Each experimental point is extracted from a two-atom spin-exchange experiment. (a) Interaction strength as a function of the interatomic distance r_0 for a fixed angle $\theta = 90°$. The solid red line shows the calculated values using PairInteraction, and the dotted and dashed black lines are power-law fits by respectively $1/r_0^3$ and $1/r_0^6$. (b) Angular dependence for a fixed distance $r_0 = 9.9$ μm. The angle θ is defined as the angle between the magnetic field and the interatomic axis. Vertical black lines indicate the magic angle $\theta_{\text{magic}} \equiv \arccos\left(\frac{1}{\sqrt{3}}\right)$ at which $|J_{SP}|$ theoretically vanishes. Inset: same measurement, represented in polar coordinates.

no mixing, $\hbar J_{SP} = \langle S, P_1 | V_{\text{dd}} | P_1, S \rangle$ (dotted line). Note that this mixing does not affect the angular dependence of $J_{S\tilde{P}}$, since all terms involve a d^+d^- transition and thus have the same angular dependence $\propto 1 - 3\cos^2(\theta)$.

Contrary to the ideal case where the interaction completely vanishes at the magic angle $\theta_{\text{magic}} \equiv \arccos\left(\frac{1}{\sqrt{3}}\right)$, the experimentally measured dipole-dipole interaction $|J_{SP}|/2\pi$ goes down to a few tens of kHz. For such low interactions, the measurement gets limited by many effects: for example, Rydberg lifetimes and magnetic field noise tend to reduce the accuracy of the measurement; also, positional disorder causes fluctuations of the angle θ. We estimate the angle uncertainty due to the transverse positional disorder to be $\Delta\theta = \frac{\sqrt{2}\sigma_x}{r_0} \sim 0.5°$ for $r_0 = 10$ μm and $\sigma_x \sim 50$ nm[5]. Overall, we can vary the value of the interaction energy over almost two orders of magnitude.

[5]This calculation is valid when the magnetic field is in the plane, in which case the main contribution to the angle fluctuations is the radial position uncertainty σ_x. For experiments where the magnetic field is perpendicular to the atomic plane, the dominant contribution is the axial uncertainty $\sigma_x \sim 300$ nm, leading to larger fluctuations $\Delta\theta \sim 2.5°$.

A curiosity: a d^+d^0 "spin exchange" Some off-resonant dipole-dipole couplings can be made resonant using local lightshifts. In the remaining of this section, I will show measurements of a d^+d^0 "spin-exchange" experiment that involves four Rydberg levels: $|S\rangle = \left|60S_{1/2}, m_J = 1/2\right\rangle$, $|S'\rangle = \left|60S_{1/2}, m_J = -1/2\right\rangle$, $|P\rangle = \left|60P_{3/2}, m_J = -1/2\right\rangle$, $|P'\rangle = \left|60P_{3/2}, m_J = 3/2\right\rangle$, as illustrated in Fig. 3.11(a). The dipole-dipole interaction given by Eq. (3.3) couples $|S, P\rangle$ to $|P', S'\rangle$ with a matrix element

$$\begin{aligned} J_{SP,P'S'} &\equiv \langle S, P| V_{\mathrm{dd}}(\mathbf{r}) |P', S'\rangle /\hbar \\ &= \frac{3}{4\sqrt{2}\pi\epsilon_0\hbar r^3} \sin(\theta)\cos(\theta)e^{-i\phi} \langle S| d^+ |P'\rangle \langle P| d^0 |S'\rangle . \end{aligned} \tag{3.18}$$

For a distance $r = 9.9$ µm, a magnetic field $B = 46$ G and an angle $\theta = 50°$, we estimate $|J_{SP,P'S'}| = 2\pi \times 3.7$ MHz. However, due to the magnetic field, the associated transition is off-resonant by an amount $E_{P',S'} - E_{S,P} = 2\pi \times 42$ MHz which is much larger than $|J_{SP,P'S'}|$. On the contrary, one needs $|E_{P',S'} - E_{S,P}| < |J_{SP,P'S'}|$ to effectively transfer population between $|S, P\rangle$ and $|P', S'\rangle$. This can be achieved using a local light shift δ_{ls} on the second atom, to shift down the energy of $|S'\rangle$ by $\delta_{\mathrm{ls}} \approx E_{P',S'} - E_{S,P}$.

To observe a coherent exchange between $|S, P\rangle$ and $|P', S'\rangle$, we thus apply the sequence shown in Fig. 3.11(b). It is the same as the one of a usual spin exchange, except that the addressing lightshift is kept on during the whole time evolution. We use a different value of the addressing lightshift for the preparation and for the evolution, so that we limit the effect of interactions during the preparation. At the end of the sequence, the deexcitation pulse affects both in $|S\rangle$ and $|S'\rangle$, so that the recapture probability is the sum of populations in $|S\rangle$ and $|S'\rangle$ (up to detection errors). This means that we do not distinguish an atom in $|S\rangle$ from an atom in $|S'\rangle$, but this does not matter for this proof-of-principle measurement.

As shown in Fig. 3.11 for $r_0 = 9.9$ µm and $\theta = 50°$, we obtain a coherent oscillation between the populations in $|S, P\rangle$ and $|P', S'\rangle$[6], that proves the two-atom transfer. A fit by a damped sine wave gives $|J_{SP,P'S'}|/2\pi = 3.4 \pm 0.1$ MHz. We repeat this measurement for various angles θ and obtain a reasonable agreement with the theory predictions [Fig. 3.11(d)]. This experiment is, to our knowledge, the first measurement of a coherent d^+d^0 spin exchange with Rydberg atoms.

[6]The mapping of the recapture data to the population in the target states $|S, P\rangle$ and $|P', S'\rangle$ is only approximate, due to the fact that we cannot distinguish all four states from each other: we only resolve whether the atom is in an S state or a P state. For example, the probability of the event "atom 1 is recaptured and atom 2 is lost" is, up to detection errors, the sum of the populations in the states $|S, P\rangle$, $|S', P\rangle$, $|S, P'\rangle$ and $|S', P'\rangle$. But we assume that the three last states have a negligible population, since they are associated to off-resonant couplings.

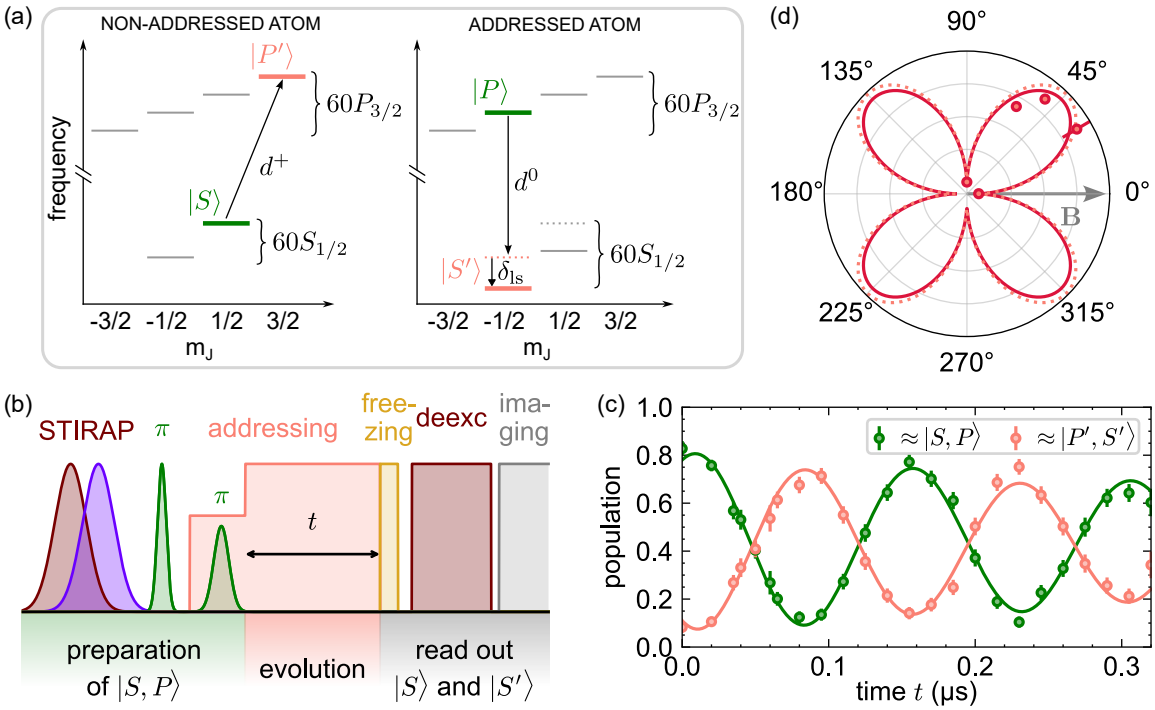

Figure 3.11: Spin exchange d^+d^0 induced by a local lightshift. (a) Sketch of the energy levels involved in the interaction. The dipole-dipole interaction couples $|S,P\rangle$ to $|P',S'\rangle$ but the transition is off-resonant by $E_{P',S'} - E_{S,P} = 42$ MHz in the presence of a magnetic field $B = 46$ G; to make it resonant, we address the second atom, to apply a lightshift δ_{ls} on $|S'\rangle$. (b) Experimental sequence for observing a coherent d^+d^0 transition. The sequence is the same as for a usual spin exchange [see Fig. 3.6(b)], except that the addressing is kept on during the evolution. Note that both levels $|S\rangle$ and $|S'\rangle$ are deexcited and thus measured, despite the large Zeeman splitting. (c) Example of a d^+d^0 spin exchange, for a distance $r_0 = 9.9$ μm and an angle $\theta = 50°$. The colors correspond to the probabilities of the events "atom 1 is recaptured and atom 2 is lost" (green), and "atom 1 is lost and atom 2 is recaptured" (pink), which approximately correspond to the populations in $|S,P\rangle$ and $|P',S'\rangle$. Solid lines are fits by a damped sine wave that gives $|J_{SP,P'S'}|/2\pi = 3.4 \pm 0.1$ MHz. (d) Angular dependence of the d^+d^0 spin exchange. The solid (resp. dotted) line is the theory prediction with $B = 46$ G (resp. $B = 0$ G).

Beyond a curiosity, could it be useful for quantum simulation? A peculiarity of the d^+d^0 spin exchange is that the coupling includes a complex phase [see Eq. (3.18)]. This leads to a Hamiltonian that breaks time-reversal symmetry and can lead to some topological phenomena such as already showed in de Léséleuc et al. (2019) and in Lienhard et al. (2020). Such couplings could also be used for simulating more complex Hamiltonians that spins 1/2 (Mögerle et al., 2024). However, the use of the addressing to locally lightshift one atom may not be the most suitable solution, since the addressing has to be applied for a long time, leading to accumulation of various errors (see sec. 2.2 of chapter 2). For the simulation of simpler spin Hamiltonians such

as the XXZ spin model, this d^+d^0 spin exchange is an unwanted side effect of the addressing: for example, one has to be careful not to hit such resonances during local rotations.

Take-home message

The simplest resonant transition due to the dipole-dipole interaction is the coupling J_{SP} between the states $|S,P\rangle$ and $|P,S\rangle$, that has a $1-3\cos^2(\theta)$ angular dependence and whose sign also depends on the particular chosen $|P\rangle$ state (d^0d^0 or d^+d^- coupling). We measure the coupling strength using two methods that involve a coherent transfer between those states, and we identify the limitations to the time coherence of the oscillations. In the range of chosen parameters ($n = 60$ and interatomic distance $r_0 \sim 15$ µm), the major limiting factors are positional disorder and Rydberg lifetimes.

Among the many other off-resonant dipole-dipole couplings, we can select one between states $|S,P\rangle$ and $|P',S'\rangle$ and make it resonant using a local lightshift. Here, we recover another angular dependence $\sin(\theta)\cos(\theta)$ which is characteristic of a d^+d^0 coupling.

3.3 Measurement of an off-diagonal van der Waals interaction

In this section, I present the another off-diagonal interaction, between two states that are coupled at second order by the dipole-dipole interaction. Let us consider two states $|S\rangle$ and $|S'\rangle$ such that they are not dipole coupled. According to the effective Hamiltonian theory [Eq. (3.4)], the coupling between the states $|S, S'\rangle$ and $|S', S\rangle$ is given by

$$J_{S,S'} \equiv \sum_{\substack{P,\,P' \\ E_{P,P'} \neq E_{S,S'}}} \frac{\langle S, S'| V_{\mathrm{dd}}(\mathbf{r}) |P, P'\rangle \langle P', P| V_{\mathrm{dd}}(\mathbf{r}) |S', S\rangle}{\hbar \left(E_{S,S'} - E_{P,P'}\right)}. \tag{3.19}$$

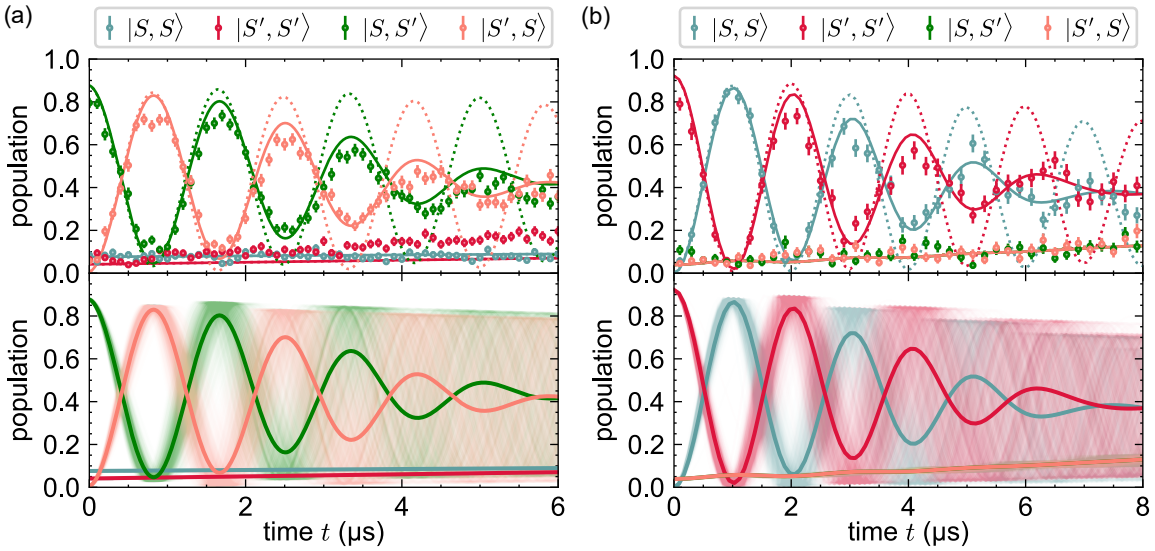

Figure 3.12: Measurement of the off-diagonal van der Waals interaction between $|S, S'\rangle$ and $|S', S\rangle$. Experimental parameters: $|S\rangle = \left|60S_{1/2}, m_J = 1/2\right\rangle$ and $|S'\rangle = \left|61S_{1/2}, m_J = 1/2\right\rangle$, average distance $r_0 = 10.44$ μm, angle $\theta = 90°$. (a) Spin exchange giving $|J_{S,S'}|2/\pi = 290 \pm 10$ kHz. The experimental sequence is the same as in Fig. 3.6(b), except that single-photon pulses are replaced by two-photon pulses between $|S\rangle$ and $|S'\rangle$ [see sec. 2.1.1 of chapter 2]. Top: data points are compared with simulations including Rydberg lifetimes, preparation and detection errors, positional disorder at $T_{x,y} = 8$ μK and $T_z = 20$ μK (solid lines). The same simulation in the absence of positional disorder is shown as dotted lines. Bottom: all simulated trajectories for the Monte-Carlo simulations and their average. (b) Same as (a), with a two-atom Ramsey sequence [see Fig. 3.9]. The interaction energies of the simulation are: $J_{SS'}/2\pi = 299$ kHz, $V_{SS}/2\pi = 102$ kHz, $V_{S'S'}/2\pi = 125$ kHz and $V_{SS'}/2\pi = 315$ kHz, which correspond to an oscillation at the effective frequency $\tilde{J}_{SS'} = J_{SS'} + V_{SS'} - \frac{V_{SS}+V_{S'S'}}{2} = 2\pi \times 500$ kHz.

To measure $|J_{S,S'}|$, we use the same methods as for the first order dipole coupling, since both cases are described by the same effective Hamiltonian for two atoms

with two levels each [Eq. (3.5)]; only the dependence with distance and with the angle differs. In Fig. 3.12, I show two types of coherent oscillations involving this interaction. The first one [Fig. 3.12(a)] is a *spin exchange* at a frequency $2J_{S,S'}$ with $|J_{S,S'}|2/\pi = 290 \pm 10$ kHz. The experimental sequence is the same as in Fig. 3.6(b), except that the single-photon π pulse is replaced by a two-photon π-pulse. The experimental data is correctly reproduced by simulations including positional disorder, Rydberg lifetimes, preparation and detection errors. Here, the effect of positional disorder is even more detrimental than in the first-order spin exchange, due to the faster spatial decay of the second-order interactions ($1/r^6$ instead of $1/r^3$).

The second calibration is the two-atom Ramsey measurement, which is presented in Fig. 3.12(b). In this case, the compensation of the accumulated phase is less crucial because the states $|S, S\rangle$ and $|S, S'\rangle$ have very similar van der Waals shifts: $V_{SS}/2\pi = 102$ kHz and $V_{S'S'}/2\pi = 125$ kHz at $r_0 = 10.44$ µm and $\theta = 90°$, which in spin language translate into a weak effective magnetic field $b_z = (V_{SS} - V_{S'S'})/2 = -2\pi \times 12$ kHz. However, since the van der Waals shifts are on the same order as the off-diagonal coupling, the effective frequency of the oscillation is strongly modified with respect to the spin exchange method: we measure an oscillation at 480 ± 10 kHz, which is close to the expected value of $\tilde{J}_{SS'}/2\pi = \left(J_{SS'} + V_{SS'} - \frac{V_{SS}+V_{S'S'}}{2}\right)/2\pi = 500$ kHz.

Angular and distance dependence We now use the spin exchange method to measure the dependence of $|J_{SS'}|$ with the average interatomic distance r_0 and with the magnetic field angle θ. In Fig. 3.13(a), we recover the expected power law dependence $1/r_0^6$. In Fig. 3.13(b), we measure the angular dependence of $|J_{SS'}|$ and find weak variations that are compatible with the theory calculations at a magnetic field $B = 46$ G. The slight angular dependence of $|J_{SS'}|$ originates from the average between many virtual transitions to $|P, P'\rangle$ states, with various angular dependences; contrary to the first order dipole-dipole interaction, the angular dependence of $|J_{SS'}|$ can be modified by the magnitude of the magnetic field, which affects the energy differences between the states and thus changes the weight of the contribution of each state $|P, P'\rangle$ in Eq. (3.19). Another important difference with the first-order interaction is that $J_{SS'}$ is always positive (for $B < 90$ G).

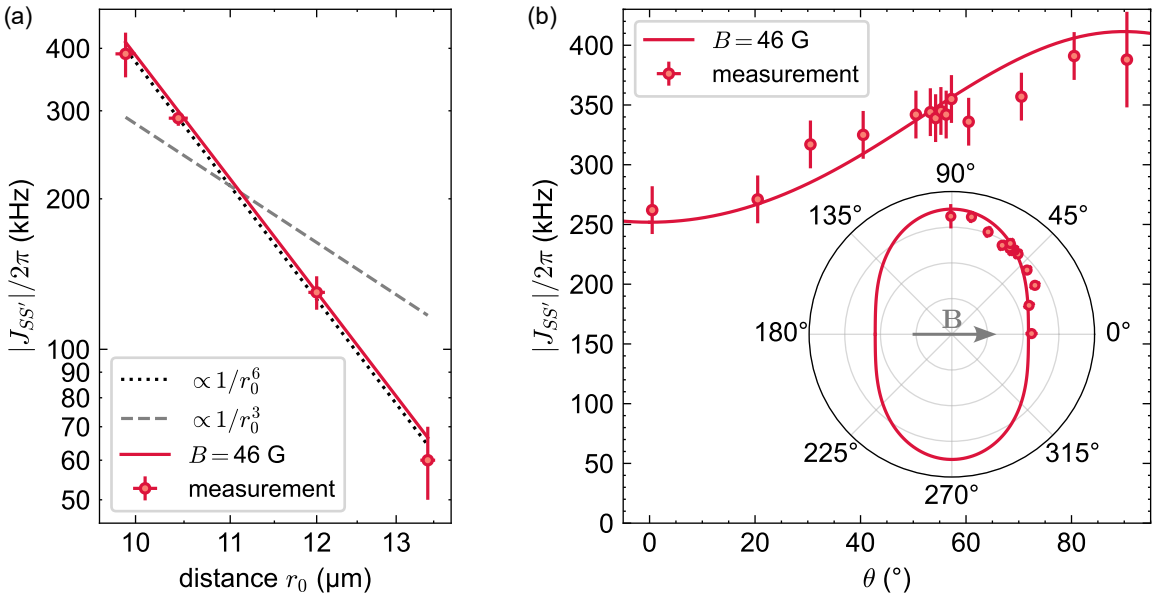

Figure 3.13: Dependence of the off-diagonal van der Waals interaction $|J_{SS'}|$ with the interatomic distance r_0 and with the magnetic field angle θ, for states $|S\rangle = |60S_{1/2}, m_J = 1/2\rangle$ and $|S'\rangle = |61S_{1/2}, m_J = 1/2\rangle$. (a) Interaction strength as a function of r_0 for a fixed angle $\theta = 90°$. The solid red line shows the calculated values using PairInteraction, and the dotted and dashed black lines are power-law fits by respectively $1/r_0^6$ and $1/r_0^3$. (b) Interaction strength as a function of θ for a fixed distance $r_0 = 9.9$ μm. Inset: same measurement, represented in polar coordinates.

3.4 Focus on spin-motion coupling

In the previous sections, I used a simplified model to describe the atomic motion, where I neglected the quantum fluctuations of the external degrees of freedom (position and velocity) and replaced them by thermal fluctuations. This classical treatment of the motion prevents the possibility of entanglement between internal and external degrees of freedom, a phenomenon known as *spin-motion coupling* in the literature (Méhaignerie et al., 2023; Bharti et al., 2024; Meng, 2020). In this section, I question this approximation and study the effect of positional disorder from a full quantum point of view. I mainly ask two questions: first, when does the approximation of independent internal and external degrees of freedom fail? Second, how does the dipole-dipole interaction affect the atomic position?

To answer those questions, I will first present a theoretical framework for treating two interacting atoms, allowing for entanglement between internal and external degrees of freedom. This translates the problem into a set of simple differential equations, that I integrate numerically. This allows me to to compare the results of a spin exchange to the classical model, and to predict the effect of the dipole-dipole interaction, when

seen as a force that acts on the atomic position.

This section does not include any experimental data. Experimental signatures of spin-motion coupling with Rydberg atoms are not numerous; a noteworthy work can be found in Bharti et al. (2024). A detailed theoretical study of spin-motion coupling was also done in Méhaignerie et al. (2023), in the case of trapped atoms.

Two interacting atoms with a quantum description of the motion In the following, I will consider a simplified problem where motion is restricted to one dimension labeled by x, and the internal degrees of freedom are restricted to two levels $|\uparrow\rangle$ and $|\downarrow\rangle$. For one atom, we need two external wavefunctions to describe the atomic motion, one per internal degree of freedom. Formally, the state of the atom can be written

$$|\psi_{1\text{ atom}}\rangle \equiv |\varphi_\uparrow\rangle \otimes |\uparrow\rangle + |\varphi_\downarrow\rangle \otimes |\downarrow\rangle \tag{3.20}$$

where $\varphi_\uparrow(x) \equiv \langle x|\varphi_\uparrow\rangle$ and $\varphi_\downarrow(x) \equiv \langle x|\varphi_\downarrow\rangle$ are spatial distributions that satisfy the normalization condition: $\int dx\,(|\varphi_\uparrow(x)|^2 + |\varphi_\downarrow(x)|^2) = 1$. The internal and external degrees of freedom are said to be separable, if the distributions $|\varphi_\uparrow\rangle$ and $|\varphi_\downarrow\rangle$ are proportional to each other, in which case the external degrees of freedom can be factorized in Eq. (3.20).

For two atoms, we use the same description, except that there are now four possible internal states: $|\uparrow,\uparrow\rangle$, $|\uparrow,\downarrow\rangle$, $|\downarrow,\uparrow\rangle$ and $|\downarrow,\downarrow\rangle$. Each internal state $|k,k'\rangle$ is associated to a spatial wavefunction for atom 1, $\left|\varphi^{(1)}_{k,k'}\right\rangle$, and a spatial wavefunction for atom 2, $\left|\varphi^{(2)}_{k,k'}\right\rangle$. A general expression for the two-atom state is thus

$$|\psi_{2\text{ atoms}}\rangle \equiv \sum_{(k,k')\in\{\uparrow,\downarrow\}^2} \left|\varphi^{(1)}_{k,k'}, \varphi^{(2)}_{k,k'}\right\rangle \otimes |k,k'\rangle\,. \tag{3.21}$$

We define x_j the position operator associated to atom j, $p_j \equiv -i\hbar\frac{\partial}{\partial x_j}$ its momentum operator and m its mass. For a system of two untrapped atoms interacting under the dipole-dipole interaction, the Hamiltonian is given by

$$H = \frac{p_1^2}{2m} + \frac{p_2^2}{2m} + H^{\text{eff}}(x_2 - x_1), \tag{3.22}$$

where $\frac{p_j^2}{2m}$ is the kinetic energy of atom j and H^{eff} is the effective Hamiltonian for the internal degrees of freedom, including the effects of the dipole-dipole interaction. Let

us be reminded its expression in the basis $\{|\uparrow,\uparrow\rangle, |\uparrow,\downarrow\rangle, |\downarrow,\uparrow\rangle, |\downarrow,\downarrow\rangle\}$:

$$H^{\text{eff}}(r) = \hbar \begin{bmatrix} V_{\uparrow\uparrow}(r) & 0 & 0 & 0 \\ 0 & V_{\uparrow\downarrow}(r) & J_{\uparrow\downarrow}(r) & 0 \\ 0 & J_{\uparrow\downarrow}(r) & V_{\uparrow\downarrow}(r) & 0 \\ 0 & 0 & 0 & V_{\downarrow\downarrow}(r) \end{bmatrix} \tag{3.23}$$

where $r \equiv x_2 - x_1$ is the interatomic distance. This two-body problem can be simplified using the well-known change of variables:

$$\begin{cases} x_1 \\ x_2 \\ p_1 \\ p_2 \end{cases} \longmapsto \begin{cases} x_{\text{cm}} & \equiv & \frac{1}{2}(x_1 + x_2) & \text{(position of center of mass)} \\ r & = & x_2 - x_1 & \text{(interatomic distance)} \\ p_{\text{cm}} & \equiv & p_1 + p_2 & \text{(momentum of center of mass)} \\ p & \equiv & \dfrac{p_2 - p_1}{2} & \text{(momentum of a virtual particle)} \end{cases} \tag{3.24}$$

After this transformation, the two-body Hamiltonian given by Eq. (3.22) becomes the sum of two independent one-body Hamiltonians:

$$H = H_{\text{cm}} + H_{\text{rel}} \quad \text{with} \quad \begin{cases} H_{\text{cm}} & \equiv & \dfrac{p_{\text{cm}}^2}{4m} \\ H_{\text{rel}} & \equiv & \dfrac{p^2}{2\mu} + H^{\text{eff}}(r). \end{cases} \tag{3.25}$$

The first term, H_{cm}, describes the free motion of the center of mass (with mass $2m$). The second term corresponds to a virtual particle at effective position r and with an effective mass $\mu \equiv \frac{m}{2}$. In the following, we will call this particle the *relative particle*. Thanks to this simplification, the motional part of the two-atom state can be written as a separable state for the center of mass and the relative particle:

$$|\psi_{2\text{ atoms}}\rangle = |\psi_{\text{cm}}\rangle \otimes |\psi_{\text{rel}}\rangle \quad \text{with} \quad |\psi_{\text{rel}}\rangle \equiv \sum_{(k,k')\in\{\uparrow,\downarrow\}^2} |\varphi_{k,k'}\rangle \otimes |k,k'\rangle\,. \tag{3.26}$$

Here, each motional state $|\varphi_{k,k'}\rangle$ can be interpreted as the spatial wavefunction of the virtual particle in the internal state $|k,k'\rangle$. They satisfy the normalization condition $\sum_{k,k'} \int dr |\varphi_{k,k'}(r)|^2 = 1$.

Quantum equations of motion We now forget about the center of mass, whose motion is a free flight, and we want to solve the time-dependent Schrödinger equation

for the relative particle:

$$i\hbar\frac{\partial\left|\psi_{\mathrm{rel}}\right\rangle}{\partial t}=H_{\mathrm{rel}}\left|\psi_{\mathrm{rel}}\right\rangle. \tag{3.27}$$

To do that, let us express $H^{\mathrm{eff}}(r)$ in its eigenbasis $\{|\uparrow,\uparrow\rangle,|+\rangle,|-\rangle,|\downarrow,\downarrow\rangle\}$ with $|\pm\rangle\equiv\frac{1}{\sqrt{2}}\left(|\uparrow,\downarrow\rangle\pm|\uparrow,\downarrow\rangle\right)$:

$$H^{\mathrm{eff}}(r)=\hbar\begin{bmatrix}V_{\uparrow\uparrow}(r) & 0 & 0 & 0\\ 0 & J_{\uparrow\downarrow}(r)+V_{\uparrow\downarrow}(r) & 0 & 0\\ 0 & 0 & -J_{\uparrow\downarrow}(r)+V_{\uparrow\downarrow}(r) & 0\\ 0 & 0 & 0 & V_{\downarrow\downarrow}(r)\end{bmatrix}. \tag{3.28}$$

In this new basis of internal states, Eq. (3.27) is equivalent to a set of four independent differential equations, one for each wavefunction associated to an internal eigenstate:

$$\begin{cases}\dfrac{\partial\varphi_{\uparrow,\uparrow}}{\partial t} &= \dfrac{i\hbar}{2\mu}\dfrac{\partial^2\varphi_{\uparrow,\uparrow}}{\partial r^2} & -iV_{\uparrow,\uparrow}(r)\varphi_{\uparrow,\uparrow}\\ \dfrac{\partial\varphi_{+}}{\partial t} &= \dfrac{i\hbar}{2\mu}\dfrac{\partial^2\varphi_{+}}{\partial r^2} & -i\left[J_{\uparrow\downarrow}(r)+V_{\uparrow\downarrow}(r)\right]\varphi_{+}\\ \dfrac{\partial\varphi_{-}}{\partial t} &= \dfrac{i\hbar}{2\mu}\dfrac{\partial^2\varphi_{-}}{\partial r^2} & -i\left[-J_{\uparrow\downarrow}(r)+V_{\uparrow\downarrow}(r)\right]\varphi_{-}\\ \dfrac{\partial\varphi_{\downarrow,\downarrow}}{\partial t} &= \dfrac{i\hbar}{2\mu}\dfrac{\partial^2\varphi_{\downarrow,\downarrow}}{\partial r^2} & -iV_{\downarrow,\downarrow}(r)\varphi_{\downarrow,\downarrow}\end{cases} \tag{3.29}$$

where $\varphi_{\pm}\equiv\frac{1}{\sqrt{2}}\left(\varphi_{\uparrow,\downarrow}\pm\varphi_{\downarrow,\uparrow}\right)$. What is new compared to the previous part is the second-order derivative with respect to r; if one forgets the spatial dependence of the wavefunctions and replace them by simple coefficients, those derivatives vanish and the system of equations simply describes the dynamics as a phase accumulation on the coefficients associated to each eigenstate. In the presence the spatial derivative, the effect of the interaction energies is not only a phase accumulation, but also a force that acts on the relative wavefunction. The potential energy acting on an eigenstate is simply given by the associated eigenenergy. The resulting force can be either attractive or repulsive, depending on the sign of the eigenenergy.

Effect of spin-motion coupling: splitting of the wavepacket To illustrate the effects of the dipole-dipole interaction on the spatial wavefunction, I perform numerical simulations of Eq. (3.29), in the same regime as the experimental data shown in sec. 3.2 where the first-order dipole-dipole coupling $J_{\uparrow\downarrow}$ dominates. The relevant interaction

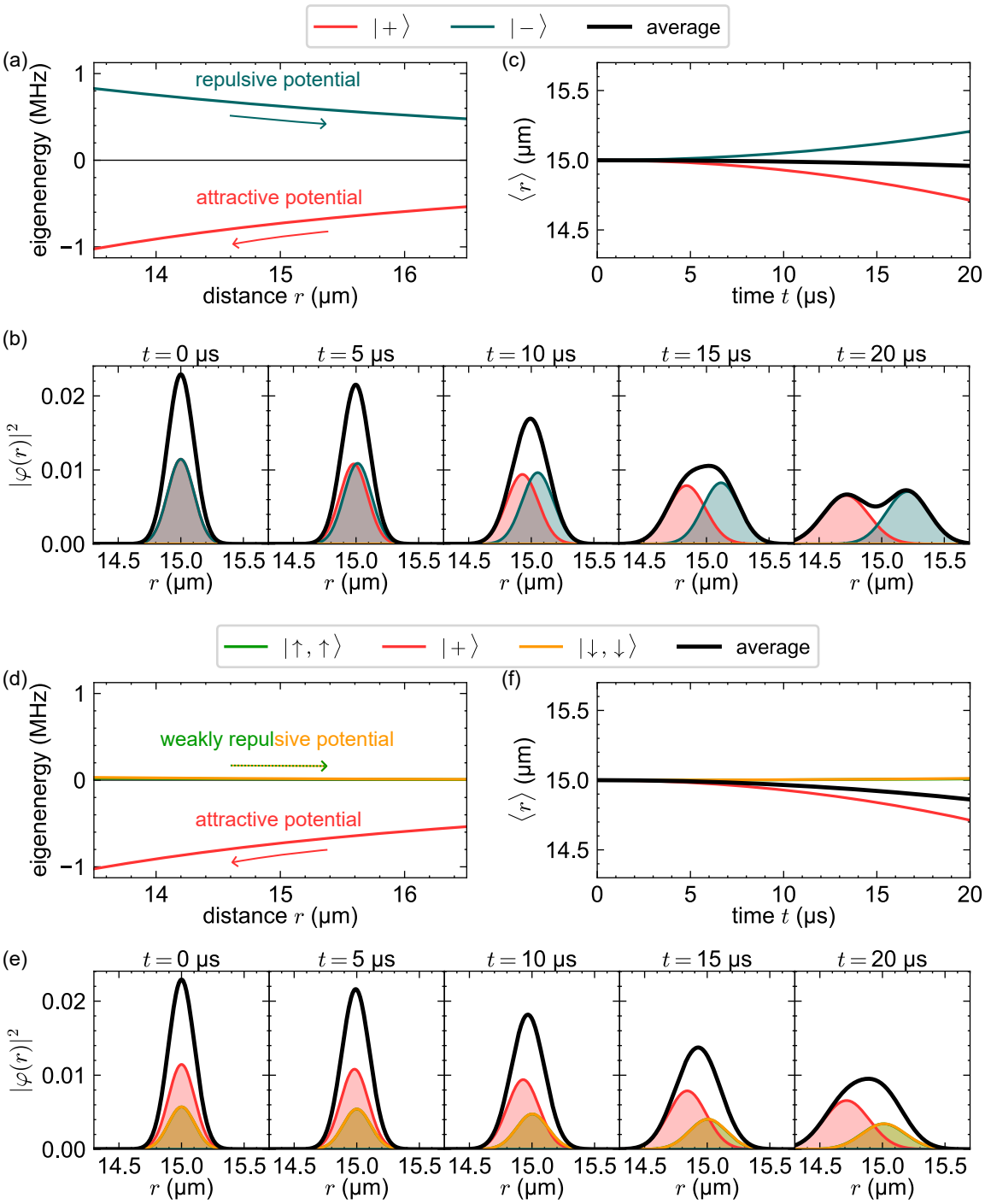

Figure 3.14: Wavepacket splitting due to spin-motion coupling, with the same interaction parameters as in sec. 3.2. (a) Relevant energies of the populated eigenstates $|+\rangle$ and $|-\rangle$ in a spin-exchange sequence. (b) Simulated time evolution of the wavefunctions in each eigenstate. The simulation consists of the integration of Eq. (3.29) starting from the relative state $|\psi_{\mathrm{rel}}\rangle\,(t=0) = |\varphi_0\rangle \otimes |\uparrow,\downarrow\rangle$ where $\varphi_0(r)$ is a Gaussian centered at $\langle r\rangle(t=0) = 15$ μm, with standard deviation $\sigma_r = 100$ nm. The total wavefunction is shown with a solid black line. (c) Evolution of the average distance in $|+\rangle$, in $|-\rangle$ and in the full state during the spin exchange. (d,e,f) Same as (a,b,c) for the initial state $|\psi_{\mathrm{rel}}\rangle\,(t=0) = |\varphi_0\rangle \otimes |{\rightarrow},{\rightarrow}\rangle$, which is a superposition of $|+\rangle$, $|\uparrow,\uparrow\rangle$ and $|\downarrow,\downarrow\rangle$.

energies are shown in Fig. 3.14(a).

The simulation starts from a simple product state, where internal and external degrees of freedom are separated: $|\psi_{\mathrm{rel}}\rangle\,(t=0) = |\varphi_0\rangle \otimes |\uparrow,\downarrow\rangle$. The initial motional state $\varphi_0(r)$ is a Gaussian centered at $\langle r\rangle(t=0) = 15$ µm, with standard deviation $\sigma_r = 100$ nm; since it is a pure state, it amounts to considering only quantum fluctuations of the interatomic distances and to neglecting the thermal fluctuations.

The time evolution of the wavefunction of each eigenstate is shown in Fig. 3.14(b). At times $t > 10$ µs, a clear dissociation of the wavefunction is visible: the atomic wavefunction associated to $|+\rangle$ is attracted towards smaller distances $r < 15$ µm, whereas the one associated to $|-\rangle$ is repelled towards larger distances $r > 15$ µm. The average distance between the two wavepackets reaches 0.5 µm after 20 µs [Fig. 3.14(c)]; at this time, the total wavefunction shows a clear bimodal distribution, similarly to the Stern-Gerlach experiment (Gerlach and Stern, 1922).

I can perform the same simulation starting from the initial state of a Ramsey-experiment: $|\psi_{\mathrm{rel}}\rangle\,(t=0) = |\varphi_0\rangle \otimes |\rightarrow,\rightarrow\rangle$, which is a superposition of $|+\rangle$, $|\uparrow,\uparrow\rangle$ and $|\downarrow,\downarrow\rangle$. In the considered regime of parameters, only the wavepacket associated to $|+\rangle$ is visibly translated due ot the dipole-dipole interaction, because the van der Waals repulsion on $|\uparrow,\uparrow\rangle$ and $|\downarrow,\downarrow\rangle$ is weak [Fig. 3.14(d,e,f)].

Does it affect the measured population in the internal states? The remaining question we want to answer is whether spin-motion coupling affects the population in the internal states, such as measured in sec. 3.2. To do so, I plot in Fig. 3.15(a) the populations in the measurement basis $\{|\uparrow,\uparrow\rangle, |\uparrow,\downarrow\rangle, |\downarrow,\uparrow\rangle, |\downarrow,\downarrow\rangle\}$ in two situations:

- pure quantum fluctuations with the dipole-dipole force [simulation of Eq. (3.29)];
- pure thermal fluctuations without the dipole dipole force [Monte-Carlo simulation such as described in sec. 3.2, assuming that the atoms are in free flight].

The populations in $|\uparrow,\downarrow\rangle$ and $|\downarrow,\uparrow\rangle$ show exactly the same damping in the two situations. In both cases, the damping comes from the average between many oscillations with fluctuating frequencies. However, their physical origin is very different: in the thermal case, the motional state is a shot-to-shot, statistical mixture of classical trajectories, each one having a different interaction energy; whereas in the quantum case, each wavepacket oscillates in space due to the dispersion of interaction energies [Fig. 3.15(b)]. Fundamentally, the reason why a coherent superposition of positions does not differ from a statistical mixture is that the wavepackets associated to the eigenstates are

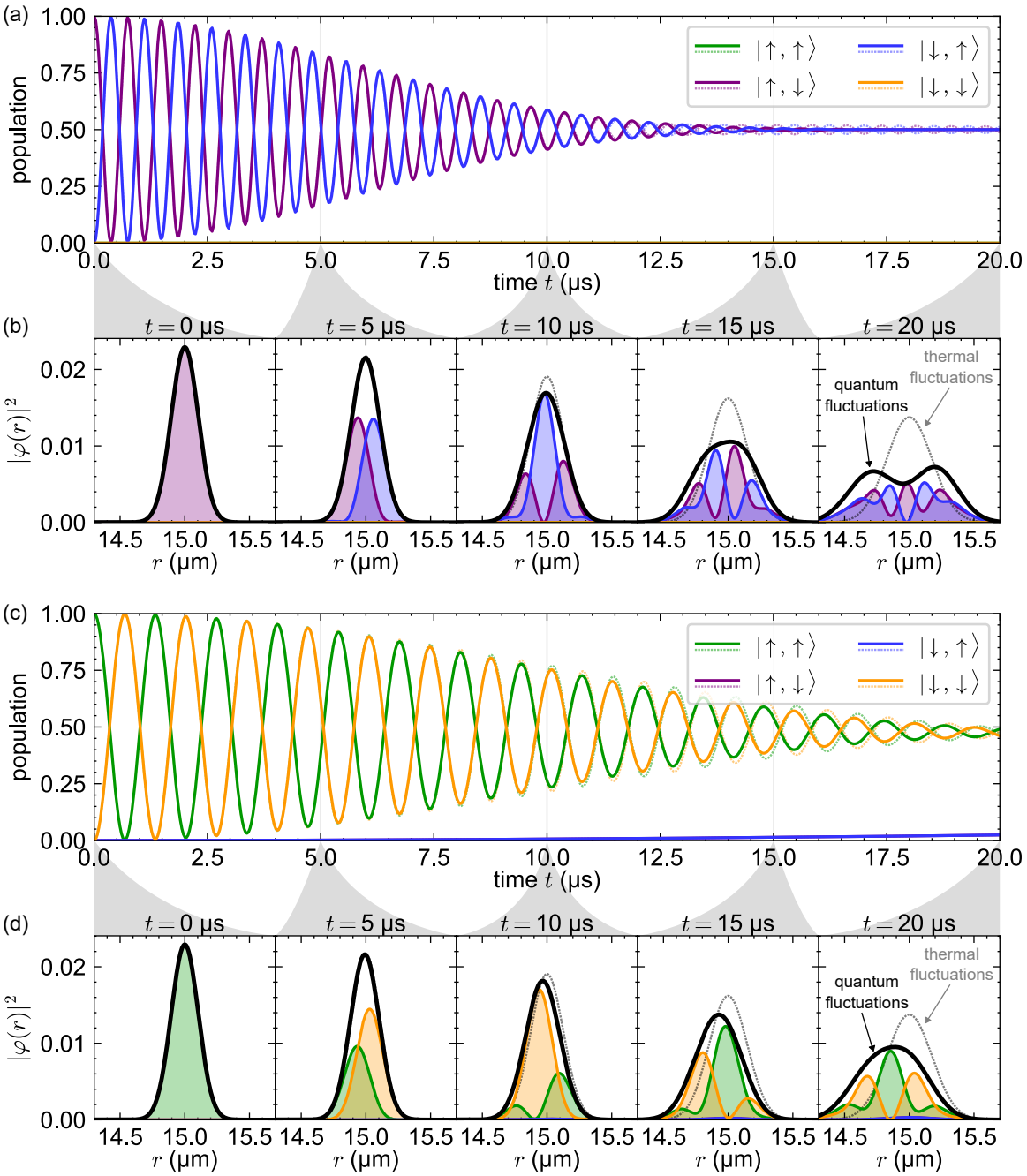

Figure 3.15: Effect of quantum and thermal fluctuations on the population of the internal states. (a) Time-evolution of the population in the four possible internal states in a spin-exchange experiment, with position fluctuations as the only source of imperfections [same parameters as in Fig. 3.14(a,b,c)]. Solid lines are simulated assuming only quantum fluctuations, whereas dotted lines assume only incoherent thermal fluctuations. (b) Evolution of the wavepacket in the measurement basis, according to the quantum evolution (solid lines) or the thermal evolution (dotted line). This is the same plot as in Fig. 3.14(b), but this time in the measurement basis. Each part of the wavefunctions oscillate at their own frequency in time, leading to spatial oscillations for each wavefunction, that explain the damping of the populations in (a). (c,d) Same as (a,b), for a Ramsey sequence [same parameters as in Fig. 3.14(d,e,f)].

mutually orthogonal, so there is no possible interference between them. Experimentally, we probably have both quantum and quantum fluctuations [see chapter 1].

I conclude that in the considered regime of parameters, the measurement of the internal states alone does not allow to distinguish between thermal and quantum fluctuations of motion, nor to reveal the effect of spin-motion coupling. However, observing the entanglement between external and internal degrees of freedom might be doable if the experiment has enough resolution to measure the displacement of the wavepacket associated to each eigenstate. From a pragmatic point of view, this validates the thermal simulations performed in sec. 3.2. I obtain the same conclusions in the case of the two-atom Ramsey.

What about trapped atoms? The previous equations can be easily adapted to take into account the effect of a trapping potential. If the first atom is trapped by a harmonic potential centered at $-\frac{r_0}{2}$, $\frac{1}{2}m\omega^2\left(x_1+\frac{r_0}{2}\right)^2$ and the second atom by the same potential centered at $\frac{r_0}{2}$, $\frac{1}{2}m\omega^2\left(x_2-\frac{r_0}{2}\right)^2$, the resulting trapping potential in the relative system of coordinates is $m\omega^2 x_{\mathrm{cm}}^2+\frac{1}{2}\mu\omega^2\left(r-r_0\right)^2$. This situation was carefully studied in Méhaignerie et al. (2023) in the case of circular Rydberg atoms. Several regimes were identified, from a low-damping regime with minor effect of the motion, to full spin-motion entanglement with the realization of cats states.

Take-home message

For two atoms, the spin-motion coupling translates into a state-dependent force that is simply equal to the eigenenergy of the state. Starting from a superposition of eigenstates, the wavepacket associated to each eigenstate evolves according to different equations of motion, leading to entanglement between internal and external degrees of freedom. However, this entanglement cannot be seen from the measurement of the internal degrees of freedom alone. In the regime of experimental parameters studied in this chapter, the wavepacket splitting occurs at sufficiently long times that we can neglect it during the first few microseconds, which is our usual time window for quantum simulation.

Part B:
Preparation and characterization of correlated spin states

Je me rends compte que c'est maintenant, et maintenant seulement, que je commence mon histoire. Les pages que je viens d'écrire n'auront servi qu'à préciser les conditions requises par le hasard ou le destin pour que se produise l'événement incroyable.

Jorge Luis Borges, *Le Livre de sable*

Chapter 4

Adiabatic preparation of ordered spin states of the XY model

> Order leads to all virtues, but what leads to order?
>
> Georg Christoph Lichtenberg, *Scrapbooks*

This chapter tackles the question of low-energy, equilibrium states of spin lattices interacting under the dipolar XY model:

$$H_{\mathrm{XY}} = \frac{\hbar J}{2} \sum_{i<j} \left[\frac{a}{r_{ij}}\right]^3 \left(\sigma_i^x \sigma_j^x + \sigma_i^y \sigma_j^y\right) \tag{4.1}$$

where J is the nearest-neighbor interaction energy, a is the lattice spacing, r_{ij} is the distance between spins i and j, and σ_j^μ is the Pauli matrix acting on spin j in direction μ. Here, the word "dipolar" refers to the $1/r^3$ power-law decay of the interactions.

Several properties of the dipolar XY model make it appealing for an in-depth study. First, quantum fluctuations are believed to play a strong role in its ground state properties, related to the rotational symmetry of H_{XY} called a $U(1)$ symmetry. Those fluctuations make it harder to come up with an exact analytical description of the ground state for a large number of spins. This is in contrast with the well-known Ising model where, in the absence of an external transverse field, the ground state is a simple product state of aligned, or anti-aligned, spins.

Second, the role of the power-law interactions enhances the diversity of the phase diagram (Peter et al., 2012), by breaking the symmetry between the ferromagnetic ground state ($J < 0$) and the antiferromagnetic ground state ($J > 0$). This is in contrast with the nearest-neighbor XY model, where the two ground states on bipartite lattices (linear chain, square array) are related by a sublattice rotation [which will be made explicit in the following].

The questions that we will try to answer are the following: how to use a Rydberg-based quantum simulator to study the low-energy properties of the dipolar XY model? How does the ground state depend on the geometry and on the dimensionality? What is the role played by the dipolar part of the interactions?

As shown in the previous part, the dipolar XY model is the effective Hamiltonian when spin states are mapped to two dipole-coupled Rydberg atoms, for example

$|\uparrow\rangle = |S\rangle$ and $|\downarrow\rangle = |P\rangle$, leading to a first-order resonant dipole interaction between the two-atom states $|S,P\rangle$ and $|P,S\rangle$. The Rydberg levels and the lattice spacing is chosen such that the residual van der Waals terms are negligible compared to $|J|$. We will mainly study two geometries: a two-dimensional square lattice; and a one-dimensional chain with periodic boundary conditions.

Contents

Contributors

This chapter is based on two papers: Chen et al. (2023a) for the two-dimensional square lattice and Emperauger et al. (2025) for the one-dimensional chain.

4.1 Long-range order on a 2D square lattice

In this section, I present our experimental results on the preparation of magnetically-ordered low-energy phases of the XY model on a square lattice with up to 100 spins. Before diving in the details of the preparation method, let us describe more precisely the states that we aim to prepare.

4.1.1 Basic intuitions about the energy spectrum

Symmetries The XY Hamiltonian from Eq. (5.12) is rotationally symmetric around the z-axis, which is equivalent to say that it commutes with the total magnetization along z: $[H_{\mathrm{XY}}, M^z] = 0$ with $M^z \equiv \sum_j \sigma_j^z$. Consequently, there exists a basis of eigenstates that is common to H_{XY} and M^z. Among each manifold with a given value

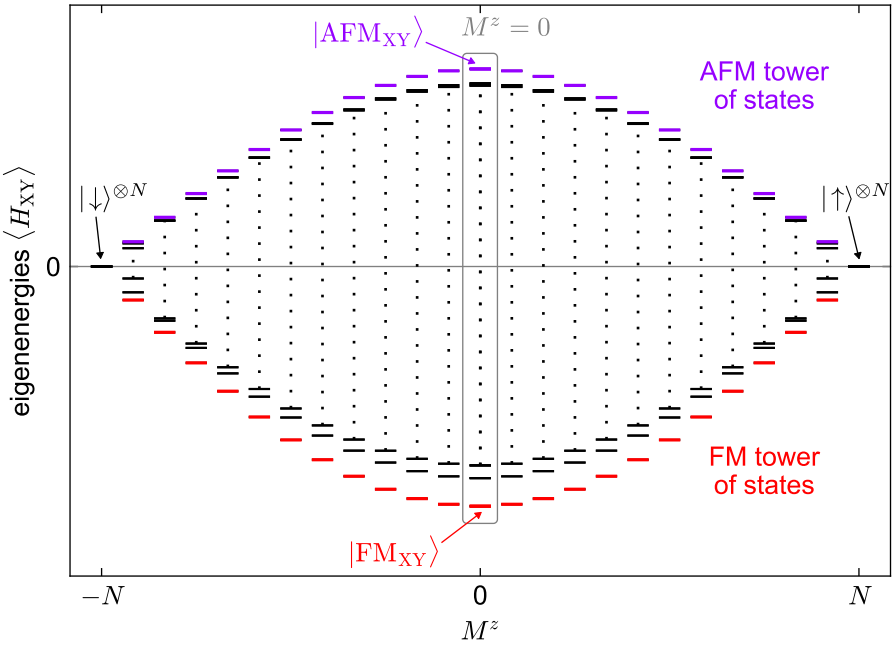

Figure 4.1: Sketch of the energy spectrum of the dipolar XY model. States are split by their z-magnetization M^z, which goes between $-N$ and N, with N the number of atoms. The target states for this chapter are the ground state and highest energy state at $M^z = 0$, which are respectively labeled by $|\mathrm{FM_{XY}}\rangle$ and $|\mathrm{AFM_{XY}}\rangle$.

of M^z, the ground state of H_{XY} for $J < 0$ is a state where spins have a tendency to align in the xy-plane. This can be understood from the fact that the XY energy is the sum of spin-spin correlations in the xy-plane, so it is maximized for large positive correlations. For this reason, we call such a state the ferromagnetic (FM) ground state. On the other side of the spectrum, the highest energy state for $J < 0$ has strong negative correlations in the xy-plane, which correspond to anti-aligned spins: we call it the antiferromagnetic (AFM) ground state. The term "ground state" can be unsettling since it is actually the highest energy state; but it can simply be seen as the ground state of $-H_{\mathrm{XY}}$. The set of FM and AFM ground states of $\pm H_{\mathrm{XY}}$ for each value of M^z are referred to as the *Anderson tower of states* in the literature (Anderson, 1952; Wietek et al., 2017; Tasaki, 2019). A schematic spectrum is shown in Fig. 4.1. Note the symmetry around $M^z = 0$, which is a consequence of the particle-hole symmetry (i.e. exchange between $|\uparrow\rangle$ and $|\downarrow\rangle$).

In this chapter, the states we want to prepare are the ground state and highest energy state at $M^z = 0$, also called half-filling, which are respectively labeled by $|\mathrm{FM_{XY}}\rangle$ and $|\mathrm{AFM_{XY}}\rangle$. Among the tower of states, those are the states where the XY order parameter $\langle H_{\mathrm{XY}}\rangle$ is the strongest.

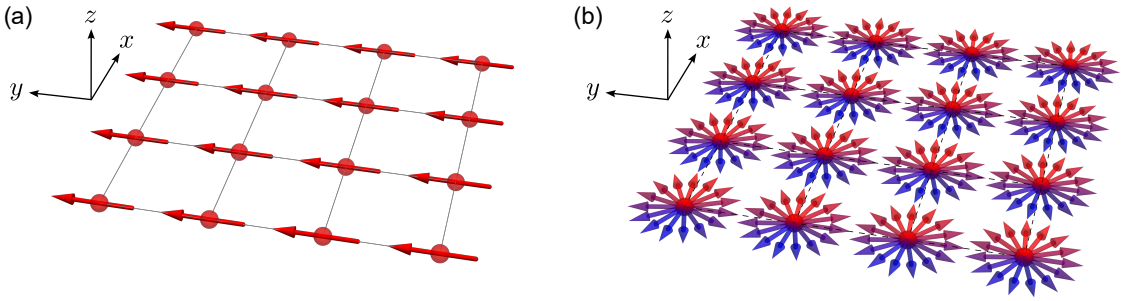

Figure 4.2: Intuitive representation of the FM ground state. (a) A classical ferromagnet along y. (b) Ansatz for the XY FM ground state: the Dicke state $|\mathrm{FM}^{\infty}_{\mathrm{XY}}\rangle$ is the superposition of all classical ferromagnets in the xy-plane.

Comparison with two extreme cases To get some intuition about the energy spectrum of the dipolar XY model, let us allow oneself to vary the range of interactions. Let us define the XY Hamiltonian with interaction range α as

$$H^{\alpha}_{\mathrm{XY}} = \frac{\hbar J}{2} \sum_{i<j} \left[\frac{a}{r_{ij}}\right]^{\alpha} \left(\sigma^x_i \sigma^x_j + \sigma^y_i \sigma^y_j\right) \tag{4.2}$$

In the following, I consider two theoretical regimes of interactions: nearest-neighbor interactions ($\alpha = +\infty$), and all-to-all interactions ($\alpha = 0$). Some of the following analytical results are derived in appendix A.

The FM ground state of the all-to-all XY Hamiltonian is the superposition of all classical ferromagnets in the xy-plane:

$$|\mathrm{FM}^{\infty}_{\mathrm{XY}}\rangle = \frac{2^{N/2}}{2\pi\sqrt{\binom{N}{N/2}}} \int_0^{2\pi} |\mathrm{FM}_{\theta}\rangle \, d\theta. \tag{4.3}$$

Here, we have defined $|\mathrm{FM}_{\theta}\rangle \equiv |{\rightarrow_{\theta}}\rangle^{\otimes N}$ with $|{\rightarrow_{\theta}}\rangle \equiv \frac{1}{\sqrt{2}}\left(e^{-i\frac{\theta}{2}}|{\uparrow}\rangle + e^{i\frac{\theta}{2}}|{\downarrow}\rangle\right)$. The state $|\mathrm{FM}_{\theta}\rangle$ is the product state of all spins pointing along a direction $\mathbf{u} = \cos(\theta)\mathbf{e}_x + \sin(\theta)\mathbf{e}_y$. Of course, we do not expect this state to be also the ground state of the dipolar XY model, but in the absence of analytical expression for the ground state, it can be used as an ansatz. $|\mathrm{FM}^{\infty}_{\mathrm{XY}}\rangle$ is characterized by a *long range order* (LRO) in the xy plane, in the sense that spin-spin correlations do not decay to zero even at large distances (Tasaki, 2019). In the particular case of $|\mathrm{FM}^{\infty}_{\mathrm{XY}}\rangle$, the correlations between two spins do not even depend on their distance (appendix A).

Is there a similar picture for the AFM ground state? The AFM ground state of the all-to-all Hamiltonian is a highly-degenerate manifold of valence-bond solids (appendix A); but it is less relevant for the comparison with the actual ground state

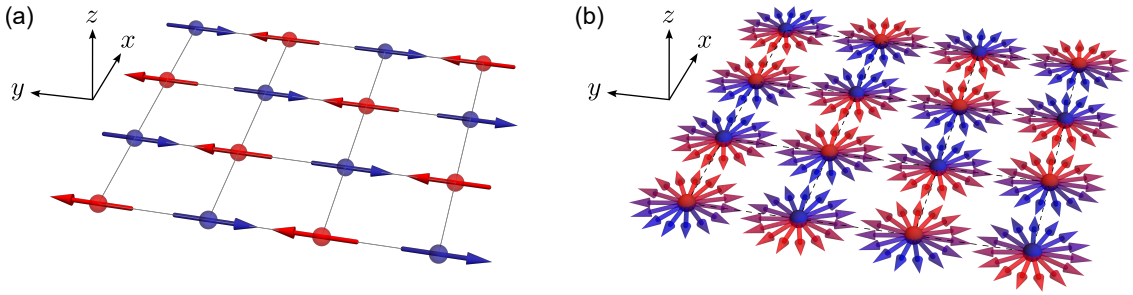

Figure 4.3: Intuitive representation of the AFM ground state. (a) A classical antiferromagnet along y. (b) Ansatz for the XY AFM ground state: a the superposition of all classical antiferromagnets in the xy-plane.

on the square lattice. To get an intuition of how the AFM ground state relates to the FM ground state, it is useful to consider the XY model with nearest neighbor interactions. In this case, the FM and AFM ground states on the square lattice are related by a simple sublattice rotation

$$R \equiv \bigotimes_{j\in B} e^{-i\frac{\pi}{2}\sigma_j^z} \tag{4.4}$$

where we have split the spins into two sublattices A and B that form a checkerboard pattern, such that each spin in sublattice A has only nearest neighbors in sublattice B. Assuming that the FM ansatz of Eq. (4.3) still holds, this gives us the following ansatz for the AFM ground state:

$$\begin{aligned} |\mathrm{AFM}_{\mathrm{XY}}\rangle &\sim R\,|\mathrm{FM}^{\infty}_{\mathrm{XY}}\rangle \\ &= \frac{2^{N/2}}{2\pi\sqrt{\binom{N}{N/2}}}\int_0^{2\pi} |\mathrm{AFM}_\theta\rangle\, d\theta \end{aligned} \tag{4.5}$$

with $|\mathrm{AFM}_\theta\rangle \equiv \bigotimes_{j\in A} |{\rightarrow_\theta}\rangle_j \bigotimes_{j'\in B} |{\leftarrow_\theta}\rangle_{j'}$.

With nearest-neighbor interactions, both FM and AFM ground states are long-range-ordered. But in the thermodynamic limit, this order is sufficiently fragile to be destroyed for at any finite temperature, according to the Mermin-Wagner theorem (Mermin and Wagner, 1966; Bruno, 2001).

The dipolar XY model lies in between those two extreme ranges of interactions. Its theoretical study is rather recent, and started with the development of experimental systems that can implement it (dipolar gases, Rydberg atoms, dipolar molecules...). In the FM case, next-nearest neighbor interactions tend to favor the alignment of spins located at larger distances, leading to a stronger FM order than with nearest-neighbor.

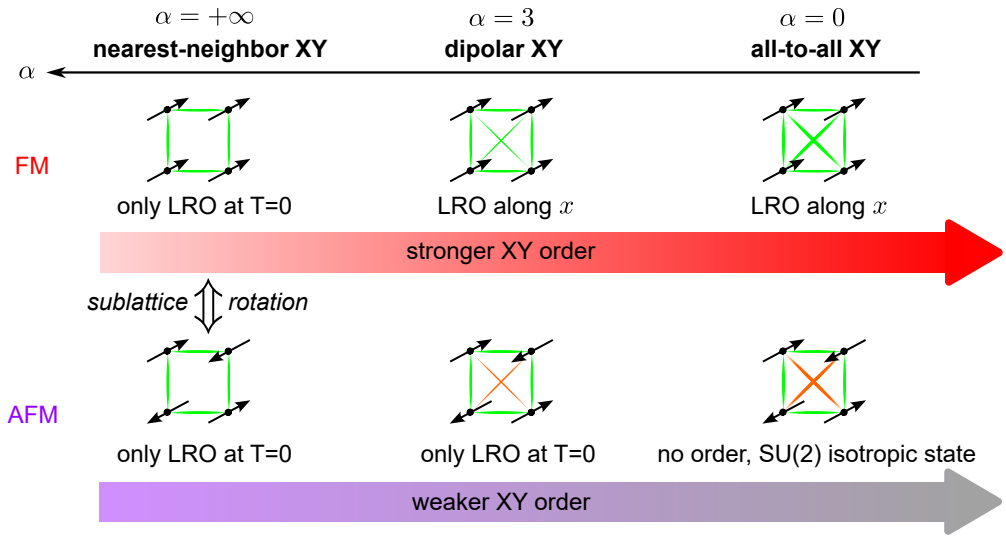

Figure 4.4: Role of long-range XY interactions. The horizontal axis represents the range of interactions, denoted by α, such that the XY coupling varies with distance as $1/r^\alpha$. Spins are represented by black arrows that point along an arbitrary direction in the xy-plane. The green (resp. orange) links between the spins indicate energetically satisfied (resp. unsatisfied) bonds. Some of the properties from this figure are derived in appendix A, for $\alpha = +\infty$ and $\alpha = 0$.

Using linear spin-wave theory, Peter et al. (2012) predicted that the FM ground state of the dipolar XY model is long-range ordered even at finite temperatures, below a critical temperature T_c. The value of T_c was numerically calculated in Sbierski et al. (2024).

In the AFM case, the effect of long-range couplings is quite the opposite. Any antiferromagnetic configuration of spins in the xy-plane contains pairs that are aligned (for example, the pairs located on the diagonal of a square). With nearest-neighbor couplings, those pairs are not coupled so it has no impact on the order. However, long-range interactions increase the energy of the aligned bonds, weakening the AFM ordering – a phenomenon known as *geometrical frustration* (Lhuillier and Misguich, 2001). Frustration reaches its peak for all-to-all interactions, where the AFM order is lost, the ground state being a macroscopic degeneracy of valence-bond solids.

4.1.2 Adiabatic protocol with staggered lightshifts

Experimental protocol We use the spin mapping explained in chapter 3 to implement the dipolar XY Hamiltonian of Eq. (5.12): we choose $|\uparrow\rangle \equiv \left|60S_{1/2}, m_J = 1/2\right\rangle$ and $|\downarrow\rangle \equiv \left|60P_{1/2}, m_J = -1/2\right\rangle$ which give nearest-neighbor interaction energy $J =$

$-2\pi\times0.77$ MHz at lattice spacing $a = 12.1$ µm and with a magnetic field $B \approx 45$ G[1]. To prepare the XY FM and AFM ground states, we add an ingredient to the Hamiltonian: we apply local lightshifts on level $|\uparrow\rangle$ of half the array with a checkerboard geometry, using the addressing laser off-resonant with the transition $6P_{3/2} \leftrightarrow |\uparrow\rangle$ (see chapter 2). If we denote by B the sublattice of addressed atoms, the resulting Hamiltonian is

$$H_{\mathrm{Z}}(\delta) \equiv \hbar\delta \sum_{j\in B} \frac{1+\sigma_j^z}{2}, \tag{4.6}$$

and the total Hamiltonian is simply the sum of the XY part and the addressing part:

$$H_{\mathrm{tot}}(\delta) \equiv H_{\mathrm{XY}} + H_{\mathrm{Z}}(\delta). \tag{4.7}$$

Those two ingredients are illustrated on Fig. 4.5(a,b). We make use of the fact that the ground state of H_{Z} in the manifold of $M^z = 0$, for $\delta > 0$, is a simple product state of staggered spins, that we call a *Néel state*:

$$|\psi_{\mathrm{Néel}}\rangle \equiv \bigotimes_{j\in A} |\uparrow\rangle_j \bigotimes_{j'\in B} |\downarrow\rangle_{j'}\,. \tag{4.8}$$

As a result, $|\psi_{\mathrm{Néel}}\rangle$ is also the ground state of H_{tot} in the limit $\delta \gg |J|$, since $H_{\mathrm{tot}}(\delta \gg |J|) \approx H_{\mathrm{Z}}$. Looking at the spectrum of H_{tot} as a function of δ, we observe that $|\psi_{\mathrm{Néel}}\rangle$ is continuously connected to the ground state of $H_{\mathrm{XY}} = H_{\mathrm{tot}}(\delta = 0)$ [Fig. 4.5(c)]. A natural protocol for preparing $|\mathrm{FM}_{\mathrm{XY}}\rangle$ is thus the following:

1. Prepare the state $|\psi_{\mathrm{Néel}}\rangle$ in the presence of a strong lightshift $\delta_0 \gg |J|$, to be in the ground state of $H_{\mathrm{tot}}(\delta_0) \approx H_{\mathrm{Z}}$.

2. Adiabatically ramp down δ from δ_0 to 0.

3. Measure the obtained state in z- or x-basis.

The experimental sequence for applying this protocol is shown on Fig. 4.5(d). We use an exponential shape for the ramp: $\delta(t) = \delta_0 e^{-t/\tau}$ with $|\delta_0|/2\pi > 10$ MHz and $\tau = 0.3$ µs.

Remarkably, this protocol can be easily adapted to prepare $|\mathrm{AFM}_{\mathrm{XY}}\rangle$, which is the highest energy state of H_{XY}. To do that, we can simply invert the sign of the lightshift

[1] With the conventions used in chapter 3, this corresponds to $J_\perp = 2J = -2\pi \times 1.54$ MHz. The residual van der Waals interactions lead to $J_z = 2\pi \times 11$ kHz which is less than one percent of $J_\perp$.

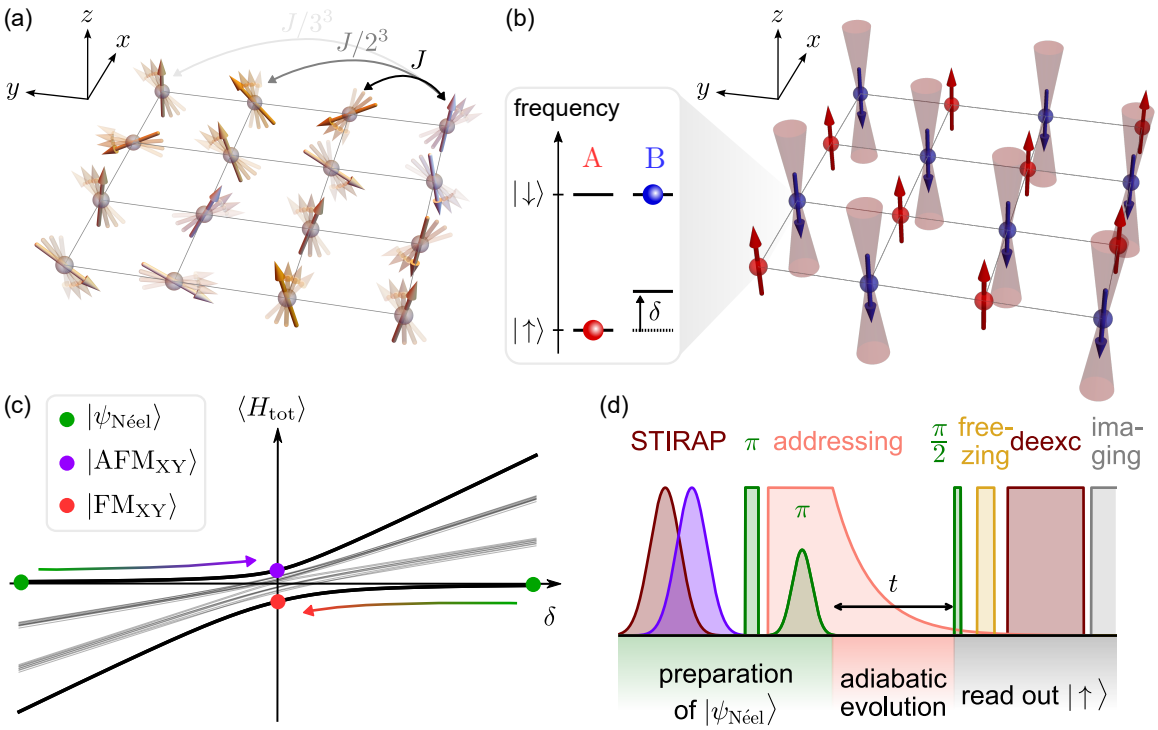

Figure 4.5: Method for adiabatic preparation of the XY FM and AFM ground states using staggered lightshifts. The total Hamiltonian H_{tot} is composed of two ingredients: the dipolar XY interactions, pictured in (a) on a 4×4 square lattice, and a set of addressing beams (b) which exert local lightshifts δ on atoms from sublattice B. The ground state of the addressing Hamiltonian in the $M_z = 0$ manifold, for $\delta > 0$, is the Néel state $|\psi_{\text{Néel}}\rangle$ represented here by the colored arrows. (c) Sketch of the energy spectrum of $H_{\text{tot}}(\delta)$ for $J < 0$ in the $M_z = 0$ manifold (simulated by Lucas Leclerc on a 2×3 system). The ground state of H_{tot} continuously connects $|\psi_{\text{Néel}}\rangle$ (for $\delta \gg |J|$) to the FM ground state $|\text{FM}_{\text{XY}}\rangle$ (at $\delta = 0$). Similarly, a path connects $|\psi_{\text{Néel}}\rangle$ at large negative δ to the AFM ground state $|\text{AFM}_{\text{XY}}\rangle$. (d) Experimental sequence for preparing $|\text{FM}_{\text{XY}}\rangle$ and $|\text{AFM}_{\text{XY}}\rangle$. First, we prepare $|\psi_{\text{Néel}}\rangle$ using local rotations (for this sequence, the second π-pulse was actually a microwave sweep); second, we ramp down δ adiabatically; finally, we read out the state by imaging the atoms in level $|\uparrow\rangle$. During the read-out, an optional $\pi/2$ microwave pulse is used to measure in the x- or y-basis of the spins.

δ, so that $|\psi_{\text{Néel}}\rangle$ is now the highest energy state of H_{tot} for large negative δ[2]. This is achieved by changing the sign of the detuning of the addressing laser.

Building up some intuition on a small system size As a start, we apply the above protocol on a $N = 2 \times 2$ plaquette. This small system size allows us to perform numerical simulations of the dynamics (Leclerc, 2024) taking into account several

[2] An equivalent solution would have been to keep $\delta > 0$, but change the initial state to the symmetric Néel state, where atoms from sublattice B are in $|\uparrow\rangle$ and atoms from A are in $|\downarrow\rangle$. However, this would require the addressed atoms to be initialized in the level which is lightshifted, leading to fast depumping by the addressing (see section 2.2 of chapter 2) and thus creating decoherence.

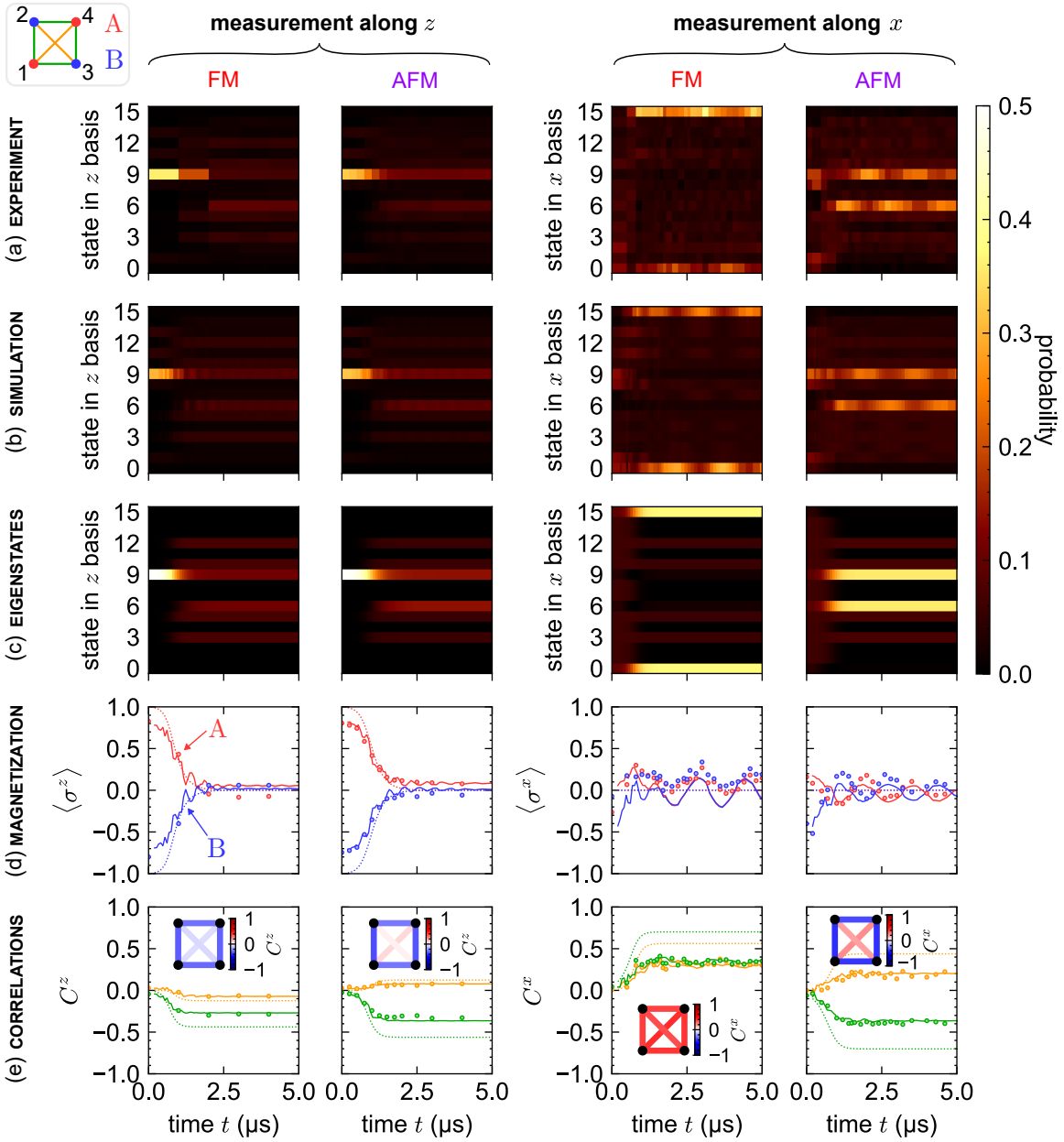

Figure 4.6: Benchmark of the adiabatic preparation protocol on a 2×2 square. The geometry and labelling of the spins is shown on the top-left inset. We use the sequence shown in Fig. 4.5(d) with an initial lightshift $|\delta_0|/2\pi = 15$ MHz and an exponential decay time $\tau = 0.3$ μs. The four columns represent the two possible states (FM and AFM) along two measurement bases (z and x). (a) Time evolution of the experimentally-measured probability of each many-body state in the measurement basis. The 16 states are ordered in ascending order, as bit strings using the correspondence $0 = |\downarrow\rangle$ and $1 = |\uparrow\rangle$. For example, the initial Néel state $|\uparrow,\downarrow,\downarrow,\uparrow\rangle$ is represented by the bit string 1001 which is the binary representation of 9. The data is compared with numerical simulations of the dynamics explained in Leclerc (2024), which take into account various experimental imperfections (b), and to instantaneous eigenstates of $H_{\text{tot}}[\delta(t)]$ (c). (d) Magnetization averaged over sublattices A and B. Solid lines are the simulations of the dynamics, and dotted lines are the ideal eigenstates. (e) Spin-spin correlations for nearest neighbors (green) and next-nearest neighbors (orange). Insets: representation of the experimental correlations at $t = 2$ μs, where the color codes for the value of the correlation.

experimental imperfections: residual van der Waals interactions, preparation errors, positional disorder and detection errors (see details in chapter 3). The results are gathered in Fig. 4.6, for both FM and AFM cases.

First, let us look at the results in the z-basis (two left columns of the figure). The full information of the measurement outcomes is contained in the *histogram of states*, which is the probability of each of the $2^N = 16$ states of the measurement basis. The resulting dynamics is very similar in the FM and AFM cases. The most probable initial state is the target state $|\psi_{\text{Néel}}\rangle = |\uparrow,\downarrow,\downarrow,\uparrow\rangle$, whose probability decreases in a few µs and melts down over many different states. This dynamics is well reproduced by the simulations of the dynamics with imperfections [Fig. 4.6(b)], and it agrees qualitatively with the exact eigenstates of the target Hamiltonian $H_{\text{tot}}\,[\delta(t)]$ [Fig. 4.6(c)]. Based on the histogram of states, we can compute local observables such as the magnetization $\langle\sigma_j^z\rangle$ of any spin j, which is its mean orientation along z. In Fig. 4.6(d), we show the magnetization averaged over spins from the two sublattices A and B. At $t = 0$ µs, the two sublattices have opposite magnetization, signaling the Néel order along z, and then the two magnetization sectors merge together. Finally, we can have a look at the spin-spin correlations, which tell the tendency of spins to align or anti-align:

$$C_{i,j}^{\mu} \equiv \langle\sigma_i^{\mu}\sigma_j^{\mu}\rangle - \langle\sigma_i^{\mu}\rangle\langle\sigma_j^{\mu}\rangle \tag{4.9}$$

for $\mu \in \{x, y, z\}$. Note that we consider connected correlations, or in other words the covariance of σ_i^{μ} and σ_j^{μ}, where the contribution of the magnetization is subtracted to avoid possible biases due to non-zero magnetization. The correlations start at 0, which signals the fact that the initial state is indeed a non-correlated product state. Then, we distinguish two cases: the nearest-neighbor correlations, which converge to a strong negative value in both FM and AFM cases; and the next-nearest neighbor correlations (along the diagonal of the square) which remain close to zero. In the z basis, the dynamics becomes stationary after ~ 2 µs, when $\delta(t = 2\ \mu\text{s})/J \approx 2$ %.

In the x-basis, the situation is very different. At $t = 0$ µs, the state appears distributed over many states, without any dominant contribution; the magnetization of both sublattices is close to 0 and the correlations as well. This gives the picture of a random disordered configuration along x, whereas the state is ordered along z. As time evolves, two states emerge with a dominant contribution: $|\downarrow,\downarrow,\downarrow,\downarrow\rangle$ and $|\uparrow,\uparrow,\uparrow,\uparrow\rangle$ in the FM case, and $|\downarrow,\uparrow,\uparrow,\downarrow\rangle$ and $|\uparrow,\downarrow,\downarrow,\uparrow\rangle$ in the AFM case. This corresponds to FM (resp. AFM) order along x, and it translates into large positive (resp. staggered) correlations [Fig. 4.6(e)]. Interestingly, although the correlations are stabilized after

~ 2 µs, the state is not perfectly stationary, as we would expect from an ideal adiabatic preparation. There are residual oscillations between the two main states [Fig. 4.6(a)], which are also present in the simulations [Fig. 4.6(b)]. They translate into oscillations of the x-magnetization for both A and B sublattices, that are in phase in the FM case and out of phase in the AFM case. We attribute those errors to preparation errors, which result in an initial state that is not perfectly the ground state of the initial Hamiltonian; starting from a state with finite energy density, even a perfectly adiabatic ramp will lead to a state with residual energy density. More precisely, we identified that the oscillation frequency (~ 0.6 MHz $\sim J/2\pi$) corresponds to the energy difference between the ground state and the first excited states of the $|M_z| = 2$ manifolds [see spectrum in Fig. 5.4(a) of Leclerc (2024)].

Larger system sizes Let us now see what happens for a larger system: a $N = 6 \times 7$ square lattice, with the same adiabatic ramp. As shown in Fig. 4.7(a), the global picture is similar to the previous case. We start from a state which magnetization is ordered along z. This state is close to the ideal Néel state, the finite contrast being due to preparation and detection errors. After correcting the effect of the detection errors, we estimate the probability of successful preparation in the target state to be about 90 % per spin. This gives of course a very low probability of overlap with the target initial state ($0.9^{42} \approx 1$ %) but as we will see, this still allows us to observe the qualitative features of the expected phase.

As δ is ramped down, the Néel order along z melts down. The lightshift at which the crossover happens is larger in the FM than in the AFM case. This is an experimental evidence of the role of the dipolar tail of the interactions, which, contrary to the nearest-neighbor case, creates an asymmetry between the FM and the AFM spectra. This observation is consistent with the theoretical expectation for the critical lightshift δ_c of the crossover, which is marked by vertical dotted lines: $\delta_c^{\mathrm{FM}}/J = 7.1(3)$ in the dipolar FM case and $\delta_c^{\mathrm{AFM}}/J = 0.8(1)$ in the dipolar AFM case, whereas $\delta_c^{\mathrm{NN}}/J = 2.4(1)$ with only nearest-neighbor interactions. Those values are calculated numerically on the finite-size system $N = 42$ [see Chen et al. (2023a) for details]. The critical field of the phase transition in the thermodynamic limit was calculated in Sbierski et al. (2024) using finite-size scaling analysis, and it was found to be $\delta_c^{\mathrm{FM}}/J = 4.03(2)$.

In Fig. 4.7(b), we also monitor the correlations averaged over pairs separated by the

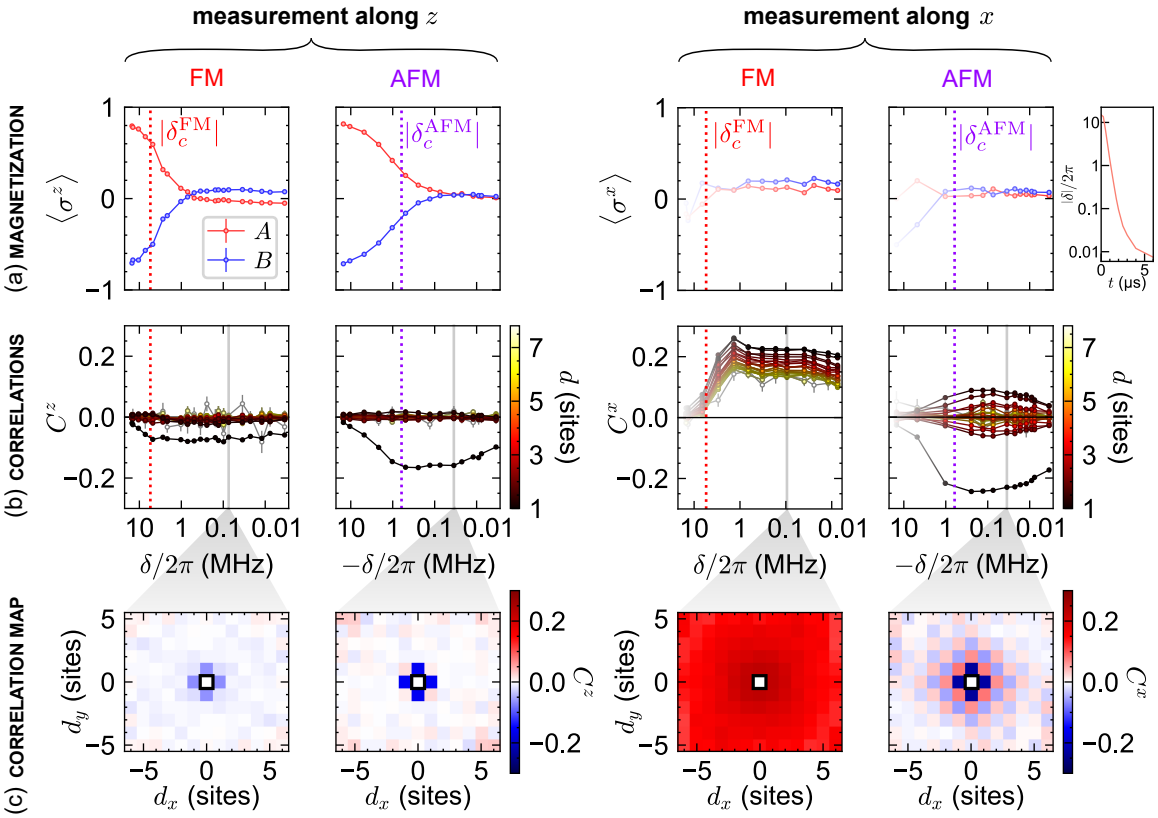

Figure 4.7: Adiabatic preparation of low-energy XY FM and AFM states on a 6×7 square array, with the same parameters as in Fig. 4.6. (a) Magnetization per sublattice as a function of the lightshift $\delta/2\pi$. The vertical dotted line indicates the expected critical lightshift δ_c, which differs in the FM and AFM cases. Along x, the measurement can only be trusted for $\delta \ll \Omega$ with $\Omega/2\pi = 9$ MHz the Rabi frequency of the measurement pulse, we put a white shading to avoid over-interpreting the initial times. Inset on the right: measured lightshift as a function of preparation time t. (b) Correlations as a function of δ. The color indicates the distance between the particles, from dark red (nearest neighbors) to white (furthest pairs along the diagonal of the array). (c) Correlation maps at a given lightshift, corresponding to $t = 2$ μs.

same distance:

$$C^\mu(d) \equiv \frac{1}{N_d} \sum_{\substack{i,j \\ r_{ij}=d}} C^\mu_{i,j} \tag{4.10}$$

where N_d is the number of pairs (i, j) which satisfy $r_{ij} = d$. Along z, nearest-neighbor correlations $C^z(d = 1)$ build up as δ decreases, but correlations for $d \gg 1$ remain close to 0. For a more visual representation, I plot in Fig. 4.7(c) the spatial map of correlations $C^\mu(d_x, d_y)$ averaged over pairs separated by the same distance d_x along x and d_y along y, at a fixed measurement time $t = 2$ μs which corresponds to a lightshift

well below δ_c. this confirms that the prepared state after the adiabatic ramp has short-range correlations along z.

Along x, on the contrary, the magnetization remains around 0 along the whole preparation, and correlations build up for all distances d: in the FM case, correlations are positive for all distances, whereas they are staggered in the AFM case. This is the signature of a strong FM (resp. AFM) order.

Two effects appear in the dynamics, that should not be present in an ideal adiabatic preparation. First, the FM state at the end of the ramp is not perfectly homogeneous: the atoms from sublattice B have a higher magnetization than the ones from sublattice A, in both z and x bases. We identified the origin of this inhomogeneity as the depumping induced by the addressing beam on the atoms from sublattice B: due to the finite detuning of the addressing, the lightshift creates a leak from level $|\uparrow\rangle$ to the ground state manifold, which is then recaptured and imaged, and thus cannot be distinguished from level $|\uparrow\rangle$ in the measurement. The depumping cannot happen at $|\delta| \gg |\delta_c|$ for which the B sublattice is in level $|\downarrow\rangle$, neither at $|\delta| \sim 0$ for which the depumping rate is zero, but rather at $|\delta| \sim |\delta_c|$, in the middle of the adiabatic preparation. We believe this is the reason why its effect is much stronger in the FM case than in the AFM case, since $|\delta_c^{\mathrm{FM}}| \gg |\delta_c^{\mathrm{AFM}}|$. From the offset magnetization, we estimate the percentage of depumped atoms in B to be at least 6 %. These losses from the ideal spin 1/2 manifold contribute to increase the energy of the prepared state: for example, if a system composed of N spins is in the instantaneous ground state of the Hamiltonian during the ramp, the state after a loss of one spin is not necessarily the ground state of the remaining $N-1$ spins. Moreover, depumped atoms cannot be distinguished from atoms in $|\uparrow\rangle$, which leads to detection errors.

The second imperfection that we can identify on Fig. 4.7 is that the prepared state at the end of the ramp is not stationary. This can be seen from the fact that correlations decay at small $|\delta|$, i.e. at long times $t > 2$ µs. At this stage, the origin of this damping is not clearly understood. The most obvious explanation would be a lack of adiabaticity, however we checked that varying the speed of the ramp (by choosing $\tau = 0.15$ µs instead of $\tau = 0.3$ µs) does not change the obtained correlations (Chen et al., 2023a). Numerical simulations of the dynamics were also performed to comfort us that the preparation is adiabatic for the system size $N = 6 \times 7$ (Chen et al., 2023a). A possible explanation would be a decoherence effect, due to the Rydberg lifetimes for example. In the following, we will focus on intermediate times $t \sim 2$ µs, such that $|\delta(t)| \ll |\delta_c|$ and at the same time we are not affected too much by the decay of correlations.

4.1.3 Role of the dipolar interactions on the magnetic order

To get more insight about the nature of the order along x, I plot the correlation profiles $C^x(d)$ for the system size $N = 6 \times 7$ [Fig. 4.8(a)] and also for a larger system size $N = 10 \times 10$ [Fig. 4.8(b)], together with numerical simulations of the ideal ground state. Let us start by comparing the FM and AFM behaviors.

Frustration for AFM, long-range order for FM? The relative behavior of FM and AFM x-correlations is similar in both system sizes: starting from the same value of nearest-neighbor correlations, the FM correlations decay much slower than AFM correlations. This asymmetry can be understood as a consequence of long-range correlations. For nearest-neighbor interactions, the FM and AFM ground states would be equivalent under a sublattice rotation, so we would have expected the same decay for the absolute value of the correlations. On the contrary, the dipolar FM ground state is predicted to be long-range ordered (Peter et al., 2012), whereas the AFM ground state is destabilized by frustration.

Proving long-range order experimentally is however delicate, since this concept is well-defined only in the thermodynamic limit — a finite plateau of correlations — but can be affected by edge effects. Especially, I find that the value of the plateau strongly depends on the functional form used to fit it. The theoretical functional form in the thermodynamic limit is a power law according to Peter et al. (2012), and the FM data for the 6×7 system is compatible with this prediction [line in log-log scale in Fig. 4.8(a)]; however, trying to fit $C^x(d)$ by the sum of a power law and a constant leads to a vanishing plateau [not shown]. A fit with an exponential functional form, as done for example in Feng et al. (2023), is compatible with a plateau of ~ 0.1 [not shown].

Comparison with thermal states For the larger system size ($N = 10 \times 10$ at $t = 2$ µs), the FM correlation profile is not compatible with a power law at large distances, but rather with an exponential decay. We believe this is related to the preparation errors, which are larger for $N = 10 \times 10$ than for $N = 6 \times 7$ (as it will be discussed later). In Sbierski et al. (2024), our data was compared to simulations of the thermal phase diagram of the dipolar XY model fo $N = 10 \times 10$. The measured correlations are compared to the thermal expectations in Fig. 4.9(a), after correction from detection errors. Because of the already-mentioned temporal decay of the correlations, we plot them at several times ranging from $t = 1$ µs to $t = 8$ µs. The authors found

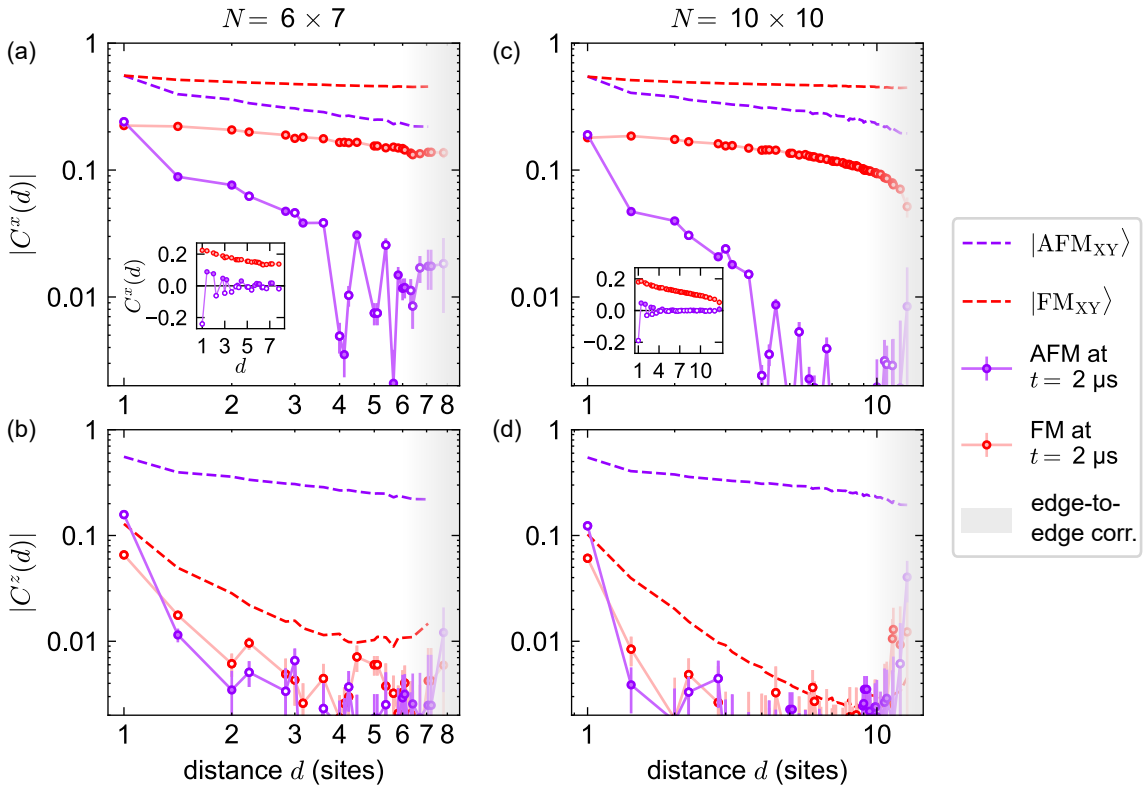

Figure 4.8: Correlation profiles at $t = 2$ µs, in the $N = 6 \times 7$ system (a,b) and in the $N = 10 \times 10$ system (c,d). The first line is the correlations along x (a,c) and the second line is along z (b,d). Colored data points (resp. white data points) represent positive (resp. negative) correlations. The dashed lines are DMRG simulations of the ground state performed by Marcus Bintz from Harvard (with $N = 6 \times 6$ instead of 6×7). The gray regions correspond to correlations between two edges of the square lattice, and are thus strongly affected by edge effects. Insets show the signed correlations, in linear scale. Error bars are estimates of the statistical noise, using bootstrapping. For the $N = 10 \times 10$ data sets, the data set also contains imperfect initial arrays with up to two holes in the rearrangement process, in order to increase the number of experimental shots.

that the highest correlations at $t = 1$ µs cannot be explained by a thermal state; this intriguing feature suggests a non-equilibrium effect with unexplained origin — coherent preparation errors might play a role, as well as decoherence effects, default of adiabaticity, or atoms out of the $\{|\uparrow\rangle, |\downarrow\rangle\}$ manifold ("holes"). The agreement is better, but still not perfect, at longer times $t \leq 4$ µs, with a temperature $T/J \sim 1.7$. This temperatures lies below the critical temperature $T_c/J = 1.923(1)$ of the classical phase transition from the paramagnetic (PM) to the XY FM phase [Fig. 4.9(b)].

What about correlations along z? In the z basis, nearest-neighbor correlations are stronger in the AFM case compared with the FM case [Fig.4.8(b,d)]. The z-correlations for the AFM ground state show a weak, short-range AFM ordering, also visible

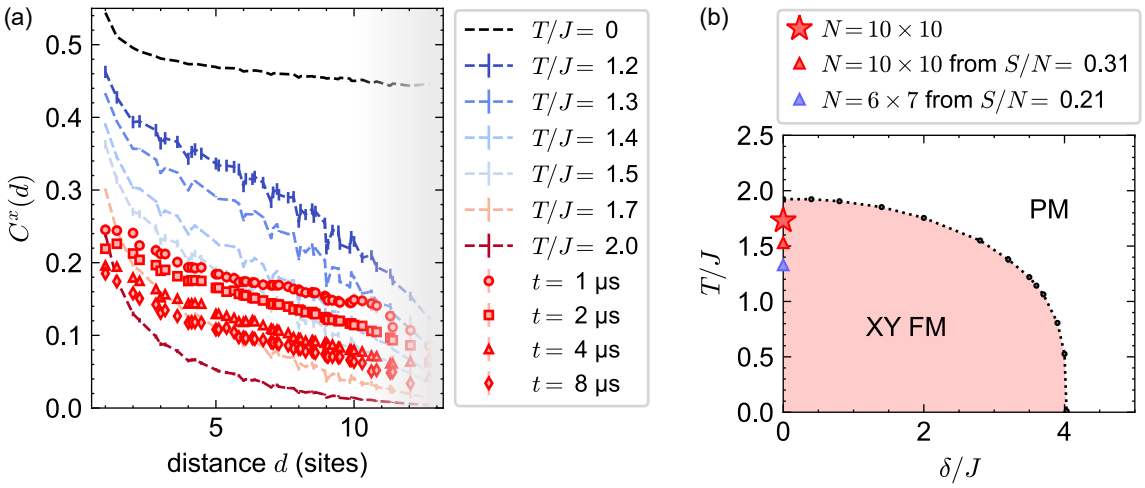

Figure 4.9: Thermometry of the experimentally prepared FM state. All results are reproduced from Sbierski et al. (2024). (a) Correlation profiles along x at times $t \in \{1, 2, 4, 8\}$ µs for $N = 10 \times 10$ (red markers), compared with quantum Monte-Carlo simulations of thermal states (dashed lines). On this plot, contrary to Fig. 4.8, experimental data are corrected for detection errors, by dividing them by a factor $1 - 2(\varepsilon_\uparrow + \varepsilon_\downarrow) = 0.82$ with $\epsilon_\uparrow = 0.04$ and $\epsilon_\downarrow = 0.05$; we also allow for 2 holes in the initial array, in order to increase the number of experimental repetitions to at least 600. (b) Approximate positions of the experimentally-prepared states in the thermal phase diagram of the dipolar XY model. The boundary between the XY FM phase (pink shaded area) and the paramagnetic phase (PM, white area) was calculated using finite-size scaling analysis, in the absence of holes. The red star indicates the closest temperature to the experimental state according to (a). The two triangles indicate the expected temperature from the entropy per spin S/N in the initial state, assuming that the adiabatic preparation is perfectly conserving the entropy. The conversion function from entropy to temperature can be found in Fig. 2 of Sbierski et al. (2024).

in 4.7(c), contrary to the FM case which has negative correlations $C^z(d)$ for all distances d. This feature is rather general, since in the next section we will see that it is also present in a one-dimensional chain.

4.1.4 Symmetry of the state in the xy plane

A natural question is whether the prepared state breaks the $U(1)$ symmetry of the XY Hamiltonian. Ideally, this should not be the case, because the initial state $|\psi_{\text{Néel}}\rangle$ as well as the total Hamiltonian H_{tot} are symmetric under z rotation, so the final state should also be symmetric. However, one may also think that as system size increases, the prepared state gets more sensitive to any small $U(1)$-symmetry-breaking perturbation, such as tiny microwave leakages for example. Spontaneous symmetry breaking is even predicted in the thermodynamic limit, due to the presence of the

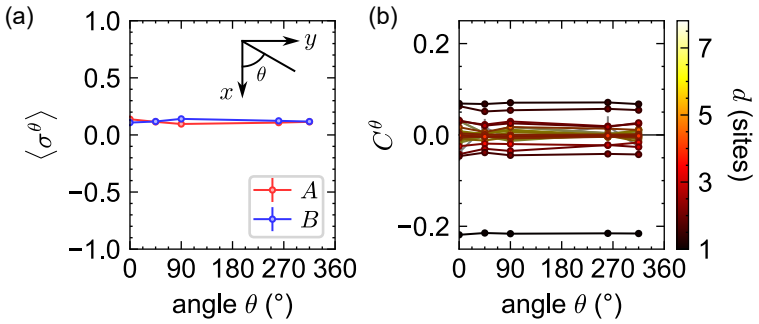

Figure 4.10: Checking the $U(1)$-symmetry of the AFM state, for $N = 6 \times 7$ at $t = 2$ µs, allowing for two holes in the initial array. (a) Magnetization per sublattice along θ, where θ is the angle of the measurement basis in the xy-plane (as defined in the inset). (b) Correlations $C^\theta(d)$, averaged over pairs separated by the same distance d.

nearby states from the tower of states (Schuler and Läuchli).

A first experimental test is simply to measure the prepared state along various angles in the xy-plane. To do so, we scan the phase of the $\pi/2$ measurement pulse, so to measure along the direction $\mathbf{u} = \cos(\theta)\mathbf{e}_x + \sin(\theta)\mathbf{e}_y$. The results are shown in Fig. 4.10, in the AFM case. Both the average magnetization $\langle\sigma^\theta\rangle$ and the correlations $C^\theta(d)$ are reasonably isotropic.

But having an isotropic average over many experimental repetitions does not mean that each realization of the experiment satisfies the $U(1)$ symmetry. For example, one could imagine that each realization of the experiment is a classical ferromagnet (or antiferromagnet) in a random direction given by a classical probability. The associated density matrix in the FM case would be

$$\rho_{\mathrm{XY}}^{\infty} \equiv \frac{1}{2\pi}\int_0^{2\pi} |\mathrm{FM}_\theta\rangle\langle\mathrm{FM}_\theta|\, d\theta, \tag{4.11}$$

which, like the FM ansatz $|\mathrm{FM}_{\mathrm{XY}}^{\infty}\rangle$ given by Eq. (4.3), has a vanishing magnetization in all directions and isotropic long-range correlations in the xy-plane (see appendix A). To distinguish those two states, a relevant observable is the variance of the total z-magnetization:

$$(\Delta M^z)^2 \equiv \left\langle (M^z)^2 \right\rangle - \langle M^z\rangle^2 . \tag{4.12}$$

On the one side, the superposition state $|\mathrm{FM}_{\mathrm{XY}}^{\infty}\rangle$, and also the exact dipolar FM ground state, which both preserve the $U(1)$ symmetry, are eigenstates of M^z, so they satisfy $(\Delta M^z)^2 = 0$. On the other side, $\rho_{\mathrm{XY}}^{\infty}$ is a statistical mixture of classical ferromagnets $|\mathrm{FM}_\theta\rangle$, each one being the equal-weight superposition of all possible

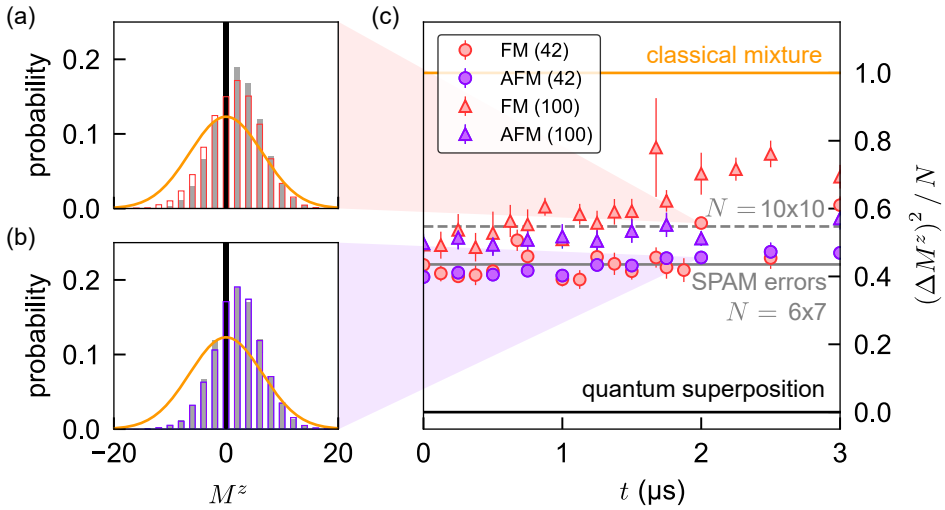

Figure 4.11: Analysis of the z-magnetization during the adiabatic ramp. (a,b) Experimental histograms of the z-magnetization M^z for $N = 6 \times 7$ in the FM (a) and AFM (b) case, together with the ideal symmetric ground state (black) and the expected distribution including SPAM errors (grey bars). The orange line is the binomial distribution corresponding to a classical, symmetry-breaking magnet. (c) Normalized variance $(\Delta M^z)^2$ as a function of ramp time, for the experiment (circles for $N = 6 \times 7$, triangles for $N = 10 \times 10$), the classical magnet (orange line) and the theoretical ground state (black line). The gray lines show the expected effect of SPAM errors. For $N = 10 \times 10$, we allow for two holes and two potential extra-atoms in the initial array, to increase the number of experimental shots.

spin configurations along z. As a consequence, the probability of measuring m spins up along z follows a binomial distribution, and the variance can be computed to be $(\Delta M^z)^2 = N$ (see appendix A for a proof).

Figure 4.11(a,b) shows experimental histograms of the z-magnetization at $t = 2$ μs in the FM and AFM cases. Figure 4.11(c) presents the variance for various times t. We find that the states have a variance smaller than that of a binomial distribution, indicating that we do not prepare a classical magnet with fully broken symmetry. In fact, the measured non-zero variances can be fully explained by the state preparation and measurement (SPAM) errors applied to the ideal distribution.

4.1.5 Another adiabatic protocol with a global microwave field

The adiabatic ramp down of the staggered field δ is not the only way to prepare the XY FM ground state. In the remaining of this section, I show another adiabatic route that makes use of a global resonant microwave field, which is an effective magnetic

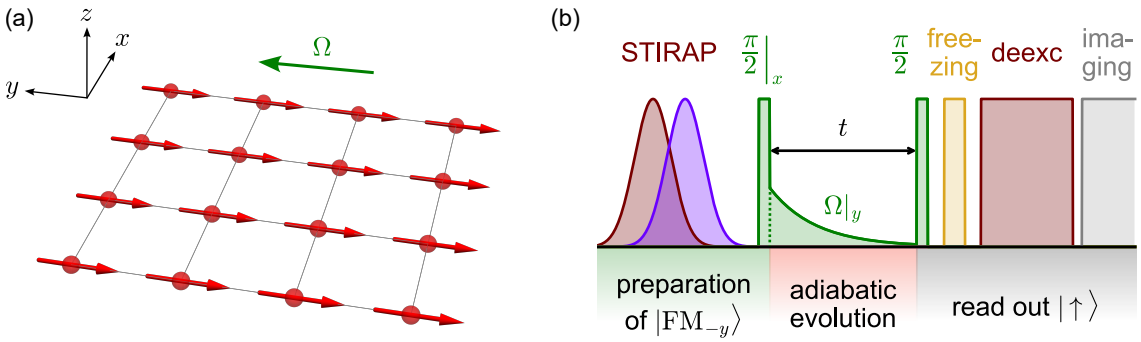

Figure 4.12: Method for adiabatic preparation of the XY FM and AFM ground states using a global microwave field. (a) The microwave field implements a global magnetic field along y, with Rabi frequency Ω. For $\Omega > 0$, the ground state of the Hamiltonian is the classical ferromagnetic state $|\mathrm{FM}_{-y}\rangle$ represented here by the colored arrows. (b) Experimental sequence for preparing $|\mathrm{FM}_{\mathrm{XY}}\rangle$. First, we prepare $|\mathrm{FM}_{-y}\rangle$ using a global $\pi/2$ pulse with rotation axis along x; second, we ramp down Ω adiabatically; finally, we read out the state by imaging the atoms in level $|\uparrow\rangle$. During the read-out, an optional $\pi/2$ microwave pulse is used to measure in the x- or y-basis of the spins.

field in spin language:

$$H_{\mathrm{Y}}(\Omega) = \hbar\Omega\, M^y \tag{4.13}$$

with $M^y \equiv \sum_j \sigma_j^y$ the total magnetization along y. The total Hamiltonian is now

$$H_{\mathrm{tot}}(\Omega) = H_{\mathrm{XY}} + H_{\mathrm{Y}}(\Omega). \tag{4.14}$$

In the regime $\Omega \gg |J|$, the ground state of $H_{\mathrm{tot}} \approx H_{\mathrm{Y}}$ is the classical FM state $|\mathrm{FM}_{-y}\rangle$, which is represented in Fig. 4.12(a). It can be adiabatically connected to the XY FM ground state by ramping down the field Ω to 0. The experimental sequence to do so is illustrated in Fig. 4.12(b), and works as follows:

1. We apply a global $\pi/2$ pulse (which is an effective magnetic field along x) to prepare $|\mathrm{FM}_{-y}\rangle$.

2. Immediately after the pulse, we change the phase of the microwave field by $\pi/2$ to change the direction of the effective magnetic field from x to y, thus implementing the Hamiltonian given by Eq. (4.14). We ramp down the field as $\Omega(t) = \Omega_0\, e^{-t/\tau}$ with $\Omega_0/2\pi = 2.1$ MHz and $\tau = 1$ µs.

3. We read out the state.

For this set of data, we use the mapping $|\uparrow\rangle \equiv \left|60S_{1/2}, m_J = 1/2\right\rangle$ and $|\downarrow\rangle \equiv$

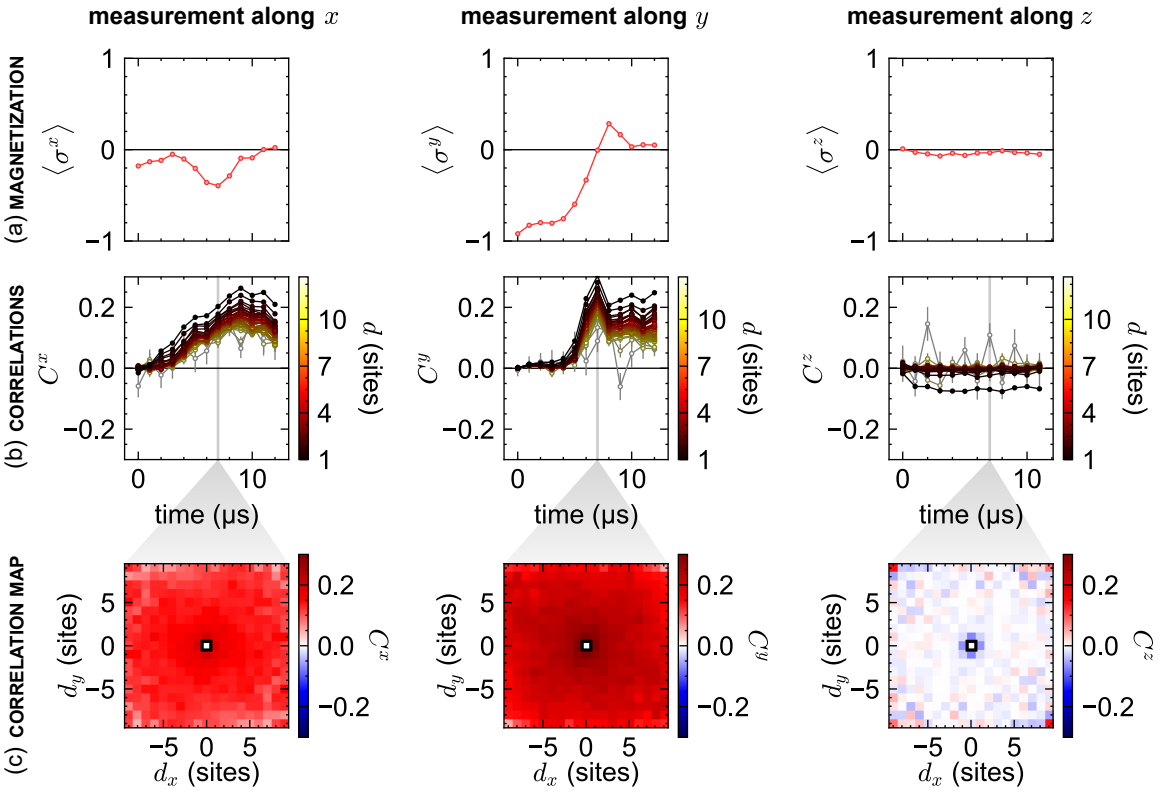

Figure 4.13: Adiabatic preparation of an XY FM state on a $N = 10 \times 10$ square array, using a global microwave field, allowing for two holes in the initial array. Each column is a basis of measurement. (a) Magnetization as a function of ramping time t. (b) Correlations versus distance d. (c) Correlation map at $t = 7$ μs.

$\left|60P_{3/2}, m_J = -1/2\right\rangle$ with a lattice spacing $a \approx 15$ μm, which gives a nearest-neighbor interaction energy $J/2\pi = -0.25$ MHz.

In Fig. 4.13, I show the experimental results on a $N = 10 \times 10$ array. Starting from -1, the y-magnetization $\langle\sigma_j^y\rangle$ slowly decays in absolute value to a value close to 0, signaling the depolarization of the initial FM state $|\mathrm{FM}_{-y}\rangle$. In the other bases, the magnetization should remain at zero all the time; however, this is not the case along x, where fluctuations with a large amplitude ~ 0.4 are observed. The origin of those fluctuations will be discussed later. In both x and y bases, the correlations start at zero and rise up for all distances [Fig. 4.13(b)]; correlation maps are shown at $t = 7$ μs in Fig. 4.13(c) and qualitatively show the expected "long-range" behavior. Along z, only short-range negative correlations build up, similarly to the previous sets of data using staggered lightshifts.

To better understand the fluctuations of the magnetization in the xy plane, we sit at $t = 7$ μs and scan the measurement angle θ. As shown in Fig. 4.14(a), the magnetization $\langle\sigma^\theta\rangle$ oscillates as a sine wave with a period of 360°, indicating that the

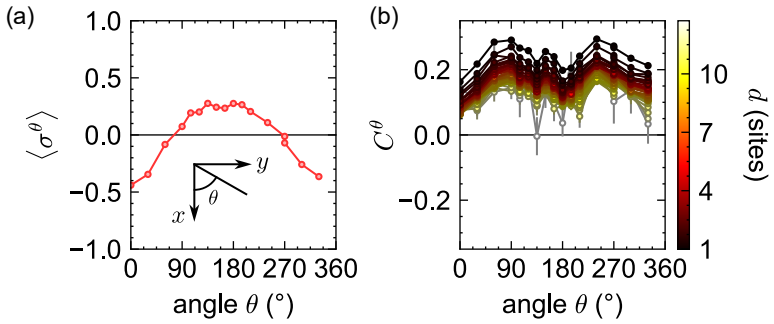

Figure 4.14: Checking the $U(1)$-symmetry of the FM state, prepared with a global microwave field, for $N = 10 \times 10$ at $t = 7$ µs, allowing for two holes and one extra-atom in the initial array. (a) Magnetization per sublattice along θ, where θ is the angle of the measurement basis in the xy-plane (as defined in the inset). (b) Correlations $C^\theta(d)$, averaged over pairs separated by the same distance d.

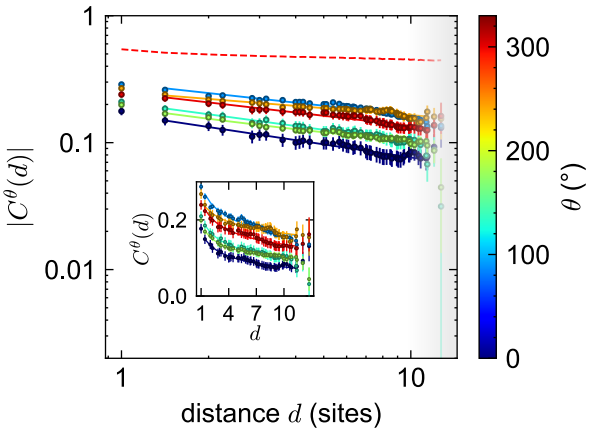

Figure 4.15: Correlation profiles in the xy plane after preparation with a global microwave field, for $N = 10 \times 10$ at $t = 7$ µs, allowing for three holes and two extra-atom in the initial array. The red dashed line is the predicted ground state profile using DMRG, and the solid lines are fits by a power-law function.

prepared state has a residual magnetization along x. This residual symmetry breaking is also visible in the associated correlations, whose oscillation frequency is twice as large: the correlations are minimal when $|\langle\sigma^\theta\rangle|$ is maximal (along $+x$ and $-x$), and they are maximal when it vanishes (along $+y$ and $-y$). Looking in more detail at the correlation profiles [Fig. 4.15], one obtains power laws up up the largest distances, although with still large deviations compared with the ideal ground state.

We interpret the residual symmetry breaking as a default of adiabaticity, which leads to residual population in the $M^z \neq 0$ manifolds. This can be understood quantitatively by looking at the simulated energy gap as a function of Ω [red curves in Fig. 4.16(b)]; the larger the energy gap, the easier it is to remain adiabatic. For $\Omega > |J|$, the gap is close to be linear with Ω, however it goes to zero as $\Omega \to 0$, making the adiabatic

preparation more and more difficult. The first excited states for $\Omega \ll |J|$ are the ones of the tower of states which lie in the manifold $M^z \neq 0$. By contrast, in the adiabatic protocol using a staggered lightshift δ, the relevant energy gaps in the ideal case are only the ones of the $M^z = 0$ manifold, since the initial state $|\psi_{\text{Néel}}\rangle$ as well as the lightshift Hamiltonian $H_{\text{Z}}(\delta)$ preserve the $U(1)$ symmetry. This results in a larger gap at $\delta = 0$, making the adiabatic preparation easier [red curves in Fig. 4.16(a)].

This picture also allows us to understand that the Ω sweep does not work in the AFM case. One could naively expect that if we switch the sign of Ω, the direction of the effective magnetic field is inverted from $+y$ to $-y$; the initial state $|\text{FM}_{-y}\rangle$ becomes the highest excited state and thus one can connect adiabatically the initial state $|\text{FM}_{-y}\rangle$ to the AFM ground state. However, the efficiency of this protocol is drastically reduced by the presence of a gap closing at a critical field Ω_c^{AFM}, even for finite-size systems [blue curves in Fig. 4.16(a)]. To extend the adiabatic protocol for the AFM case, one would rather need to apply a sublattice rotation on both the initial state and the field, but experimentally we cannot implement a sublattice-dependent microwave field along y.

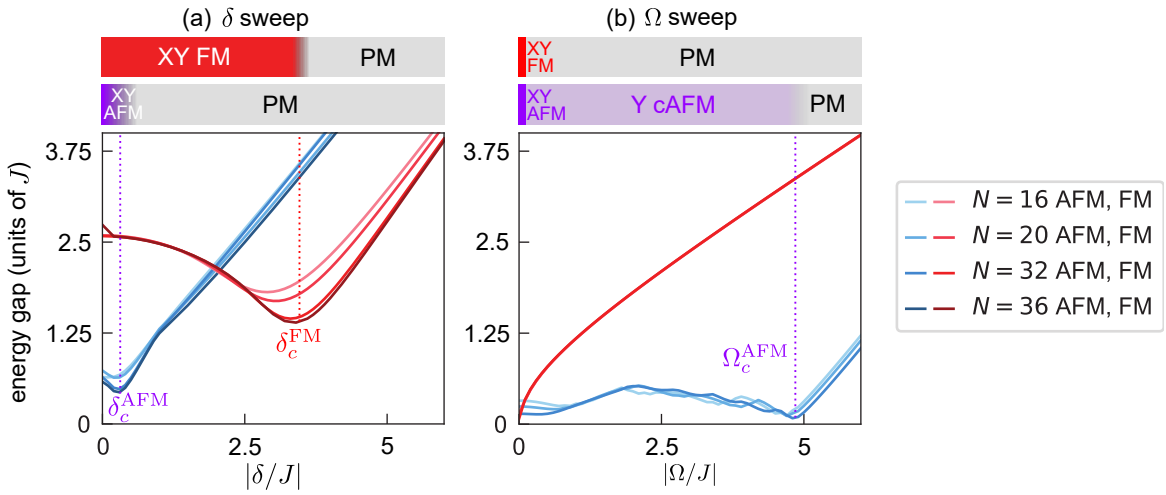

Figure 4.16: Simulated excitation gaps for two preparation protocols. Simulations were performed by Michael Schuler and Andreas Läuchli from Innsbruck, for systems with periodic boundary conditions. (a) Energy gap between the ground state and the first excited state of $H_{\mathrm{XY}} + H_{\mathrm{Z}}(\delta)$ as a function of the staggered lightshift δ. Only states from the $M^z = 0$ manifold are taken into account. Blue (resp. red) curves show the results in the AFM (res. FM) case. Darker colors correspond to larger system sizes. The smallest gap indicates the approximate position of the critical fields between the XY FM/AFM phases and a paramagnetic (PM) phase. (b) Energy gap of $H_{\mathrm{XY}} + H_{\mathrm{Y}}(\Omega)$ as a function of the global microwave Rabi frequency Ω. Here we cannot restrict to a single M^z sector since it is not conserved; this explains in particular why the gaps for $\Omega = 0$ in (b) are not the same as the ones for $\delta = 0$ in (a). Any non-zero Ω breaks the $U(1)$ symmetry and, in the thermodynamic limit, immediately destroys the LRO, resulting in a paramagnetic phase for in the FM case, and a canted AFM phase along y (Y cAFM) in the AFM case. This Y cAFM phase is stable up to a critical value of Ω where it finally undergoes a quantum phase transition to a PM phase.

Take-home message

The ground state and highest excited state of the dipolar XY model are respectively characterized by FM and AFM magnetic orders. Those can be experimentally unveiled by measuring the correlations between the spins, making use of the single-atom resolution of our setup. We have tested two adiabatic protocols to prepare low-energy states of the model: one makes use of staggered lightshifts, and the other one utilizes a global microwave field.

In spite of various experimental imperfections in the state preparation and in the measurement, we are able to qualitatively probe the fundamental features of the model. In particular, we make the role of dipolar couplings evident, by showing that the FM ordering is reinforced by the long-range couplings, whereas the AFM ordering is weakened due to geometrical frustration. This work also made us realize the importance of finite-size effects compared with predictions of the thermodynamic limit: for a finite-size system, long-range order does not necessarily imply breaking the continuous $U(1)$ symmetry. More specifically, the protocol with staggered lightshifts is compatible with a symmetry-preserving state, whereas the protocol with a global microwave field leads to a symmetry-broken state.

4.2 Luttinger liquid on a 1D spin chain

How does the physics of the dipolar XY model change in one dimension, compared with the case of a two-dimensional square lattice?

Part of the intuition that we built on the square lattice remains true in 1D. The dipolar FM and AFM ground states are approximately related by a sublattice rotation, which is exact in the case of nearest-neighbor interactions. At first-order, the FM and AFM ansätze introduced in sec. 4.1 still provide an approximate description of the ground states. Like in the 2D case, frustration induced by next-nearest neighbor interactions is also expected to break the symmetry between the FM and AFM states.

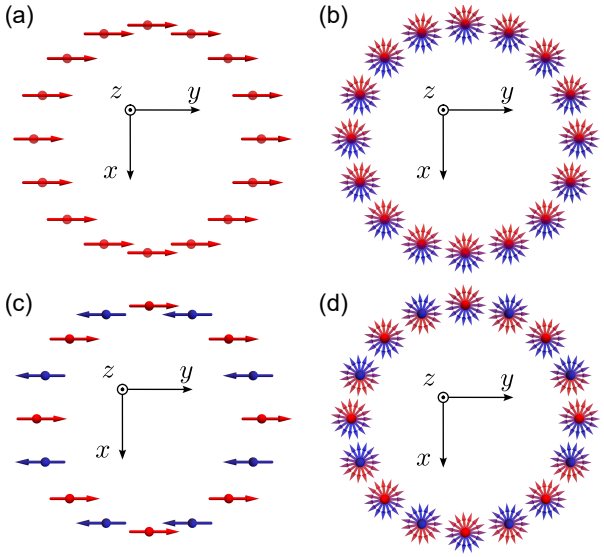

Figure 4.17: FM and AFM ansätze in one dimension. (a) Classical FM. (b) Approximate picture for the XY FM ground state, as the superposition of all classical FM in the xy-plane. (c) Classical AFM. (b) Approximate picture for the XY AFM ground state.

However, in 1D frustration is expected to have a weaker role than in 2D. With dipolar interactions, both FM and AFM ground states are expected to be in the same phase, called a *Tomonaga-Luttinger liquid* (TLL) (Bethe, 1931; Tomonaga, 1950; Luttinger, 1960; Haldane, 1981; Giamarchi, 2004). The TLL theory is a universal harmonic quantum field theory, which predicts that all long-wavelength properties of the system can be related to the knowledge of only two numbers: the dimensionless Luttinger parameter K and the sound velocity u. More precisely, the dipolar XY model can be mapped onto the following Hamiltonian (Maghrebi et al., 2017)

$$H_{\mathrm{TLL}} = \frac{\hbar u}{2\pi} \int dx \left[K \left(\nabla\theta(x)\right)^2 + \frac{1}{K} \left(\nabla\phi(x)\right)^2 \right] \tag{4.15}$$

where θ and $\nabla\phi$ are field operators defined on a continuous space x, which satisfy bosonic commutation relations. According to Maghrebi et al. (2017), "roughly speaking, the field θ gives the spin orientation in the xy plane, while the gradient of ϕ characterizes the spin component along the z axis". Mathematically, $S_j^+ \sim e^{i\theta(x_j)}$ and $S_j^z \sim \nabla\phi(x_j)$.

In both FM or AFM cases, analytical and numerical calculations (Maghrebi et al., 2017; Schneider et al., 2022; Lee et al., 2023; Gupta et al., 2025) predict that the ground state lies within the TLL phase, but with distinct K and u with respect to the NN case for which $K = 1$ and $u = 1$: in the FM case, the dipolar interactions reinforce each other and yield $K_{\mathrm{FM}} > 1$, while dipolar AFM interactions are frustrated and lead to $K_{\mathrm{AFM}} < 1$. The FM dipolar case also lies close to a transition from a TLL phase to a phase with continuous symmetry breaking (Maghrebi et al., 2017; Schneider et al., 2022).

The TLL theory was already shown to be applicable to many experimental systems: semi-conducting wires (Yacoby et al., 1996; Auslaender et al., 2002), edge states of quantum Hall effect (Grayson et al., 1998), organic conductors (Schwartz et al., 1998; Jérome, 2004), carbon nanotubes (Bockrath et al., 1999; Lee et al., 2004; Li et al., 2024), Heisenberg spin chains (Lake et al., 2005), spin ladders (Klanjšek et al., 2008), and 1D Bose gases (Paredes et al., 2004; Kinoshita et al., 2004; Fabbri et al., 2015; Hofferberth et al., 2008; Yang et al., 2017, 2018; Pagano et al., 2020; Hilker et al., 2017). Universal signatures of TLL physics were found in various observables such as the electrical conductance (Grayson et al., 1998; Schwartz et al., 1998; Bockrath et al., 1999; Jérome, 2004), the relaxation times in nuclear magnetic resonance (Klanjšek et al., 2008), the spectrum of excitations (Auslaender et al., 2002; Lake et al., 2005; Fabbri et al., 2015; Yang et al., 2017, 2018), or the momentum distribution of the particles (Paredes et al., 2004; Pagano et al., 2020). In this section, we report a new example of this broadband range of applicability, with two specificities compared with the above literature:

- dipolar interactions, in contrast with *e.g.* quantum magnetism in condensed matter, in which spin-spin interactions have typically a finite range;
- local control and readout, that allow us to probe the spin correlations in real space.

4.2.1 Quasi-long range order

Experimental scheme We first consider a closed ring geometry that realizes periodic boundary conditions (PBC). This geometry reduces finite-size effects compared to an open-boundary condition (OBC) chain, and enables improved statistics of observables by averaging over sites, which are all equivalent; this geometry is also more compact than a 1D line, allowing us to put more atoms in the finite field of view of our aspheric lens, for a fixed lattice spacing. We encode a pseudo-spin 1/2 using the two Rydberg states $|\uparrow\rangle = \left|70S_{1/2}, m_J = 1/2\right\rangle$ and $|\downarrow\rangle = \left|70P_{1/2}, m_J = -1/2\right\rangle$, which leads to a nearest-neighbor interaction energy $J \approx 2\pi \times 0.55$ MHz at distance 16.2 µm.

We aim at preparing the FM and AFM ground states of H_{XY}. To do so, we use a quasi-adiabatic scheme similar to the one of the previous section. First, we apply large light shifts $|\delta_0| \approx 2\pi \times 23$ MHz $\gg |J|$ on a staggered sublattice B (Fig. 4.18); then, we prepare the ground state of the addressing Hamiltonian H_{Z} at half-filling ($M_z = 0$), which is the product state $|\psi_{\text{Néel}}\rangle = |\uparrow\downarrow \cdots \uparrow\downarrow\rangle$; finally, we ramp down the light shifts $\delta(t)$ in order to end up in a state close to the ground state of H_{XY}. The same protocol is used to prepare a state close to the AFM ground state of $-H_{\mathrm{XY}}$, by changing the sign of $\delta(t)$.

Shape of the ramp profile In the particular case where the energy gap between the ground state and the first excited state depends linearly on δ, one can derive the following analytical expression for the adiabatic ramp (Richerme et al., 2013; Fang et al., 2024):

$$\delta(t) = \frac{E_0 \delta_c t + E_c \delta_0 (T - t)}{E_0 t + E_c (T - t)}, \tag{4.16}$$

with T the duration of the ramp, δ_0 the initial light shift, δ_c the light shift at the critical point, E_0 the energy gap for $\delta = \delta_0$ and E_c the gap for $\delta = \delta_c$. For the 1D XY model, the critical point occurs at $\delta_c = 0$, so that Eq. (4.16) can be simplified into

$$\delta(t) = \delta_0 \frac{T - t}{T - (1 - \alpha)t} \tag{4.17}$$

where $\alpha = E_0/E_c$ (E_c is a finite-size energy gap, expected to vanish in the thermodynamic limit). Eq. (4.17) is the profile that we used for the preparation, up to the response time of the AOM. The values of T and α are optimized empirically to maximize the experimentally-measured x-correlations, and we use: $(T, \alpha) = (1.5\ \mu\text{s}, 20)$ in the FM case, and $(T, \alpha) = (2.5\ \mu\text{s}, 100)$ in the AFM case. The value of α is larger in the AFM case, in agreement with the fact that the critical gap E_c is smaller in the

AFM case, due to the weak frustration induced by next-nearest neighbor couplings.

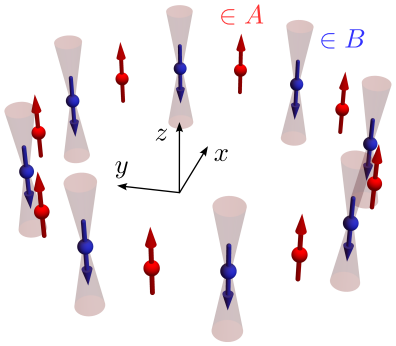

Figure 4.18: Initial state for the adiabatic preparation. Addressed atoms (sublattice B) are prepared in $|\downarrow\rangle$, whereas non-addressed atoms (sublattice A) are prepared in $|\uparrow\rangle$.

Build-up of XY magnetic order During the adiabatic ramp, we monitor the dynamics of the spins. Figure 4.19(a) shows the z-magnetization of each sublattice, respectively in the FM and AFM cases. At the beginning of the preparation, the z-magnetizations of sublattices A and B are opposite, reflecting the staggered spin pattern of the initial state $|\psi_{\text{Néel}}\rangle$. As we ramp down the light shifts, they merge to zero, signaling the meltdown of the initial pattern into a translation-invariant state in the x, y plane. To further characterize the FM and AFM states prepared during the ramp, we compute the spin-spin correlations $C^x(r)$ and $C^z(r)$, averaged over pairs separated by the same chord distance r.

Here, we use the chord distance $r_{ij} = \frac{N}{\pi}\sin\left(\frac{\pi}{N}d_{ij}\right)$ instead of the perimeter distance $d_{ij} = |i-j|$. The reason is *not* that this is the true physical distance between the atoms in our circular geometry — interactions across the circle are smaller by a factor $\left(\frac{N}{\pi}\right)^3 \sim 500$ compared with nearest-neighbor interactions, so they can be safely neglected — but rather to avoid biases due to the periodic boundary conditions in a finite-size system. A theoretical justification for the choice of the chord distance relies on conformal field theory, see for instance Di Francesco et al. (2011); Slagle et al. (2021).

Similarly to the 2D case, we observe the progressive buildup of FM or AFM correlations along x as $\delta(t)$ is ramped down to 0. Along the z axis, we observe fast-decaying negative correlations.

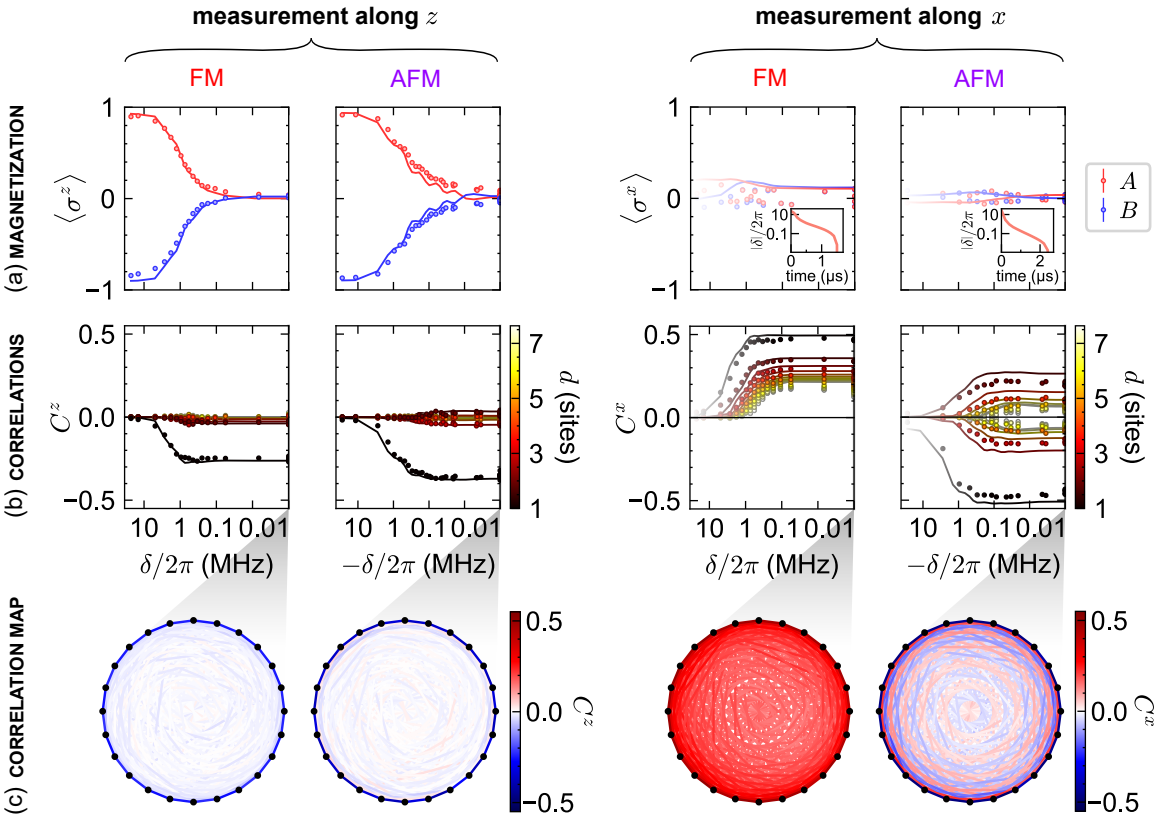

Figure 4.19: Adiabatic preparation of low-energy XY FM and AFM states on a $N = 24$ circular array. (a) Magnetization per sublattice as a function of the lightshift $\delta/2\pi$. The solid lines are numerical simulations of the dynamics in the presence of the calibrated experimental imperfections, with no free parameter. Along x, the measurement can only be trusted for $\delta \ll \Omega$ with $\Omega/2\pi = 9$ MHz the Rabi frequency of the measurement pulse, we put a white shading to avoid over-interpreting the initial times. Insets: measured lightshift as a function of preparation time t. (b) Correlations as a function of δ. The color indicates the distance between the particles, from dark red (nearest neighbors) to white (furthest pairs along the diagonal of the array). (c) Correlation maps at the end of the ramp: each atom is represented by a black dot, and the color of each segment encodes the value of the corresponding correlation.

Power-law correlations: FM case We now examine in detail the correlation profiles of the final state, shown in Fig. 4.20. TLL theory predicts that these correlations are scale-invariant, indicative of a quantum critical state. More specifically, $C^x(r)$ and $C^z(r)$ should decay with distance as sums of power-laws, whose exponents are universally determined by the single Luttinger parameter, K. We first focus on the FM case in the x basis, for which the dominant power-laws (i.e. at asymptotic distances

$r \gg 1$) are expected to be (Giamarchi, 2004):

$$C^x_{\mathrm{FM}}(r) \approx A \left(\frac{1}{r}\right)^{\frac{1}{2K}} + B\,(-1)^{d(r)} \left(\frac{1}{r}\right)^{2K + \frac{1}{2K}} \tag{4.18}$$

where A and B are non-universal amplitudes, and $d(r) \equiv \frac{N}{\pi} \arcsin\left(\frac{\pi}{N} r\right)$ is the perimeter distance in units of the lattice spacing. Numerical calculations predict $K_{\mathrm{FM}} = 1.8(1)$ for our $N = 24$ atom ring.

The FM experimental data feature a power-law decay of the x-correlations up to ~ 5 sites [blue points on Fig. 4.20(a)]. At larger distances, the correlations decay faster than a power-law; we attribute this deviation to preparation errors (see below). To account for this deviation, we follow the approach of Fang et al. (2024) and use a modified fit function for the data: $\tilde{C}^x_{\mathrm{FM}}(r) = C^x_{\mathrm{FM}}(r) e^{-r/\xi}$, where ξ is an empirical correlation length. We obtain $K_{\mathrm{FM}} = 1.6(4)$, already close to the theoretical value, and a correlation length $\xi = 15(4)$ sites.

Next, we examine the FM z-correlations, whose theoretical behavior at long distance takes the form,

$$C^z(r) \approx -\frac{2K}{\pi^2} \left(\frac{1}{r}\right)^2 + D\,(-1)^{d(r)} \left(\frac{1}{r}\right)^{2K} . \tag{4.19}$$

The structure of the first term, with an integer exponent and K appearing as a simple prefactor, encodes the special role of σ^z as the local density of a conserved quantity, M_z. By contrast, the second term reflects the presence of emergent gapless fluctuations at wavevector $k = \pi$, which, similar to the x correlations, has a non-universal amplitude, D, and a K-dependent exponent. In the measured correlations, the $1/r^2$ term dominates, as highlighted by the black dotted line in Fig. 4.20(b). We find that Eq. (4.19) fits the experimental data well, without the need for an exponential correction, but estimating K is challenging for two reasons. First, the K-dependent prefactor in Eq. (4.19) is affected by our preparation and detection errors, leading to smaller values of K. To limit this effect, we take into account the experimentally-calibrated detection errors in our fitting function, by rescaling it as $\tilde{C}^z(r) = (1 - 2\varepsilon_\downarrow - 2\varepsilon_\uparrow)\, C^z(r)$ with $\varepsilon_\downarrow = 0.03$ and $\varepsilon_\uparrow = 0.025\%$. Second, fitting the full correlation profile does not give a value of K compatible with the one obtained along x, even in the ideal ground state simulated by DMRG. Actually, there is no reason for the theory profiles to describe accurately the full range of distances, since the TLL theory is only valid in the large-wavelength limit $r \gg 1$. To avoid this bias,

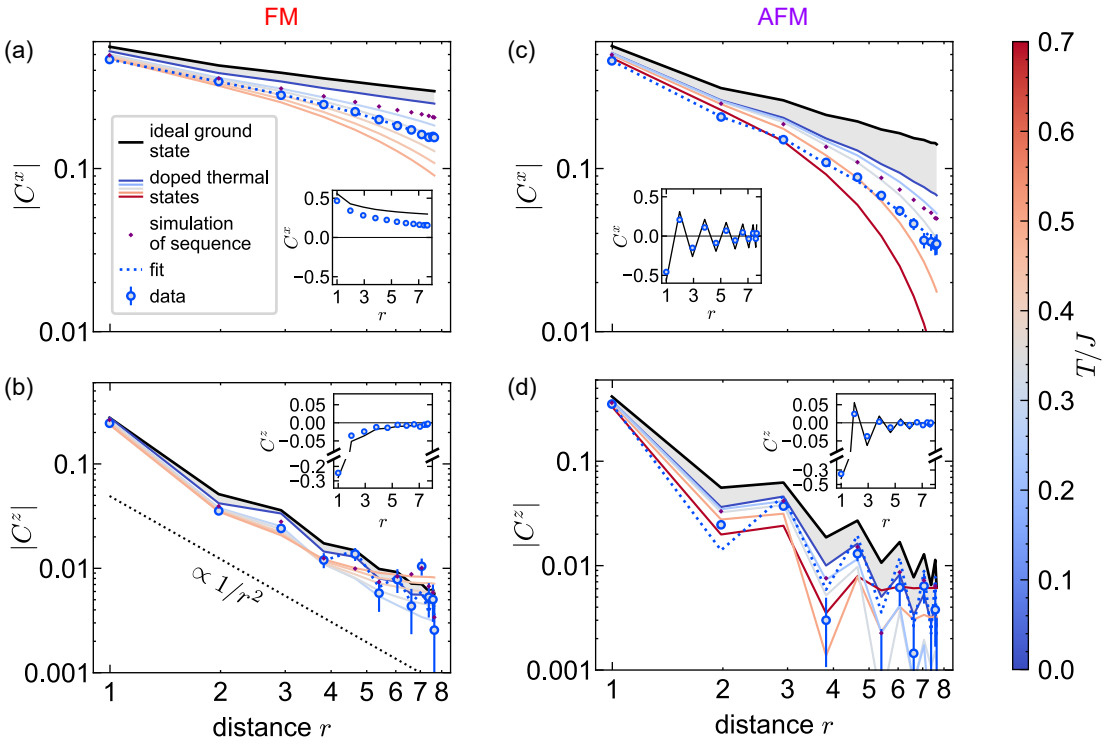

Figure 4.20: Spatial profiles of the correlations in the ferromagnetic (FM) and antiferromagnetic (AFM) ground states. The left panels show the FM correlations at $t = 1600$ ns along x (a) and along z (b). The right panels display the AFM correlations along x at $t = 3000$ ns (c) and along z at $t = 3200$ ns (d). The blue points represent experimental data, while the purple points correspond to simulated sequences with imperfections. The dotted lines indicate fits by the theoretical profiles (see text). The solid lines depict simulations of the ideal ground state (in black) and thermal states in the presence of randomly placed holes, with the color of the lines coding for the temperature. For a fair comparison with the data, all simulated correlations are multiplied by a factor of 0.89, corresponding to experimentally measured detection errors. The doping with holes is 4% in the FM case and 6% in the AFM case, and its effect is highlighted by the grey region.

we introduce a cutoff distance r_c and fit the correlations for distances $r \leq r_c$. We set the value of r_c by repeating the fits for different values of r_c on the ideal ground state (simulated by DMRG), and choose the smallest cutoff that gives a satisfying convergence. This analysis is shown in Fig. 4.21(b). Finally, our experimental fit yields $K_{\mathrm{FM}} \approx 1.4(1)$ with $r_c = 3$ sites.

Power-law correlations: AFM case Proceeding now to the AFM, we expect the same critical correlation structure, except with a global staggered sign $(-1)^{d(r)}$ multiplying the x-correlations, and a different Luttinger parameter $K_{\mathrm{AFM}} = 0.85$ for $N = 24$. The measured z-correlations are fitted reasonably well by Eq. (4.19), and we obtain $K_{\mathrm{AFM}} \approx 0.90(1)$ [Fig. 4.20(d)]. However, the x-correlations again require

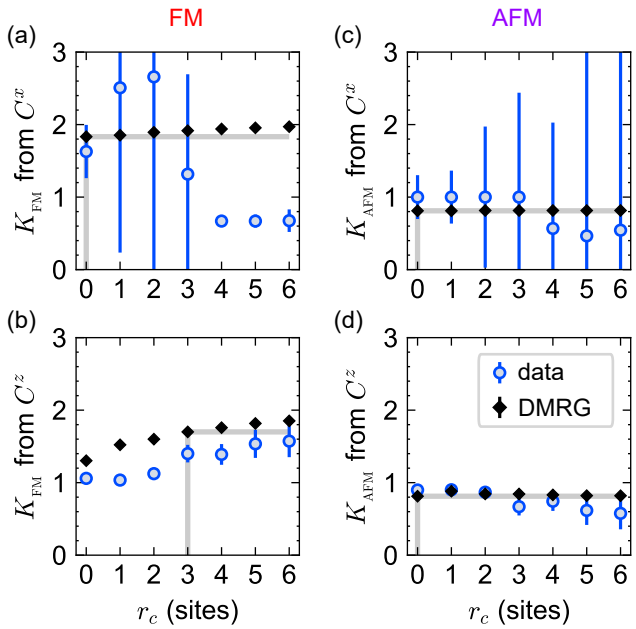

Figure 4.21: Effect of a lower cutoff on the fitted Luttinger parameter K. Each panel corresponds to one of the four spatial correlation profiles shown in Fig. 4.20: $C^x(r)$ in the FM case (a) and in the AFM case (c); $C^z(r)$ in the FM case (b) and in the AFM case (d). For each correlation profile, we fit the correlations for distances $r \geq r_c$, for both the ideal ground state (simulated with DMRG, black diamonds) and the data (blue points), and we repeat the fit for various cutoff distances r_c. The chosen value of r_c is indicated by the grey vertical line. The difference of error bars between (a,c) and (b,d) is due to the fact that the functional form along x includes two additional fitting parameter compared with the one along z (4 instead of 2).

the introduction of an exponential decay, with a short correlation length of $\xi = 5(1)$ sites [Fig. 4.20(c)]; this leads to larger uncertainty in our estimate of the Luttinger parameter, $K_{\mathrm{AFM}} \approx 1.0(3)$. To check the robustness of the analysis, we applied the same preparation protocol for different system sizes (ranging from $N = 16$ to $N = 28$) and obtained similar values of K and ξ. The small value of ξ indicates that the AFM is particularly sensitive to experimental imperfections.

Benchmark of the data Motivated by this observation, we carried out numerical simulations of the state preparation procedure, including all known experimental imperfections. The results of these calculations (Fig. 4.20, purple diamonds) quantitatively reproduce part of the deviation between the measurements and the ideal ground state. Among the included errors, we find that a finite density p of holes is especially important, i.e. atoms lying outside the Rydberg manifold due to either a failed excitation or spontaneous decay. We estimate $p = 0.04$ for the FM, while $p = 0.06$ for the AFM due to a longer adiabatic preparation. Owing to the dipolar interactions, sites separated

by a hole remain coupled with a reduced strength $J/8$. However, each hole leads to a slip of the sublattice structure, which causes snapshot-averaged measurements of correlations to decay over an perimeter distance $\xi_p = 1/|\ln(1-2p)|$ (Bocini et al., 2024). This disordered-readout effect is most significant in the AFM x-correlations, where the staggered part dominates; the preceding formula for ξ_p corresponds to a chord distance of 6.5, which quantitatively accounts for the observed exponential decay. Now fitting the simulated FM correlations with holes by Eqs. (4.18,4.19), we obtain $K_{\mathrm{FM}} = 1.55(1)$ from the C^x correlations and $K_{\mathrm{FM}} = 1.44(1)$ from the C^z correlations, in good agreement with the experimental values. The hole-doped AFM prepared is not in the TLL phase, although this point deserves more investigation. Finally, the other imperfections, such as non-adiabaticity, effectively raise the temperature of the final prepared state: comparing to equilibrium calculations that include holes, we find that both the FM and AFM experimental correlations are compatible with thermal ones at a temperature of $T/J \approx 0.35$.

4.2.2 Friedel oscillations

The prediction: oscillations of the magnetization close to an impurity or an edge The single-atom control of our experiment allows us to test another prediction of TLL theory, namely the existence of Friedel oscillations at the edges of an open chain (Giamarchi, 2004). To do so, we modify the geometry of the chain by removing one atom, which amounts to considering a chain of $N = 23$ spins with open boundary conditions (OBC) – modulo the weak dipolar coupling across the hole [Fig. 4.23(a)]. The AFM ground state is then expected to exhibit spatial oscillations of the local z-magnetization around the hole, akin to Friedel oscillations in fermionic systems. Examples of such behaviors have been observed with scanning tunneling microscopy at the edges of carbon nanotubes (Lee et al., 2004) and near defects in WS_2 heterostructures (Li et al., 2024). For an open chain with an odd number of atoms N and a total magnetization M_z, the z-magnetization at a site j away from the impurity takes the form:

$$\langle \sigma_z^j \rangle \approx A \cos(2k_{\mathrm{F}} j) \left[\frac{N}{\pi} \cos\left(\frac{\pi j}{N} \right) \right]^{-K} . \tag{4.20}$$

Here A is an overall amplitude and $2k_{\mathrm{F}}$ is the Friedel wavevector. Both K and k_{F} depend on the magnetization M_z; in particular, the Friedel wavevector obeys the

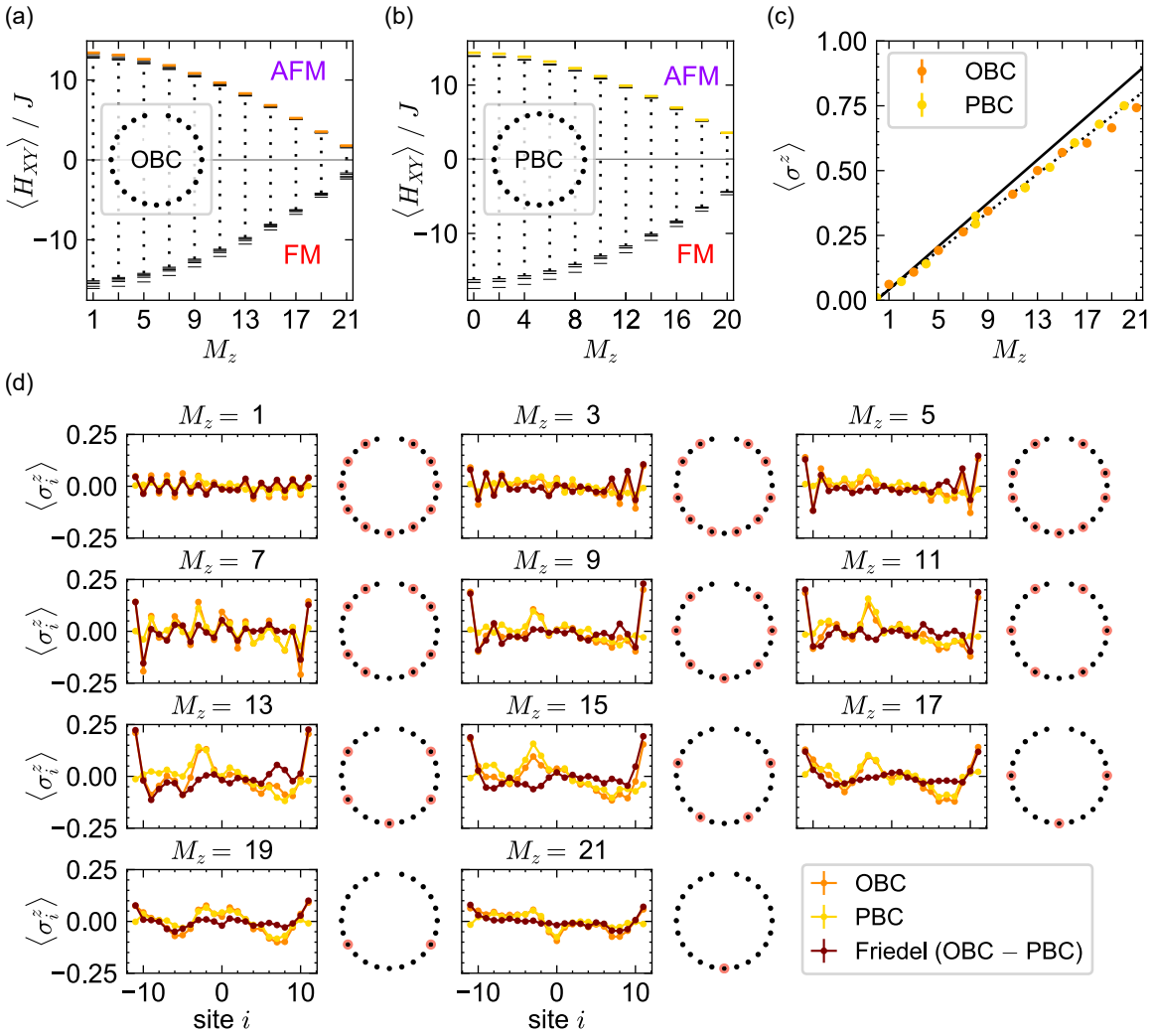

Figure 4.22: Method for observing Friedel oscillations. (a) Simulated low- and high-energy spectrum of the XY model on an open circle (OBC) with $N = 23$ spins, as a function of the total z-magnetization M_z. The colors highlight the AFM ground state of each M_z sector, which are the target of the adiabatic preparation. (b) Same spectrum in a closed circle (PBC) with $N + 1$ spins, where no Friedel oscillations are expected. (c) z-magnetization averaged over all atoms, as a function of the target magnetization. The solid line is the theoretical expectation $\langle\sigma^z\rangle = \frac{1}{N+1}M_z$, and the dotted line is the same curve in the presence of detection errors: $\langle\sigma^z\rangle = (1 - 2\varepsilon_\downarrow - 2\varepsilon_\uparrow)\frac{1}{N+1}M_z + (\varepsilon_\downarrow - \varepsilon_\uparrow)$. The ramp times differ for the different M_z sectors ($T = 2500$ ns for $M_z = 1$, $T = 5000$ ns for $M_z \in [3, 5, 7, 9, 11, 13, 15]$, $T = 8000$ ns for $M_z \in [17, 19, 21]$), and the measurements were always taken 500 ns after the end of the ramp. (d) Spatial dependence of the z-magnetization $\langle\sigma_z^i\rangle$ with the site positions i (the average magnetization $\sum_{j=1}^{N}\langle\sigma_z^j\rangle$ / N is removed for clarity), for different M_z sectors. For each value m of the total magnetization, a different initial state $|\psi_m\rangle$ is used for the adiabatic preparation, with $(N + m)/2$ spins in $|\uparrow\rangle$ (non-addressed atoms) and $(N - m)/2$ spins in $|\downarrow\rangle$ (addressed atoms); the position of the addressed atoms is indicated by pink circles. The Friedel signal (OBC − PBC) at site i is the difference of the OBC magnetization and the PBC magnetization measured with the same sequence and the same addressing pattern.

relation

$$k_{\mathrm{F}} = \frac{\pi}{2}\left(1 - \frac{M_z}{N}\right). \tag{4.21}$$

Protocol for the observation of Friedel oscillations To check this prediction, we use the quasi-adiabatic preparation described above in order to drive the system close to the AFM ground state of the XY Hamiltonian on the open ring at fixed total magnetization M_z, as illustrated by the spectrum in Fig. 4.22(a). To control the magnetization, we initialize $(N + M_z)/2$ spins in $|\uparrow\rangle$ (non-addressed atoms) and $(N - M_z)/2$ spins in $|\downarrow\rangle$ (addressed atoms), in a way that distributes as uniformly as possible the net magnetization across the circle [see addressing patterns in Fig. 4.22(d)]. Then, we ramp down the light shifts δ acting on sublattice B and measure the final state in the z basis.

Following this protocol, we observe the expected linear evolution of the magnetization $\langle\sigma^z\rangle$ averaged over all sites as we change the addressing patterns [Fig. 4.22(c)] — with deviations at large M_z that can be explained by our detection errors. But the single-site resolved magnetization $\langle\sigma_i^z\rangle$ [orange points in Fig. 4.22(d)] is not symmetric around the position of the hole, as it should be given the symmetry of the geometry; a closer analysis reveals gradients and localized peaks. The amplitude of those inhomogeneities are on the same order as the expected Friedel signal: $\langle\sigma_i^z\rangle \sim 0.1$. Several effects could explain them: non-adiabaticity of the ramp leading to a reminiscence of the initial addressing pattern; positional disorder on the average atomic position; inhomogeneous spin frequencies due to residual gradients of electric or magnetic field.

To remove the inhomogeneities that are not due to the Friedel signal, we measure a "background signal" in a situation where we expect no Friedel oscillation. The background is measured on the PBC geometry [closed circle, Fig. 4.22(b)], using the same addressing pattern and the same experimental sequence as in the OBC case. The site-resolved magnetization with PBC [yellow points in Fig. 4.22(d)] reveals similar inhomogeneities as in the OBC case, making us confident that this is a reproducible bias of our experiment. Finally, we compute the difference between the OBC and the PBC magnetizations, which we interpret as the Friedel signal [dark red points in Fig. 4.22(d)]. Now, oscillations are much more symmetric around the hole.

Analysis of the Friedel signal To probe the spatial frequency of the Friedel oscillations, we Fourier-transform the z-magnetization profile: $\langle\sigma_z^q\rangle = \sum_j e^{i\,qj}\langle\sigma_z^j\rangle$ for $q \in \{2\pi n/N\}_{0\leqslant n<N}$. In Fig. 4.23(b), we plot $|\langle\sigma_z^q\rangle|$ as a function of the wavevector q and the magnetization sector M_z. For each value of M_z, $|\langle\sigma_z^q\rangle|$ peaks at a given value

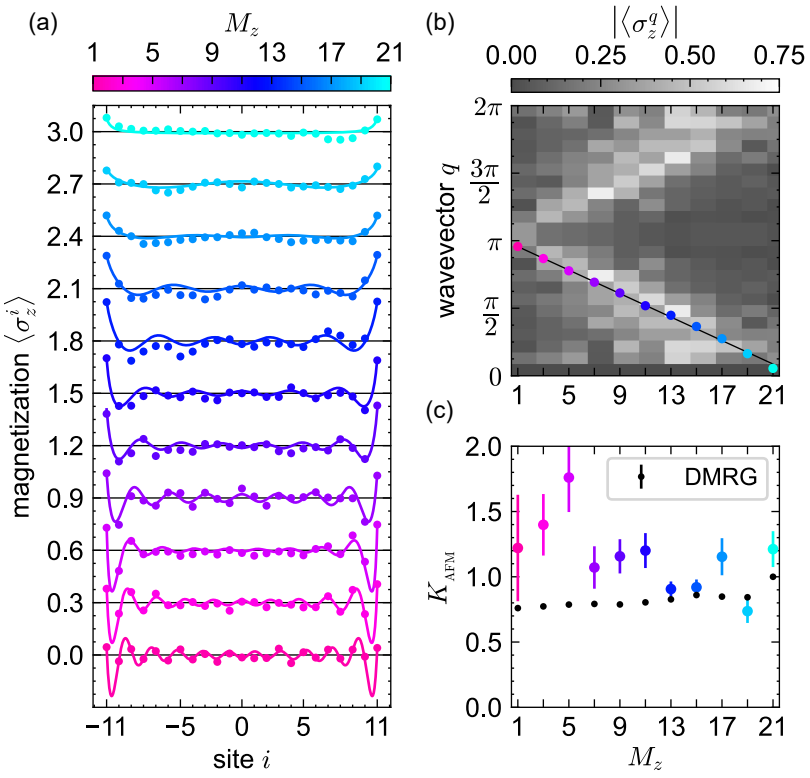

Figure 4.23: Evidence of Friedel oscillations in an open chain. (a) z-magnetization per site at the end of the adiabatic state preparation, for various M_z sectors. The y-axis corresponds to the magnetization of the open chain (OBC), minus the PBC background. Curves are offset for clarity. Solid lines are fits with Eq. (4.20). (b) Background: Fourier transform of the z-magnetization for each M_z sector, showing a linear shift of the spatial frequency. Points on top of the background are fitted values of the oscillation frequency ($2k_{\mathrm{F}}$) using Eq. (4.20). The solid black line is the theory prediction given by Eq. (4.21), with no free parameter. (c) Fitted values of the Luttinger parameter K_{AFM} using Eq. (4.20). The black points are the values extracted from DMRG simulations using the same method.

of q; this value is consistent with the wavevector of the Friedel oscillation, $2k_{\mathrm{F}}$, linearly shifting from π at small M_z to 0 at large M_z [Eq. (4.21)].

Finally, we test whether one can extract information about the Luttinger parameter from the envelope of the Friedel signal. To this end, we fit each magnetization profile in Fig. 4.23(a) by the functional form given by Eq. (4.20), with k_{F}, A and K_{AFM} as free parameters. The obtained values of $2k_{\mathrm{F}}$ are shown as colored points in Fig. 4.23(b), and agree perfectly with the theory prediction. In contrast, the obtained values of K_{AFM} [Fig. 4.23(c)] are more scattered around $K \sim 1$; this method does not turn out to give a precise estimate for the Luttinger exponent.

Take-home message

In this section, we have shown that a 1D chain of Rydberg-encoded spins interacting under the dipolar XY Hamiltonian realizes the physics of a Luttinger liquid.

First, the measured FM and AFM correlation profiles reveal the expected power-law decays at short distances. Experimental imperfections (holes and preparation errors) lead to a finite correlation length in the xy-plane, whereas z-correlations appear quite robust to imperfections and feature the expected $1/r^2$ decay. However, extracting universal critical exponents from the correlation profiles is complicated by many possible biases, mainly: finite temperature, finite-size effects and detection errors.

Second, we have observed Friedel oscillations around an impurity and have verified the expected dependence of the oscillation wavevector with the magnetization.

Chapter 5

Quench spectroscopy, a new method to measure the dispersion relation of quasi-particles

> If you want to find the secrets of the universe,
> think in terms of energy, frequency, and vibration.
>
> Nikola Tesla

In the previous chapter, I have shown some equilibrium properties of the low-energy phases of the dipolar XY model. What is the nature of the energy spectrum above the ground state? The answer to this question governs the dynamics of the system at low energy. In this chapter, I present the first experimental realization of a new method to characterize the spectrum, termed *quench spectroscopy*. After a general presentation of the method (sec. 5.1), I show our results in the case of a one-dimensional chain (sec. 5.2) and in the case of a two-dimensional square lattice (sec. 5.3).

Contents

Contributors

This chapter is based on two papers: Emperauger et al. (2025) for the 1D spin chain, and Chen et al. (2023b) for the 2D square lattice. Those papers were written in collaboration with two teams of theoreticians based in Lyon (Filippo Caleca, Saverio Bocini, Fabio Mezzacapo, Tommaso Roscilde) and at Harvard (Marcus Bintz, Shubhayu Chatterjee, Vincent Liu, Norman Yao). Our work is based on the preliminary proposals Frérot et al. (2018); Villa et al. (2019, 2020) that introduced the theory of quench spectroscopy.

5.1 Presentation of the method

Let us consider a system with translational invariance, that hosts quasi-particles with a given dispersion relation. This means that excitations of the system are described by approximate eigenstates with a well-defined momentum $\mathbf{k}$ and energy $\omega_{\mathbf{k}}$. Mathematically, the Hamiltonian H of the many-body system at low $|\mathbf{k}|$ can be approximated to the one of free quasi-particles:

$$H = \sum_{\mathbf{k}} \hbar\omega_{\mathbf{k}}\, a^\dagger_{\mathbf{k}} a_{\mathbf{k}} + \text{higher-order terms in } \{a_{\mathbf{k}}, a^\dagger_{\mathbf{k}}\}. \tag{5.1}$$

Here $a_{\mathbf{k}}$ and $a^\dagger_{\mathbf{k}}$ are respectively the annihilation and creation operators for the quasi-particle with momentum $\mathbf{k}$. The dispersion relation $\omega_{\mathbf{k}}$ dictates the properties of the system at thermal equilibrium, such as the heat capacity, the electrical conductivity, the thermal conductivity, the compressibility, the susceptibility, etc. (Kittel, 2018). As we will see in this chapter, it also governs the dynamics of the system when quenching it from a low-energy state.

Traditional spectroscopy VS quench spectroscopy The aim of spectroscopy is to measure the dispersion relation $\omega_{\mathbf{k}}$. To this end, the traditional method in condensed matter systems is to prepare the system in an equilibrium state, ideally the vacuum state $|0\rangle$ that contains no quasi-particle, or more realistically a low-temperature state. Then, one applies a weak probe (light or matter field) that couples $|0\rangle$ to a state containing one quasi-particle, $a^\dagger_{\mathbf{k}}|0\rangle$. If the frequency of the probe is on resonance with $\omega_{\mathbf{k}}$, one quasi-particle at momentum $\mathbf{k}$ is created and can be detected. By scanning the frequency and the wavevector of the probe, one probes the dispersion relation. The quantitative behavior of the system under the perturbation can be analyzed in the framework of linear response theory (Forster, 2019), and gives rise to a variety of powerful methods such as neutron scattering (Brockhouse, 1995), X-ray scattering (Compton, 1923; Ament et al., 2011), Bragg scattering (Martin et al., 1988; Stenger et al., 1999) or angle-resolved photoemission spectroscopy (Sobota et al., 2021). In Fig. 5.1, I show examples of quasi-particles that are usually found in materials: for example, phonons are elementary vibrations of a crystal; magnons are spin waves above the magnetic ground state; exciton polaritons are hybrid quasi-particles made of a photon and an exciton (particle-hole).

One limitation of traditional spectroscopy is that equilibrium properties can be affected by decoherence. The ability offered by synthetic quantum systems to monitor

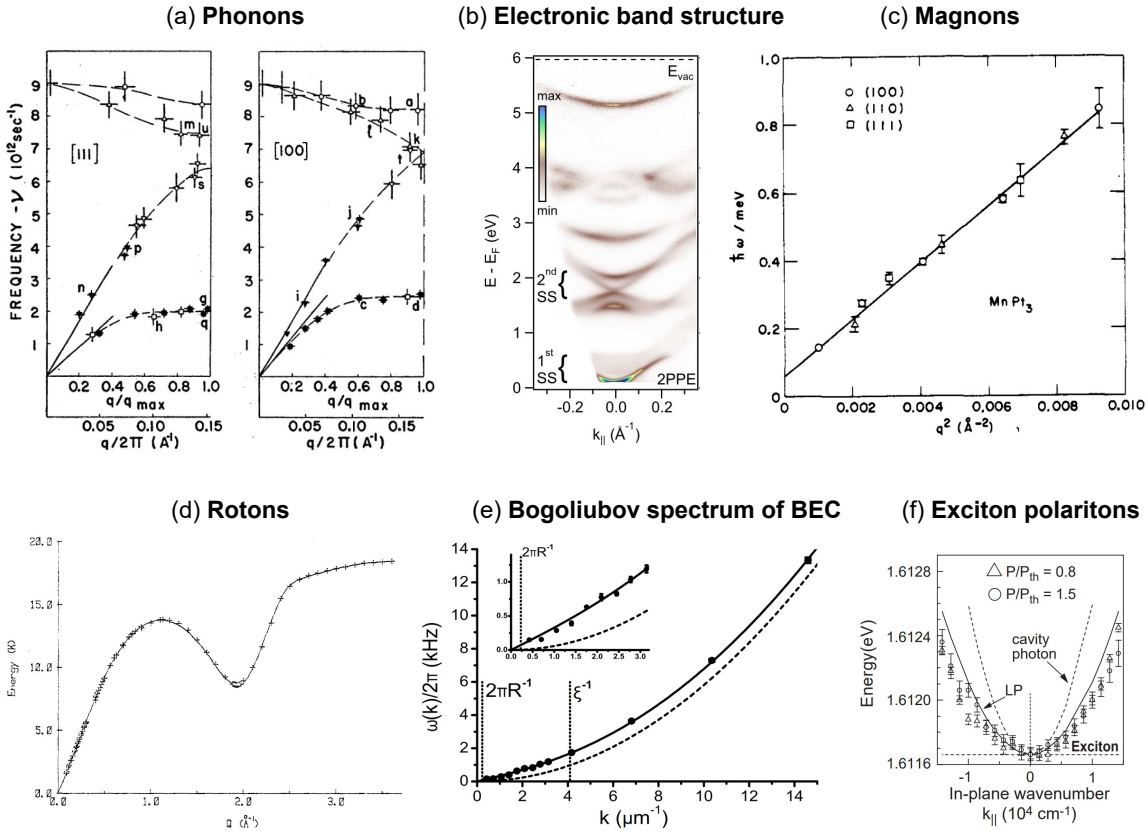

Figure 5.1: Examples of measured dispersion relations and associated quasi-particles in condensed matter materials and atomic gases. (a) Dispersion relation of phonons in a Germanium crystal using inelastic neutron scattering, taken from Brockhouse and Iyengar (1958). (b) Electronic band structure measured via ARPES, taken from Sobota et al. (2013). (c) Dispersion relation of magnons (also known as spin waves) in a ferromagnetic sample of $MnPt_3$ using inelastic neutron scattering, taken from Antonini and Minkiewicz (1972). (d) Dispersion relation of rotons in superfluid Helium II using inelastic neutron scattering, taken from Donnelly et al. (1981). (e) Bogoliubov spectrum of a Bose-Einstein condensate, measured by Bragg scattering in Steinhauer et al. (2002). (f) Dispersion relation of exciton polaritons in a GaAs multiple quantum-well microcavity, taken from Deng et al. (2002).

(nearly) unitary evolution, in both space and time, provides an alternative approach to probe the excitations: one can inject a finite density of excitations into the system and observe the subsequent dynamics – a so-called *quench experiment* (Mitra, 2018). Following the quench, the re-organization of spatial correlations is then dictated by the propagation of excitations, which is governed by their dispersion relation. In some cases, monitoring the correlations allows to reconstruct $\omega_{\mathbf{k}}$ (Frérot et al., 2018; Villa et al., 2019, 2020). This method is called *quench spectroscopy*.

"Proof" of the method In the remainder of this section, I present a framework that explains quench spectroscopy and its conditions of applications. It is adapted from the more general proof derived in Appendix A of Villa et al. (2019) [see also section 3.2 of Villa (2021)].

Let us consider the *equal-time correlator*

$$C_{ij}(t) \equiv \langle\psi(t)|\, \mathcal{O}_i\mathcal{O}_j\, |\psi(t)\rangle \tag{5.2}$$

where $\mathcal{O}_j$ is a local observable acting on spin j. Going to Fourier space, one can define the *time-dependent structure factor* (TSF) as

$$S(\mathbf{k},t) \equiv \frac{1}{N}\sum_{i,j} e^{i\mathbf{k}\cdot\mathbf{r}_{ij}} C_{ij}(t) \tag{5.3}$$

with $\mathbf{r}_{ij} \equiv \mathbf{r}_i - \mathbf{r}_j$ the distance between the spins i and j. The TSF can be written more simply as

$$S(\mathbf{k},t) = \langle\psi(t)|\, \mathcal{O}_{\mathbf{k}}\mathcal{O}_{-\mathbf{k}}\, |\psi(t)\rangle \tag{5.4}$$

with $\mathcal{O}_{\mathbf{k}} \equiv \frac{1}{\sqrt{N}}\sum_j e^{i\mathbf{k}\cdot\mathbf{r}_j}\mathcal{O}_j$ the Fourier transform of the local observable of interest. The TSF should not be confused with a very similar quantity used in spectroscopy, called the *dynamical structure factor* $\mathfrak{S}(\mathbf{k},\omega)$, which is defined as the spatial and temporal Fourier transform of the correlator at different times: $\mathfrak{S}(\mathbf{k},\omega) = \int dt\, \langle\psi(t)|\, \mathcal{O}_{\mathbf{k}}\mathcal{O}_{-\mathbf{k}}\, |\psi(0)\rangle\ e^{-i\omega t}$.

We are interested in the time evolution of the TSF $S(\mathbf{k},t)$ after a quench from the initial state $|\psi(0)\rangle$. If we denote by $|n\rangle$ the exact eigenstates of the many-body Hamiltonian H with eigenenergies ω_n, the unitary evolution of the state under H is given by

$$|\psi(t)\rangle = \sum_n c_n e^{-i\omega_n t}\, |n\rangle \tag{5.5}$$

with $c_n \equiv \langle n|\psi(0)\rangle = |c_n|e^{-i\varphi_n}$ the overlap of the initial state with eigenstate $|n\rangle$. Injecting Eq. (5.5) in Eq. (5.4), one gets

$$S(\mathbf{k},t) = \sum_{n,n'} |c_n||c_{n'}| e^{i(\omega_n-\omega_{n'})t + i(\varphi_n-\varphi_{n'})}\, \langle n|\, \mathcal{O}_{\mathbf{k}}\mathcal{O}_{-\mathbf{k}}\, |n'\rangle\,. \tag{5.6}$$

From Eq. (5.6), the evolution of the TSF is a complicated sum of many terms, each one oscillating at the difference of frequency $\omega_n - \omega_{n'}$ between two eigenstates $|n\rangle$ and

$|n'\rangle$. To simplify the expression, we make the hypothesis of a *weak quench*, that is to say, we assume that the initial state has a large overlap with the true ground state $|0\rangle$ and small overlaps with the excited states:

$$\forall n \neq 0,\ |c_n| \ll |c_0|. \tag{5.7}$$

For the simplicity of the notations, we also set $\omega_0 = 0$ and $\phi_0 = 0$, which can be simply interpreted as fixing a global energy offset and the origin of time. Using the assumption of a weak quench given by Eq. (5.7), one can rewrite Eq. (5.6) at first order in the coefficients $\{|c_n|\}_{n\neq 0}$:

$$S(\mathbf{k},t) \approx \underbrace{|c_0|^2 \langle 0|\, \mathcal{O}_{\mathbf{k}}\mathcal{O}_{-\mathbf{k}}\, |0\rangle}_{0^{\text{th}}\text{ order}} + \underbrace{|c_0| \sum_{n\neq 0} |c_n| e^{i(\omega_n t+\varphi_n)} \langle n|\, \mathcal{O}_{\mathbf{k}}\mathcal{O}_{-\mathbf{k}}\, |0\rangle + \text{c.c.}}_{1^{\text{rst}}\text{ order}} \tag{5.8}$$

Defining the amplitude

$$A_n(\mathbf{k}) \equiv \frac{1}{2}|c_0|\ |c_n|\ \left|\langle n|\, \mathcal{O}_{\mathbf{k}}\mathcal{O}_{-\mathbf{k}}\, |0\rangle\right| \tag{5.9}$$

and the renormalized phase $\phi_n(\mathbf{k}) \equiv \varphi_n + \arg\left(\langle 0|\, \mathcal{O}_{\mathbf{k}}\mathcal{O}_{-\mathbf{k}}\, |0\rangle\right)$, one can finally rewrite the TSF as

$$S(\mathbf{k},t) \approx \underbrace{A_0(\mathbf{k})}_{0^{\text{th}}\text{ order}} + \underbrace{\sum_{n\neq 0} A_n(\mathbf{k}) \cos\left[\omega_n t + \phi_n(\mathbf{k})\right]}_{1^{\text{rst}}\text{ order}}. \tag{5.10}$$

While the zeroth-order term is a constant, the first order term is a sum of sine waves corresponding to the eigenvectors of the Hamiltonian. A necessary condition for the oscillation at frequency ω_n to be measured is that the associated amplitude $A_n(\mathbf{k})$ is not zero. According to Eq. (5.9), this is the case when

1. $|c_n| \neq 0$: the initial state has an overlap with eigenstate $|n\rangle$;

2. $\left|\langle n|\, \mathcal{O}_{\mathbf{k}}\mathcal{O}_{-\mathbf{k}}\, |0\rangle\right| \neq 0$: the two-body operator couples $|0\rangle$ to $|n\rangle$.

To satisfy the second condition, it is sufficient that the eigenstate $|n\rangle$ is composed of two quasi-particles with opposite momenta: $|n\rangle = a^\dagger_{\mathbf{k}} a^\dagger_{-\mathbf{k}} |0\rangle$. In this case, one gets that $\omega_n = \omega_{\mathbf{k}} + \omega_{-\mathbf{k}}$. Hence, if $\omega_{\mathbf{k}} = \omega_{-\mathbf{k}}$ (time-reversal invariance), $S(\mathbf{k},t)$ oscillates at frequency $2\omega_{\mathbf{k}}$.

	Traditional spectroscopy	Quench spectroscopy
Momentum resolution	Scan wavevector of probe field	Measure with single-particle resolution and perform Fourier transform in space
Frequency resolution	Scan frequency of probe field	Scan evolution time and extract oscillation frequency (Fourier transform in time or fit)
Requirements	- Weak probe (linear response regime) - non-zero coupling of initial state to excited states via the probe	- Weak quench (low-energy initial state) - non-zero coupling of initial state to excited states via the measured correlator

Table 5.1: Comparison between traditional and quench spectroscopy.

Protocol The previous derivation suggests the following protocol for measuring the dispersion relation:

1. quench the system from an initial state $|\psi(0)\rangle$ that has a large overlap with the ground state, but still some overlap with the excited states (typically, $|\psi(0)\rangle$ can be a mean-field ground state);

2. measure the equal-time correlations between all pairs of spins, and compute the TSF for every wavevector $\mathbf{k}$ (in practice, the observable $\mathcal{O}_j$ can be chosen as a spin component σ_j^z);

3. extract the oscillation frequency $2\omega_{\mathbf{k}}$ of every $S(\mathbf{k}, t)$.

According to the previous reasoning, $\omega_{\mathbf{k}}$ can be interpreted as the dispersion relation of the quasi-particle with momentum $\mathbf{k}$. We summarize in Tab. 5.1 the differences and similitudes between traditional and quench spectroscopy.

The way to extract the oscillation frequency of $S(\mathbf{k}, t)$ can be to perform a fit by a sine wave, or a Fourier transform in time. For this reason, some authors define another quantity called the *quench spectral function* (Villa et al., 2019), which is simply the Fourier transform in time of the TSF:

$$\begin{aligned} S(\mathbf{k}, \omega) &\equiv \int dt\, S(\mathbf{k}, t)\, e^{-i\omega t} \\ &\approx \underbrace{2\pi A_0(\mathbf{k})\, \delta(\omega)}_{0^{\text{th}}\text{ order}} + \underbrace{2\pi \sum_{n\neq 0} A_n(\mathbf{k}) \left[e^{i\phi_n(\mathbf{k})}\, \delta(\omega_n - \omega) + e^{-i\phi_n(\mathbf{k})}\, \delta(\omega - \omega_n)\right]}_{1^{\text{rst}}\text{ order}} \end{aligned} \tag{5.11}$$

A similar method was already demonstrated by Jurcevic et al. (2015) with trapped ions: it consisted in preparing superposition states with well-defined wavevector $|\psi(t=0)\rangle = c_{\mathbf{k}} a^\dagger_{\mathbf{k}} + c_{\mathbf{k}'} a^\dagger_{\mathbf{k}'}$ (by means of local rotations), monitoring its time evolution and performing a Fourier-transform in time of the single-atom magnetization to access the frequency difference $\omega_{\mathbf{k}'} - \omega_{\mathbf{k}}$. One of the key differences with our method is that quench spectroscopy can extract the dispersion relation from the dynamics of a single initial state, whereas in their case the measurement of the dynamics had to be repeated for different initial states characterized by various wavevectors $\mathbf{k}, \mathbf{k}'$.

Take-home message

Quench spectroscopy is a method that allows to reconstruct the dispersion relation of a system by monitoring the correlations during its time evolution. It is based on three conditions:

- translational invariance, to allow for the existence of a dispersion relation;
- weak quench: the initial state must have small, but non-zero overlap with the quasi-particles ($|c_n| \neq 0$);
- non-zero coupling of the eigenstates $|n\rangle$ with the vacuum state $|0\rangle$ through the two-body correlator of interest ($|\langle n| \mathcal{O}_{\mathbf{k}} \mathcal{O}_{-\mathbf{k}} |0\rangle| \neq 0$).

5.2 Excitations of a 1D spin chain

To start with, we apply the method of quench spectroscopy to a chain of $N = 30$ spins arranged in a circular geometry, similar to the system studied in chapter 4. The periodic boundary conditions make the system truly invariant under translation, which, as we saw in sec. 5.1, is a necessary condition for a well-defined dispersion relation.

We use the mapping $|\uparrow\rangle = \left|60S_{1/2}, m_J = 1/2\right\rangle$ and $|\downarrow\rangle = \left|60P_{1/2}, m_J = -1/2\right\rangle$ to implement the dipolar XY model:

$$H_{\mathrm{XY}} = \frac{\hbar J}{2} \sum_{i<j} \left[\frac{a}{r_{ij}}\right]^3 \left(\sigma_i^x \sigma_j^x + \sigma_i^y \sigma_j^y\right) \tag{5.12}$$

with lattice spacing $a = 13$ µm and nearest-neighbor interaction energy $J/2\pi = -0.62$ MHz.

Ballistic propagation of correlations Let us start by explaining how we measure the dispersion relation for the excitations above the FM ground state. To do so, we initialize the system in the classical FM state along y [Fig. 5.2(a)]: $|\psi(0)\rangle = |\mathrm{FM}_y\rangle = |{\rightarrow_y}\rangle^{\otimes N}$, which is the mean-field ground state of the XY model [see appendix A]. Although having a low energy, this state is not the many-body ground-state, as explained in chapter 5: it has a large overlap with the ground states of each M_z manifold, but also with excited states.

After preparing $|\mathrm{FM}_y\rangle$, we let the state evolve under H_{XY} during a time t, and measure the state along z. The experimental sequence is shown in Fig. 5.2(c). We monitor the connected spin correlations $C_{ij}^z(t)$ for all pairs i and j, and compute their average over pairs separated by the same distance, $C^z(d,t)$, where d is the perimeter distance along the ring. The results are shown in Fig. 5.3(a). We observe two distinct behaviors depending on the distance: on the one side, nearest-neighbor correlations ($d = 1$ site) build-up in less than $1/J$ and reach a quasi-stationary negative value; on the other side, for $d > 1$ sites, a positive correlation wavefront spreads ballistically from $d = 2$ sites up to the largest distances. We interpret this ballistic propagation as a light-cone having a velocity v_{FM}, such that $d = v_{\mathrm{FM}}\, tJ$. The value of v_{FM} is extracted by a two-dimensional fit of $C^z(d,t)$ for $d > 1$, and shown by the dotted black line in Fig. 5.3(a). We obtain $v_{\mathrm{FM}} = 4.68 \pm 0.09$[1].

[1] This velocity is given in dimensionless units, since distance is in units of the lattice spacing $a = 13$ µm, and time in units of $1/J = 0.26$ µs. Physically, $v_{\mathrm{FM}} = 4.68$ corresponds to $v_{\mathrm{FM}} a\, J \approx 240$ µm/µs.

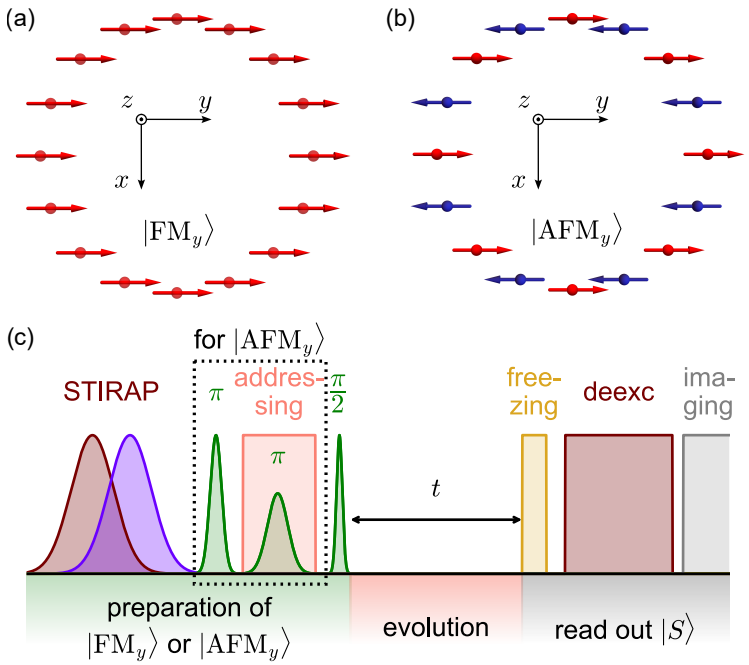

Figure 5.2: Protocol for the quench experiment. The initial state of the quench is a classical ferromagnet along y (a), or a classical antiferromagnet along y (b). The experimental sequence is shown in (c): we first prepare the classical magnet, then let it evolve under the dipolar XY Hamiltonian, and finally read out the state in the z-basis.

A linear dispersion relation To obtain the dispersion relation, we first perform a spatial Fourier transform of the correlations to get the time-dependent structure factor (TSF)

$$S(k,t) \equiv \frac{1}{N} \sum_{i,j} e^{i\,k\,d_{ij}} C^z_{ij}(t). \tag{5.13}$$

Here, the distances d_{ij} are expressed in lattice sites, and the wavevector k in rad/sites living in the Brillouin zone $[0, 2\pi]$. In Fig. 5.3(b), we plot the TSF after having removed its time average $\bar{S}(k) \equiv \frac{1}{T}\int_0^T S(k,t)$ on the full duration T of the experimental sequence. For each value of k, we observe a short-lived oscillation, with a period that gets smaller as k approaches π. Finally, we perform a Fourier transform in time to get the quench spectral function

$$S(k,\omega) \equiv \int dt\, S(\mathbf{k},t)\, e^{-i\omega t}, \tag{5.14}$$

whose real part is plotted in Fig. 5.3(c). Two linear energy branches appear from $k = 0$ and $k = 2\pi$, corresponding to $\omega/J = v_{\mathrm{FM}}\, k$. According to sec. 5.1, the dispersion

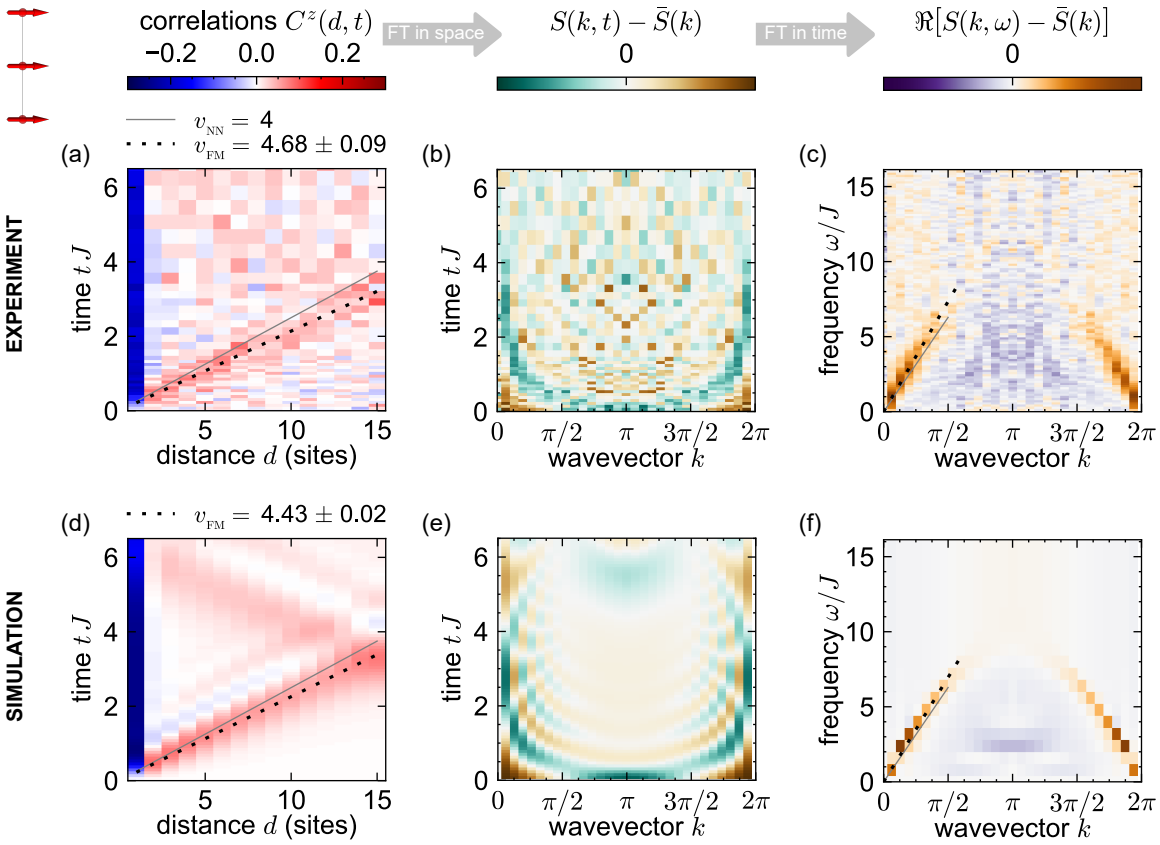

Figure 5.3: Quench spectroscopy of the 1D dipolar XY model in the FM sector, for a linear chain of $N = 30$ spins. (a) Measured spin-spin correlations along z, $C^z(d,t)$, starting from the initial state $|\mathrm{FM}_y\rangle$. The lines show a ballistic spreading with velocity v: $d = v\,tJ$, with v_{NN} the expected sound velocity in the nearest-neighbor case, and v_{FM} the velocity extracted from a two-dimensional fit of the positive ballistic wavefront. (b) Time-dependent structure factor $S(k,t)$ for different wavevectors k in the first Brillouin zone. For clarity, we remove the time average $\bar{S}(k)$ for each k. (c) Real part of the quench spectral function $S(k,\omega)$ (after removing $\bar{S}(k)$), showing twice the dispersion relation. The lines show linear energy branches $\omega/J = v\,k$, with the same velocities as in (a). (d,e,f) Numerical simulations of the same quantities as in (a,b,c), performed by Cheng Chen using the software ITensor (Fishman et al., 2022).

relation of quasi-particles can be interpreted as

$$\begin{aligned} \omega_k/J &= \frac{1}{2} v_{\mathrm{FM}}\, k \\ &= u_{\mathrm{FM}}\, k \end{aligned} \tag{5.15}$$

with $u_{\mathrm{FM}} \equiv v_{\mathrm{FM}}/2$ the *sound velocity* of the quasi-particles. u_{FM} can be interpreted as the group velocity of the quasi-particles: $u_{\mathrm{FM}} = \nabla\omega_k/J$. This is in agreement with the theory of Tomonaga-Luttinger liquids (TLL), which predicts a linear dispersion relation at low k [see appendix B]; the associated quasi-particles are often referred to

as the sound modes of the TLL phase.

Effect of dipolar interactions on the sound velocity To estimate u_{FM}, we perform a two-dimensional fit of the ballistic propagation, from which we extract $v_{\mathrm{FM}} = 4.68 \pm 0.09$. This velocity can be compared to the expected sound velocity in the case of nearest-neighbor interactions, $v_{\mathrm{NN}} = 4 < v_{\mathrm{FM}}$. We interpret this result as an effect of dipolar interactions: in the FM case, interactions are ferromagnetic for all distances, which lead to a faster propagation of correlations compared with the nearest-neighbor case. Interestingly, the obtained FM sound velocity is smaller than the one extracted based on thermodynamic considerations with the TLL theory[2]. Numerical simulations of the ideal unitary dynamics [Fig. 5.3(d,e,f)] agree very well with our data, ruling out experimental imperfections as the origin of the discrepancy. Instead, we attribute the failure of the TLL prediction to a finite-size effect: additional numerical simulations of the spectrum (not shown) reveal that the linear sound mode involves only very few wavevectors in our $N = 24$ ring. Our interpretation is thus that the observed quasi-linear energy branches are actually already slightly curved towards smaller energies, resulting in a slower ballistic propagation than the one in the thermodynamic limit.

Going beyond TLL theory, the Bethe-Ansatz theory predicts a continuum of excitations at $k = \pi$ [see for instance Fig. 5.6 of Giamarchi (2004)] which was already observed in condensed matter compounds, such as in Heisenberg spin chains (Tennant et al., 1995; Lake et al., 2005; Scheie et al., 2022). However, we do not observe such a well-defined continuum in our data, neither in the ideal simulation. One hypothesis to explain the absence of the continuum in the quench spectrum is that the initial state $|\mathrm{FM}_y\rangle$ has a vanishing overlap with this part of the spectrum, preventing from seeing oscillations around $k = \pi$.

We can adapt the previous method to measure the dispersion relation of excitations above the AFM ground state (that is to say, excitations of $-H_{\mathrm{XY}}$). Instead of starting the quench from a classical FM state, we initialize the system in a classical antiferromagnetic state along y, as pictured in Fig. 5.2(b). This state is a mean-field approximation of the true AFM ground state. The analysis of the results is shown in Fig. 5.4. We observe features that are qualitatively identical to the FM case, with a sound velocity $v_{\mathrm{AFM}} = 3.26 \pm 0.01$ which is now smaller than the nearest-neighbor case $v_{\mathrm{NN}} = 4$. The dipolar interactions have an opposite effect compared with the FM case:

[2] The TLL sound velocity can be estimated numerically, from the compressibility κ_{FM} and the relation $\kappa_{\mathrm{FM}} = \dfrac{K_{\mathrm{FM}}}{u_{\mathrm{FM}}\pi}$ [see Eq. (2.59) of Giamarchi (2004)].

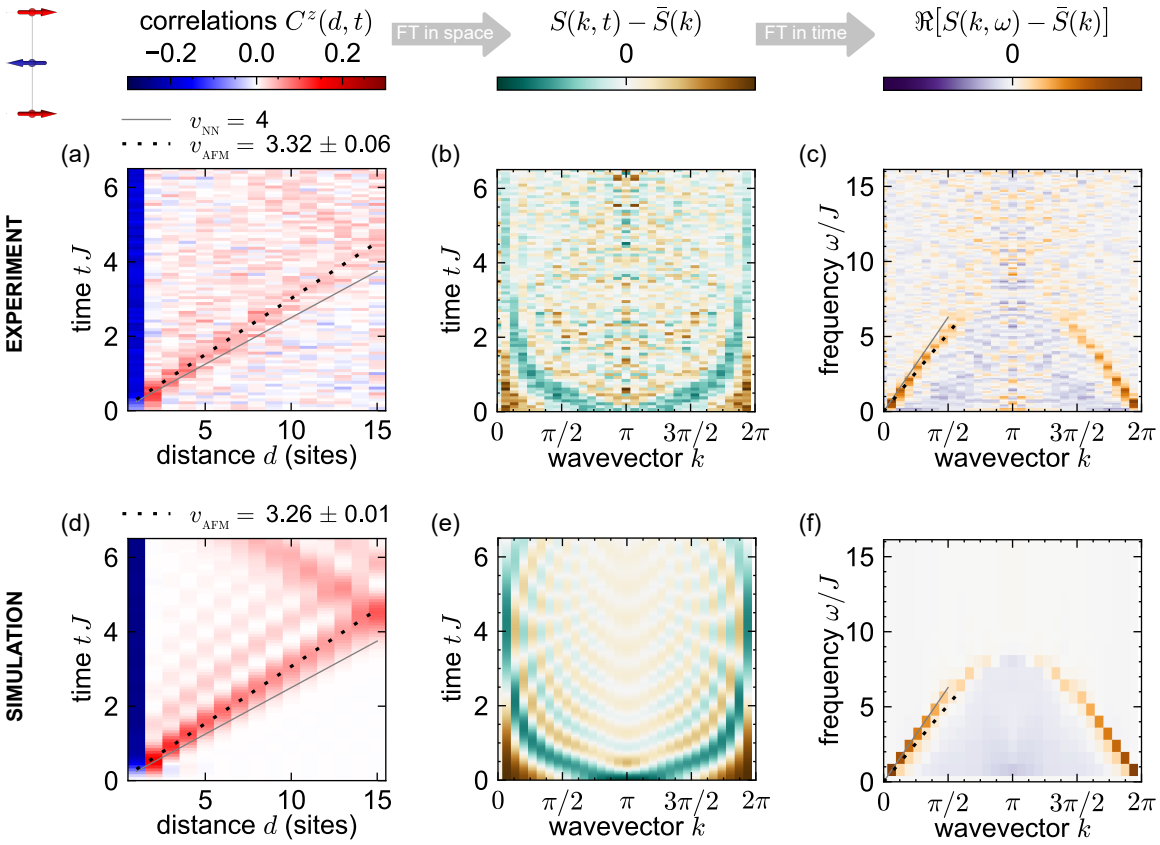

Figure 5.4: Quench spectroscopy of the 1D dipolar XY model in the AFM sector, for a linear chain of $N = 30$ spins. The quantities are the same as Fig. 5.3, but starting from the initial state $|\mathrm{AFM}_y\rangle$.

this time, interactions are staggered, so they partially compensate each other, which lead to a slower propagation than in the nearest-neighbor case (and also than the FM case). Compared with the expected sound velocity at low k in the thermodynamic limit $v_{\mathrm{AFM}} = 3.6$, the obtained sound velocity is still smaller, probably for the same reason as in the FM case.

What limits the resolution of the method? At first, the resolution of the spectrum is set by the discretization of the Fourier transforms. The momentum steps are fixed to $\delta k = 2\pi/N$ with N the number of spins, and the frequency steps to $\delta\omega = 2\pi/\Delta t$ with Δt the time window of the experiment. We can also do zero-padding to decrease "artificially" those steps. However, the quench spectral functions shown in Fig. 5.3(c,f) and 5.4(c,f) have a width that is larger than the steps. In the time domain, this corresponds to damped oscillations, an effect that goes beyond the simple picture of free quasi-particles presented in sec. 5.1. Several effects can induce a damping of the TSF:

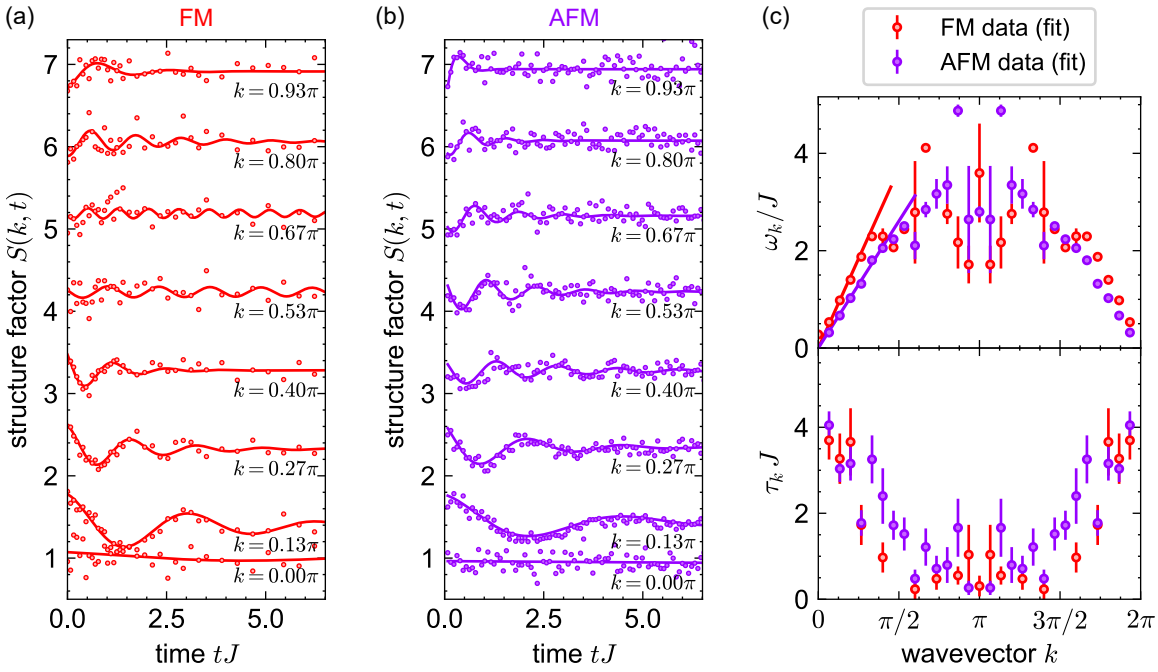

Figure 5.5: Beyond free quasi-particles? Analysis of the damping of the time-dependent structure factor. (a) Selection of fits of the TSF by Eq. (A.5) in the FM case. (b) Same in the AFM case. (c) Angular frequency and exponential damping time extracted from the fits. Points with too large error bars are removed. The solid lines correspond to the expected linear dispersion relation at low k, $\omega_k/J = \frac{1}{2} v\, k$, where $v_{\mathrm{FM}} = 4.68$ and $v_{\mathrm{AFM}} = 3.32$ are extracted from the propagation of the correlations [see Fig. 5.3(a) and Fig. 5.4(a)].

- the finite lifetime of the quasi-particles, due to interactions between them;
- the presence of several bands of quasi-particles, or even a continuum of them, at a given k;
- the breakdown of the approximation of a "weak quench", leading to the apparition of many more oscillation frequencies corresponding to the transitions between two arbitrary eigenstates, and not only the transitions from the ground state to the excited states [see sec. 5.1];
- decoherence, due to interactions with the environment.

Interestingly, the damping present in the experimental data [Fig. 5.3(b) and 5.4(b)] also occurs in the ideal simulation [Fig. 5.3(e) and 5.4(e)], ruling out decoherence as the only source of damping.

Disentangling the various possible sources of damping would require further analysis. However, one can use the data to quantify it. To do so, we fit $S(k,t)$ for each value

of k by a damped sine wave:

$$S(k,t) = A_k \cos\left(2\omega_k t + \phi_k\right) e^{-t/\tau_k} + C_k. \tag{5.16}$$

The results are shown in Fig. 5.5. As k increases, the angular frequency of the oscillations $2\omega_k$ increases, in agreement with the dispersion relation obtained previously. Meanwhile, τ_k decreases, signaling a faster damping. Compared with the extracted damping of the ideal simulations (not shown), the experimental damping is on average faster by about 50 %, but the general tendency remains the same. Around $k = \pi$, the extracted oscillation frequencies have very large error bars due to the fast damping. The physical origin of this damping remains to be explained.

Take-home message

Applying the method of quench spectroscopy on a dipolar XY spin chain, we observe the propagation of a ballistic correlation wavefront. This translates into a linear dispersion relation at low wavevectors, in agreement with the Tomonaga-Luttinger theory. The associated sound velocity is rescaled compared with the well-studied case of nearest-neighbor interactions: it is increased in the FM case and decreased in the AFM case. A more careful analysis reveals that the time-dependent structure factor is damped, an effect that goes beyond the linear regime presented in sec. 5.1.

5.3 Spin waves of a 2D square lattice

What do we expect in 2D? We now turn to the analysis of the quasi-particle excitations on a two-dimensional square lattice. Due to the dipolar character of the interactions, the dispersion relation at low wavevector $\mathbf{k}$ is predicted to remain linear ($\omega_{\mathbf{k}} \propto |\mathbf{k}|$) in the AFM case, whereas it becomes $\omega_{\mathbf{k}} \propto \sqrt{|\mathbf{k}|}$ in the FM case (Peter et al., 2012). The associated quasi-particles are called *spin waves* or *magnons*, and the link with the XY Hamiltonian can be understood in the framework of *linear spin wave* (LSW) theory (Frérot et al., 2017, 2018). More precisely, Roscilde et al. (2023) predicted that the dynamics of the system following a quench is governed by two independent Hamiltonians: on the one side, a "rotor" term with all-to-all couplings; on the other side, the spin wave excitations. By working in the z-basis, we can forget about the dynamics induced by the rotor part, since it commutes with all spin observables along z[3]. We thus expect the dynamics to be dictated mainly by the spin waves. In the following work, we aim at testing the validity of LSW theory experimentally.

Here, we use the mapping $|\uparrow\rangle = \left|60S_{1/2}, m_J = 1/2\right\rangle$ and $|\downarrow\rangle = \left|60P_{3/2}, m_J = -1/2\right\rangle$ with lattice spacing $a = 15$ µm, which leads to a nearest-neighbor interaction energy $J/2\pi = -0.25$ MHz. We use the same experimental sequence as in the 1D case, on a $N = 10 \times 10$ square lattice.

Here, contrary to the 1D case, we do not have periodic boundary conditions (PBC), so the lattice is not invariant under translation, and the momentum $\mathbf{k}$ is not strictly speaking a good quantum number. However, edge effects should decrease as the system size increases, so one can hope that the dispersion relation can be observed for large-enough system size. In the following, I will show that this approximation is actually quite crude, but that one can rely on further approximations to access the dispersion relation. I will show three methods that allow us to probe the dispersion relation, from the most naive to the most educated one.

A first naive and blind approach: Fourier transforms First, we perform the same blind analysis as in the 1D case: we measure the space-time evolution of the connected correlations along z and compute their two-dimensional Fourier transform to get the quench spectral function. Let us start by analyzing the quench from the classical FM

[3]The time evolution of $|\psi(0)\rangle = |\mathrm{FM}_y\rangle$ due to the rotor is actually very rich and was already studied theoretically in Comparin et al. (2022b,a). In particular, it was predicted to lead to the apparition of squeezed states and multi-headed cat states. We checked those predictions experimentally in Bornet et al. (2023), together with Franke et al. (2023) and Eckner et al. (2023).

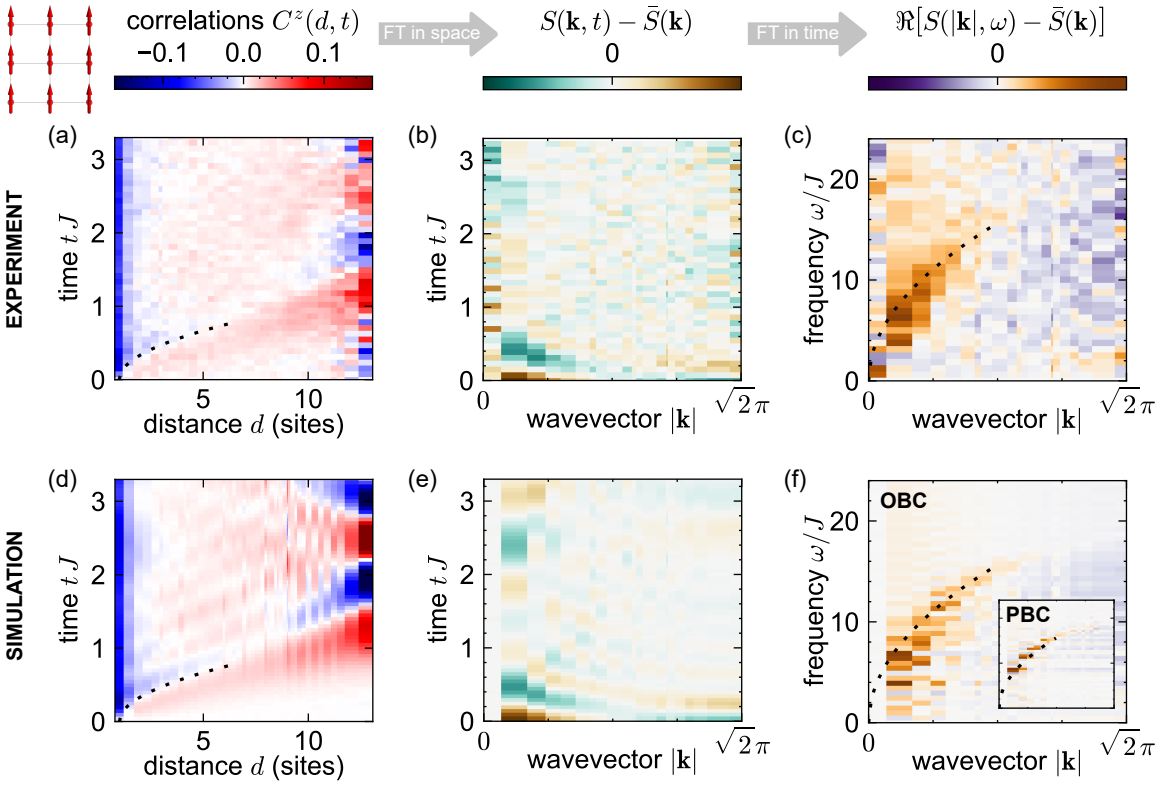

Figure 5.6: Quench spectroscopy of the 2D dipolar XY model in the FM sector, on a $N = 10 \times 10$ square lattice. To reduce statistical error bars, we allow for at most two holes and two extra-atoms in the initial array. (a) Measured spin-spin correlations along z, $C^z(d,t)$, starting from the initial state $|\mathrm{FM}_y\rangle$. The dotted line is a guide-to-the-eye showing superballistic propagation starting at site 1 ($d-1 \propto t^2$). (b) Time-dependent structure factor $S(\mathbf{k},t)$ for different wavevectors $|\mathbf{k}|$ in the first Brillouin zone. For clarity, we remove the time average $\bar{S}(\mathbf{k})$ for each $\mathbf{k}$. (c) Real part of the quench spectral function $S(\mathbf{k},\omega)$ (after removing $\bar{S}(\mathbf{k})$), showing twice the dispersion relation. The dotted line shows a dispersion relation $\omega/J \propto \sqrt{|\mathbf{k}|}$. (d,e,f) Numerical simulations of the same quantities as in (a,b,c), performed with open boundary conditions (OBC) by our theory team in ENS Lyon using tVMC. Inset of (f) shows the quench spectral function simulated with periodic boundary conditions (PBC).

state $|\mathrm{FM}_y\rangle = |{\rightarrow_y}\rangle^{\otimes N}$. The correlations in the 2D FM case are shown in Fig. 5.6(a). They evolve quite differently from the 1D case: whereas the 1D FM quench was showing a well-defined ballistic spreading of a positive correlation wavefront [Fig. 5.3(a)], the 2D FM quench shows a more complex structure with alternating signs of correlations up to the largest distances. We cannot identify a single wavefront anymore, and correlations seem to build up faster than ballistically, as pictured by the dashed line $d-1 \propto t^2$ in Fig. 5.6(a).

We then apply a spatial Fourier transform to obtain the time-dependent structure factor $S(\mathbf{k},t)$ [Fig. 5.6(b)], with $\mathbf{k} \in \left\{\frac{2\pi}{10}\left(n_x\mathbf{e}_x + n_y\mathbf{e}_y\right)\right\}_{n_x,n_y\in[\![0,9]\!]}$. In Fig. 5.6(b), we

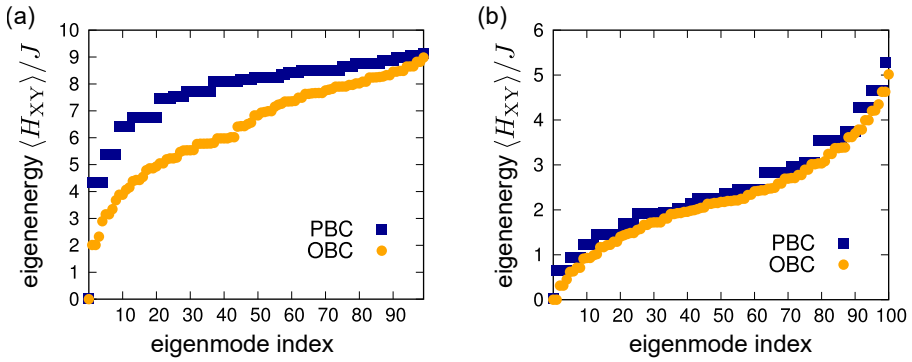

Figure 5.7: Simulated spin-wave eigenmodes of the 2D dipolar XY model on a $N = 10 \times 10$ square array, for FM (a) and AFM (b) interactions (Chen et al., 2023b). We contrast periodic (PBC) with open (OBC) boundary conditions.

plot $S(\mathbf{k}, t)$ as a function of the norm of the wavevector $|\mathbf{k}|$, and observe oscillations that are rather short-lived. A Fourier transform in time finally gives us the quench spectral function $S(\mathbf{k}, \omega)$, which shows a broad energy branch at small $|\mathbf{k}|$. The dispersion relation appears less clearly than in the 1D case; in particular, for some values of $\mathbf{k}$, the TSF does not even oscillate at a single frequency. A numerical simulation of the dynamics under the XY Hamiltonian on an ideal 10×10 system with open boundary conditions shows very similar features [Fig. 5.6(d,e,f)], showing that the broad range of frequencies is not due to experimental imperfections. Instead, the same simulation can be performed with periodic boundary conditions, revealing a much cleaner dispersion relation $\omega \propto \sqrt{|\mathbf{k}|}$ [inset of Fig. 5.6(f)]. A simulation of the low-energy eigenstates of the XY model, as shown in Fig. 5.7(a), confirms that the low-energy eigenstates with OBC have much lower eigenenergies as compared with PBC. From this analysis, we conclude that our system size is not large enough to remove the effects of OBC in the FM case. The experimentally-obtained spectrum is not incompatible with the PBC dispersion relation, if we only consider the "highest frequencies" that are populated in the quench. Such a dispersion relation is materialized by a guide-to-the-eye $\omega \propto \sqrt{|\mathbf{k}|}$ in Fig. 5.7(c,f).

We now perform the same analysis in the AFM case. The propagation of correlations starting from the AFM mean-field ground state $|\mathrm{AFM}_y\rangle$ is shown in Fig. 5.7(a). It looks closer to the 1D case than to the FM 2D case, with a positive wavefront that propagates at a speed $v_{\mathrm{AFM}} \approx 2.2$ (in units of aJ). The dynamics is much slower than in the FM case, an effect that can be attributed to the long-range dipolar tail of the interactions as in the 1D case. The corresponding quench spectral function [Fig. 5.7(c)] is compatible with the predicted linear dispersion relation $\omega \propto |\mathbf{k}|$, although with a large width in the frequency domain (or equivalently, a fast damping in the time

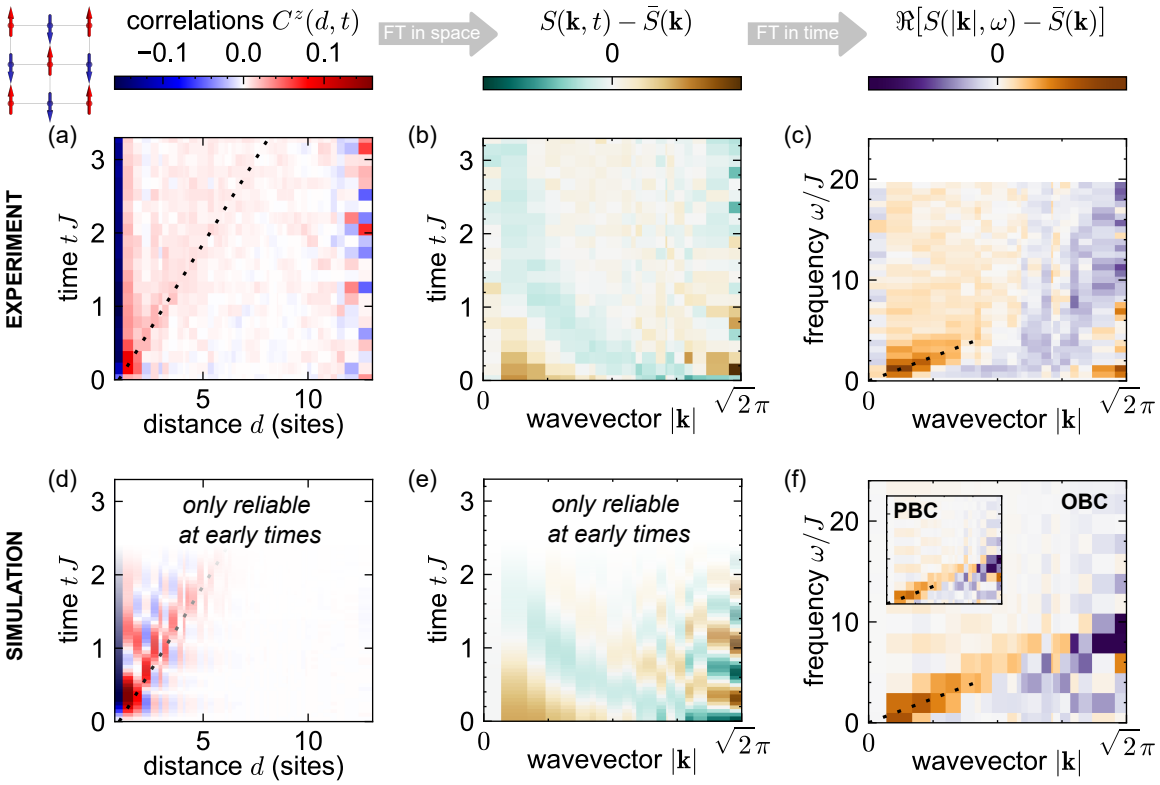

Figure 5.8: Quench spectroscopy of the 2D dipolar XY model in the AFM sector, on a $N = 10 \times 10$ square lattice. To reduce statistical error bars, we allow for at most two holes and two extra-atoms in the initial array. The quantities are the same as Fig. 5.6, but starting from the initial state $|\mathrm{AFM}_y\rangle$. Note that the simulations in the AFM sector are much harder than in the FM case due to frustration, making it only reliable at short times. For the Fourier transform, we only consider times smaller than $tJ = 1.5$, resulting in the small frequency resolution in Fig. 5.8(f).

domain). Contrary to the FM case, two numerical simulations rule out the OBC as the physical origin of the damping in the AFM case[4]: first, according to Fig. 5.8(f), the quench spectral function is very similar with OBC and PBC; second, according to Fig. 5.7(b), the eigenenergies are also very similar. This suggests that the eigenstates of the AFM state depend weakly on the boundary conditions, an effect that can be intuitively understood as the fact that the staggered AFM interactions average each other, resulting in an effective short-range description. As explained later, we believe that the physical origin of the damping is rather related to frustration, which reduces the lifetime of the spin waves.

From this first analysis, we conclude that reading the dispersion relation on the

[4]Note however that those numerical simulations (time-dependent variational Monte-Carlo, and LSW theory) rely on uncontrolled approximations to reduce the size of the Hilbert space of our $N = 10 \times 10$ array. As we will see in the following, those approximations become less justified in the AFM case due to geometrical frustration.

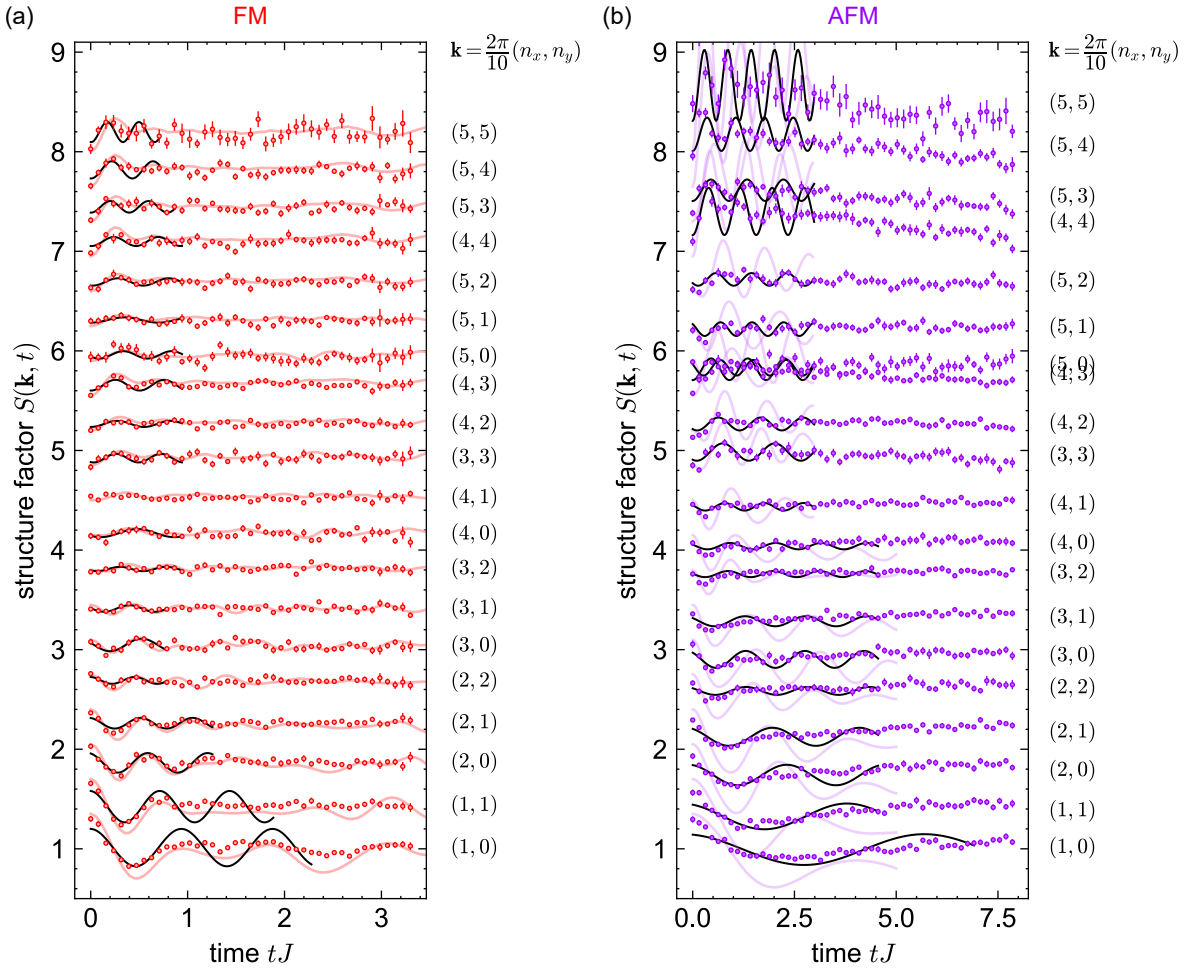

Figure 5.9: Fitting the early-time dynamics of the time-dependent structure factor, in the FM (a) and AFM (b) cases. Curves are offseted by 0.35 for clarity. The fits are indicated by the solid black lines. Solid colored lines show the ideal simulation of the dynamics using tVMC (only reliable at short times $tJ \ll 1$ in the AFM case).

quench spectral function is not obvious for a finite-size system with OBC. Still, the obtained spectra are not incompatible with the theory predictions of LSW theory, that is to say, at low $|\mathbf{k}|$, $\omega_{\mathbf{k}} \propto |\mathbf{k}|$ in the FM case and $\omega_{\mathbf{k}} \propto \sqrt{|\mathbf{k}|}$ in the AFM case. The qualitative difference between the 2D FM and the AFM cases is particularly striking, both in real space-time and in the Fourier domain, highlighting the role of the long-range tail of the dipolar interactions.

A more educated approach: fitting the early-time dynamics Is it possible to go further, and measure the dispersion relation of an ideal PBC system, despite the fact that our experimental system has OBC? To answer this question, we will make the assumption that the dynamics at short times is not affected by edge effects, such that

the early-time propagation of correlations is the same as in a system with PBC. This approximation is justified by a projective equivalence between OBC and PBC at short times [see Sec. V of the SM in Chen et al. (2023b)]. Based on this, one can try to fit the first oscillations of the TSF $S(\mathbf{k}, t)$ by a sine wave:

$$S(\mathbf{k}, t) = A_{\mathbf{k}} \cos\left(2\omega_{\mathbf{k}} t + \phi_{\mathbf{k}}\right) + C_{\mathbf{k}}. \tag{5.17}$$

Note that compared with the 1D case, we have removed the damping term, since we only care about the early dynamics. The resulting fits are all shown on Fig. 5.9. We now plot the fitted frequency $\omega_{\mathbf{k}}$ as a function of $|\mathbf{k}|$ in Fig. 5.10, and compare it with the prediction from LSW theory (Frérot et al., 2017, 2018):

$$\omega_{\mathbf{k}}^{\mathrm{LSW}} \equiv J_0 \sqrt{1 - \frac{J_{\mathbf{k}}}{J_0}}, \tag{5.18}$$

where the $\{J_{\mathbf{k}}\}$ are defined as the Fourier transforms of the interactions

$$J_{\mathbf{k}} \equiv \frac{1}{N} \sum_{i \neq j} e^{i\mathbf{k}\cdot\mathbf{r}_{ij}} J_{ij} \qquad \text{with} \quad J_{ij} \equiv J \left[\frac{a}{r_{ij}}\right]^3 \times \begin{cases} 1 & \text{in the FM case} \\ (-1)^{i+j+1} & \text{in the AFM case.} \end{cases} \tag{5.19}$$

To calculate $J_{\mathbf{k}}$, we use the physical interactions on our $N = 10 \times 10$ array with OBC.

As a result, the fitted frequencies provide a better defined dispersion relation, especially at low $|\mathbf{k}|$, meaning that we have partially filtered the multiple frequencies due to the OBC. The difference between the AFM and the FM cases appears even more clearly: the dispersion relation is slow and linear in the AFM case, and it is fast and non-linear in the FM case. In the FM case, we still obtain scattered data points at $|\mathbf{k}| > \pi/2$; and these residual deviations also appears when fitting the early dynamics of the ideal simulation, showing that this is not due to experimental imperfections. In Chen et al. (2023b), we explain the origin of these deviations as a subtle frequency shift at early times due to a constraint on the LSW theory.

An even more educated guess making use of linear spin-wave theory Finally, we discovered that the dispersion relation can also be accessed from the equilibration of the system. Indeed, the fit also provides us with a constant $C_{\mathbf{k}}$, which can be interpreted as the values towards which the TSF would converge after thermalization [in that sense, it is very similar to the time average of the TSF, $\bar{S}(\mathbf{k})$]. It turns out that LSW theory can predict the value of this constant. The analytical expression of

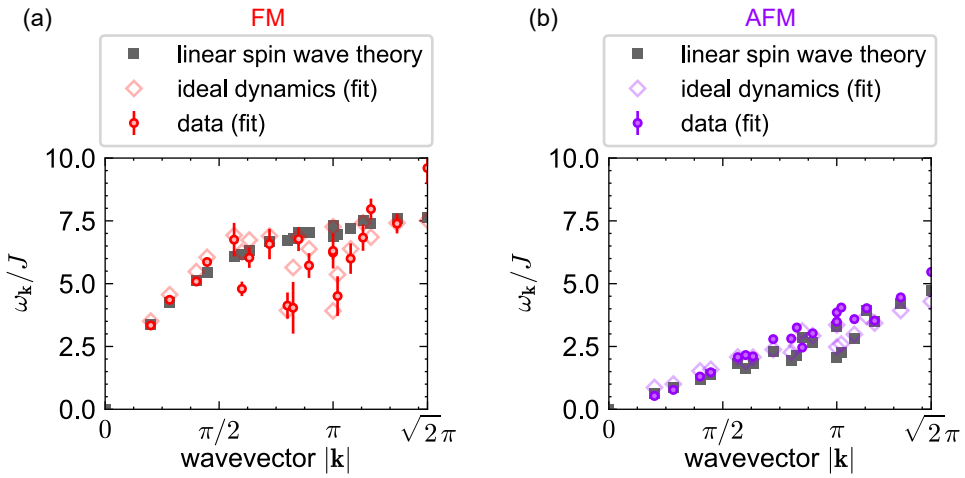

Figure 5.10: Dispersion relation obtained from the fitted frequencies of the time-dependent structure factor at early times, in the FM (a) and AFM (b) cases. The data points correspond to the frequency of fits shown in Fig 5.9. The empty red squares are fits of the ideal dynamics, simulated numerically using tVMC, using the same fitting windows as the data. The filled grey squares are $\{\omega_{\mathbf{k}}^{\mathrm{LSW}}\}$ from Eq. (5.19), calculated on our $N = 10 \times 10$ array.

the TSF according under the assumption of linear spin waves is

$$S^{\mathrm{LSW}}(\mathbf{k}, t) = A_{\mathbf{k}}^{\mathrm{LSW}} \cos\left(2\omega_{\mathbf{k}}^{\mathrm{LSW}} t\right) + C_{\mathbf{k}}^{\mathrm{LSW}}. \tag{5.20}$$

with

$$C_{\mathbf{k}}^{\mathrm{LSW}} \equiv 1 - \frac{J_{\mathbf{k}}}{2J_0}. \tag{5.21}$$

Combining Eq. (5.21) with Eq. (5.19), one obtains a relation between the offset and the frequency of the spin waves:

$$\omega_{\mathbf{k}}^{\mathrm{LSW}} = J_0\sqrt{2C_{\mathbf{k}}^{\mathrm{LSW}} - 1}. \tag{5.22}$$

In Fig. 5.11, we plot the fitted values of $C_{\mathbf{k}}$ and the obtained frequencies $J_0\sqrt{2C_{\mathbf{k}} - 1}$. In the FM case, we obtain a very good match the theory expectation, and a much smoother dispersion relation. Of course, this analysis is assuming that LSW theory applies, so this extraction procedure is nothing more than a self-consistency check. In the AFM case, the agreement of $C_{\mathbf{k}}$ with the spin wave prediction is correct, and so is the associated dispersion relation, although they show some deviations at small and at large wavevectors that we attribute to experimental imperfections. We can understand the effect of imperfections on the TSF by a simple model that assumes a

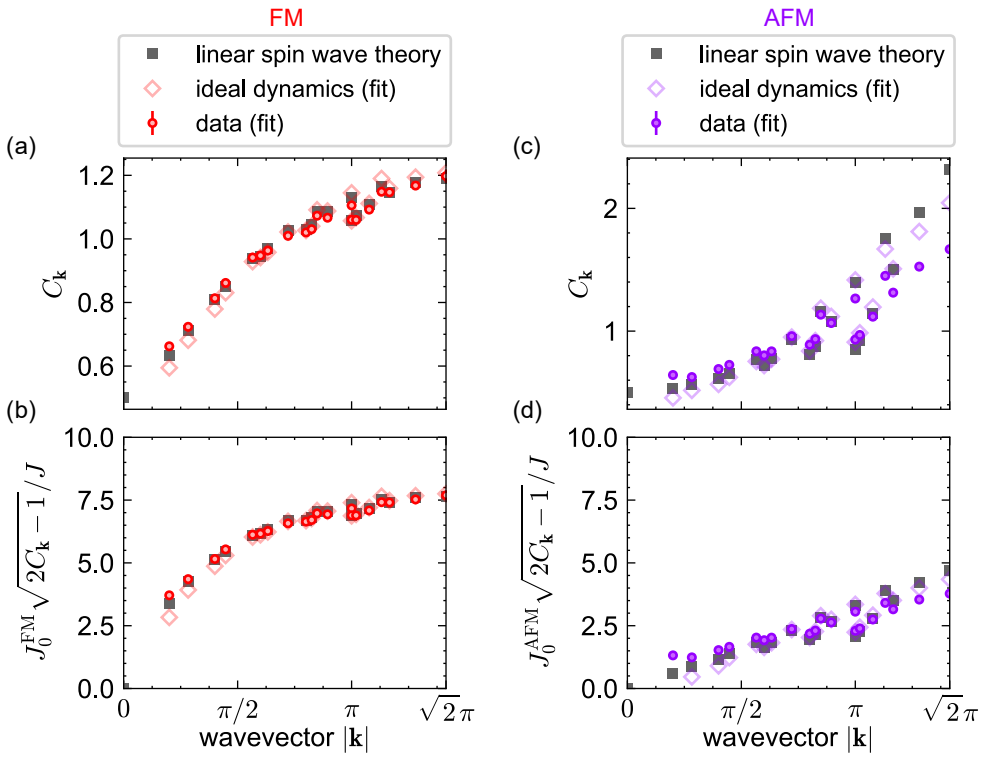

Figure 5.11: Dispersion relation obtained from the fitted offset of the time-dependent structure factor, and assuming that LSW theory holds. (a) Fitted offset of the fits shown in Fig 5.9. The empty red squares are fits of the ideal dynamics, simulated numerically using tVMC, using the same fitting windows as the data. The filled grey squares are $\{C_{\mathbf{k}}^{\mathrm{LSW}}\}$ from Eq. (5.21) for our $N = 10 \times 10$ array. (b) Inferred dispersion relation, obtained by injecting $C_{\mathbf{k}}$ in Eq. (5.22). (c,d) Same as (a,b) in the AFM case.

loss of contrast on the correlations. Let us consider that spin-spin correlations C_{ij}^z in the presence of errors are reduced by a factor α compared with the ideal prediction $\tilde{C}_{ij}^z$: $C_{ij}^z = \alpha\,\tilde{C}_{ij}^z$, for $i \neq j$. We also assume that self-correlations are not affected at first-order: $\tilde{C}_{ii}^z = C_{ii}^z \approx \langle(\sigma_i^z)^2\rangle = 1$. For example, the sole effect of independent detection errors is to set $\alpha = 1 - 2(\varepsilon_\uparrow + \varepsilon_\downarrow) \approx 0.92$ [see appendix A of Bornet (2024)]. According to this model, the contrast of the TSF is reduced around 1 by a factor α: $S(\mathbf{k}) - 1 = \alpha\left(\tilde{S}(\mathbf{k}) - 1\right)$. As a consequence, $C_{\mathbf{k}} - 1 = \alpha\left(\tilde{C}_{\mathbf{k}} - 1\right)$. This is why we observe the largest deviations when $C_{\mathbf{k}}$ is away from 1.

Spin wave theory provides a simple explanation to the fact that AFM spin waves are slower than FM spin waves: the predicted dispersion relation is proportional to $J_0 = \frac{1}{N}\sum_{i\neq j} J_{ij}$. In the FM case, all interaction strengths J_{ij} are positive, leading to a constructive buildup of the interactions, whereas in the AFM case they are staggered, leading to destructive interferences. We find $|J_0^{\mathrm{FM}}| \approx 6.51|J| \gg |J_0^{\mathrm{AFM}}| \approx 2.47|J|$.

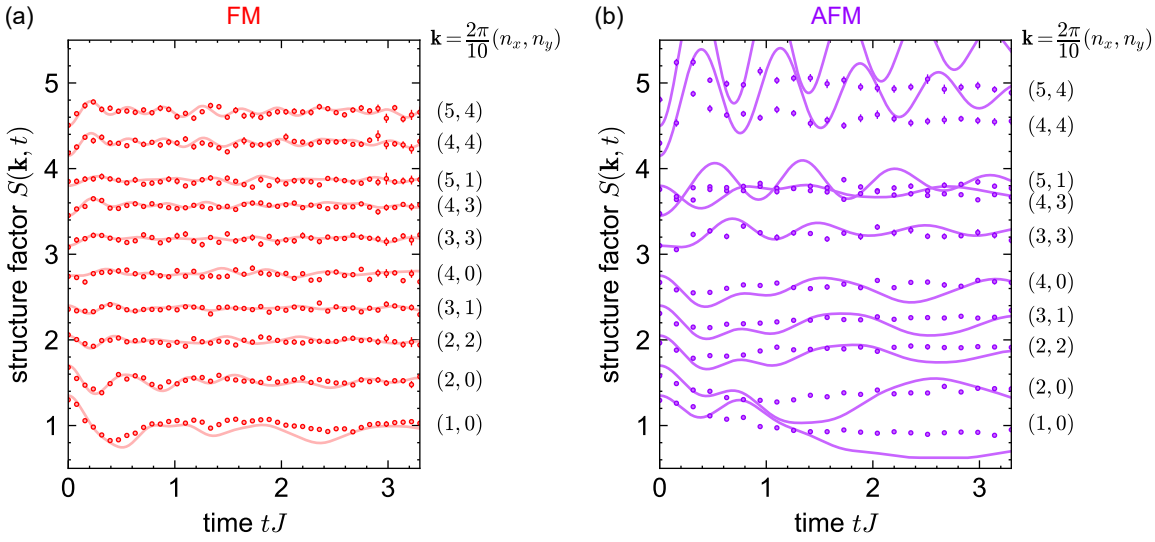

Figure 5.12: Comparison of the measured time-dependent structure factors with predictions of LSW theory for a selection of values of $\mathbf{k}$, showing a good agreement in the FM case (a) and large deviations in the AFM case (b). Curves are offseted by 0.35 for clarity. The LSW theory is performed with OBC [see supplementary material in Chen et al. (2023b)], and includes no errors.

Beyond linear spin waves From the above analysis, LSW theory seems to describe fairly well the early dynamics after the quench, as well as the low-lying dispersion relation. But what about longer times? To check the validity of LSW theory, we plot again in Fig. 5.12 the experimentally-measured TSF, together with the prediction of LSW theory with OBC (calculated by our theory collaborators in Lyon). We obtain a good agreement in the FM case even at the longest times, but large deviations in the AFM case. In particular, the experimental TSF is much more damped than the theory predictions. This damping could be due trivially to the preparation errors for the initial state $|\mathrm{AFM}_y\rangle$. However, a careful benchmarking on a smaller system size ($N = 4 \times 4$) also showed a larger damping in the AFM case than in the FM case [see Fig. 3 of Chen et al. (2023b)]. So, we rather interpret this failure of LSW theory in the AFM case as a real physical effect, which originates from two potential effects:

- Due to geometrical frustration, the AFM ground state contains more quantum fluctuations than its FM counterpart, so the initial product state $|\mathrm{AFM}_y\rangle$ is farther from the ground state and it triggers a larger density of excitations than $|\mathrm{FM}_y\rangle$. As a result, the initial population of spin waves is higher;
- The interaction terms between the spin waves are stronger in the AFM case.

Those effects imply that interactions between the spin waves cannot be neglected anymore, and lead to the observed damping.

Take-home message

In two dimensions, the quench dynamics is very different in the FM and AFM cases, signaling the strong effect of dipolar interactions. Extracting the dispersion relation is complicated by the open boundary conditions which break translational invariance. We use three methods to probe the low-energy spectrum:

1. the quench spectral function, which relies on few assumptions but does not provide a well-defined dispersion relation due to edge effects;
2. a fit of the structure factor at early times, which partially filtrates the multiple frequencies due to the open boundary conditions;
3. a self-consistent analysis that relies on the time-averaged structure factor, and leads to a very clean dispersion relation, although with the strong assumption that spin-wave theory is valid.

All extracted spectra are compatible with the predictions of LSW theory. However, if the FM dynamics are well-described by OBC linear spin waves up to times $> 1/J$, the AFM dynamics show a fast damping which suggests that interactions between the spin waves are not negligible.

Chapter 6

Propagation of holes in doped magnets

J'fais des trous, des p'tits trous, encore des p'tits trous

Serge Gainsbourg, *Le Poinçonneur des Lilas*

Up to now, we have studied spin models making use of two atomic levels, to encode a spin 1/2 in each atom. If "holes" were present, those were unintentional: holes were atoms that happen to fall in another atomic level, which does not interact with the spin states; thus the position of the holes was frozen. However, in many real materials (metals, semi-conductors, superconductors), macroscopic properties such as the electrical conductivity are modified by the presence of mobile particles and holes. In views of making quantum simulations useful for condensed matter physics, it becomes desirable to implement models that include the possibility of transport. For example, the Fermi-Hubbard model may host a superconducting phase at low hole doping (i.e. at low density of holes) — which is still lacking an experimental observation in quantum simulators — and is sometimes considered as describing the key mechanisms of high-temperature superconductors (Dagotto, 1994). More generally, the interplay between magnetism and charge dynamics potentially leads to rich physics, that is hard to simulate, and where many open questions remain (Auerbach, 1994).

In this chapter, I will show the new implementation of a model made of three atomic levels: two levels that represent a particle with spin 1/2, and one level that represents the absence of the particle (hole). Now holes will be able to change positions within the array, with a tunneling term t; other Rydberg interactions will be interpreted as a spin exchange J, and a hole-hole interaction V. This leads to the so-called *bosonic t-J-V model*.

A similar Hamiltonian can be obtained from the Hubbard model in optical lattices, in the regime of strong on-site repulsion $|U| \gg |t|$ leading to an effective spin-exchange interaction $J = 4t^2/U \ll |t|$ (Duan et al., 2003; Gross and Bloch, 2017). The peculiarities of our Hamiltonian compared with the t-J model obtained in optical lattices are the large tunability of the ratio t/J, allowing us to reach the regime $|t| \ll |J|$ for one-dimensional spin chains; and the long-range nature of the hopping terms $t \propto 1/r^3$. Tunnelings t beyond nearest-neighbor sites are considered as a

necessary ingredient to explain the origin of high-temperature superconductivity in the Fermi-Hubbard model (Qin et al., 2020; Xu et al., 2024; Bespalova et al., 2024). In this work, we will be dealing with bosons rather than fermions, so our model cannot be directly used to explain the physics at play in high-temperature superconductors. Still, getting a better understanding of the role of long-range hopping in the motion of holes would be an important step.

A step towards this direction was already realized by Carroll et al. (2024), who directly implemented a tunable, dipolar t-J model using molecules in three dimensions, but it was limited to the high doping regime and did not have local detection. In our case, we focus on the low-doping regime, and make use of our single-atom resolution to probe the dynamics of doped magnets on 1D and 2D lattices.

Contents

Contributors

Much of this chapter is taken from Qiao et al. (2025). The project was triggered by the theory work of Homeier et al. (2024). Experiments were performed in our group together with Mu Qiao, Cheng Chen, Romain Martin, Guillaume Bornet, Thierry Lahaye and Antoine Browaeys. The project was realized in collaboration with the team of Fabian Grusdt and Annabelle Bohrdt at the Ludwig-Maximilians-Universität (LMU) in Munich, in particular with Lukas Homeier who performed numerical simulations and theory analysis. The results were also discussed with Sebastian Geier from Heidelberg University, Simon Hollerith from Harvard and Neng-Chun Chiu from Harvard University.

6.1 Mapping of the atomic Hamiltonian onto the bosonic t-J-V model

Three Rydberg levels encode two spins and a hole Here, I apply the procedure of Homeier et al. (2024) to the specific case of the dipole-dipole interaction in an array of atoms, where we isolate three Rydberg levels per atom. We consider the levels $|S\rangle \equiv \left|nS_{1/2}, m_J = 1/2\right\rangle$, $|P\rangle \equiv \left|nP_{3/2}, m_J = -1/2\right\rangle$ and $|S'\rangle \equiv \left|(n+1)S_{1/2}, m_J = 1/2\right\rangle$. As explained in sec. 3.1 of chapter 3, the dipole-dipole interaction at second order leads to the Hamiltonian

$$H_{\text{atomic}} = H^{(1)} + H^{(2)}_{\text{off-diag}} + H^{(2)}_{\text{diag}}, \tag{6.1}$$

with

$$\begin{cases} H^{(1)} & \equiv \hbar \sum_{i<j} \dfrac{a^3}{r_{ij}^3} \left(J_{SP} \left|S_i, P_j\right\rangle \left\langle P_i, S_j\right| + J_{S'P} \left|S'_i, P_j\right\rangle \left\langle P_i, S'_j\right| + \text{h.c.} \right) \\ H^{(2)}_{\text{off-diag}} & \equiv \hbar \sum_{i<j} \dfrac{a^6}{r_{ij}^6} \left(J_{SS'} \left|S_i, S'_j\right\rangle \left\langle S'_i, S_j\right| + \text{h.c.} \right) \\ H^{(2)}_{\text{diag}} & \equiv \hbar \sum_{i<j} \dfrac{a^6}{r_{ij}^6} \sum_{(\mu,\mu') \in \{S,P,S'\}^2} V_{\mu\mu'} \left|\mu_i, \mu'_j\right\rangle \left\langle \mu_i, \mu'_j\right|. \end{cases} \tag{6.2}$$

The first Hamiltonian in Eq. (6.2) is the first-order dipole-dipole interactions, the second one is the off-diagonal van der Waals interaction, and the last one gathers all diagonal van der Waals terms. To keep the notations simple, the angular dependence of the interaction coefficients J and V with respect to the quantization axis is left implicit.

We now perform the following mapping:

$$\begin{cases} |\downarrow\rangle & \equiv & |S\rangle & \text{(particle with spin down)} \\ |\uparrow\rangle & \equiv & |S'\rangle & \text{(particle with spin up)} \\ |h\rangle & \equiv & |P\rangle & \text{(hole, i.e. absence of a particle).} \end{cases} \tag{6.3}$$

Let us interpret each of the terms of the atomic Hamiltonian in terms of this mapping.

Hole tunneling First, in $H^{(1)}$, the term $|S_i, P_j\rangle \langle P_i, S_j| = |\downarrow_i, h_j\rangle \langle h_i, \downarrow_j|$ can be interpreted as the hopping of a particle with spin $\downarrow$ from an initial site i to an "empty" site j — or equivalently, the hopping of a hole from an initial site j to a site i filled by

Interaction mechanism	Interaction coefficient
Hole tunneling with a spin-up particle	$t_\uparrow = -J_{S'P}$
Hole tunneling with a spin-down particle	$t_\downarrow = -J_{SP}$
Spin exchange	$J_\perp = 2J_{SS'}$
Ising interaction	$J_z = V_{SS} + V_{S'S'} - 2V_{SS'}$
Hole-hole interaction	$V = V_{PP} - V_{SP} - V_{S'P} + \frac{1}{4}(V_{SS} + V_{S'S'} + 2V_{SS'})$
Spin-hole interaction	$W = V_{S'P} - V_{SP} + \frac{1}{2}(V_{SS} - V_{S'S'})$
Magnetic field	$b_z = \frac{1}{2}(V_{S'S'} - V_{SS})$
Chemical potential for the holes	$\mu = \frac{1}{4}(V_{SS} + V_{S'S'}) + \frac{1}{2}(V_{SS'} - V_{SP} - V_{S'P})$

Table 6.1: Dictionary of interaction coefficients between the atomic language and the spin-hole language.

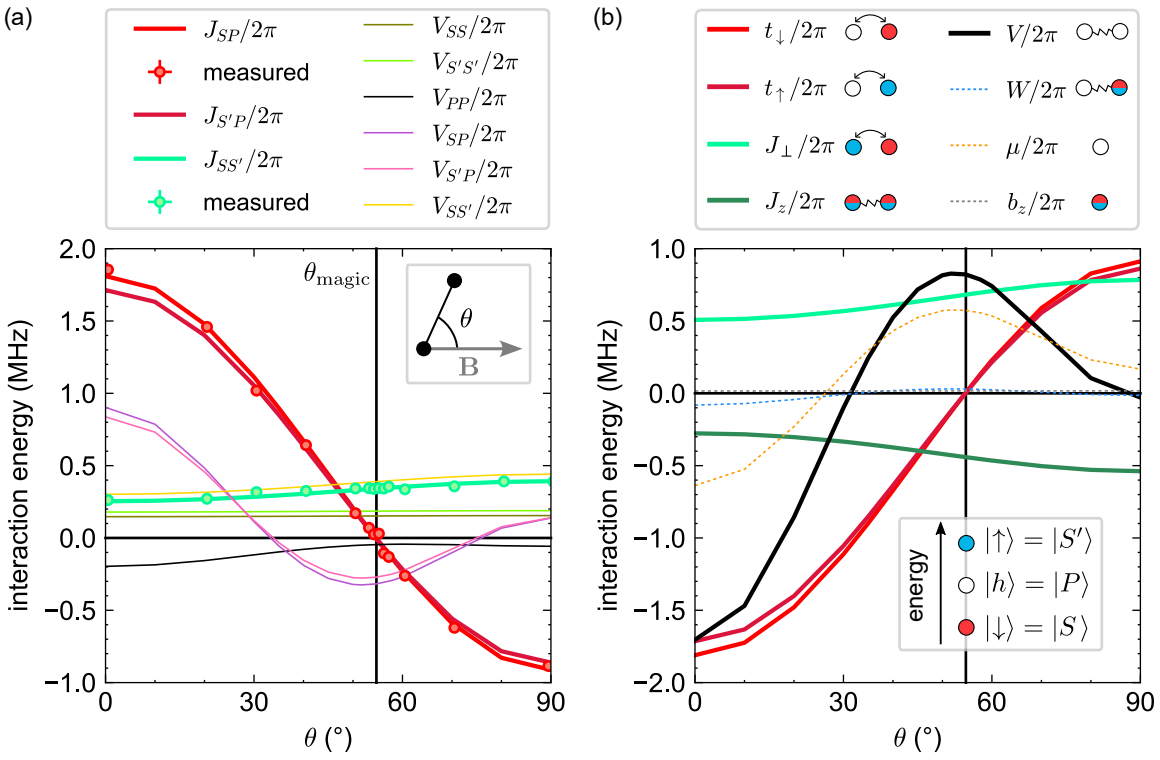

Figure 6.1: Angular dependence of the interaction energies involved in a three-level system $\{|S\rangle, |P\rangle, |S'\rangle\}$ with $|S\rangle \equiv |60S_{1/2}, m_J = 1/2\rangle$, $|P\rangle \equiv |60P_{3/2}, m_J = -1/2\rangle$ and $|S'\rangle \equiv |61S_{1/2}, m_J = 1/2\rangle$, for the following parameters: interatomic distance $r = 9.9$ µm, magnetic field $B = 46$ G, electric field $E = 0$ V/m. Here, θ is the angle between the interatomic axis and the magnetic field. (a) Interaction energies for the atomic Hamiltonian. Thick lines represent off-diagonal terms, which were measured experimentally (see sec. 3.2 and 3.3 of chapter 3). The vertical black line represents the angle $\theta_{\text{magic}} = \arccos\left(\frac{1}{\sqrt{3}}\right)$ at which $J_{SP} = 0$. (b) Associated interaction energies for the t-J-V model, under the mapping explained in this section (inset). Thick solid lines represent the dominant terms.

a particle with spin $\downarrow$. Formally, the situation can be described by so-called *Schwinger bosons*: one introduces the annihilation operator $a_{j,\sigma}$ for a particle at site j with spin $\sigma \in \{\uparrow, \downarrow\}$, and similarly the annihilation operator $a_{j,h}$ for a hole at site j, such that

$$\begin{cases} |\sigma_j\rangle\langle\sigma_j| & \equiv & a^\dagger_{j,\sigma} a_{j,\sigma} & \equiv & n_{j,\sigma} \\ |h_j\rangle\langle h_j| & \equiv & a^\dagger_{j,h} a_{j,h} & \equiv & n_{j,h} \\ |\sigma_j\rangle\langle h_j| & \equiv & a^\dagger_{j,\sigma} a_{j,h}. & & \end{cases} \tag{6.4}$$

These operators satisfy bosonic commutation relations $\left[a_{i,\sigma}, a^\dagger_{j,\sigma'}\right] = \delta_{ij}\delta_{\sigma,\sigma'}$. But contrary to real bosons for which one could have as many particles and holes per site, there are only three possible states per site: $|\uparrow\rangle$, $|\downarrow\rangle$ and $|h\rangle$. This restricts the Hilbert space to states satisfying the so-called *hard-core constraint*:

$$\forall j,\ n_{j,\uparrow} + n_{j,\downarrow} + n_{j,h} = 1. \tag{6.5}$$

Under this formalism, the first-order dipole-dipole interaction can be written as

$$H^{(1)} = -\hbar \sum_{i<j} \frac{a^3}{r_{ij}^3} \left(t_\downarrow\ a^\dagger_{i,\downarrow} a_{i,h} a^\dagger_{j,h} a_{j,\downarrow} + t_\uparrow\ a^\dagger_{i,\uparrow} a_{i,h} a^\dagger_{j,h} a_{j,\uparrow} + \text{h.c.} \right) \tag{6.6}$$

with $t_\downarrow \equiv -J_{S,P}$ and $t_\uparrow \equiv -J_{S',P}$.

Spin-exchange Second, $H^{(2)}_{\text{off-diag}}$ contains only terms that exchange the spin between two particles. Defining the spin operators as $S^z_j \equiv \frac{1}{2}\left(n_{j,\uparrow} - n_{j,\downarrow}\right)$ and $S^+_j \equiv a^\dagger_{j,\uparrow} a_{j,\downarrow}$, one obtains the spin-exchange (or XY) Hamiltonian

$$H^{(2)}_{\text{off-diag}} = \frac{\hbar J_\perp}{2} \sum_{i<j} \frac{a^6}{r_{ij}^6} \left(S^+_i S^-_j + \text{h.c.} \right) \tag{6.7}$$

with $J_\perp \equiv 2J_{S,S'}$. In appendix C, we check that the definition of the spin operators is consistent with the canonical spin algebra, thanks to the properties of the hard-core Schwinger bosons.

Diagonal spin-spin, hole-hole, spin-hole interactions... and the rest Finally, the diagonal terms of the dipole-dipole Hamiltonian can be rewritten as (up to a constant

term)

$$H_{\text{diag}}^{(2)} = \hbar \sum_{i<j} \frac{a^6}{r_{ij}^6} \left[J_z \; S_i^z S_j^z + V \; n_{i,h} n_{j,h} + W \left(S_i^z n_{j,h} + n_{i,h} S_j^z \right) \right] + \hbar \sum_i \left(\sum_{j \neq i} \frac{a^6}{r_{ij}^6} \right) \left[b_z \; S_i^z - \mu \; n_{i,h} \right] \tag{6.8}$$

where J_z is an Ising spin-spin interaction, V is a hole-hole interaction and W is a spin-hole interaction. There are also single-particle terms that we need to add to complete the mapping: b_z is an effective magnetic field and μ is a chemical potential for the holes. Those terms are weighted by a factor $\sum_{j \neq i} \frac{a^6}{r_{ij}^6}$, so they are actually site-dependent. The relation between the atomic interaction coefficients and the ones of the spin-hole model is summarized in Tab. 6.1.

A t-J-V model with large tunability In Fig. 6.1, we show the simulated interactions coefficients, in both atomic and spin language, for the experimental parameters that will be used in the following, as a function of the angle θ between the interatomic axis and the magnetic field. Overall, four energy scales dominate the interactions: the hopping term t, the spin-spin interactions $J_\perp$ and J_z, and the hole-hole interaction V. The chemical potential μ is also dominant, but it should not play a role if the number of holes is fixed[1]. In the end, the implemented Hamiltonian realizes a bosonic t-J-V model describing mobile (hardcore) bosonic holes in a lattice of spins 1/2:

$$\begin{aligned} H_{\text{atomic}} &\approx H_{tJV} \\ &\equiv -\sum_{i<j} \frac{t_\sigma}{r_{ij}^3} \left(a_{i,\sigma}^\dagger a_{j,h}^\dagger a_{i,h} a_{j,\sigma} + \text{ h.c.} \right) \\ &\quad + \sum_{i<j} \frac{1}{r_{ij}^6} \left[J^z S_i^z S_j^z + \frac{J_\perp}{2} \left(S_i^+ S_j^- + \text{h.c.} \right) \right] \\ &\quad + \sum_{i<j} \frac{V}{r_{ij}^6} n_i^h n_j^h \; . \end{aligned} \tag{6.9}$$

With our encoding scheme, the tunneling terms $t \equiv t_\uparrow$ and $t_\downarrow$ are very similar (they differ by $\sim$5 %) and exhibit a $1/r^3$ dipolar behavior, whereas all other interactions decay as $1/r^6$. The different power-law scaling of the tunneling and spin interactions

[1] Since the chemical potential is actually site-dependent according to Eq. (6.8), it can still play a role by favoring or preventing the presence of holes at certain positions. However, for a regular lattice, it is uniform in the bulk, so we expect it to only modify the physics at the edges.

with distance combined with the angular dependence of t allows us to tune the ratio $t/J_\perp$ over a wide range. At the magic angle $\theta_{\text{magic}} = \arccos\left(\frac{1}{\sqrt{3}}\right) \approx 54.7°$, the tunneling vanishes ($t = 0$), placing the system in the $|t| \ll |J|$ regime; away from the magic angle, increasing the interatomic distance r_{ij} leads to $|t| > |J|$ due to the different spatial decay of these interactions. In our experiment, for $a = 9.9\,\mu$m corresponding to the 1D chain studied below, antiferromagnetic XY interactions with calculated strength $J_\perp = 2\pi \times 692$ kHz coexist with ferromagnetic Ising interactions $J_z = -2\pi \times 443$ kHz at $\theta = 54.7°$. The hole tunneling amplitude can be tuned between $|t| = 2\pi \times (0.03 - 1)$ MHz.

Take-home message

The first- and second-order dipole-dipole interactions between three-level atoms can be exactly mapped onto a bosonic spin-hole model, where two S-levels play the role of a spin 1/2 particle, and one P-level represents a hole (i.e. the absence of a particle). In the regime that we will study in the following, the spin-hole model can be thought of as a t-J-V Hamiltonian, which describes:

- the motion of the holes via a tunneling term t ($\propto 1/r^3$);
- the spin interactions as an anisotropic XXZ model with strengths J_z along z and $J_\perp$ in the xy plane ($\propto 1/r^6$);
- the interactions between holes as V ($\propto 1/r^6$).

6.2 Experimental implementation in a 1D chain

In a first set of experiments, we demonstrate the tunability of the platform by investigating, in a one dimensional chain, the interplay between spin dynamics and hole propagation in various regimes [Fig. 6.2(a)]. To do so, we vary the angle θ of the tweezer chain with respect to the in-plane magnetic field, thus tuning the ratio of hopping amplitude t to spin-spin interaction $J_\perp$ [Fig. 6.2(b)].

Initialization of a doped magnet along z We initialize a 12-atom chain in a Néel antiferromagnetic configuration along z with four holes positioned at its center: $|\psi_0\rangle = |{\downarrow}{\uparrow}{\downarrow}{\uparrow}\, hhhh\, {\downarrow}{\uparrow}{\downarrow}{\uparrow}\rangle$. To do so, we make use of two addressing lasers to create single-site resolved light shifts respectively on the states $|{\downarrow}\rangle$ and $|{\uparrow}\rangle$. One laser is blue-detuned by 300-MHz from the transition between the intermediate state $\left|6P_{3/2}\right\rangle$

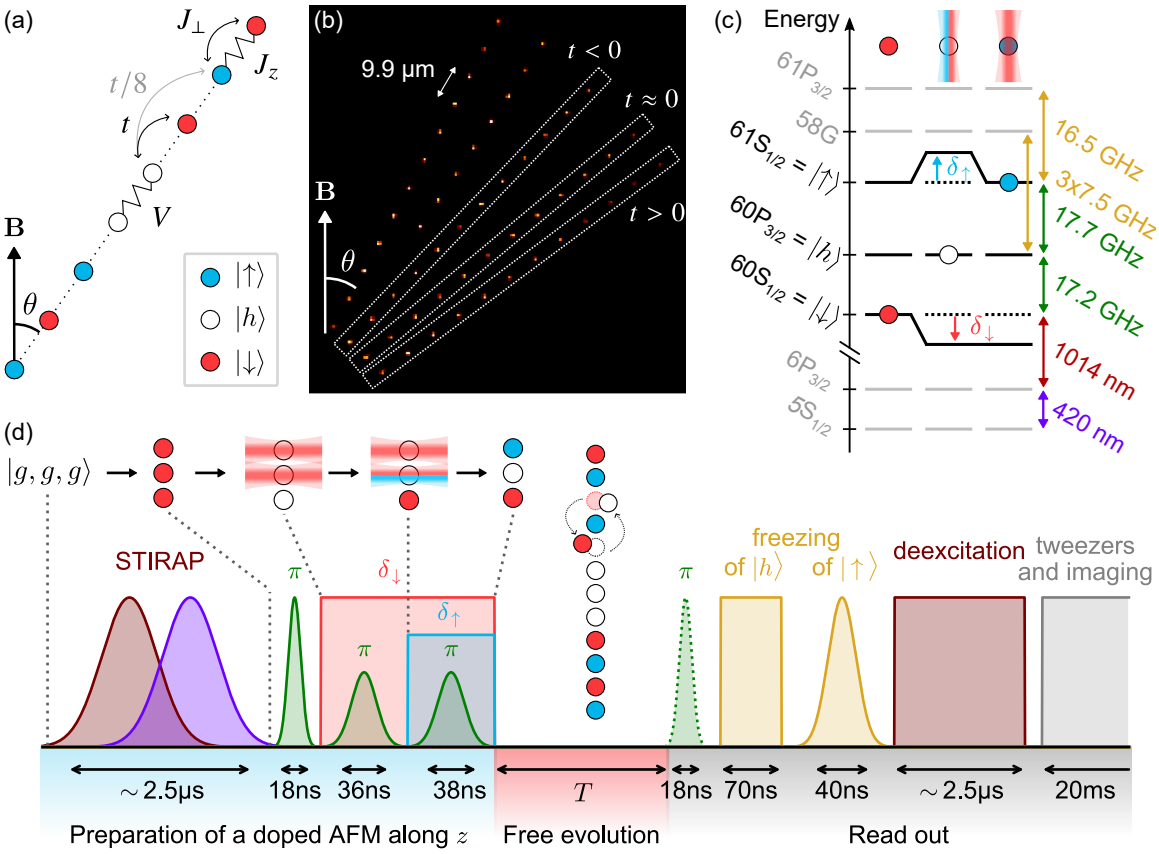

Figure 6.2: Experimental setup for the implementation of a 1D bosonic t-J-V model. (a) Sketch of a 1D magnet (red and blue disks) doped with holes (white disks) interacting under the t-J-V model, at an angle θ with the magnetic field $\mathbf{B}$. (b) Average fluorescence image of a typical array used for the sequence. In practice, we assemble only one chain at a time, in order to avoid spurious inter-chain interactions. The chain at $\theta = \theta_{\text{magic}}$ corresponds to a situation where the hole tunneling t vanishes. (c) Involved energy levels and transitions. The states used in the mapping to the t-J-V Hamiltonian are indicated in black. Each of the three columns represents one class of atoms: non-addressed atoms (left column) are prepared in $|\downarrow\rangle$, atoms with both $\delta_\downarrow$ and $\delta_\uparrow$ light shifts (center column) are prepared in $|h\rangle$, and atoms with only the $\delta_\uparrow$ light shift (right column) are prepared in $|\uparrow\rangle$. (d) Experimental sequence for the preparation of a doped magnet along z. After Rydberg excitation using STIRAP, we apply a sequence of microwave pulses combined with the site-resolved light shifts $\delta_\uparrow$ and $\delta_\downarrow$. Then, the light shifts are switched off for a duration T, during which the system evolves under the t-J-V interactions. To read out the atomic states, we first perform two freezing pulses to stop the dynamics, that respectively act on states $|h\rangle$ and $|\uparrow\rangle$. Then, we deexcite the atoms from $|\downarrow\rangle$ to the ground state manifold, switch on the tweezers and image the recaptured atoms using fluorescence. An additional microwave π-pulse (dotted green line) can be used to read out the state $|h\rangle$.

and $|\downarrow\rangle$, resulting in a light shift $\delta_\downarrow \sim -2\pi \times 40$ MHz on the state $|\downarrow\rangle$; the local control is achieved by diffraction on a spatial light modulator, as described in sec. 2.2 of chapter 2. Another laser is red-detuned by 200-MHz from the transition $\left|6P_{3/2}\right\rangle$ and $|\uparrow\rangle$, creating a light shift $\delta_\uparrow \sim 2\pi \times 30$ MHz on the state $|\uparrow\rangle$; it is diffracted on an acousto-optical modulator seeded by as many radio-frequency tones as the number of addressed atoms (between one and four), and tilted by the approximate angle of the chain. With those addressing lasers, we define three classes of sites, as shown in Fig. 6.2(c): the sites where we want to initialize an atom in $|\uparrow\rangle$ are addressed by the $\delta_\downarrow$-laser; the ones where we want an atom in $|h\rangle$ are addressed by both the $\delta_\downarrow$- and $\delta_\uparrow$-lasers; and the ones where we want an atom in $|\downarrow\rangle$ are not addressed. A sequence of microwave pulses combined with those light shifts allows us to perform the desired local rotations and prepare the target Néel state $|\psi_0\rangle$.

State detection Reading out three atomic levels with a binary outcome (an atom is either recaptured and imaged, or lost) is an experimental challenge, given that the detection must be fast compared with the typical Rydberg lifetimes. For this work, we choose to adapt our usual detection method, based on the mapping of one Rydberg state to the ground state manifold $5S_{1/2}$.

For example, to measure the population in the Rydberg state $|\downarrow\rangle$, we apply a ~ 2.5-µs pulse of 1014-nm light that deexcites $|\downarrow\rangle$ to $5S_{1/2}$ via the short-lived intermediate state $\left|6P_{3/2}\right\rangle$. After that, we switch the tweezers back on, in order to recapture the atoms in $5S_{1/2}$ while expelling the ones in Rydberg states via the ponderomotive force. We then image the recaptured atoms in $5S_{1/2}$ with site-resolved fluorescence. A recaptured atom is interpreted as $|\downarrow\rangle$; a lost atom means that the atom is in one of the two remaining states $|h\rangle$ or $|\uparrow\rangle$. However, we cannot distinguish between $|h\rangle$ or $|\uparrow\rangle$[2].

To measure the hole ($|h\rangle$) population, we add a microwave π-pulse before the deexcitation pulse, exchanging the populations of $|h\rangle$ and $|\downarrow\rangle$, and we map the recaptured atoms to $|h\rangle$ — whereas lost atoms can be in one of the two spin states $|\downarrow\rangle$ or $|\uparrow\rangle$.

The duration of the deexcitation is on the same order of magnitude as the typical interaction times $2\pi/J_\perp \sim 1.5$ µs. To prevent unwanted dynamics during the readout, we implement a two-step freezing protocol: (i) a three-photon transition at 7.5 GHz with a duration of 70 ns shelves the $\left|60P_{3/2}, m_J = -1/2\right\rangle$ population to the hydro-

[2]This is an important limitation of our measurement scheme. To go further, one could imagine mapping two Rydberg states onto the hyperfine ground states $\left|5S_{1/2}, F = 1\right\rangle$ and $\left|5S_{1/2}, F = 2\right\rangle$, and imaging those two states independently, at the cost of an additional complexity in the sequence.

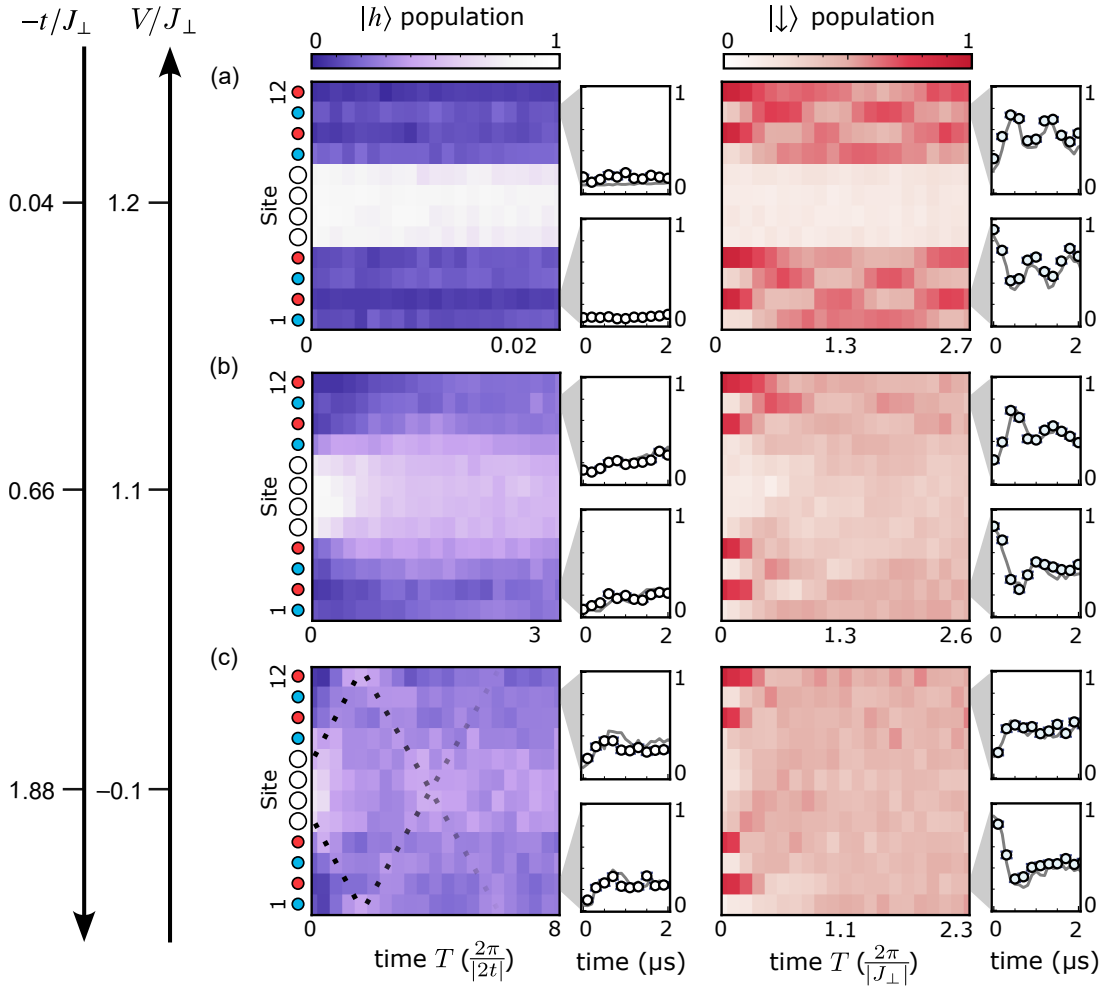

Figure 6.3: Dynamical phase separation. Time evolution of site-resolved $|h\rangle$ (hole) and $|\downarrow\rangle$ (spin-down) populations for various angles θ, corresponding to different ratios $t/J_\perp$ and $V/J_\perp$: (a) $\theta = 54.7°$; (b) $\theta = 45°$; (c) $\theta = 30°$. The initial state is indicated by colored dots in the leftmost column. Insets show population dynamics for selected sites (2nd and 11th), comparing experimental data (points, error bars denote one standard error) with numerical simulations including experimental imperfections (solid lines).

genic manifold $n = 58$, and (ii) a microwave π-pulse transfers the atoms in $|\uparrow\rangle$ to $\left|61P_{3/2}, m_J = 3/2\right\rangle$, which has negligible interaction with $|\downarrow\rangle$. Those freezing pulses are applied successively just before the deexcitation.

Hole and spin dynamics After the preparation of the doped magnet, we suddenly turn off the light shifts, let the system evolve freely under H_{tJV}, and measure the state evolution as a function of time T[3]. Figure 6.3(a,b,c) presents the time evolution of the hole density $\langle n_{i,h}\rangle$ and the spin density $\langle n_{i,\downarrow}\rangle$ for three angles. Close to the magic angle

[3]In the remainder of this chapter, I will refer to the time as T, in order not to confuse it with the tunneling t.

$\theta = 54.7°$ [Fig. 6.3(a)], where $|t/J_\perp| \ll 1$ (experimentally, $|t| = 2\pi \times 30 \pm 10$ kHz), we observe a separation of hole and spin domains. The holes, initially prepared in the center, form a static domain that remains separated from the spin magnet. This situation exhibits minimal hole diffusion while still featuring coherent spin oscillations within each magnetically ordered subdomain. We compare the results to numerical simulations including experimental imperfections, finding a good agreement between the two [insets of Fig. 6.3]. When we decrease θ to 45° [$t/J_\perp \approx -0.66$, Fig. 6.3(b)], we still measure substantial occupation of the holes on their initial sites, although the larger hole tunneling begins to destabilize the domain wall. Concurrently, we observe damped spin oscillations in the region where holes partially penetrate. Further reducing θ to 30° ($t/J_\perp \approx -1.88$) dramatically alters the holes' behavior as seen in Fig. 6.3(c). In this strong hopping regime, holes rapidly delocalize across the entire chain, and undergo reflections when they reach the end of the chain as highlighted by the dotted lines in Fig. 6.3(c). The spin dynamics become erratic, indicating the spin magnetic order is suppressed by the holes' motion.

A perturbative argument to explain the dynamics for small tunneling To understand the fact that the initial phase separation between hole-rich and spin-rich regions is maintained during the dynamics, as observed above, we need to consider the interplay between the processes described by t, $J_\perp$, J_z and V. In the limit of small tunneling $|t/J_z| \ll 1$ and $J_\perp = V = 0$, we expect a trivial binding owing to the energy cost $|J_z/4|$ of breaking a spin bond. In the presence of spin fluctuations $J_\perp$ but no hole-hole interaction ($V = 0$), the hole cluster could be destabilized when the binding energy is absorbed by the spin background, especially for large system sizes. The observation of a stable phase separation therefore points towards the role of the hole-hole interaction V as stabilization process. For instance, a pair of adjacent holes can only propagate through a second-order process where the pair temporarily breaks apart: one hole hops (amplitude t), followed by the breaking of a nearby $\uparrow,\downarrow$ pair (energy cost $E_b = V - J_z/4$), and subsequent recombination [Fig. 6.4]. This virtual process results in an effective tunneling amplitude $t_{\text{eff}}^{\text{NN}} = t^2/(V - J_z/4) \ll |t|$[4]. Extending to four adjacent holes, the hole cluster moves by a fourth-order order perturbative process $\propto t^4/(V - J_z/4)^3$. Therefore as the number of holes increases, we expect a longer-lived phase separation between hole and spin regions.

The fact that the hole clustering is favored by *repulsive* hole-hole interactions $V > 0$

[4]This perturbative argument neglects the spin-exchange coupling $J_\perp$, which leads to a modification of the spin background as a function of time. So one cannot expect it to explain the hole propagation quantitatively.

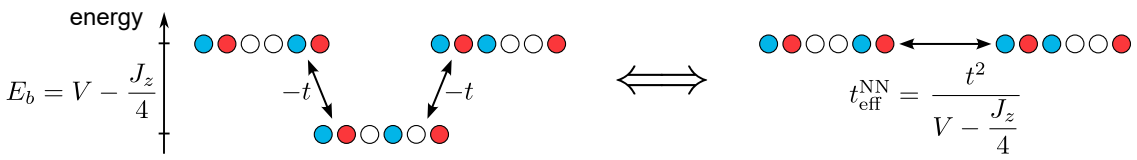

Figure 6.4: Perturbative coupling for the hopping of a bound pair by one lattice site in an AFM spin background along z, in the regime $|t| \ll |E_b|$ with $E_b = V - \frac{J_z}{4}$ the binding energy of the holes. Here, we neglect the next-nearest neighbor hopping.

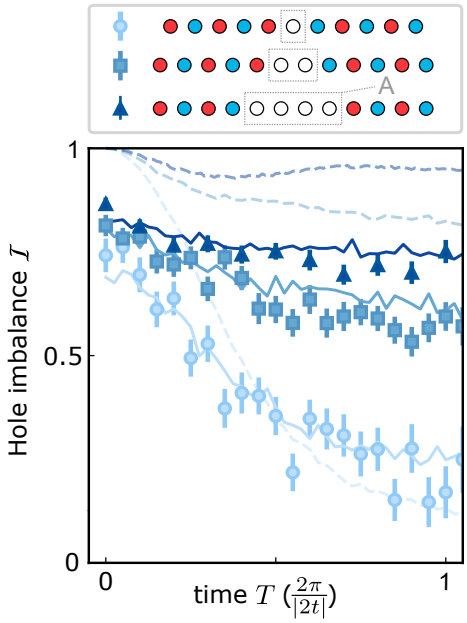

Figure 6.5: Role of the hole-hole interaction V **in the speed of propagation of the holes**. Evolution of the hole imbalance $\mathcal{I}$ for various doping densities (1 hole, 2 holes, 4 holes) at $\theta = 51.7°$ (corresponding to $t/J_\perp \approx -0.19$ and $V/J_\perp \approx 1.2$). Solid (resp. dashed) lines are simulations in the presence (resp. in the absence) of experimental imperfections. The above legend shows the definition of the sites A used in the definition of $\mathcal{I}$ [Eq. (6.10)] as the initial hole positions. We post-select experimental data containing hole numbers of 1, 2 and 4 respectively.

might sound contradictory. However, the sign of the binding energy $E_b = V - \frac{J_z}{4}$ does not matter for the perturbative argument of Fig. 6.4. Repulsive bound states were already demonstrated experimentally in Winkler et al. (2006); Fukuhara et al. (2013); Weckesser et al. (2024).

To confirm experimentally the above intuition, we study the dynamics of 1-, 2- and 4-hole initial states at fixed $t/J_\perp \approx -0.19$ and $V/J_\perp \approx 1.2$ (corresponding to an angle $\theta = 51.7°$). To this end, we quantify the spatial separation between hole-rich and

hole-free regions by the *hole imbalance*:

$$\mathcal{I} = \frac{1}{N_{\text{hole}}} \sum_{i \in \text{A}} \langle n_{i,h} \rangle - \frac{1}{N - N_{\text{hole}}} \sum_{j \notin \text{A}} \langle n_{j,h} \rangle \ , \tag{6.10}$$

where N_{hole} is the number of holes, N is the number of sites, and A denotes the sites initially occupied by holes. $\mathcal{I}$ is the difference between the average number of holes in region A and the average number of holes in the rest of the chain: a perfectly-prepared initial state corresponds to $\mathcal{I} = 1$; conversely, a state where the hole population is uniformly distributed over the N sites corresponds to $\mathcal{I} = 0$. Figure 6.5 compares the time evolution of $\mathcal{I}$ for systems with $N_{\text{hole}} = 1, 2,$ and 4. Ideally, each measurement outcome of those datasets should have exactly N_{hole} holes, but this is not the case due to the various preparation infidelities (~ 20 % per spin) and detection errors (~ 3 % per spin). This typically makes the distinction between the various cases less sharp. To compensate this effect, we post-select the measurement outcomes with exactly N_{hole} holes. The data suggests a slowdown in the melting of the boundary between hole-rich and hole-free regions as the number of holes increases from the single-hole case where the dynamics is purely governed by the tunneling amplitude t. This is also in agreement with numerical simulations.

Take-home message

Starting from a one-dimensional chain of z-antiferromagnets doped with holes, we measure the time evolution of both the hole and spin populations. We tune the interactions t and V by varying the angle of the chain with the quantization magnetic field, and observe a transition between two regimes: at small tunneling $|t| \ll |V|, |J|$, holes remain grouped together while the spins evolve independently; at large tunneling $|t| > |V|, |J|$, holes delocalize rapidly, strongly interfering with the spin dynamics.

The fact that two holes remain close to each other suggests the existence of a hole bound state, stabilized by the repulsive hole-hole interaction. We will make this assumption more solid in the following, by studying the hole-hole correlations.

6.3 Propagation of hole bound states in 1D in the perturbative regime $|t| \ll |J|$

We now focus on initial states with two holes, and study more precisely their dynamics with two questions in mind:

1. Do holes form bound pairs?
2. If so, how fast do hole bound states move in the chain?

We will show two differential measurements to probe the influence of the dipolar couplings on the one side, and the influence of the spin background on the other side.

Role of next-nearest-neighbor tunneling The perturbative argument presented above for the mobility of a 2-hole bound state neglects the fact that the tunneling amplitude t results from a dipolar interaction: the long-range tail of the tunneling allows for direct, next-nearest-neighbor hopping of one of the holes constituting the pair, as represented in Fig. 6.6. The propagation of the bound pair from one site thus results from the interference between the second-order coupling described above, and the direct tunneling with an amplitude $-t/8$. This leads to an effective tunneling amplitude of the bound pair $t_{\text{eff}}^{\text{dip}} = t^2/(V - J_z/4) - t/8$.

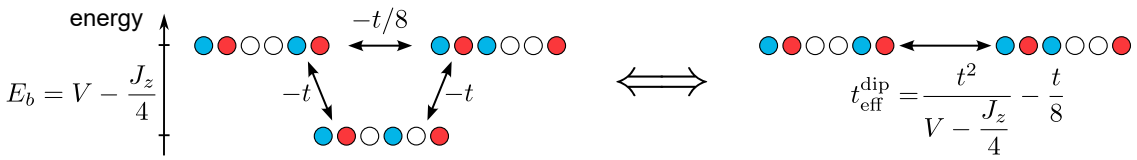

Figure 6.6: Perturbative coupling for the hopping of a bound pair by one lattice site in an AFM spin background along z, in the regime $|t| \ll |E_b|$ with $E_b = V - \frac{J_z}{4}$ the binding energy of the holes. Here, in contrast with Fig. 6.4, we take into account the next-nearest neighbor hopping which creates a direct coupling $-t/2^3$ between the two bound states.

To check experimentally that the dipolar tail of the interaction does play a role in the propagation of a bound pair, we analyze the dynamics for two different signs of t, controlled by the angle θ. We choose two values of θ on either side of the magic angle (49.7° and 59.7°), corresponding respectively to $t/J_\perp = -0.32$ and $t/J_\perp = 0.29$. We plot in Fig. 6.7(a,b) the non-connected hole-hole correlations $\langle n_{i,h} n_{j,h} \rangle$ following the preparation of a pair hh at the center of the chain, for various evolution times T, in the case $t > 0$ (a) and $t < 0$ (b). The correlator $\langle n_{i,h} n_{j,h} \rangle$ can be simply thought as

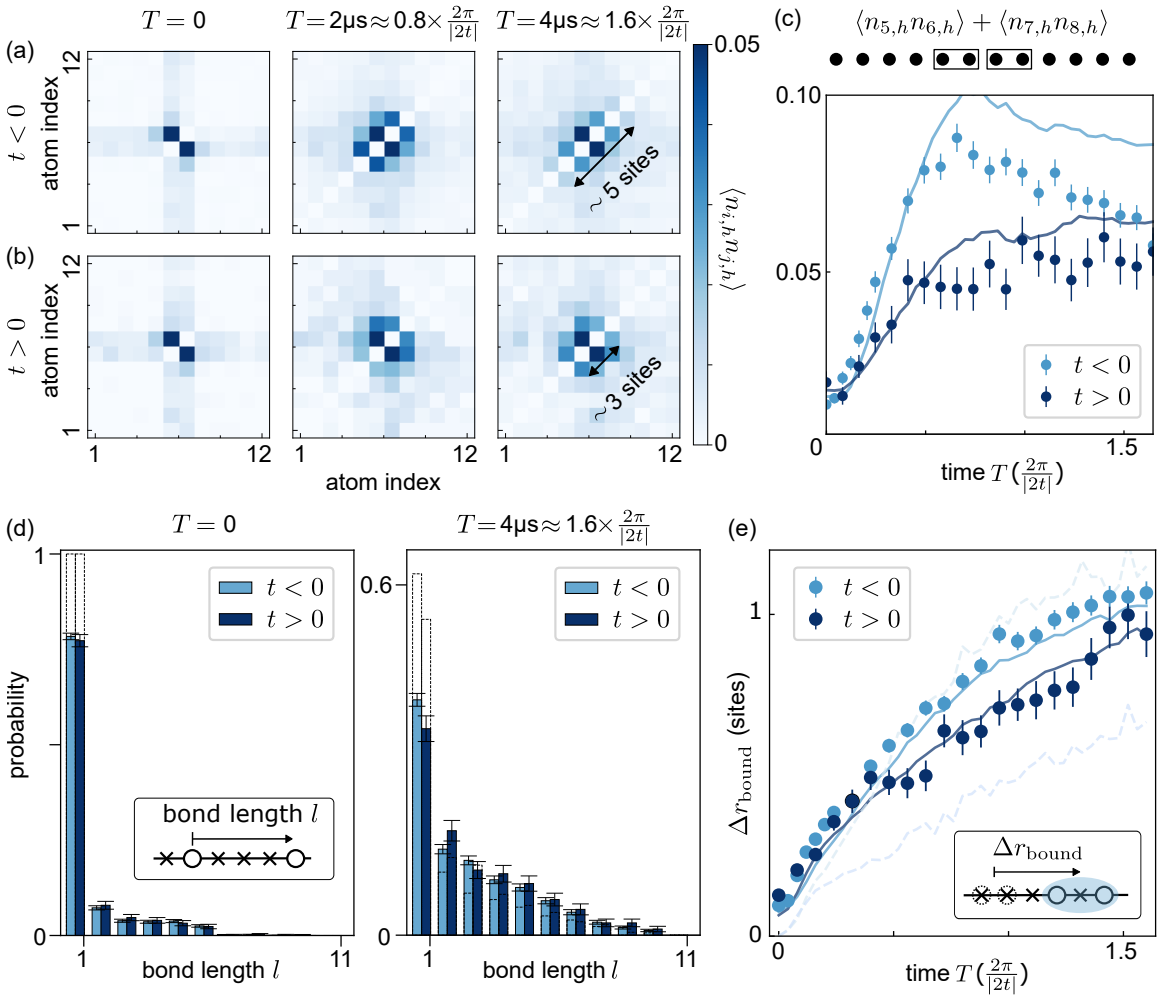

Figure 6.7: Role of next-nearest-neighbor tunneling. (a,b) Hole-hole correlations $\langle n_{i,h} n_{j,h} \rangle$ at different times for (a) $\theta = 49.7°$ ($t = -2\pi \times 211$ kHz < 0), and (b) $\theta = 59.7°$ ($t = 2\pi \times 204$ kHz > 0). (c) Time evolution of the hole-hole correlator $\langle n_{5,h} n_{6,h} \rangle + \langle n_{7,h} n_{8,h} \rangle$ corresponding to the propagation of a bound pair by one site. (d) Distribution of hole-hole separations at $T = 0$ and $T = 4\,\mu$s, comparing positive ($t > 0$, dark blue) and negative ($t < 0$, light blue) tunneling. (e) Time evolution of the bound-pair displacement $\Delta r_{\mathrm{bound}}$ (see inset) for both $t > 0$ and $t < 0$. We restrict the analysis to configurations where the holes are separated by at most two sites. Dots are experimental data, solid lines represent numerical simulations with experimental imperfections, and dashed lines are the ideal simulation. All the data is postselected, retaining only measurements containing two holes.

the probability of measuring two holes simultaneously at positions i and j. From the correlation maps, we observe that the pair remains essentially bound during the time evolution, since correlations propagate mainly along the diagonal. We also see that for $t < 0$ ($\theta = 49.7°$) the bound pair's wavepacket moves by ~ 5 sites within $T \approx 1.6 \times \frac{2\pi}{|2t|}$, while at $t > 0$ ($\theta = 59.7°$), it only moves by ~ 3 sites within the same duration, suggesting different delocalization speeds of the hole pairs. We confirm this difference by plotting in Fig. 6.7(c) the time evolution of the correlator $\langle n_{5,h} n_{6,h} \rangle + \langle n_{7,h} n_{8,h} \rangle$ in the two cases $t > 0$ and $t < 0$. A larger slope of the correlator can have two interpretations: either the holes are more tightly bound (leading to a larger amplitude of the correlator), and/or they propagate faster (which makes the correlator peaks sooner). To decouple those two explanations, we need to consider different observables.

We first plot in Fig. 6.7(d) the histogram of the distance between the two holes (bond length) l, at the initial time $T = 0$ and after a time $T \approx 1.6 \times \frac{2\pi}{|2t|}$. At $T = 0$, the dominant bond length is $l = 1$, since the initial state is composed of two holes next to each other (the residual population of bond lengths $l > 1$ is due to SPAM errors). At $T \approx 1.6 \times \frac{2\pi}{|2t|}$, the peak at $l = 1$ remains, signaling the hole bound state, while part of the holes are measured far from each other, probably due to the initial overlap of the initial state with unbound states. As the probability of $l = 1$ at $T \approx 1.6 \times \frac{2\pi}{|2t|}$ is higher for $t < 0$ than $t > 0$, the binding is tighter for the first case. This is consistent with the fact that the binding energy is lower in the first case: $E_b = 2\pi \times 0.91$ MHz for $t < 0$ and $E_b = 2\pi \times 0.85$ MHz for $t > 0$.

Second, we characterize the mobility of the bound pairs by measuring their center-of-mass displacement along the chain, defined as the distance between the center of mass of the pairs and the center of their initial position. Here, we define the bound pairs as holes with bond length $l \leq 2$. The results are shown in Fig. 6.7(e) and do feature the expected asymmetry. They are also in good agreement with numerical simulations. From panels (d,e), we conclude that light pairs propagate rapidly and remain tightly bound, whereas heavy pairs move more slowly but form a spatially extended bound state. This behavior is a direct consequence of the $1/r^3$ tail in the tunneling amplitude of the holes, and would be absent for nearest-neighbor interactions. In particular, for nearest-neighbor interactions, the hole pairs would have the same mass $m_{\text{eff}} \propto 1/(2t_{\text{eff}})$ with $t_{\text{eff}}^{\text{NN}} = 2\pi \times 49\,\text{kHz}$ according to the perturbative argument above. Taking into account the dipolar hopping, one gets instead $t_{\text{eff}}^{\text{dip}} = 2\pi \times 75$ kHz at $\theta = 49.7°(t < 0)$ and $t_{\text{eff}}^{\text{dip}} = 2\pi \times 23$ kHz at $\theta = 59.7°(t > 0)$. However, those numbers only provide a qualitative understanding of the hole propagation, since they rely on the very rough assumption that the spin backgrounds do not evolve ($J_\perp = 0$).

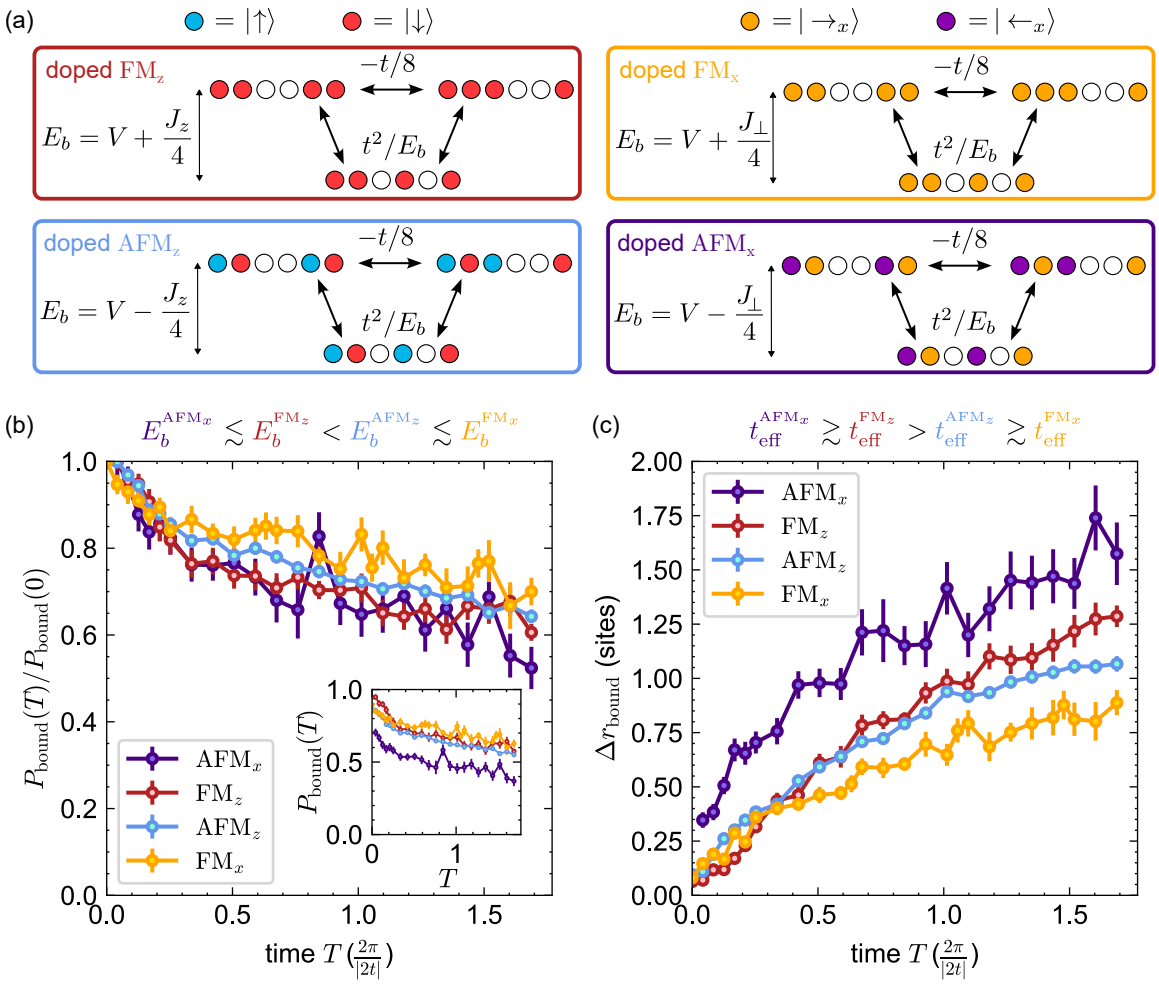

Figure 6.8: Role of spin background. (a) Perturbative coupling for the hopping of a bound pair by one lattice site in four different spin backgrounds. The binding energy E_b and thus the effective coupling t_{eff} depend on the the spin background. (b) Time evolution of the bound state population P_{bound}, defined as the probability of finding two holes with bond length $l \leq 2$, in various spin backgrounds. The inset shows the raw data, while the main panel shows the normalized probability $P_{\mathrm{bound}}/P_{\mathrm{bound}}(0)$ to get rid of the different initial state fidelities. (c) Time evolution of the bound-pair displacement $\Delta r_{\mathrm{bound}}$ [defined as in the caption of Fig. 6.7(d)]. All the data is postselected, retaining only measurements containing two holes.

Role of the spin background In a last experiment in 1D, we now make use of our ability to prepare site-resolved spin textures, to investigate how different magnetic backgrounds influence the dynamics of the hole pairs. Specifically, we answer two questions: does the spin background modify whether the pair remains bound, and if yes, how does the pair propagate? From the perturbative description of the bound pair, we infer that the binding energy and effective mass can be tuned by changing the spin contribution to the energy of the initial state. In particular, the binding energy $E_b = V \pm J_\alpha/4$ depends on the relative orientation of spins ($\pm$) and direction ($J_\alpha = J_z, J_\perp$) [Fig. 6.8(a)]. We thus expect that the spin background can either favor or disfavor the binding of the holes, depending on the sign of the spin-spin interaction J_α on the nature of the spin ordering.

To probe this effect, we use a chain at $\theta = 49.7°$ and prepare four distinct spin configurations: a ferromagnetic state (FM) and an antiferromagnetic Néel state (AFM), whose spins are oriented either along x or along z. We initialize two holes at the center of the chain and track the evolution of their center-of-mass position. We first investigate the binding of holes by analyzing the population of bound pairs P_{bound}, which we define as holes separated by at most two lattice sites (i.e. pairs of holes with a bond length $l \leq 2$). The evolution of P_{bound} with the interaction time T is shown in Fig. 6.8(b), normalized by its initial value to get rid of the various initial state preparations. We observe that $P_{\text{bound}}(T)$ slowly decreases, with a slope that depends weakly on the spin background. The results are qualitatively consistent with the ordering of the binding energies, whose values are shown in Tab. 6.2. For example, the slowest decay is obtained in the FM case along x, in which holes have the largest binding energy.

	AFM_x	FM_z	AFM_z	FM_x
Binding energy $E_b/2\pi$	0.64 MHz	0.70 MHz	0.91 MHz	0.97 MHz
Effective hopping $t_{\text{eff}}/2\pi$	0.096 MHz	0.090 MHz	0.075 MHz	0.072 MHz

Table 6.2: Calculated values for the binding energy and the effective coupling of two holes in various spin backgrounds.

We then characterize the mobility of the bound pairs by measuring their displacement. The results, shown in Fig. 6.8(c), reveal that bound pairs propagate significantly slower in the FM case along x, and faster in the AFM case along x. This behavior is again in agreement with the ordering of the effective pair tunneling amplitude $t_{\text{eff}} = t^2/E_b - t/8$, which are calculated in Tab. 6.2.

Take-home message

Two holes initialized in a one-dimensional magnet remain partially bound as they propagate under the t-J-V model, as confirmed by the correlations between their positions.

The behavior of the hole bound state is affected by the next-nearest-neighbor hole tunneling, as well as the magnetic ordering of the spin background. Perturbative arguments allow us to grasp the qualitative behavior of the hole bound pair. Specifically, the tightness of the bound is reasonably explained by its binding energy, and its speed of propagation by a second-order effective tunneling.

6.4 Propagation of holes in 2D

Finally, we extend our study to investigate the dynamics of a single hole in two dimensions. Our motivation is twofold. First, we aim at seeing the influence of the dipolar tail of the interaction in the dynamics in a square lattice. Second, we demonstrate the platform's ability to explore the hole dynamics in an AFM background, relevant for the understanding of doped AFM Mott insulators (Shraiman and Siggia, 1988; Ji et al., 2021; Koepsell et al., 2019).

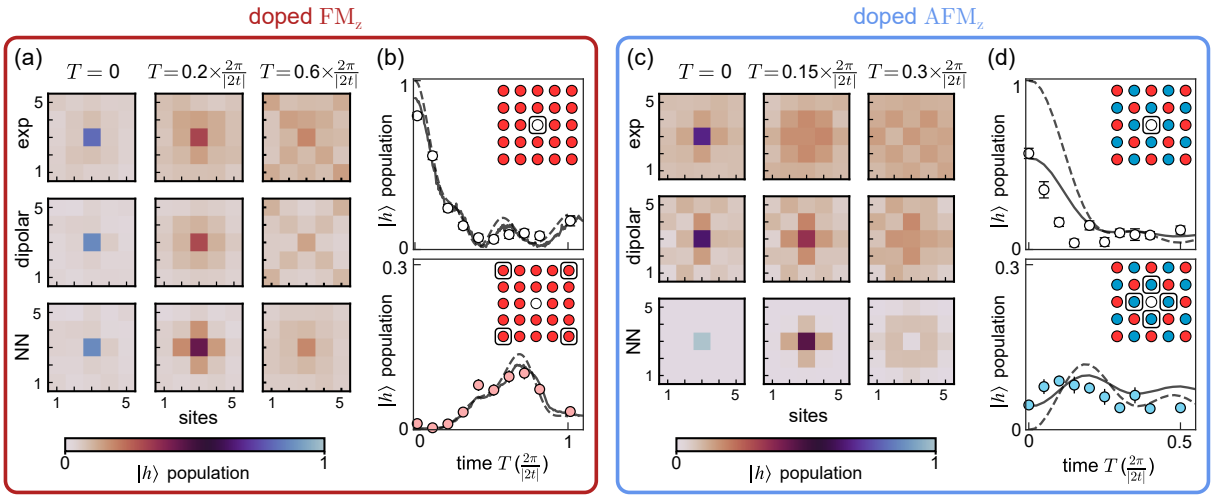

Figure 6.9: Hole dynamics in a 2D quantum magnet. (a) Spatial maps of the hole probability at various evolution times T, for a hole initialized in the 2D FM spin background $|\downarrow\rangle$. The top row shows the experimental data; the middle row is a numerical simulation with the dipolar couplings of the Rydberg interactions, in the presence of experimental imperfections; and the bottom row considers the theoretical case of nearest-neighbor interactions, with the same imperfections. (b) Time evolution of the hole probability at the initial center site (bottom row), and averaged over the four corner sites (top row). Solid (resp. dashed) lines are simulations in the presence (resp. absence) of the known experimental imperfections. (c,d) Same as (a,b) in the case of an antiferromagnetic spin background along z.

In 2D, we set the magnetic field perpendicular to the atomic plane ($\theta = 90°$) to guarantee isotropic interactions, fixing the ratios $V/J_\perp = -0.07$ and $J_z/J_\perp = -0.68$. But we can still tune the ratio $t/J_{\perp,z}$ by varying the lattice spacing, exploiting the different power-law dependence of tunneling ($\propto r^{-3}$) and spin exchange ($\propto r^{-6}$) interactions. Here, we implement a 5×5 square array with lattice spacing $a = 12$ µm, where $t/J_\perp = 2$ ($t = 2\pi \times 509\,\mathrm{kHz}$). We initialize it in a polarized FM or AFM product

state along z, with a single hole at the center[5].

Fig. 6.9(a) shows the local hole occupation number in the FM case at two different times. There, the dynamics reduces to that of a single particle (here the hole) hopping in a 2D lattice with dipolar $\propto t/r^3$ coupling. The observed coherent evolution of the hole shows a distinctive interference pattern which is a fingerprint of the associated band structure: in particular the hole occupation exhibits pronounced peaks at $T = 0.6 \times \frac{2\pi}{|2t|}$ along the diagonal of the 2D array, a feature absent in the simulation including only NN interactions. In Fig. 6.9(b), we focus on the evolution of the hole occupation at the center and corner of the array, and get a very good agreement with numerical simulations (solid and dashed lines).

The AFM case is presented in Fig 6.9(c). There, we expect that the hole's paths do not interfere because of their different spin backgrounds that "keep memory" of the trajectory (Bohrdt et al., 2024). Furthermore, the initial state leads to strong fluctuations in both the charge (i.e. the hole) and spin sectors, due to tunneling t and spin flip-flop processes $J_\perp$. In Fig. 6.9(d) we compare the evolution of the hole occupation with time-dependent matrix product state simulations (Hauschild and Pollmann, 2018) and find good agreement with our experiment, by comparing the peak at the center and its adjacent sites at early evolution times; at later times both the numerical simulations and the experiment are featureless due to the high-energy initial state prepared in the experiment.

Take-home message

The implementation of the bosonic t-J model can be easily extended to two spatial dimensions. Here, we lose the angular tunability of the interactions but we can still play with the inter-particle distance to change the ratio t/J. Our first studies reveal the influence of dipolar hopping compared with purely nearest-neighbor interactions. This work paves the way for more detailed studies of hole motion in two dimensions, a situation which is more complex and harder to simulate than the one-dimensional case.

[5] In this regime of parameters, two holes do not form a bound state since $|t| \gg |J_z|, |J_\perp| \gg |V|$. At low doping, we expect them to behave independently from each other, so we only analyze the motion of a single hole.

Conclusion

The various works gathered in this thesis can be split into two categories:

- at the "hardware" level, improvements on the existing experimental platform (mainly described in part A of this manuscript);
- at the "software" level, studies of quantum many-body phenomena emerging from spin models with dipolar couplings (detailed in part B of this manuscript).

I will conclude separately on those two themes.

Hardware: a few improvements, many remaining challenges

In the Introduction of this thesis, I have listed some general limitations of quantum simulators and possible strategies to overcome them (Tab. 1). In the specific case of Rydberg-based quantum simulators, let us review which limitations were addressed during my PhD, and which ones remain. A detailed summary is shown in Tab. 6.3, I will go through a few of them.

More diverse initial states Quantum simulation requires high fidelities in the initial state preparation, to trust the output of the simulation. Part of my thesis was devoted to design better preparation schemes, in particular by implementing local rotations with two Rydberg levels (chapter 2) and three Rydberg levels (chapter 6). We also demonstrated the use of two-photon microwave transitions between two S states (chapter 2). Those improvements allowed us to prepare new types of initial states, such as classical ferro- and antiferro-magnetic states oriented in well-controlled directions — a necessary condition for the many-body schemes that we demonstrated in part B. Right now, our preparation fidelities are limited by the Rydberg excitation errors, the dipole-dipole interactions during the pulses, and the reduced lifetime of addressed atoms due to depumping; for example, the best measured fidelities with our setup are on the order of 99 % for global rotations between two Rydberg states, and ~ 95 % for local rotations. Those infidelities are sufficiently small to see most of the qualitative features of the prepared phases, but they contribute to increase the effective temperature when we want to prepare the ground state (as shown in chapter 4).

Step of the sequence	Typical limitations	Possible strategies
State initialization	Fidelity	- Design new preparation schemes: local rotations (chapter 2), two-photon transitions (chapter 2) and additional addressing laser (chapter 6) - Postselection of realizations without errors (chapter 6) - Computer-assisted optimization - Improved stability: feedback loops on position and power of laser spots (chapter 2) - Faster repetition rates - Buy higher-performance technologies
Time evolution	Decoherence	- Better isolation from the environment - Use states with longer natural lifetimes - Design shorter sequences (increase interactions, shortcuts to adiabaticity...) - Reduce inhomogeneities and fluctuations of the Hamiltonian: Raman sideband cooling (chapter 1) - Post-selection using mid-circuit measurements - Quantum error correction
	Finite size effects (edge effects)	- Increase system size - Design systems with periodic boundary conditions: circular geometry in 1D (chapter 4)
	Limited tunability of the Hamiltonian	- Implement new geometries (various lattices, 3D...) - Design new mappings: new types of dipole-dipole interactions (chapter 3), t-J-V model (chapter 6) - Hamiltonian engineering (e.g., Floquet techniques)
Projective measurement	Fidelity	- Better detection schemes: freezing pulses (chapter 2) - Find robust observables against experimental noise
	Partial access to the state	- Enhance read-out bases: local rotations for multi-bases measurements (chapter 2) - Design strategies to extract information (randomized benchmarking...) - Non-destructive measurements

Table 6.3: Back to the experimental challenges of a quantum simulator, as listed in Tab. 1 of the Introduction, and the way they are tackled in this thesis (in black).

Going further might be achieved by a careful computer-assisted optimization of the pulse shapes, or the design of new preparation schemes (such as Raman transitions between Rydberg states).

Fighting against decoherence The dynamics of a quantum state can be affected by several decoherence effects, among which are fluctuations of the interaction energies induced by disorder of the atomic positions. In chapter 1, I showed how to reduce this effect by cooling the atoms close to their motional ground state in the tweezers. Still, the remaining quantum fluctuations of the positions are sufficient to affect the long-time coherence of a two-atom spin exchange, as we showed in chapter 3. On top of that, the finite Rydberg lifetimes create decay channels to other atomic states, transforming the unitary dynamics into that of an open system at long times. Solutions to overcome decoherence due to positional disorder and Rydberg lifetimes may involve lower durations spent in the Rydberg states (Chew et al., 2022), cryogenic environments to reduce black-body radiation (Schymik, 2022), Rydberg trapping (Cortiñas et al., 2020; Barredo et al., 2016), and circular Rydberg states (Nguyen et al., 2018; Wu et al., 2023). The possibility of cooling the atoms during the Rydberg sequence was also shown recently with two-electron atoms in circular states (Lachaud et al., 2024).

A more reliable readout A reliable readout is also a crucial requirement for a quantum simulator, since it provides access to information about the prepared state. In chapter 2, I presented some strategies to improve the detection fidelities, using for instance freezing pulses to avoid residual interactions during the readout. Local rotations also allowed us to perform a simultaneous readout of several spins in different bases, in order to measure crossed basis correlations (chapter 2). However, our detection scheme is fundamentally limited by its binary aspect: the Rydberg states are mapped into either the loss or the recapture of an atom. This increases the possibility of detection errors (since, for example, decay from the Rydberg states to the ground state lead to misinterpret the atomic state) and prevents from reading more than two atomic states simultaneously. Detection errors could be reduced by ionizing the atoms after selective deexcitation of a Rydberg state. More involved detection schemes may be used, such as mapping the internal states into different positions, as shown in Mandel et al. (2003); Lee et al. (2007); Wang et al. (2019); Wu et al. (2019); or mapping them onto different hyperfine levels of the ground-state manifold. Using atomic species with several valence electrons is also a promising road for improved state detection (Muni et al., 2022), as well as dual species arrays for mid-circuit measurements (Singh et al.,

2023; Anand et al., 2024).

Finite-size effects Throughout part B of this thesis, we illustrated some spurious effects due to the finite size of the array: edge effects can affect the spatial profile of the spin correlations (chapter 4), modify the dispersion relation of quasi-particles (chapter 5), create reflections in the propagation of an excitation (chapter 6), etc. Those effects are even more pronounced as the range of interactions increases. Part of those problems can be solved by designing a lattice with periodic boundary conditions, as done in one dimension in chapters 4 and 5. However, even in translationally-invariant systems, finite size prevents from generalizing the properties of the phase to the thermodynamic limit, as illustrated in chapter 5 with the dispersion relation of one-dimensional excitations. Scaling up the number of particles is thus an important challenge, not only for digital but also for analog quantum simulation (Tao et al., 2024; Gyger et al., 2024; Manetsch et al., 2024; Lin et al., 2024; Guo et al., 2024).

Enhanced tunability of the many-body Hamiltonians Finally, we extended the range of accessible Hamiltonians using Rydberg interactions beyond the usual spin-1/2 models. Thanks to a careful benchmark of the off-diagonal van der Waals interactions (chapter 3), we implemented a spin-hole model called the bosonic t-J-V model, which describes both magnetic interactions and tunneling terms (chapter 3). This is a step towards solving more general classes of condensed-matter problems using a Rydberg-based quantum simulator.

A new machine is currently under construction in our group, inspired by the observed limitations of the setup and by some recently-published technical improvements in the cold-atom community. More generally, a lot of work remains to be done to make quantum simulators more reliable, and bring them to a stage where they teach us something radically new about the equilibrium and out-of-equilibrium physics of strongly correlated many-body systems.

Software: insights on quantum magnetism with long-range couplings

In spite of the above limitations, our quantum simulator allows us to explore some fundamental many-body phenomena, in various regimes ranging from low-energy equilibrium properties to the dynamics of high-energy states.

Characterization of magnetic order at equilibrium We first focused on the dipolar XY spin model H_{XY}, which describes static particles that can exchange their spin with a $1/r^3$-decaying interaction strength. In chapter 4, we prepared low-energy states of $\pm H_{\mathrm{XY}}$ with a new adiabatic procedure that makes use of a staggered magnetic field to increase the many-body energy gaps. We observed direct signatures of ferromagnetic (FM) or antiferromagnetic (AFM) ordering, measured through site-resolved correlations. We demonstrated the crucial role of dipolar interactions on the ordering: while the FM order is reinforced by the long-range couplings, the AFM order is destabilized by the weak geometrical frustration between next-nearest neighbor sites. In one dimension, we measured power-law decaying correlations at short distances with an exponential correction at large distances, consistent with the Tomonaga-Luttinger theory at thermal equilibrium. In an open chain, we detected a staggered magnetization around an impurity, a phenomenon equivalent to Friedel oscillations in fermionic systems, and verified the expected dependence of the Friedel wavevector with the total magnetization of the chain.

Quench spectroscopy of the dispersion relation in quantum magnets In chapter 5, we applied a new method for measuring the dispersion relation of quasi-particles of a translationally-invariant system. This method, coined *quench spectroscopy*, reconstructs the dispersion relation by tracking the spatial and temporal evolution of the correlations, and applying a double Fourier transform to get the quench spectral function. In one dimension, we obtained a linear dispersion relation at low wavevector k in both FM and AFM cases ($\omega_k \sim |k|$), corresponding to the sound modes of a Tomonaga-Luttinger liquid. Here, the dipolar nature of the interactions only affects the value of the sound velocity, without changing the nature of the phase. By contrast, the measured dispersion relation of the two-dimensional square array shows qualitative differences: it remains linear in the AFM case ($\omega_{\mathbf{k}} \sim |\mathbf{k}|$) and becomes dispersive in the FM case ($\omega_{\mathbf{k}} \sim \sqrt{|\mathbf{k}|}$), due to the long-range dipolar couplings.

Propagation of hole bound states in doped magnets Finally, in chapter 6, we mapped the dipole-dipole interactions onto a bosonic spin-hole model called the t-J-V model, enabling studies of hole dynamics in doped spin systems. Experimental results revealed a transition between dynamical phase separation and rapid hole delocalization, depending on the tunneling strength t and the hole-hole interaction V. We observed hole bound states and characterized their propagation speed, showing the role of next-nearest neighbor tunneling t and the influence of various spin backgrounds. Preliminary two-dimensional studies showed promise for exploring more complex systems.

Outlook In the future, we would like to extend those studies to more frustrated geometries (triangular or Kagome lattice), which are expected to host exotic critical phases of matter, such as order-by-disorder (Fey et al., 2019; Villain et al., 1980) or spin liquids with topological excitations (Semeghini et al., 2021; Bintz et al., 2024).

Making use of the exchange interactions permitted by off-diagonal dipole-dipole interactions opens interesting prospects for the study of spin transport with Rydberg atoms (Ferreira and Filippone, 2020). In models similar to the t-J-V Hamiltonian, it would be interesting to probe the transport properties of several holes in two dimensions, a regime that is hard to simulate if the initial state has a high energy density. Seeing hole bound states in two dimensions due to the spin background would be particularly exciting, as it may pave the way to a better understanding of hole pairing in superconductors.

With three Rydberg levels, one could also imagine studying spin-1 physics (Mögerle et al., 2024; Liu et al., 2022), which can show radically new phenomena compared with spin-1/2 physics, such as the fractionalization of excitations in the so-called Haldane phase.

Appendix A

Some analytical results on the XY model

A.1 All-to-all XY Hamiltonian

Here, we derive the ground state of $\pm H_{\mathrm{XY}}^{\infty}$, the XY Hamiltonian with all-to-all couplings:

$$H_{\mathrm{XY}}^{\infty} \equiv \frac{\hbar J}{2} \sum_{i<j} \left(\sigma_i^x \sigma_j^x + \sigma_i^y \sigma_j^y\right) \tag{A.1}$$

which can be simplified into

$$\begin{aligned} H_{\mathrm{XY}}^{\infty} &= \frac{\hbar J}{4} \left[(M^x)^2 + (M^y)^2 - 2N\right] \\ &= \frac{\hbar J}{4} \left[\mathbf{M}^2 - (M^z)^2 - 2N\right]. \end{aligned} \tag{A.2}$$

with $M^{\mu} \equiv \sum_{j=1}^{N} \sigma_j^{\mu}$ the total magnetization along μ, and $\mathbf{M} \equiv M^x \mathbf{e}_x + M^y \mathbf{e}_y + M^z \mathbf{e}_z$. We restrict our analysis to an even number of spins N. In the scope of this thesis, the all-to-all Hamiltonian is not meant to describe a real physical situation, but rather to illustrate some effects of long-range interactions, with the advantage that analytical solutions exist.

Ferromagnetic ground state For a fixed value of the z-magnetization $M^z = m$, the ferromagnetic ground state is given by the state with the largest total magnetization: this is the *Dicke state* $\left|\frac{N}{2}, M^z = m\right\rangle$, which is an eigenstate of $\left(\frac{1}{2}\mathbf{M}\right)^2$ with eigenvalue $\frac{N}{2}\left(\frac{N}{2}+1\right)$, and an eigenstate of M^z with eigenvalue m (Dicke, 1954; Pezzè et al., 2018). For infinite-range interactions, the ferromagnetic tower of states is thus simply given by the Dicke states. In particular, the ferromagnetic (FM) ground state at

$M^z = 0$ is the superposition of all states with equal number of spins up and down:

$$\begin{aligned} |\mathrm{FM}^{\infty}_{\mathrm{XY}}\rangle &\equiv \left|\frac{N}{2}, M^z = 0\right\rangle \\ &= \frac{1}{\sqrt{\binom{N}{N/2}}} \sum_{\substack{K\subset[\![1,N]\!] \\ \#K=N/2}} \bigotimes_{j\in K} |\uparrow\rangle_j \bigotimes_{j'\notin K} |\downarrow\rangle_{j'} \end{aligned} \tag{A.3}$$

The spin-spin correlations in this phase can be computed from the microscopic picture, or more simply by noticing that the correlations have the same value for all pairs. As a consequence, the square of the total magnetization along any direction $\mu \in \{x, y, z\}$ is given by

$$\begin{aligned} \left\langle (M^\mu)^2 \right\rangle &= \sum_{i=1}^{N}\sum_{j=1}^{N} \langle \sigma_i^\mu \sigma_j^\mu \rangle \\ &= N + N(N-1)\, C_\infty^\mu \end{aligned} \tag{A.4}$$

with $C_\infty^\mu \equiv \langle \sigma_i^\mu \sigma_j^\mu \rangle$ for any pair $i \neq j$. Note that here, the connected part of the correlations does not matter since each spin j has a vanishing average magnetization in all directions: $\langle \sigma_j^\mu \rangle = 0$. Using $\left\langle (M^z)^2 \right\rangle = 0$, we obtain

$$C_\infty^z = \frac{-1}{N-1} \underset{N\to+\infty}{\longrightarrow} 0. \tag{A.5}$$

Since the state is $U(1)$ symmetric, its correlations are equal along x and y: $C_\infty^x = C_\infty^y$. Using the fact that $\left\langle \left(\frac{1}{2}\mathbf{M}\right)^2 \right\rangle = \frac{N}{2}\left(\frac{N}{2}+1\right) = \frac{1}{4}\left[\left\langle (M^x)^2 \right\rangle + \left\langle (M^y)^2 \right\rangle + \left\langle (M^z)^2 \right\rangle\right]$, we obtain

$$C_\infty^x = C_\infty^y = \frac{N}{2(N-1)} \underset{N\to+\infty}{\longrightarrow} \frac{1}{2}. \tag{A.6}$$

This state thus provides a good picture for a long-range ordered state with $U(1)$ symmetry.

Another intuitive rewriting of the FM ground state is the superposition of all classical ferromagnets in the XY plane:

$$|\mathrm{FM}^{\infty}_{\mathrm{XY}}\rangle = \frac{2^{N/2}}{2\pi\sqrt{\binom{N}{N/2}}} \int_0^{2\pi} |\mathrm{FM}_\theta\rangle \, d\theta. \tag{A.7}$$

Here, we have defined $|\mathrm{FM}_\theta\rangle \equiv |{\rightarrow_\theta}\rangle^{\otimes N}$ with $|{\rightarrow_\theta}\rangle \equiv \frac{1}{\sqrt{2}}\left(e^{-i\frac{\theta}{2}}|\uparrow\rangle + e^{i\frac{\theta}{2}}|\downarrow\rangle\right)$. $|\mathrm{FM}_\theta\rangle$ is

the product state of all spins pointing along a direction $\mathbf{u} = \cos(\theta)\mathbf{e}_x + \sin(\theta)\mathbf{e}_y$. The link between Eq. (A.3) and Eq. (A.7) can be proven by expanding $|{\rightarrow}\,(\theta)\rangle^{\otimes N}$ in the z basis, and keeping only the terms with as many spins up as spin down. The other terms vanish due to the fact that $\int_0^{2\pi} d\theta\, e^{i\theta} = 0$.

Antiferromagnetic ground state The antiferromagnetic (AFM) ground state at $M^z = 0$ satisfies $\langle \mathbf{M}^2 \rangle = 0$:

$$|\mathrm{AFM}^{\infty}_{\mathrm{XY}}\rangle \equiv \left|\mathbf{M}^2 = 0, M^z = 0\right\rangle . \tag{A.8}$$

Since $\langle \mathbf{M}^2 \rangle = 0$, the AFM ground state is also an eigenstate of M^x and M^y with eigenvalue 0. So it is completely $SU(2)$ isotropic.

The AFM ground state is actually not a single state, but rather a highly-degenerate manifold of states. For example, let us consider an arbitrary covering of the N-spin array by groups of two atoms in the singlet state $|-\rangle \equiv \frac{1}{\sqrt{2}}\left(|{\uparrow},{\downarrow}\rangle - |{\uparrow},{\downarrow}\rangle\right)$. Such a many-body state is known as a *valence-bond solid* (VBS) in the literature. A mathematical writing of a VBS on a set of spin pairs $\mathcal{P}$ is

$$|\mathrm{VBS}(\mathcal{P})\rangle \equiv \bigotimes_{(i,j)\in\mathcal{P}} |-\rangle_{i,j} . \tag{A.9}$$

Using the fact that each singlet state is an eigenstate with eigenvalue zero of the total magnetization squared for the two considered spins, one immediately finds that any VBS state satisfies $\langle \mathbf{M}^2 \rangle = 0$. So, any VBS state is part of the all-to-all AFM ground state manifold. There are $(N-1) \times (N-3) \times \cdots \times 3 \times 1 = \frac{N!}{2^{N/2}\,(N/2)!}$ such states; however they are not all orthogonal to each other, so they form an overcomplete basis of the AFM ground state manifold.

This illustrates the extreme effect of geometrical frustration: large degeneracy and potentially high degree of entanglement.

Comparison with a state breaking the continuous symmetry The true ground states $|\mathrm{FM}^{\infty}_{\mathrm{XY}}\rangle$ and $|\mathrm{AFM}^{\infty}_{\mathrm{XY}}\rangle$ both preserve the $U(1)$ symmetry of the Hamiltonian. In the FM case, one can build up a state with very similar properties, which breaks the $U(1)$ symmetry, by considering a statistical mixture of all classical ferromagnets in the xy-plane, instead of a quantum superposition. The associated density matrix is

$$\rho^{\infty}_{\mathrm{XY}} \equiv \frac{1}{2\pi}\int_0^{2\pi} |\mathrm{FM}_\theta\rangle\,\langle \mathrm{FM}_\theta|\, d\theta. \tag{A.10}$$

To dig into the properties of this state, it is convenient to expand each classical ferromagnet $|\mathrm{FM}_\theta\rangle$ in the z-basis[1]:

$$\begin{aligned}|\mathrm{FM}_\theta\rangle &= |{\rightarrow_\theta}\rangle^{\otimes N} \\ &= \frac{1}{2^{N/2}} \bigotimes_{j=1}^{N} \left(e^{-i\frac{\theta}{2}} |{\uparrow}\rangle_j + e^{i\frac{\theta}{2}} |{\downarrow}\rangle_j \right) \\ &= \frac{1}{2^{N/2}} \sum_{n=0}^{N} e^{-i\frac{\theta}{2}(N-2n)} \sum_{\substack{J\subset[\![1,N]\!] \\ \#J=n}} \bigotimes_{j\in J} |{\uparrow}\rangle_j \bigotimes_{j'\notin J} |{\downarrow}\rangle_{j'} \,. \end{aligned} \tag{A.11}$$

This sum looks very complex, but actually one can recognize the Dicke states in its terms (Pezzè et al., 2018):

$$\left| \frac{N}{2}, M^z = 2n - N \right\rangle = \frac{1}{\sqrt{\binom{N}{n}}} \sum_{\substack{J\subset[\![1,N]\!] \\ \#J=n}} \bigotimes_{j\in J} |{\uparrow}\rangle_j \bigotimes_{j'\notin J} |{\downarrow}\rangle_{j'} \tag{A.12}$$

So the expression of the classical ferromagnet simplifies into

$$|\mathrm{FM}_\theta\rangle = \frac{1}{2^{N/2}} \sum_{n=0}^{N} e^{i\frac{\theta}{2}(N-2n)} \sqrt{\binom{N}{n}} \left| \frac{N}{2}, M^z = 2n - N \right\rangle . \tag{A.13}$$

This is already a result: it means that any classical ferromagnet is a superposition of over all possible Dicke states, with weights that correspond to a binomial distribution. Since the Dicke states form the tower of states in the all-to-all Hamiltonian, this confirms the physical intuition that a classical ferromagnet in the xy-plane is a low-energy state of the XY model.

Injecting Eq. (A.13) into Eq. (A.10), and using the fact that $\int_0^{2\pi} e^{i\theta(n-n')} d\theta = \delta_{n,n'}$, one obtains the expression of the statistical mixture of ferromagnets as a binomial distribution of Dicke states:

$$\rho_{\mathrm{XY}}^{\infty} = \frac{1}{2^N} \sum_{n=0}^{N} \binom{N}{n} \left| \frac{N}{2}, M^z = 2n - N \right\rangle . \tag{A.14}$$

The correlations in the xy-plane are very similar in the true ground state and in the symmetry-breaking state. Using the fact that the correlations in a Dicke state

[1] A common name in the literature of such a classical ferromagnet is a *coherent spin state*. The latter expression is more employed in the context of metrology (Pezzè et al., 2018).

$\left|\frac{N}{2}, M^z = m\right\rangle$ are equal to $\frac{1}{2}\frac{N^2-m^2}{N(N-1)}$, one finds

$$C^x_\infty = C^y_\infty = \frac{1}{2} \quad \text{in state } \rho^\infty_{\mathrm{XY}}. \tag{A.15}$$

The value is slightly lower than the one in the true ground state, but they are the same in the thermodynamic limit. A measurement in the xy-plane can thus hardly differentiate the true ground state from the symmetry-broken state. However, the variance of the total magnetization along z is the one of a binomial distribution:

$$\left\langle (M^z)^2 \right\rangle = N \quad \text{in state } \rho^\infty_{\mathrm{XY}} \tag{A.16}$$

This is quite different from the true ground state which has $\left\langle (M^z)^2 \right\rangle = 0$. The variance of the total magnetization along z thus constitutes a good criterion to study how the continuous symmetry is broken.

A.2 Nearest-neighbor XY Hamiltonian

To get an intuition of how the AFM ground state relates to the FM ground state, it is useful to consider the XY model with nearest neighbor interactions:

$$H^{\mathrm{NN}}_{\mathrm{XY}} = \frac{\hbar J}{2} \sum_{\langle i,j \rangle} \left(\sigma^x_i \sigma^x_j + \sigma^y_i \sigma^y_j \right) \tag{A.17}$$

where the sum runs over nearest neighbor spins. In this case, there is a transformation that maps exactly the AFM ground state into the FM ground state. The square lattice is bipartite: we can split the spins into two sublattices A and B that form a checkerboard pattern, such that each spin in sublattice A has only nearest neighbors in sublattice B. In particular, $H^{\mathrm{NN}}_{\mathrm{XY}}$ can be written as

$$H^{\mathrm{NN}}_{\mathrm{XY}} = \frac{\hbar J}{2} \sum_{i \in A} \sum_{\substack{j \in B \\ \langle i,j \rangle}} \left(\sigma^x_i \sigma^x_j + \sigma^y_i \sigma^y_j \right) \tag{A.18}$$

Then, applying a half rotation around the z-axis to B-atoms results in the new Hamiltonian:

$$\begin{aligned} H_{\mathrm{XY}}^{\mathrm{NN}\prime} &\equiv R^\dagger H_{\mathrm{XY}}^{\mathrm{NN}} R \quad \text{with} \quad R \equiv \bigotimes_{j\in B} e^{-i\frac{\pi}{2}\sigma_j^z} \\ &= \frac{\hbar J}{2} \sum_{i\in A} \sum_{\substack{j\in B \\ \langle i,j\rangle}} \left(\sigma_i^x R^\dagger \sigma_j^x R + \sigma_i^y R^\dagger \sigma_j^y R\right) \\ &= -H_{\mathrm{XY}}^{\mathrm{NN}} \end{aligned} \tag{A.19}$$

where we have used the fact that $R^\dagger \sigma_j^{x,y} R = -\sigma_j^{x,y}$ for $j \in B$. The change of sign under the sublattice rotation means that the energy spectrum of the nearest-neighbor XY Hamiltonian is fully symmetric around 0, and that states with opposite energies are related by the transformation R.

Appendix B

Dispersion relation of a Luttinger liquid

In this Appendix, I diagonalize the Tomonaga-Luttinger Hamiltonian and show that it corresponds to a linear dispersion relation.

Let us consider two continuous fields $\theta(x)$ and $\phi(x)$ defined in one spatial dimension labeled by x, such that they satisfy the bosonic commutation relation

$$[\phi(x), \nabla\theta(x')] = i\pi\,\delta(x - x'). \tag{B.1}$$

We take them as real operators, i.e. $\varphi = \varphi^*$ and $\theta = \theta^*$. The Hamiltonian of a Tomonaga-Luttinger liquid (TLL) for the fields θ and ϕ reads (Giamarchi, 2004)

$$H_{\mathrm{TLL}} = \frac{\hbar u}{2\pi}\int dx\left[K\left(\nabla\theta(x)\right)^2 + \frac{1}{K}\left(\nabla\phi(x)\right)^2\right] \tag{B.2}$$

where u is a characteristic velocity and K is a dimensionless number called the Luttinger parameter. With a few changes of basis, this Hamiltonian can be written exactly as a sum of independent harmonic modes.

First, let us define $\Pi_\phi(x) \equiv \frac{1}{\pi}\nabla\theta(x)$ the conjugate field to θ. We now go to Fourier space by defining

$$\begin{cases} \phi(k) & \equiv & \dfrac{1}{\sqrt{2\pi}}\displaystyle\int_{-\infty}^{\infty} dx\ \phi(x)e^{ikx} \\ \Pi_\phi(k) & \equiv & \dfrac{1}{\sqrt{2\pi}}\displaystyle\int_{-\infty}^{\infty} dx\ \Pi_\phi(x)e^{-ikx} \end{cases} \tag{B.3}$$

From the bosonic commutation relation of the fields in real space [Eq. (B.4)], one also

gets bosonic commutation relations for $\phi(k)$ and $\Pi_\phi(k)$:

$$\begin{aligned}[\phi(k), \Pi_\phi(k')] &= \frac{1}{2\pi} \int dx \int dx' \, [\phi(x), \Pi_\phi(x')] \, e^{ikx - ik'x'} \\ &= \frac{i\pi}{2\pi} \int dx \; e^{i(k-k')x} \\ &= i\pi \, \delta(k - k'). \end{aligned} \tag{B.4}$$

Injecting the inverse Fourier transforms of Eq. (B.3) into the TLL Hamiltonian given by Eq. (B.2), the gradient translates into a simple multiplication by ik, which transforms the Hamiltonian into a sum of harmonic oscillators:

$$\begin{aligned} H_{\text{TLL}} &= \frac{\hbar u}{2\pi} \int dk \left[K\pi^2 \, \Pi_\phi(k)\Pi_\phi(-k) + \frac{1}{K} k^2 \, \phi(k)\phi(-k) \right] \\ &= \frac{\hbar u}{2\pi} \int dk \left[K\pi^2 \, |\Pi_\phi(k)|^2 + \frac{1}{K} k^2 \, |\phi(k)|^2 \right]. \end{aligned} \tag{B.5}$$

Here, we have used the fact that $\phi(x)$ and $\Pi_\phi(x)$ are real, so $\phi(-k) = \phi(k)^*$ and $\Pi_\phi(-k) = \Pi_\phi(k)^*$. To diagonalize the harmonic oscillator, one first renormalizes the bosonic fields to

$$\begin{cases} \tilde{\phi}(k) & \equiv \sqrt{\dfrac{k}{\pi K}} \; |\phi(k)| \\ \tilde{\Pi}_\phi(k) & \equiv \sqrt{\dfrac{\pi K}{k}} \; |\Pi_\phi(k)| \end{cases} \tag{B.6}$$

In this new set of bases, the TLL Hamiltonian reads

$$H_{\text{TLL}} = \frac{1}{2} \int dk \; \hbar u k \left[\tilde{\Pi}_\phi(k)^2 + \tilde{\phi}(k)^2 \right]. \tag{B.7}$$

Finally, one defines the annihilation operators

$$a(k) \equiv \frac{1}{\sqrt{2}} \left(\tilde{\phi}(k) + i \, \tilde{\Pi}_\phi(k) \right) \tag{B.8}$$

which satisfy the canonical bosonic commutation relations

$$\left[a(k), a(k')^\dagger \right] = \delta(k - k'), \tag{B.9}$$

and one obtains a collection of eigenmodes with dispersion relation $\omega_k \equiv uk$:

$$H_{\mathrm{TLL}} = \int dk\ \hbar\omega_k \left[a(k)^\dagger a(k) + \frac{1}{2} \right]. \tag{B.10}$$

Appendix C

Definition of spins from the Schwinger bosons

In this appendix, I show that the spin operators introduced in sec. 6.1 of chapter 6 satisfy the expected canonical commutation relations. This calculation can also be found in some condensed-matter books, such as in Altland and Simons (2010).

Definitions Let us consider the Schwinger bosons associated to the annihilation operators $\{a_{j,\sigma}\}$ for a particle at site j with spin $\sigma \in \{\uparrow, \downarrow\}$. They satisfy the canonical bosonic commutation relations

$$\left[a_{i,\sigma}, a^\dagger_{j,\sigma'}\right] = \delta_{ij}\delta_{\sigma,\sigma'}. \tag{C.1}$$

The spin operators on a site j are defined as:

$$\begin{cases} S^z_j &\equiv \dfrac{1}{2}\left(n_{j,\uparrow} - n_{j,\downarrow}\right) \\ S^x_j &\equiv \dfrac{1}{2}\left(S^-_j + S^+_j\right) \\ S^y_j &\equiv \dfrac{i}{2}\left(S^-_j - S^+_j\right). \end{cases} \quad \text{where} \quad \begin{cases} n_{j,\sigma} &\equiv a^\dagger_{j,\sigma}a_{j,\sigma} \quad \forall\sigma \in \{\uparrow,\downarrow\} \\ S^+_j &\equiv a^\dagger_{j,\uparrow}a_{j,\downarrow} \\ S^-_j &\equiv a^\dagger_{j,\downarrow}a_{j,\uparrow}. \end{cases} \tag{C.2}$$

Commutation relations Let us now compute the commutation relations between the spin components. For example,

$$\begin{aligned} \left[S^x_i, S^y_j\right] &= \frac{i}{2}\left[S^+_i, S^-_j\right] \\ &= \frac{i}{2}\left(a^\dagger_{i,\uparrow}a_{i,\downarrow}a^\dagger_{j,\downarrow}a_{j,\uparrow} - a^\dagger_{j,\downarrow}a_{j,\uparrow}a^\dagger_{i,\uparrow}a_{i,\downarrow}\right) \\ &= \frac{i}{2}\delta_{ij}\left(a^\dagger_{i,\uparrow}a_{j,\uparrow} - a^\dagger_{j,\downarrow}a_{i,\downarrow}\right) \quad \text{using Eq. (C.1)} \\ &= i\ \delta_{ij}\ S^z_j. \end{aligned} \tag{C.3}$$

Similarly, using Eq. (C.1),

$$\begin{aligned}\left[S_i^y, S_j^z\right] &= \frac{i}{4}\left(\left[S_i^-, n_{j,\uparrow}\right] - \left[S_i^-, n_{j,\downarrow}\right] - \left[S_i^+, n_{j,\uparrow}\right] + \left[S_i^+, n_{j,\downarrow}\right]\right) \\ &= \frac{i}{4}\left(a_{i,\downarrow}^\dagger\left[a_{i,\uparrow}, a_{j,\uparrow}^\dagger a_{j,\uparrow}\right] - \left[a_{i,\downarrow}^\dagger, a_{j,\downarrow}^\dagger a_{j,\downarrow}\right] a_{i,\uparrow} - \left[a_{i,\uparrow}^\dagger, a_{j,\uparrow}^\dagger a_{j,\uparrow}\right] a_{i,\downarrow} + a_{i,\uparrow}^\dagger\left[a_{i,\downarrow}, a_{j,\downarrow}^\dagger a_{j,\downarrow}\right]\right) \\ &= \frac{i}{4}\delta_{ij}\left(a_{i,\downarrow}^\dagger a_{i,\uparrow} + a_{i,\downarrow}^\dagger a_{i,\uparrow} + a_{i,\uparrow}^\dagger a_{i,\downarrow} + a_{i,\uparrow}^\dagger a_{i,\downarrow}\right) \\ &= \frac{i}{2}\delta_{ij}\left(S_i^- + S_i^+\right) \\ &= i\ \delta_{ij}\ S_j^x \end{aligned} \tag{C.4}$$

and following the same method,

$$\left[S_i^z, S_j^x\right] = i\ \delta_{ij}\ S_j^y. \tag{C.5}$$

Equations (C.3), (C.4) and (C.5) correspond to the expected commutation relations of a spin algebra for $\mathbf{S}_i \equiv S_i^x \mathbf{e}_x + S_i^y \mathbf{e}_y + S_i^z \mathbf{e}_z$.

Spin squared The spin squared on a given site j is given by

$$\begin{aligned}\mathbf{S}_j^2 &= (S_j^x)^2 + (S_j^y)^2 + (S_j^z)^2 \\ &= \frac{1}{2}\left(S_j^+ S_j^- + S_j^- S_j^+\right) + (S_j^z)^2 \\ &= \frac{n_{j,\uparrow} + n_{j,\downarrow}}{2}\left[\frac{n_{j,\uparrow} + n_{j,\downarrow}}{2} + 1\right] \end{aligned} \tag{C.6}$$

In the case of pure spin models (Heisenberg, XY), the hard-core constraint on the populations is $n_{j,\uparrow} + n_{j,\downarrow} = 1$, which ensures that the total spin of every site is fixed to $\mathbf{S}_j^2 = \frac{1}{2}\left(\frac{1}{2} + 1\right)$. But in our mapping, the hard-core constraint also involves the holes: $n_{j,\uparrow} + n_{j,\downarrow} + n_{j,h} = 1$, so $n_{j,\uparrow} + n_{j,\downarrow} \leq 1$ and $\mathbf{S}_j^2 \leq \frac{1}{2}\left(\frac{1}{2} + 1\right)$. For example, if site j is occupied by a hole, $n_{j,\uparrow} = n_{j,\downarrow} = 0$ so $\mathbf{S}_j^2 = 0$.

Bibliography

W. Alt, D. Schrader, S. Kuhr, M. Müller, V. Gomer, and D. Meschede. Single atoms in a standing-wave dipole trap. *Physical Review A*, 67(3):033403, Mar. 2003. doi:10.1103/PhysRevA.67.033403. URL https://link.aps.org/doi/10.1103/PhysRevA.67.033403. Publisher: American Physical Society. [cited on page 44].

A. Altland and B. D. Simons. *Condensed matter field theory*. Cambridge University Press, Leiden, second edition edition, 2010. ISBN 978-0-511-78928-1 978-0-511-78782-9 978-0-511-78668-6 978-0-511-78998-4. [cited on page 225].

L. J. P. Ament, M. van Veenendaal, T. P. Devereaux, J. P. Hill, and J. van den Brink. Resonant inelastic x-ray scattering studies of elementary excitations. *Reviews of Modern Physics*, 83(2):705–767, June 2011. doi:10.1103/RevModPhys.83.705. URL https://link.aps.org/doi/10.1103/RevModPhys.83.705. Publisher: American Physical Society. [cited on page 164].

S. Anand, C. E. Bradley, R. White, V. Ramesh, K. Singh, and H. Bernien. A dual-species Rydberg array. *Nature Physics*, 20(11):1744–1750, Nov. 2024. ISSN 1745-2481. doi:10.1038/s41567-024-02638-2. URL https://www.nature.com/articles/s41567-024-02638-2. Publisher: Nature Publishing Group. [cited on page 212].

M. H. Anderson, J. R. Ensher, M. R. Matthews, C. E. Wieman, and E. A. Cornell. Observation of Bose-Einstein Condensation in a Dilute Atomic Vapor. *Science*, 269(5221):198–201, July 1995. doi:10.1126/science.269.5221.198. URL https://www.science.org/doi/10.1126/science.269.5221.198. Publisher: American Association for the Advancement of Science. [cited on page 15].

P. W. Anderson. An Approximate Quantum Theory of the Antiferromagnetic Ground State. *Physical Review*, 86(5):694–701, June 1952. doi:10.1103/PhysRev.86.694. URL https://link.aps.org/doi/10.1103/PhysRev.86.694. Publisher: American Physical Society. [cited on page 127].

B. Antonini and V. J. Minkiewicz. Neutron scattering study of spin waves and phonons in MnPt3. *Solid State Communications*, 10(2):203–206, Jan. 1972. ISSN 0038-

1098. doi:10.1016/0038-1098(72)90381-X. URL https://www.sciencedirect.com/science/article/pii/003810987290381X. [cited on page 165].

A. Aspect, J. Dalibard, and G. Roger. Experimental Test of Bell's Inequalities Using Time-Varying Analyzers. *Physical Review Letters*, 49(25):1804–1807, Dec. 1982. doi:10.1103/PhysRevLett.49.1804. URL https://link.aps.org/doi/10.1103/PhysRevLett.49.1804. Publisher: American Physical Society. [cited on page 2].

A. Auerbach. *Interacting Electrons and Quantum Magnetism*. Graduate Texts in Contemporary Physics. Springer New York, New York, NY, 1994. ISBN 978-1-4612-6928-1 978-1-4612-0869-3. doi:10.1007/978-1-4612-0869-3. URL http://link.springer.com/10.1007/978-1-4612-0869-3. [cited on page 187].

O. M. Auslaender, A. Yacoby, R. de Picciotto, K. W. Baldwin, L. N. Pfeiffer, and K. W. West. Tunneling Spectroscopy of the Elementary Excitations in a One-Dimensional Wire. *Science*, 295(5556):825–828, Feb. 2002. doi:10.1126/science.1066266. URL https://www.science.org/doi/full/10.1126/science.1066266. Publisher: American Association for the Advancement of Science. [cited on page 151].

Y. Bao, S. S. Yu, L. Anderegg, E. Chae, W. Ketterle, K.-K. Ni, and J. M. Doyle. Dipolar spin-exchange and entanglement between molecules in an optical tweezer array. *Science*, 382(6675):1138–1143, Dec. 2023. doi:10.1126/science.adf8999. URL https://www.science.org/doi/10.1126/science.adf8999. Publisher: American Association for the Advancement of Science. [cited on pages 95 and 105].

D. Barredo, S. Ravets, H. Labuhn, L. Béguin, A. Vernier, F. Nogrette, T. Lahaye, and A. Browaeys. Demonstration of a Strong Rydberg Blockade in Three-Atom Systems with Anisotropic Interactions. *Physical Review Letters*, 112(18):183002, May 2014. doi:10.1103/PhysRevLett.112.183002. URL https://link.aps.org/doi/10.1103/PhysRevLett.112.183002. Publisher: American Physical Society. [cited on page 94].

D. Barredo, H. Labuhn, S. Ravets, T. Lahaye, A. Browaeys, and C. S. Adams. Coherent Excitation Transfer in a Spin Chain of Three Rydberg Atoms. *Physical Review Letters*, 114(11):113002, Mar. 2015. doi:10.1103/PhysRevLett.114.113002. URL https://link.aps.org/doi/10.1103/PhysRevLett.114.113002. Publisher: American Physical Society. [cited on pages 95 and 99].

D. Barredo, S. de Léséleuc, V. Lienhard, T. Lahaye, and A. Browaeys. An atom-by-atom assembler of defect-free arbitrary two-dimensional atomic arrays. *Science*, 354(6315):

1021–1023, Nov. 2016. doi:10.1126/science.aah3778. URL https://www.science.org/doi/full/10.1126/science.aah3778. Publisher: American Association for the Advancement of Science. [cited on pages 19, 20, and 211].

D. Barredo, V. Lienhard, S. de Léséleuc, T. Lahaye, and A. Browaeys. Synthetic three-dimensional atomic structures assembled atom by atom. *Nature*, 561(7721): 79–82, Sept. 2018. ISSN 1476-4687. doi:10.1038/s41586-018-0450-2. URL https://www.nature.com/articles/s41586-018-0450-2. Number: 7721 Publisher: Nature Publishing Group. [cited on page 17].

D. Barredo, V. Lienhard, P. Scholl, S. de Léséleuc, T. Boulier, A. Browaeys, and T. Lahaye. Three-Dimensional Trapping of Individual Rydberg Atoms in Ponderomotive Bottle Beam Traps. *Physical Review Letters*, 124(2):023201, Jan. 2020. doi:10.1103/PhysRevLett.124.023201. URL https://link.aps.org/doi/10.1103/PhysRevLett.124.023201. Publisher: American Physical Society. [cited on page 78].

J.-L. Basdevant and J. Dalibard. *Quantum Mechanics*. Springer Science & Business Media, May 2006. ISBN 978-3-540-28805-3. Google-Books-ID: 7EcBCAAAQBAJ. [cited on pages 1 and 57].

L. Beguin. *Mesure de l'interaction de van der Waals entre deux atomes de Rydberg*. These de doctorat, Palaiseau, Institut d'optique théorique et appliquée, Dec. 2013. URL https://www.theses.fr/2013IOTA0004. [cited on page 21].

T. A. Bespalova, K. Delić, G. Pupillo, F. Tacchino, and I. Tavernelli. Simulating the Fermi-Hubbard model with long-range hopping on a quantum computer, Oct. 2024. URL http://arxiv.org/abs/2410.07789. arXiv:2410.07789 [quant-ph]. [cited on page 188].

I. I. Beterov, I. I. Ryabtsev, D. B. Tretyakov, and V. M. Entin. Quasiclassical calculations of blackbody-radiation-induced depopulation rates and effective lifetimes of Rydberg nS, nP, and nD alkali-metal atoms with n<=80. *Physical Review A*, 79 (5):052504, May 2009. doi:10.1103/PhysRevA.79.052504. URL https://link.aps.org/doi/10.1103/PhysRevA.79.052504. Publisher: American Physical Society. [cited on page 65].

H. Bethe. Zur Theorie der Metalle. *Zeitschrift für Physik*, 71(3):205–226, Mar. 1931. ISSN 0044-3328. doi:10.1007/BF01341708. URL https://doi.org/10.1007/BF01341708. [cited on page 150].

V. Bharti, S. Sugawa, M. Kunimi, V. S. Chauhan, T. Mahesh, M. Mizoguchi, T. Matsubara, T. Tomita, S. de Léséleuc, and K. Ohmori. Strong Spin-Motion Coupling in the Ultrafast Dynamics of Rydberg Atoms. *Physical Review Letters*, 133(9):093405, Aug. 2024. doi:10.1103/PhysRevLett.133.093405. URL https://link.aps.org/doi/10.1103/PhysRevLett.133.093405. Publisher: American Physical Society. [cited on pages 114 and 115].

R. V. Bijnen. *Quantum engineering with ultracold atoms*. PhD thesis, Technische Universiteit Eindhoven, 2013. URL https://research.tue.nl/en/publications/quantum-engineering-with-ultracold-atoms(8deb2f3c-8a4d-4243-af6c-6f45ccd128e1).html. [cited on page 90].

M. Bintz, V. S. Liu, J. Hauschild, A. Khalifa, S. Chatterjee, M. P. Zaletel, and N. Y. Yao. Dirac spin liquid in quantum dipole arrays, May 2024. URL http://arxiv.org/abs/2406.00098. arXiv:2406.00098 [cond-mat, physics:quant-ph]. [cited on page 214].

G. Birkl and J. Fortágh. Micro traps for quantum information processing and precision force sensing. *Laser & Photonics Reviews*, 1 (1):12–23, 2007. ISSN 1863-8899. doi:10.1002/lpor.200610002. URL https://onlinelibrary.wiley.com/doi/abs/10.1002/lpor.200610002. _eprint: https://onlinelibrary.wiley.com/doi/pdf/10.1002/lpor.200610002. [cited on page 69].

R. Blatt and C. F. Roos. Quantum simulations with trapped ions. *Nature Physics*, 8(4):277–284, Apr. 2012. ISSN 1745-2481. doi:10.1038/nphys2252. URL https://www.nature.com/articles/nphys2252. Number: 4 Publisher: Nature Publishing Group. [cited on pages 5 and 7].

I. Bloch, J. Dalibard, and W. Zwerger. Many-body physics with ultracold gases. *Reviews of Modern Physics*, 80(3):885–964, July 2008. doi:10.1103/RevModPhys.80.885. URL https://link.aps.org/doi/10.1103/RevModPhys.80.885. Publisher: American Physical Society. [cited on page 7].

I. Bloch, J. Dalibard, and S. Nascimbène. Quantum simulations with ultracold quantum gases. *Nature Physics*, 8(4):267–276, Apr. 2012. ISSN 1745-2481. doi:10.1038/nphys2259. URL https://www.nature.com/articles/nphys2259. Number: 4 Publisher: Nature Publishing Group. [cited on page 7].

D. Bluvstein, A. Omran, H. Levine, A. Keesling, G. Semeghini, S. Ebadi, T. T. Wang, A. A. Michailidis, N. Maskara, W. W. Ho, S. Choi, M. Serbyn, M. Greiner, V. Vuletić, and M. D. Lukin. Controlling quantum many-body dynamics in driven Rydberg atom arrays. *Science*, 371(6536):1355–1359, Mar. 2021. ISSN 0036-8075, 1095-9203. doi:10.1126/science.abg2530. URL https://www.science.org/doi/10.1126/science.abg2530. [cited on page 10].

D. Bluvstein, S. J. Evered, A. A. Geim, S. H. Li, H. Zhou, T. Manovitz, S. Ebadi, M. Cain, M. Kalinowski, D. Hangleiter, J. P. Bonilla Ataides, N. Maskara, I. Cong, X. Gao, P. Sales Rodriguez, T. Karolyshyn, G. Semeghini, M. J. Gullans, M. Greiner, V. Vuletić, and M. D. Lukin. Logical quantum processor based on reconfigurable atom arrays. *Nature*, 626(7997):58–65, Feb. 2024. ISSN 1476-4687. doi:10.1038/s41586-023-06927-3. URL https://www.nature.com/articles/s41586-023-06927-3. Publisher: Nature Publishing Group. [cited on page 14].

S. Bocini, F. Caleca, F. Mezzacapo, and T. Roscilde. Non-local quench spectroscopy of fermionic excitations in 1D quantum spin chains, July 2024. URL http://arxiv.org/abs/2407.14802. arXiv:2407.14802 [cond-mat, physics:quant-ph]. [cited on page 158].

M. Bockrath, D. H. Cobden, J. Lu, A. G. Rinzler, R. E. Smalley, L. Balents, and P. L. McEuen. Luttinger-liquid behaviour in carbon nanotubes. *Nature*, 397 (6720):598–601, Feb. 1999. ISSN 1476-4687. doi:10.1038/17569. URL https://www.nature.com/articles/17569. Publisher: Nature Publishing Group. [cited on page 151].

A. Bohrdt, D. Wei, D. Adler, K. Srakaew, S. Agrawal, P. Weckesser, I. Bloch, F. Grusdt, and J. Zeiher. Microscopy of bosonic charge carriers in staggered magnetic fields, Oct. 2024. URL http://arxiv.org/abs/2410.19500. arXiv:2410.19500. [cited on page 207].

G. Bornet. *Quantum simulation of the dipolar XY model using arrays of Rydberg atoms*. phdthesis, Université Paris-Saclay, 2024. URL https://theses.fr/s252139?domaine=theses. [cited on pages 21, 22, 57, 58, 77, 84, 99, and 184].

G. Bornet, G. Emperauger, C. Chen, B. Ye, M. Block, M. Bintz, J. A. Boyd, D. Barredo, T. Comparin, F. Mezzacapo, T. Roscilde, T. Lahaye, N. Y. Yao, and A. Browaeys. Scalable spin squeezing in a dipolar Rydberg atom array.

Nature, pages 1–6, Aug. 2023. ISSN 1476-4687. doi:10.1038/s41586-023-06414-9. URL https://www.nature.com/articles/s41586-023-06414-9. Publisher: Nature Publishing Group. [cited on pages 13 and 177].

G. Bornet, G. Emperauger, C. Chen, F. Machado, S. Chern, L. Leclerc, B. Gély, Y. T. Chew, D. Barredo, T. Lahaye, N. Y. Yao, and A. Browaeys. Enhancing a Many-Body Dipolar Rydberg Tweezer Array with Arbitrary Local Controls. *Physical Review Letters*, 132(26):263601, June 2024. doi:10.1103/PhysRevLett.132.263601. URL https://link.aps.org/doi/10.1103/PhysRevLett.132.263601. Publisher: American Physical Society. [cited on pages 69 and 84].

S. Bravyi, D. DiVincenzo, and D. Loss. Schrieffer–Wolff transformation for quantum many-body systems. *Annals of Physics*, 326(10):2793–2826, Oct. 2011. ISSN 0003-4916. doi:10.1016/j.aop.2011.06.004. URL https://www.sciencedirect.com/science/article/abs/pii/S0003491611001059. Publisher: Academic Press. [cited on page 93].

B. N. Brockhouse. Slow neutron spectroscopy and the grand atlas of the physical world. *Reviews of Modern Physics*, 67(4):735–751, Oct. 1995. ISSN 0034-6861, 1539-0756. doi:10.1103/RevModPhys.67.735. URL https://link.aps.org/doi/10.1103/RevModPhys.67.735. [cited on page 164].

B. N. Brockhouse and P. K. Iyengar. Normal Modes of Germanium by Neutron Spectrometry. *Physical Review*, 111(3):747–754, Aug. 1958. doi:10.1103/PhysRev.111.747. URL https://link.aps.org/doi/10.1103/PhysRev.111.747. Publisher: American Physical Society. [cited on page 165].

A. Browaeys and T. Lahaye. Many-body physics with individually controlled Rydberg atoms. *Nature Physics*, 16(2):132–142, Feb. 2020. ISSN 1745-2481. doi:10.1038/s41567-019-0733-z. URL https://www.nature.com/articles/s41567-019-0733-z. Number: 2 Publisher: Nature Publishing Group. [cited on pages 7 and 97].

A. Browaeys, D. Barredo, and T. Lahaye. Experimental investigations of dipole–dipole interactions between a few Rydberg atoms. *Journal of Physics B: Atomic, Molecular and Optical Physics*, 49(15):152001, Aug. 2016. ISSN 0953-4075, 1361-6455. doi:10.1088/0953-4075/49/15/152001. URL https://iopscience.iop.org/article/10.1088/0953-4075/49/15/152001. [cited on pages 20 and 90].

P. Bruno. Absence of Spontaneous Magnetic Order at Nonzero Temperature in One- and Two-Dimensional Heisenberg and XY Systems with Long-Range Interactions. *Physical Review Letters*, 87(13):137203, Sept. 2001. doi:10.1103/PhysRevLett.87.137203. URL https://link.aps.org/doi/10.1103/PhysRevLett.87.137203. Publisher: American Physical Society. [cited on page 129].

L. Béguin, A. Vernier, R. Chicireanu, T. Lahaye, and A. Browaeys. Direct Measurement of the van der Waals Interaction between Two Rydberg Atoms. *Physical Review Letters*, 110(26):263201, June 2013. doi:10.1103/PhysRevLett.110.263201. URL https://link.aps.org/doi/10.1103/PhysRevLett.110.263201. Publisher: American Physical Society. [cited on page 94].

A. N. Carroll, H. Hirzler, C. Miller, D. Wellnitz, S. R. Muleady, J. Lin, K. P. Zamarski, R. R. W. Wang, J. L. Bohn, A. M. Rey, and J. Ye. Observation of Generalized t-J Spin Dynamics with Tunable Dipolar Interactions, Apr. 2024. URL http://arxiv.org/abs/2404.18916. arXiv:2404.18916 [cond-mat, physics:physics]. [cited on page 188].

I. Carusotto and C. Ciuti. Quantum fluids of light. *Reviews of Modern Physics*, 85(1): 299–366, Feb. 2013. doi:10.1103/RevModPhys.85.299. URL https://link.aps.org/doi/10.1103/RevModPhys.85.299. Publisher: American Physical Society. [cited on page 8].

C. Chen, G. Bornet, M. Bintz, G. Emperauger, L. Leclerc, V. S. Liu, P. Scholl, D. Barredo, J. Hauschild, S. Chatterjee, M. Schuler, A. M. Läuchli, M. P. Zaletel, T. Lahaye, N. Y. Yao, and A. Browaeys. Continuous symmetry breaking in a two-dimensional Rydberg array. *Nature*, 616(7958):691–695, Apr. 2023a. ISSN 1476-4687. doi:10.1038/s41586-023-05859-2. URL https://www.nature.com/articles/s41586-023-05859-2. Number: 7958 Publisher: Nature Publishing Group. [cited on pages 126, 135, and 137].

C. Chen, G. Emperauger, G. Bornet, F. Caleca, B. Gély, M. Bintz, S. Chatterjee, V. Liu, D. Barredo, N. Y. Yao, T. Lahaye, F. Mezzacapo, T. Roscilde, and A. Browaeys. Spectroscopy of elementary excitations from quench dynamics in a dipolar XY Rydberg simulator, Nov. 2023b. URL http://arxiv.org/abs/2311.11726. arXiv:2311.11726 [cond-mat, physics:physics, physics:quant-ph]. [cited on pages 163, 179, 182, and 185].

Y. Chew, T. Tomita, T. P. Mahesh, S. Sugawa, S. de Léséleuc, and K. Ohmori. Ultrafast

energy exchange between two single Rydberg atoms on a nanosecond timescale. *Nature Photonics*, 16(10):724–729, Oct. 2022. ISSN 1749-4893. doi:10.1038/s41566-022-01047-2. URL https://www.nature.com/articles/s41566-022-01047-2. Publisher: Nature Publishing Group. [cited on page 211].

Y. T. Chew, M. Poitrinal, T. Tomita, S. Kitade, J. Mauricio, K. Ohmori, and S. de Léséleuc. Ultra-precise holographic optical tweezers array, July 2024. URL http://arxiv.org/abs/2407.20699. arXiv:2407.20699 [physics, physics:quant-ph]. [cited on pages 46 and 77].

S. Chu, L. Hollberg, J. E. Bjorkholm, A. Cable, and A. Ashkin. Three-dimensional viscous confinement and cooling of atoms by resonance radiation pressure. *Physical Review Letters*, 55(1):48–51, July 1985. doi:10.1103/PhysRevLett.55.48. URL https://link.aps.org/doi/10.1103/PhysRevLett.55.48. Publisher: American Physical Society. [cited on page 15].

S. Chu, J. E. Bjorkholm, A. Ashkin, and A. Cable. Experimental Observation of Optically Trapped Atoms. *Physical Review Letters*, 57(3):314–317, July 1986. doi:10.1103/PhysRevLett.57.314. URL https://link.aps.org/doi/10.1103/PhysRevLett.57.314. Publisher: American Physical Society. [cited on page 15].

C. R. Clark, H. N. Tinkey, B. C. Sawyer, A. M. Meier, K. A. Burkhardt, C. M. Seck, C. M. Shappert, N. D. Guise, C. E. Volin, S. D. Fallek, H. T. Hayden, W. G. Rellergert, and K. R. Brown. High-Fidelity Bell-State Preparation with 40Ca+ Optical Qubits. *Physical Review Letters*, 127(13):130505, Sept. 2021. doi:10.1103/PhysRevLett.127.130505. URL https://link.aps.org/doi/10.1103/PhysRevLett.127.130505. Publisher: American Physical Society. [cited on page 7].

C. Cohen-Tannoudji, B. Diu, and F. Laloë. Forces de van der Waals (complément C XI). In *Mécanique quantique*, volume 2 of *Collection Enseignement des sciences*, pages 1120–1130. Hermann, [2e éd.] rev., corr. et augm. d'une bibliogr. étendue edition, 1994. ISBN 978-2-7056-6121-2. [cited on pages 90 and 91].

C. Cohen-Tannoudji, J. Dupont-Roc, and G. Grynberg. *Atom-Photon Interactions: Basic Processes and Applications*. John Wiley & Sons, Mar. 1998. ISBN 978-0-471-29336-1. Google-Books-ID: hNWbEAAAQBAJ. [cited on page 93].

C. N. Cohen-Tannoudji. Nobel Lecture: Manipulating atoms with photons. *Reviews of Modern Physics*, 70(3):707–719, July 1998. doi:10.1103/RevModPhys.70.707. URL

https://link.aps.org/doi/10.1103/RevModPhys.70.707. Publisher: American Physical Society. [cited on page 15].

collaboration LIGO. Enhanced sensitivity of the LIGO gravitational wave detector by using squeezed states of light. *Nature Photonics*, 7(8):613–619, Aug. 2013. ISSN 1749-4893. doi:10.1038/nphoton.2013.177. URL https://www.nature.com/articles/nphoton.2013.177. [cited on page 12].

T. Comparin, F. Mezzacapo, M. Robert-de Saint-Vincent, and T. Roscilde. Scalable Spin Squeezing from Spontaneous Breaking of a Continuous Symmetry. *Physical Review Letters*, 129(11):113201, Sept. 2022a. doi:10.1103/PhysRevLett.129.113201. URL https://link.aps.org/doi/10.1103/PhysRevLett.129.113201. Publisher: American Physical Society. [cited on page 177].

T. Comparin, F. Mezzacapo, and T. Roscilde. Multipartite Entangled States in Dipolar Quantum Simulators. *Physical Review Letters*, 129(15):150503, Oct. 2022b. doi:10.1103/PhysRevLett.129.150503. URL https://link.aps.org/doi/10.1103/PhysRevLett.129.150503. Publisher: American Physical Society. [cited on page 177].

A. H. Compton. A Quantum Theory of the Scattering of X-rays by Light Elements. *Physical Review*, 21(5):483–502, May 1923. ISSN 0031-899X. doi:10.1103/PhysRev.21.483. URL https://link.aps.org/doi/10.1103/PhysRev.21.483. [cited on page 164].

S. L. Cornish, M. R. Tarbutt, and K. R. A. Hazzard. Quantum computation and quantum simulation with ultracold molecules. *Nature Physics*, 20(5):730–740, May 2024. ISSN 1745-2481. doi:10.1038/s41567-024-02453-9. URL https://www.nature.com/articles/s41567-024-02453-9. Publisher: Nature Publishing Group. [cited on page 7].

R. G. Cortiñas, M. Favier, B. Ravon, P. Méhaignerie, Y. Machu, J. M. Raimond, C. Sayrin, and M. Brune. Laser Trapping of Circular Rydberg Atoms. *Physical Review Letters*, 124(12):123201, Mar. 2020. doi:10.1103/PhysRevLett.124.123201. URL https://link.aps.org/doi/10.1103/PhysRevLett.124.123201. Publisher: American Physical Society. [cited on page 211].

E. Dagotto. Correlated electrons in high-temperature superconductors. *Reviews of Modern Physics*, 66(3):763–840, July 1994. doi:10.1103/RevModPhys.66.763. URL

https://link.aps.org/doi/10.1103/RevModPhys.66.763. Publisher: American Physical Society. [cited on page 187].

L. D'Alessio, Y. Kafri, A. Polkovnikov, and M. Rigol. From quantum chaos and eigenstate thermalization to statistical mechanics and thermodynamics. *Advances in Physics*, 65(3):239–362, May 2016. ISSN 0001-8732. doi:10.1080/00018732.2016.1198134. URL https://doi.org/10.1080/00018732.2016.1198134. [cited on page 3].

J. Dalibard. Optical lattices. *Collège de France, chair Atoms and radiation*, 2012. URL https://pro.college-de-france.fr/jean.dalibard/CdF/2013/total_en_2013.pdf. [cited on page 40].

J. Dalibard. Laser cooling of atomic gases. *Collège de France, chair Atoms and radiation*, 2014. URL https://pro.college-de-france.fr/jean.dalibard/CdF/2015/total_en_2015.pdf. [cited on page 29].

S. de Léséleuc. *Quantum simulation of spin models with assembled arrays of Rydberg atoms*. These de doctorat, Université Paris-Saclay (ComUE), Dec. 2018. URL http://www.theses.fr/2018SACLO007. [cited on pages 17, 20, 22, and 72].

S. de Léséleuc and Y. T. Chew. Ground-state cooling of large atomic arrays in tweezers (internal communication), 2022. [cited on page 46].

S. de Léséleuc, D. Barredo, V. Lienhard, A. Browaeys, and T. Lahaye. Optical Control of the Resonant Dipole-Dipole Interaction between Rydberg Atoms. *Physical Review Letters*, 119(5):053202, Aug. 2017. doi:10.1103/PhysRevLett.119.053202. URL https://link.aps.org/doi/10.1103/PhysRevLett.119.053202. Publisher: American Physical Society. [cited on page 70].

S. de Léséleuc, D. Barredo, V. Lienhard, A. Browaeys, and T. Lahaye. Analysis of imperfections in the coherent optical excitation of single atoms to Rydberg states. *Physical Review A*, 97(5):053803, May 2018. doi:10.1103/PhysRevA.97.053803. URL https://link.aps.org/doi/10.1103/PhysRevA.97.053803. Publisher: American Physical Society. [cited on pages 64 and 65].

S. de Léséleuc, V. Lienhard, P. Scholl, D. Barredo, S. Weber, N. Lang, H. P. Büchler, T. Lahaye, and A. Browaeys. Observation of a symmetry-protected topological phase of interacting bosons with Rydberg atoms. *Science*, 365(6455):775–780,

Aug. 2019. ISSN 0036-8075, 1095-9203. doi:10.1126/science.aav9105. URL https://www.science.org/doi/10.1126/science.aav9105. [cited on pages 9 and 110].

M. DeCross, R. Haghshenas, M. Liu, E. Rinaldi, J. Gray, Y. Alexeev, C. H. Baldwin, J. P. Bartolotta, M. Bohn, E. Chertkov, J. Cline, J. Colina, D. DelVento, J. M. Dreiling, C. Foltz, J. P. Gaebler, T. M. Gatterman, C. N. Gilbreth, J. Giles, D. Gresh, A. Hall, A. Hankin, A. Hansen, N. Hewitt, I. Hoffman, C. Holliman, R. B. Hutson, T. Jacobs, J. Johansen, P. J. Lee, E. Lehman, D. Lucchetti, D. Lykov, I. S. Madjarov, B. Mathewson, K. Mayer, M. Mills, P. Niroula, J. M. Pino, C. Roman, M. Schecter, P. E. Siegfried, B. G. Tiemann, C. Volin, J. Walker, R. Shaydulin, M. Pistoia, S. A. Moses, D. Hayes, B. Neyenhuis, R. P. Stutz, and M. Foss-Feig. The computational power of random quantum circuits in arbitrary geometries, June 2024. URL http://arxiv.org/abs/2406.02501. arXiv:2406.02501 [quant-ph]. [cited on page 12].

J. Delpy, N. Fayard, F. Bretenaker, and F. Goldfarb. Long-range interactions revealed by collective spin noise spectra in atomic vapors, June 2024. URL http://arxiv.org/abs/2407.00177. arXiv:2407.00177 [quant-ph]. [cited on page 89].

H. Deng, G. Weihs, C. Santori, J. Bloch, and Y. Yamamoto. Condensation of Semiconductor Microcavity Exciton Polaritons. *Science*, 298(5591):199–202, Oct. 2002. ISSN 0036-8075, 1095-9203. doi:10.1126/science.1074464. URL https://www.science.org/doi/10.1126/science.1074464. [cited on page 165].

P. Di Francesco, P. Mathieu, and D. Sénéchal. 11. Finite-Size Scaling and Boundaries 11.1 Conformal Invariance on a Cylinder. In *Conformal Field Theory*, Graduate texts in contemporary physics, pages 409–412. Springer, New York, nachdr. edition, 2011. ISBN 978-0-387-94785-3. URL https://link.springer.com/book/10.1007/978-1-4612-2256-9. [cited on page 153].

R. H. Dicke. Coherence in Spontaneous Radiation Processes. *Physical Review*, 93 (1):99–110, Jan. 1954. doi:10.1103/PhysRev.93.99. URL https://link.aps.org/doi/10.1103/PhysRev.93.99. Publisher: American Physical Society. [cited on page 215].

R. J. Donnelly, J. A. Donnelly, and R. N. Hills. Specific heat and dispersion curve for helium II. *Journal of Low Temperature Physics*, 44(5):471–489, Sept. 1981. ISSN 1573-7357. doi:10.1007/BF00117839. URL https://doi.org/10.1007/BF00117839. [cited on page 165].

L.-M. Duan, E. Demler, and M. D. Lukin. Controlling Spin Exchange Interactions of Ultracold Atoms in Optical Lattices. *Physical Review Letters*, 91(9):090402, Aug. 2003. doi:10.1103/PhysRevLett.91.090402. URL https://link.aps.org/doi/10.1103/PhysRevLett.91.090402. Publisher: American Physical Society. [cited on page 187].

P. T. Dumitrescu, J. G. Bohnet, J. P. Gaebler, A. Hankin, D. Hayes, A. Kumar, B. Neyenhuis, R. Vasseur, and A. C. Potter. Dynamical topological phase realized in a trapped-ion quantum simulator. *Nature*, 607(7919):463–467, July 2022. ISSN 1476-4687. doi:10.1038/s41586-022-04853-4. URL https://www.nature.com/articles/s41586-022-04853-4. Publisher: Nature Publishing Group. [cited on page 69].

S. K. Dutta, J. R. Guest, D. Feldbaum, A. Walz-Flannigan, and G. Raithel. Ponderomotive Optical Lattice for Rydberg Atoms. *Physical Review Letters*, 85(26):5551–5554, Dec. 2000. doi:10.1103/PhysRevLett.85.5551. URL https://link.aps.org/doi/10.1103/PhysRevLett.85.5551. Publisher: American Physical Society. [cited on page 78].

S. Ebadi, T. T. Wang, H. Levine, A. Keesling, G. Semeghini, A. Omran, D. Bluvstein, R. Samajdar, H. Pichler, W. W. Ho, S. Choi, S. Sachdev, M. Greiner, V. Vuletić, and M. D. Lukin. Quantum phases of matter on a 256-atom programmable quantum simulator. *Nature*, 595(7866):227–232, July 2021. ISSN 1476-4687. doi:10.1038/s41586-021-03582-4. URL https://www.nature.com/articles/s41586-021-03582-4. Number: 7866 Publisher: Nature Publishing Group. [cited on pages 8, 9, and 97].

W. J. Eckner, N. Darkwah Oppong, A. Cao, A. W. Young, W. R. Milner, J. M. Robinson, J. Ye, and A. M. Kaufman. Realizing spin squeezing with Rydberg interactions in an optical clock. *Nature*, 621(7980):734–739, Sept. 2023. ISSN 1476-4687. doi:10.1038/s41586-023-06360-6. URL https://www.nature.com/articles/s41586-023-06360-6. Publisher: Nature Publishing Group. [cited on pages 13 and 177].

A. Elben, S. T. Flammia, H.-Y. Huang, R. Kueng, J. Preskill, B. Vermersch, and P. Zoller. The randomized measurement toolbox. *Nature Reviews Physics*, 5(1):9–24, Jan. 2023. ISSN 2522-5820. doi:10.1038/s42254-022-00535-2. URL https://www.nature.com/articles/s42254-022-00535-2. Publisher: Nature Publishing Group. [cited on page 69].

G. Emperauger, M. Qiao, C. Chen, F. Caleca, S. Bocini, M. Bintz, G. Bornet,

R. Martin, B. Gély, L. Klein, D. Barredo, S. Chatterjee, N. Yao, F. Mezzacapo, T. Lahaye, T. Roscilde, and A. Browaeys. Tomonaga-Luttinger Liquid Behavior in a Rydberg-encoded Spin Chain, Jan. 2025. URL http://arxiv.org/abs/2501.08179. arXiv:2501.08179 [quant-ph]. [cited on pages 126 and 163].

S. J. Evered, D. Bluvstein, M. Kalinowski, S. Ebadi, T. Manovitz, H. Zhou, S. H. Li, A. A. Geim, T. T. Wang, N. Maskara, H. Levine, G. Semeghini, M. Greiner, V. Vuletić, and M. D. Lukin. High-fidelity parallel entangling gates on a neutral-atom quantum computer. *Nature*, 622(7982):268–272, Oct. 2023. ISSN 1476-4687. doi:10.1038/s41586-023-06481-y. URL https://www.nature.com/articles/s41586-023-06481-y. Publisher: Nature Publishing Group. [cited on page 94].

N. Fabbri, M. Panfil, D. Clément, L. Fallani, M. Inguscio, C. Fort, and J.-S. Caux. Dynamical structure factor of one-dimensional Bose gases: experimental signatures of beyond-Luttinger liquid physics. *Physical Review A*, 91(4):043617, Apr. 2015. ISSN 1050-2947, 1094-1622. doi:10.1103/PhysRevA.91.043617. URL http://arxiv.org/abs/1406.2176. arXiv:1406.2176 [cond-mat, physics:quant-ph]. [cited on page 151].

F. Fang, K. Wang, V. S. Liu, Y. Wang, R. Cimmino, J. Wei, M. Bintz, A. Parr, J. Kemp, K.-K. Ni, and N. Y. Yao. Probing critical phenomena in open quantum systems using atom arrays, Feb. 2024. URL http://arxiv.org/abs/2402.15376. arXiv:2402.15376 [cond-mat, physics:physics, physics:quant-ph]. [cited on pages 152 and 155].

L. Feng, O. Katz, C. Haack, M. Maghrebi, A. V. Gorshkov, Z. Gong, M. Cetina, and C. Monroe. Continuous symmetry breaking in a trapped-ion spin chain. *Nature*, 623(7988):713–717, Nov. 2023. ISSN 1476-4687. doi:10.1038/s41586-023-06656-7. URL https://www.nature.com/articles/s41586-023-06656-7. Publisher: Nature Publishing Group. [cited on page 138].

J. S. Ferreira and M. Filippone. Ballistic-to-diffusive transition in spin chains with broken integrability. *Physical Review B*, 102(18):184304, Nov. 2020. doi:10.1103/PhysRevB.102.184304. URL https://link.aps.org/doi/10.1103/PhysRevB.102.184304. Publisher: American Physical Society. [cited on page 214].

S. Fey, S. C. Kapfer, and K. P. Schmidt. Quantum Criticality of Two-Dimensional Quantum Magnets with Long-Range Interactions. *Physical Review Letters*, 122 (1):017203, Jan. 2019. doi:10.1103/PhysRevLett.122.017203. URL https://link.

aps.org/doi/10.1103/PhysRevLett.122.017203. Publisher: American Physical Society. [cited on page 214].

R. P. Feynman. Simulating physics with computers. *International Journal of Theoretical Physics*, 21(6):467–488, June 1982. ISSN 1572-9575. doi:10.1007/BF02650179. URL https://doi.org/10.1007/BF02650179. [cited on page 4].

M. Fishman, S. White, and E. M. Stoudenmire. The ITensor Software Library for Tensor Network Calculations. *SciPost Physics Codebases*, page 004, Aug. 2022. ISSN 2949-804X. doi:10.21468/SciPostPhysCodeb.4. URL https://scipost.org/10.21468/SciPostPhysCodeb.4. [cited on page 172].

C. Flühmann, T. L. Nguyen, M. Marinelli, V. Negnevitsky, K. Mehta, and J. P. Home. Encoding a qubit in a trapped-ion mechanical oscillator. *Nature*, 566(7745):513–517, Feb. 2019. ISSN 1476-4687. doi:10.1038/s41586-019-0960-6. URL https://www.nature.com/articles/s41586-019-0960-6. Publisher: Nature Publishing Group. [cited on page 7].

Q. Fontaine, D. Squizzato, F. Baboux, I. Amelio, A. Lemaître, M. Morassi, I. Sagnes, L. Le Gratiet, A. Harouri, M. Wouters, I. Carusotto, A. Amo, M. Richard, A. Minguzzi, L. Canet, S. Ravets, and J. Bloch. Kardar–Parisi–Zhang universality in a one-dimensional polariton condensate. *Nature*, 608(7924):687–691, Aug. 2022. ISSN 1476-4687. doi:10.1038/s41586-022-05001-8. URL https://www.nature.com/articles/s41586-022-05001-8. Publisher: Nature Publishing Group. [cited on page 10].

D. Forster. *Hydrodynamic Fluctuations, Broken Symmetry, And Correlation Functions*. CRC Press, Boca Raton, May 2019. ISBN 978-0-429-49368-3. doi:10.1201/9780429493683. [cited on page 164].

J. Franke, S. R. Muleady, R. Kaubruegger, F. Kranzl, R. Blatt, A. M. Rey, M. K. Joshi, and C. F. Roos. Quantum-enhanced sensing on optical transitions through finite-range interactions. *Nature*, 621(7980):740–745, Sept. 2023. ISSN 1476-4687. doi:10.1038/s41586-023-06472-z. URL https://www.nature.com/articles/s41586-023-06472-z. Publisher: Nature Publishing Group. [cited on pages 13 and 177].

T. Franz, S. Geier, C. Hainaut, A. Braemer, N. Thaicharoen, M. Hornung, E. Braun, M. Gärttner, G. Zürn, and M. Weidemüller. Observation of anisotropy-independent

magnetization dynamics in spatially disordered Heisenberg spin systems. *Physical Review Research*, 6(3):033131, Aug. 2024. doi:10.1103/PhysRevResearch.6.033131. URL https://link.aps.org/doi/10.1103/PhysRevResearch.6.033131. Publisher: American Physical Society. [cited on page 95].

A. Friedenauer, H. Schmitz, J. T. Glueckert, D. Porras, and T. Schaetz. Simulating a quantum magnet with trapped ions. *Nature Physics*, 4(10):757–761, Oct. 2008. ISSN 1745-2481. doi:10.1038/nphys1032. URL https://www.nature.com/articles/nphys1032. Publisher: Nature Publishing Group. [cited on page 9].

I. Frérot, P. Naldesi, and T. Roscilde. Entanglement and fluctuations in the XXZ model with power-law interactions. *Physical Review B*, 95(24):245111, June 2017. doi:10.1103/PhysRevB.95.245111. URL https://link.aps.org/doi/10.1103/PhysRevB.95.245111. Publisher: American Physical Society. [cited on pages 177 and 182].

I. Frérot, P. Naldesi, and T. Roscilde. Multispeed Prethermalization in Quantum Spin Models with Power-Law Decaying Interactions. *Physical Review Letters*, 120(5):050401, Jan. 2018. doi:10.1103/PhysRevLett.120.050401. URL https://link.aps.org/doi/10.1103/PhysRevLett.120.050401. Publisher: American Physical Society. [cited on pages 163, 165, 177, and 182].

T. Fukuhara, P. Schauß, M. Endres, S. Hild, M. Cheneau, I. Bloch, and C. Gross. Microscopic observation of magnon bound states and their dynamics. *Nature*, 502(7469):76–79, Oct. 2013. ISSN 1476-4687. doi:10.1038/nature12541. URL https://www.nature.com/articles/nature12541. Publisher: Nature Publishing Group. [cited on pages 69 and 198].

J. P. Gaebler, A. M. Meier, T. R. Tan, R. Bowler, Y. Lin, D. Hanneke, J. D. Jost, J. P. Home, E. Knill, D. Leibfried, and D. J. Wineland. Randomized Benchmarking of Multiqubit Gates. *Physical Review Letters*, 108(26):260503, June 2012. doi:10.1103/PhysRevLett.108.260503. URL https://link.aps.org/doi/10.1103/PhysRevLett.108.260503. Publisher: American Physical Society. [cited on page 69].

T. F. Gallagher. *Rydberg Atoms*. Cambridge Monographs on Atomic, Molecular and Chemical Physics. Cambridge University Press, Cambridge, 1994. ISBN 978-0-521-02166-1. doi:10.1017/CBO9780511524530. URL https://www.cambridge.

org/core/books/rydberg-atoms/B610BDE54694936F496F59F326C1A81B. [cited on pages 20 and 66].

T. F. Gallagher and P. Pillet. Dipole–Dipole Interactions of Rydberg Atoms. In *Advances In Atomic, Molecular, and Optical Physics*, volume 56 of *Advances in Atomic, Molecular, and Optical Physics*, pages 161–218. Academic Press, Jan. 2008. doi:10.1016/S1049-250X(08)00013-X. URL https://www.sciencedirect.com/science/article/pii/S1049250X0800013X. [cited on page 90].

J. M. Gambetta, A. D. Córcoles, S. T. Merkel, B. R. Johnson, J. A. Smolin, J. M. Chow, C. A. Ryan, C. Rigetti, S. Poletto, T. A. Ohki, M. B. Ketchen, and M. Steffen. Characterization of Addressability by Simultaneous Randomized Benchmarking. *Physical Review Letters*, 109(24):240504, Dec. 2012. doi:10.1103/PhysRevLett.109.240504. URL https://link.aps.org/doi/10.1103/PhysRevLett.109.240504. Publisher: American Physical Society. [cited on page 69].

M. Garwood and L. DelaBarre. The Return of the Frequency Sweep: Designing Adiabatic Pulses for Contemporary NMR. *Journal of Magnetic Resonance*, 153(2): 155–177, Dec. 2001. ISSN 1090-7807. doi:10.1006/jmre.2001.2340. URL https://www.sciencedirect.com/science/article/pii/S1090780701923407. [cited on page 46].

A. Gaëtan, Y. Miroshnychenko, T. Wilk, A. Chotia, M. Viteau, D. Comparat, P. Pillet, A. Browaeys, and P. Grangier. Observation of collective excitation of two individual atoms in the Rydberg blockade regime. *Nature Physics*, 5 (2):115–118, Feb. 2009. ISSN 1745-2481. doi:10.1038/nphys1183. URL https://www.nature.com/articles/nphys1183. Publisher: Nature Publishing Group. [cited on page 94].

S. Geier. *Shaping the Hamiltonian of many-body spin systems on a Rydberg-atom quantum simulator*. PhD thesis, Combined Faculty of Mathematics, Engineering and Natural Sciences of Heidelberg University, Germany, Heidelberg, 2023. URL https://archiv.ub.uni-heidelberg.de/volltextserver/34235/1/Dissertation_Sebastian_Geier.pdf. [cited on page 90].

S. Geier, A. Braemer, E. Braun, M. Müllenbach, T. Franz, M. Gärttner, G. Zürn, and M. Weidemüller. Time-reversal in a dipolar quantum many-body spin system. *Physical Review Research*, 6(3):033197, Aug. 2024. doi:10.1103/PhysRevResearch.6.033197.

URL https://link.aps.org/doi/10.1103/PhysRevResearch.6.033197. Publisher: American Physical Society. [cited on page 99].

I. M. Georgescu, S. Ashhab, and F. Nori. Quantum simulation. *Reviews of Modern Physics*, 86(1):153–185, Mar. 2014. doi:10.1103/RevModPhys.86.153. URL https://link.aps.org/doi/10.1103/RevModPhys.86.153. Publisher: American Physical Society. [cited on pages 2, 5, 6, 7, and 9].

W. Gerlach and O. Stern. Der experimentelle Nachweis der Richtungsquantelung im Magnetfeld. *Zeitschrift für Physik*, 9(1):349–352, Dec. 1922. ISSN 0044-3328. doi:10.1007/BF01326983. URL https://doi.org/10.1007/BF01326983. [cited on page 119].

T. Giamarchi. *Quantum physics in one dimension*. Number 121 in The international series of monographs on physics. Clarendon ; Oxford University Press, Oxford : New York, 2004. ISBN 978-0-19-852500-4. OCLC: ocm52784724. [cited on pages 150, 155, 158, 173, and 221].

A. W. Glaetzle, M. Dalmonte, R. Nath, C. Gross, I. Bloch, and P. Zoller. Designing Frustrated Quantum Magnets with Laser-Dressed Rydberg Atoms. *Physical Review Letters*, 114(17):173002, Apr. 2015. doi:10.1103/PhysRevLett.114.173002. URL https://link.aps.org/doi/10.1103/PhysRevLett.114.173002. Publisher: American Physical Society. [cited on page 69].

Google. Quantum supremacy using a programmable superconducting processor. *Nature*, 574(7779):505–510, Oct. 2019. ISSN 1476-4687. doi:10.1038/s41586-019-1666-5. URL https://www.nature.com/articles/s41586-019-1666-5. Publisher: Nature Publishing Group. [cited on page 12].

Google. Suppressing quantum errors by scaling a surface code logical qubit. *Nature*, 614 (7949):676–681, Feb. 2023. ISSN 1476-4687. doi:10.1038/s41586-022-05434-1. URL https://www.nature.com/articles/s41586-022-05434-1. [cited on page 14].

Google. Thermalization and Criticality on an Analog-Digital Quantum Simulator, July 2024. URL http://arxiv.org/abs/2405.17385. arXiv:2405.17385 [cond-mat, physics:quant-ph]. [cited on pages 9 and 10].

Google. Quantum error correction below the surface code threshold. *Nature*, 638 (8052):920–926, Feb. 2025. ISSN 1476-4687. doi:10.1038/s41586-024-08449-y.

URL https://www.nature.com/articles/s41586-024-08449-y. Publisher: Nature Publishing Group. [cited on page 14].

M. Grayson, D. C. Tsui, L. N. Pfeiffer, K. W. West, and A. M. Chang. Continuum of Chiral Luttinger Liquids at the Fractional Quantum Hall Edge. *Physical Review Letters*, 80(5):1062–1065, Feb. 1998. doi:10.1103/PhysRevLett.80.1062. URL https://link.aps.org/doi/10.1103/PhysRevLett.80.1062. Publisher: American Physical Society. [cited on page 151].

M. Greiner, O. Mandel, T. Esslinger, T. W. Hänsch, and I. Bloch. Quantum phase transition from a superfluid to a Mott insulator in a gas of ultracold atoms. *Nature*, 415(6867):39–44, Jan. 2002. ISSN 1476-4687. doi:10.1038/415039a. URL https://www.nature.com/articles/415039a. Publisher: Nature Publishing Group. [cited on page 9].

D. J. Griffiths. *Introduction to elementary particles*. Physics textbook. Wiley-VCH, Weinheim, 2., rev. ed., 5. reprint edition, 2011. ISBN 978-3-527-40601-2. [cited on page 1].

R. Grimm, M. Weidemüller, and Y. B. Ovchinnikov. Optical Dipole Traps for Neutral Atoms. In B. Bederson and H. Walther, editors, *Advances In Atomic, Molecular, and Optical Physics*, volume 42, pages 95–170. Academic Press, Jan. 2000. doi:10.1016/S1049-250X(08)60186-X. URL https://www.sciencedirect.com/science/article/pii/S1049250X0860186X. [cited on pages 15 and 17].

C. Gross and I. Bloch. Quantum simulations with ultracold atoms in optical lattices. *Science*, 357(6355):995–1001, Sept. 2017. doi:10.1126/science.aal3837. URL https://www.science.org/doi/10.1126/science.aal3837. Publisher: American Association for the Advancement of Science. [cited on page 187].

C. Gross, T. Zibold, E. Nicklas, J. Estève, and M. K. Oberthaler. Nonlinear atom interferometer surpasses classical precision limit. *Nature*, 464(7292):1165–1169, Apr. 2010. ISSN 0028-0836, 1476-4687. doi:10.1038/nature08919. URL http://www.nature.com/articles/nature08919. [cited on page 13].

S.-A. Guo, Y.-K. Wu, J. Ye, L. Zhang, W.-Q. Lian, R. Yao, Y. Wang, R.-Y. Yan, Y.-J. Yi, Y.-L. Xu, B.-W. Li, Y.-H. Hou, Y.-Z. Xu, W.-X. Guo, C. Zhang, B.-X. Qi, Z.-C. Zhou, L. He, and L.-M. Duan. A site-resolved two-dimensional quantum simulator with hundreds of trapped ions. *Nature*, 630(8017):613–618, June 2024.

ISSN 1476-4687. doi:10.1038/s41586-024-07459-0. URL https://www.nature.com/articles/s41586-024-07459-0. Publisher: Nature Publishing Group. [cited on pages 7, 8, 14, and 212].

T. Gupta, G. Masella, F. Mattiotti, N. V. Prokof'ev, and G. Pupillo. Scale-invariant phase transition of disordered bosons in one dimension. *Physical Review B*, 111(2): L020503, Jan. 2025. doi:10.1103/PhysRevB.111.L020503. URL https://link.aps.org/doi/10.1103/PhysRevB.111.L020503. Publisher: American Physical Society. [cited on page 151].

F. Gyger, M. Ammenwerth, R. Tao, H. Timme, S. Snigirev, I. Bloch, and J. Zeiher. Continuous operation of large-scale atom arrays in optical lattices. *Physical Review Research*, 6(3):033104, July 2024. doi:10.1103/PhysRevResearch.6.033104. URL https://link.aps.org/doi/10.1103/PhysRevResearch.6.033104. Publisher: American Physical Society. [cited on page 212].

F. D. M. Haldane. 'Luttinger liquid theory' of one-dimensional quantum fluids. I. Properties of the Luttinger model and their extension to the general 1D interacting spinless Fermi gas. *Journal of Physics C: Solid State Physics*, 14(19):2585, July 1981. ISSN 0022-3719. doi:10.1088/0022-3719/14/19/010. URL https://dx.doi.org/10.1088/0022-3719/14/19/010. [cited on page 150].

J. Hauschild and F. Pollmann. Efficient numerical simulations with Tensor Networks: Tensor Network Python (TeNPy). *SciPost Physics Lecture Notes*, page 005, Oct. 2018. ISSN 2590-1990. doi:10.21468/SciPostPhysLectNotes.5. URL https://scipost.org/10.21468/SciPostPhysLectNotes.5. [cited on page 207].

T. A. Hilker, G. Salomon, F. Grusdt, A. Omran, M. Boll, E. Demler, I. Bloch, and C. Gross. Revealing hidden antiferromagnetic correlations in doped Hubbard chains via string correlators. *Science*, 357(6350):484–487, Aug. 2017. doi:10.1126/science.aam8990. URL https://www.science.org/doi/10.1126/science.aam8990. Publisher: American Association for the Advancement of Science. [cited on page 151].

S. Hofferberth, I. Lesanovsky, T. Schumm, A. Imambekov, V. Gritsev, E. Demler, and J. Schmiedmayer. Probing quantum and thermal noise in an interacting many-body system. *Nature Physics*, 4(6):489–495, June 2008. ISSN 1745-2481. doi:10.1038/nphys941. URL https://www.nature.com/articles/nphys941. Publisher: Nature Publishing Group. [cited on page 151].

C. M. Holland, Y. Lu, and L. W. Cheuk. On-demand entanglement of molecules in a reconfigurable optical tweezer array. *Science*, 382(6675):1143–1147, Dec. 2023. doi:10.1126/science.adf4272. URL https://www.science.org/doi/full/10.1126/science.adf4272. Publisher: American Association for the Advancement of Science. [cited on pages 8 and 95].

L. Homeier, T. J. Harris, T. Blatz, S. Geier, S. Hollerith, U. Schollwöck, F. Grusdt, and A. Bohrdt. Antiferromagnetic Bosonic t-J Models and Their Quantum Simulation in Tweezer Arrays. *Physical Review Letters*, 132(23):230401, June 2024. doi:10.1103/PhysRevLett.132.230401. URL https://link.aps.org/doi/10.1103/PhysRevLett.132.230401. Publisher: American Physical Society. [cited on pages 188 and 189].

O. Hosten, N. J. Engelsen, R. Krishnakumar, and M. A. Kasevich. Measurement noise 100 times lower than the quantum-projection limit using entangled atoms. *Nature*, 529(7587):505–508, Jan. 2016. ISSN 1476-4687. doi:10.1038/nature16176. URL https://www.nature.com/articles/nature16176. Publisher: Nature Publishing Group. [cited on page 13].

T. W. Hänsch. Nobel Lecture: Passion for precision. *Reviews of Modern Physics*, 78(4):1297–1309, Nov. 2006. ISSN 0034-6861, 1539-0756. doi:10.1103/RevModPhys.78.1297. URL https://link.aps.org/doi/10.1103/RevModPhys.78.1297. [cited on page 2].

L. Isenhower, E. Urban, X. L. Zhang, A. T. Gill, T. Henage, T. A. Johnson, T. G. Walker, and M. Saffman. Demonstration of a Neutral Atom Controlled-NOT Quantum Gate. *Physical Review Letters*, 104(1):010503, Jan. 2010. doi:10.1103/PhysRevLett.104.010503. URL https://link.aps.org/doi/10.1103/PhysRevLett.104.010503. Publisher: American Physical Society. [cited on page 69].

R. Islam, E. E. Edwards, K. Kim, S. Korenblit, C. Noh, H. Carmichael, G.-D. Lin, L.-M. Duan, C.-C. Joseph Wang, J. K. Freericks, and C. Monroe. Onset of a quantum phase transition with a trapped ion quantum simulator. *Nature Communications*, 2(1):377, July 2011. ISSN 2041-1723. doi:10.1038/ncomms1374. URL https://www.nature.com/articles/ncomms1374. Publisher: Nature Publishing Group. [cited on page 9].

G. Ji, M. Xu, L. H. Kendrick, C. S. Chiu, J. C. Brüggenjürgen, D. Greif, A. Bohrdt, F. Grusdt, E. Demler, M. Lebrat, and M. Greiner. Coupling a Mobile Hole to an

Antiferromagnetic Spin Background: Transient Dynamics of a Magnetic Polaron. *Physical Review X*, 11(2):021022, Apr. 2021. doi:10.1103/PhysRevX.11.021022. URL https://link.aps.org/doi/10.1103/PhysRevX.11.021022. Publisher: American Physical Society. [cited on page 206].

M. P. A. Jones, J. Beugnon, A. Gaëtan, J. Zhang, G. Messin, A. Browaeys, and P. Grangier. Fast quantum state control of a single trapped neutral atom. *Physical Review A*, 75(4):040301, Apr. 2007. doi:10.1103/PhysRevA.75.040301. URL https://link.aps.org/doi/10.1103/PhysRevA.75.040301. Publisher: American Physical Society. [cited on page 69].

M. K. Joshi, F. Kranzl, A. Schuckert, I. Lovas, C. Maier, R. Blatt, M. Knap, and C. F. Roos. Observing emergent hydrodynamics in a long-range quantum magnet. *Science*, 376(6594):720–724, May 2022. doi:10.1126/science.abk2400. URL https://www.science.org/doi/full/10.1126/science.abk2400. Publisher: American Association for the Advancement of Science. [cited on page 10].

P. Jurcevic, P. Hauke, C. Maier, C. Hempel, B. P. Lanyon, R. Blatt, and C. F. Roos. Spectroscopy of Interacting Quasiparticles in Trapped Ions. *Physical Review Letters*, 115(10):100501, Sept. 2015. doi:10.1103/PhysRevLett.115.100501. URL https://link.aps.org/doi/10.1103/PhysRevLett.115.100501. Publisher: American Physical Society. [cited on page 169].

D. Jérome. Organic Conductors: From Charge Density Wave TTF-TCNQ to Superconducting (TMTSF)2PF6. *Chemical Reviews*, 104(11):5565–5592, Nov. 2004. ISSN 0009-2665. doi:10.1021/cr030652g. URL https://doi.org/10.1021/cr030652g. Publisher: American Chemical Society. [cited on page 151].

A. Kaufman. *Laser cooling atoms to indistinguishability: Atomic Hong-Ou-Mandel interference and entanglement through spin exchange*. PhD thesis, 2009. [cited on pages 30 and 34].

A. M. Kaufman, B. J. Lester, and C. A. Regal. Cooling a Single Atom in an Optical Tweezer to Its Quantum Ground State. *Physical Review X*, 2(4):041014, Nov. 2012. ISSN 2160-3308. doi:10.1103/PhysRevX.2.041014. URL https://link.aps.org/doi/10.1103/PhysRevX.2.041014. [cited on pages 29, 43, and 46].

A. J. Kerman. *Raman sideband cooling and cold atomic collisions in optical lattices*. PhD thesis, Jan. 2002. URL https://ui.adsabs.harvard.edu/abs/2002PhDT.

.....146K. Publication Title: Ph.D. Thesis ADS Bibcode: 2002PhDT.....146K. [cited on pages 29 and 30].

D. Kiesenhofer, H. Hainzer, A. Zhdanov, P. C. Holz, M. Bock, T. Ollikainen, and C. F. Roos. Controlling Two-Dimensional Coulomb Crystals of More Than 100 Ions in a Monolithic Radio-Frequency Trap. *PRX Quantum*, 4(2):020317, Apr. 2023. ISSN 2691-3399. doi:10.1103/PRXQuantum.4.020317. URL https://link.aps.org/doi/10.1103/PRXQuantum.4.020317. [cited on page 7].

T. Kinoshita, T. Wenger, and D. S. Weiss. Observation of a One-Dimensional Tonks-Girardeau Gas. *Science*, 305(5687):1125–1128, Aug. 2004. ISSN 0036-8075, 1095-9203. doi:10.1126/science.1100700. URL https://www.science.org/doi/10.1126/science.1100700. [cited on page 151].

M. Kitagawa and M. Ueda. Squeezed spin states. *Physical Review A*, 47(6):5138–5143, June 1993. doi:10.1103/PhysRevA.47.5138. URL https://link.aps.org/doi/10.1103/PhysRevA.47.5138. Publisher: American Physical Society. [cited on page 12].

C. Kittel. *Introduction to solid state physics*. Wiley, Hoboken, NJ, global edition, [9th edition] edition, 2018. ISBN 978-1-119-45416-8. [cited on page 164].

M. Klanjšek, H. Mayaffre, C. Berthier, M. Horvatić, B. Chiari, O. Piovesana, P. Bouillot, C. Kollath, E. Orignac, R. Citro, and T. Giamarchi. Controlling Luttinger Liquid Physics in Spin Ladders under a Magnetic Field. *Physical Review Letters*, 101(13):137207, Sept. 2008. doi:10.1103/PhysRevLett.101.137207. URL https://link.aps.org/doi/10.1103/PhysRevLett.101.137207. Publisher: American Physical Society. [cited on page 151].

E. Knill, D. Leibfried, R. Reichle, J. Britton, R. B. Blakestad, J. D. Jost, C. Langer, R. Ozeri, S. Seidelin, and D. J. Wineland. Randomized benchmarking of quantum gates. *Physical Review A*, 77(1):012307, Jan. 2008. doi:10.1103/PhysRevA.77.012307. URL https://link.aps.org/doi/10.1103/PhysRevA.77.012307. Publisher: American Physical Society. [cited on page 69].

J. Koepsell, J. Vijayan, P. Sompet, F. Grusdt, T. A. Hilker, E. Demler, G. Salomon, I. Bloch, and C. Gross. Imaging magnetic polarons in the doped Fermi–Hubbard model. *Nature*, 572(7769):358–362, Aug. 2019. ISSN 1476-4687. doi:10.1038/s41586-019-1463-1. URL https://www.nature.com/articles/s41586-019-1463-1. Publisher: Nature Publishing Group. [cited on page 206].

F. Kranzl, A. Lasek, M. K. Joshi, A. Kalev, R. Blatt, C. F. Roos, and N. Yunger Halpern. Experimental Observation of Thermalization with Noncommuting Charges. *PRX Quantum*, 4(2):020318, Apr. 2023. doi:10.1103/PRXQuantum.4.020318. URL https://link.aps.org/doi/10.1103/PRXQuantum.4.020318. Publisher: American Physical Society. [cited on page 10].

H. Labuhn, S. Ravets, D. Barredo, L. Béguin, F. Nogrette, T. Lahaye, and A. Browaeys. Single-atom addressing in microtraps for quantum-state engineering using Rydberg atoms. *Physical Review A*, 90(2):023415, Aug. 2014. doi:10.1103/PhysRevA.90.023415. URL https://link.aps.org/doi/10.1103/PhysRevA.90.023415. Publisher: American Physical Society. [cited on page 69].

L. Lachaud, B. Muraz, A. Couto, J.-M. Raimond, M. Brune, and S. Gleyzes. Slowing Down a Coherent Superposition of Circular Rydberg States of Strontium. *Physical Review Letters*, 133(12):123202, Sept. 2024. doi:10.1103/PhysRevLett.133.123202. URL https://link.aps.org/doi/10.1103/PhysRevLett.133.123202. Publisher: American Physical Society. [cited on page 211].

B. Lake, D. A. Tennant, C. D. Frost, and S. E. Nagler. Quantum criticality and universal scaling of a quantum antiferromagnet. *Nature Materials*, 4(4):329–334, Apr. 2005. ISSN 1476-4660. doi:10.1038/nmat1327. URL https://www.nature.com/articles/nmat1327. Publisher: Nature Publishing Group. [cited on pages 151 and 173].

L. Leclerc. Modelling a QPU : understanding noise contributions for better predictions. In *Quantum computing with Rydberg atoms: control and modelling for quantum simulation and practical algorithms*, pages 47–49. 2024. [cited on pages 22, 84, 132, 133, and 135].

J. Lee, S. Eggert, H. Kim, S.-J. Kahng, H. Shinohara, and Y. Kuk. Real Space Imaging of One-Dimensional Standing Waves: Direct Evidence for a Luttinger Liquid. *Physical Review Letters*, 93(16):166403, Oct. 2004. doi:10.1103/PhysRevLett.93.166403. URL https://link.aps.org/doi/10.1103/PhysRevLett.93.166403. Publisher: American Physical Society. [cited on pages 151 and 158].

J. Y. Lee, J. Ramette, M. A. Metlitski, V. Vuletić, W. W. Ho, and S. Choi. Landau-Forbidden Quantum Criticality in Rydberg Quantum Simulators. *Physical Review Letters*, 131(8):083601, Aug. 2023. doi:10.1103/PhysRevLett.131.083601.

URL https://link.aps.org/doi/10.1103/PhysRevLett.131.083601. Publisher: American Physical Society. [cited on page 151].

P. J. Lee, M. Anderlini, B. L. Brown, J. Sebby-Strabley, W. D. Phillips, and J. V. Porto. Sublattice Addressing and Spin-Dependent Motion of Atoms in a Double-Well Lattice. *Physical Review Letters*, 99(2):020402, July 2007. doi:10.1103/PhysRevLett.99.020402. URL https://link.aps.org/doi/10.1103/PhysRevLett.99.020402. Publisher: American Physical Society. [cited on page 211].

D. Leibfried, R. Blatt, C. Monroe, and D. Wineland. Quantum dynamics of single trapped ions. *Reviews of Modern Physics*, 75(1):281–324, Mar. 2003. doi:10.1103/RevModPhys.75.281. URL https://link.aps.org/doi/10.1103/RevModPhys.75.281. Publisher: American Physical Society. [cited on page 29].

C. Lhuillier and G. Misguich. Frustrated Quantum Magnets. In C. Berthier, L. P. Lévy, and G. Martinez, editors, *High Magnetic Fields: Applications in Condensed Matter Physics and Spectroscopy*, Lecture Notes in Physics, pages 161–190. Springer, Berlin, Heidelberg, 2001. ISBN 978-3-540-45649-0. doi:10.1007/3-540-45649-X. URL https://doi.org/10.1007/3-540-45649-X. [cited on page 130].

H. Li, Z. Xiang, T. Wang, M. H. Naik, W. Kim, J. Nie, S. Li, Z. Ge, Z. He, Y. Ou, R. Banerjee, T. Taniguchi, K. Watanabe, S. Tongay, A. Zettl, S. G. Louie, M. P. Zaletel, M. F. Crommie, and F. Wang. Imaging tunable Luttinger liquid systems in van der Waals heterostructures. *Nature*, 631(8022):765–770, July 2024. ISSN 1476-4687. doi:10.1038/s41586-024-07596-6. URL https://www.nature.com/articles/s41586-024-07596-6. Publisher: Nature Publishing Group. [cited on pages 151 and 158].

V. Lienhard, P. Scholl, S. Weber, D. Barredo, S. de Léséleuc, R. Bai, N. Lang, M. Fleischhauer, H. P. Büchler, T. Lahaye, and A. Browaeys. Realization of a Density-Dependent Peierls Phase in a Synthetic, Spin-Orbit Coupled Rydberg System. *Physical Review X*, 10(2):021031, May 2020. ISSN 2160-3308. doi:10.1103/PhysRevX.10.021031. URL https://link.aps.org/doi/10.1103/PhysRevX.10.021031. [cited on page 110].

R. Lin, H.-S. Zhong, Y. Li, Z.-R. Zhao, L.-T. Zheng, T.-R. Hu, H.-M. Wu, Z. Wu, W.-J. Ma, Y. Gao, Y.-K. Zhu, Z.-F. Su, W.-L. Ouyang, Y.-C. Zhang, J. Rui, M.-C. Chen, C.-Y. Lu, and J.-W. Pan. AI-Enabled Rapid Assembly of Thousands of Defect-Free Neutral Atom Arrays with Constant-time-overhead, Dec. 2024.

URL http://arxiv.org/abs/2412.14647. arXiv:2412.14647 [quant-ph]. [cited on page 212].

M. G. Littman, M. M. Kash, and D. Kleppner. Field-Ionization Processes in Excited Atoms. *Physical Review Letters*, 41(2):103–107, July 1978. doi:10.1103/PhysRevLett.41.103. URL https://link.aps.org/doi/10.1103/PhysRevLett.41.103. Publisher: American Physical Society. [cited on page 66].

P. Liu, Z. Liu, S. Chen, and X. Ma. Fundamental Limitation on the Detectability of Entanglement. *Physical Review Letters*, 129(23):230503, Nov. 2022. ISSN 0031-9007, 1079-7114. doi:10.1103/PhysRevLett.129.230503. URL http://arxiv.org/abs/2208.02518. arXiv:2208.02518 [quant-ph]. [cited on page 214].

J. M. Luttinger. Fermi Surface and Some Simple Equilibrium Properties of a System of Interacting Fermions. *Physical Review*, 119(4):1153–1163, Aug. 1960. doi:10.1103/PhysRev.119.1153. URL https://link.aps.org/doi/10.1103/PhysRev.119.1153. Publisher: American Physical Society. [cited on page 150].

C. M. Löschnauer, J. M. Toba, A. C. Hughes, S. A. King, M. A. Weber, R. Srinivas, R. Matt, R. Nourshargh, D. T. C. Allcock, C. J. Ballance, C. Matthiesen, M. Malinowski, and T. P. Harty. Scalable, high-fidelity all-electronic control of trapped-ion qubits, July 2024. URL http://arxiv.org/abs/2407.07694. arXiv:2407.07694 [quant-ph]. [cited on page 12].

M. F. Maghrebi, Z.-X. Gong, and A. V. Gorshkov. Continuous Symmetry Breaking in 1D Long-Range Interacting Quantum Systems. *Physical Review Letters*, 119 (2):023001, July 2017. doi:10.1103/PhysRevLett.119.023001. URL https://link.aps.org/doi/10.1103/PhysRevLett.119.023001. Publisher: American Physical Society. [cited on pages 150 and 151].

O. Mandel, M. Greiner, A. Widera, T. Rom, T. W. Haensch, and I. Bloch. Coherent transport of neutral atoms in spin-dependent optical lattice potentials. *Physical Review Letters*, 91(1):010407, July 2003. ISSN 0031-9007, 1079-7114. doi:10.1103/PhysRevLett.91.010407. URL http://arxiv.org/abs/cond-mat/0301169. arXiv:cond-mat/0301169. [cited on page 211].

H. J. Manetsch, G. Nomura, E. Bataille, K. H. Leung, X. Lv, and M. Endres. A tweezer array with 6100 highly coherent atomic qubits, Mar. 2024. URL http://arxiv.org/abs/2403.12021. arXiv:2403.12021 [cond-mat, physics:physics, physics:quant-ph]. [cited on pages 14 and 212].

P. J. Martin, B. G. Oldaker, A. H. Miklich, and D. E. Pritchard. Bragg scattering of atoms from a standing light wave. *Physical Review Letters*, 60(6):515–518, Feb. 1988. doi:10.1103/PhysRevLett.60.515. URL https://link.aps.org/doi/10.1103/PhysRevLett.60.515. Publisher: American Physical Society. [cited on page 164].

A. Mazurenko, C. S. Chiu, G. Ji, M. F. Parsons, M. Kanász-Nagy, R. Schmidt, F. Grusdt, E. Demler, D. Greif, and M. Greiner. A cold-atom Fermi–Hubbard antiferromagnet. *Nature*, 545(7655):462–466, May 2017. ISSN 1476-4687. doi:10.1038/nature22362. URL https://www.nature.com/articles/nature22362. Publisher: Nature Publishing Group. [cited on page 9].

Y. Meng. *Spin-motion coupling of nanofiber-trapped atoms and its applications*. PhD thesis, TU Wien, Berlin, 2020. URL https://www.physik.hu-berlin.de/de/gop/publications/meng-yijian-2021-spin-motion-coupling-of-nanofiber-trapped-atoms.pdf. [cited on page 114].

N. D. Mermin and H. Wagner. Absence of Ferromagnetism or Antiferromagnetism in One- or Two-Dimensional Isotropic Heisenberg Models. *Physical Review Letters*, 17(22):1133–1136, Nov. 1966. doi:10.1103/PhysRevLett.17.1133. URL https://link.aps.org/doi/10.1103/PhysRevLett.17.1133. Publisher: American Physical Society. [cited on page 129].

A. Mitra. Quantum Quench Dynamics. *Annual Review of Condensed Matter Physics*, 9(Volume 9, 2018):245–259, Mar. 2018. ISSN 1947-5454, 1947-5462. doi:10.1146/annurev-conmatphys-031016-025451. URL https://www.annualreviews.org/content/journals/10.1146/annurev-conmatphys-031016-025451. Publisher: Annual Reviews. [cited on page 165].

C. Monroe, D. M. Meekhof, B. E. King, S. R. Jefferts, W. M. Itano, D. J. Wineland, and P. Gould. Resolved-Sideband Raman Cooling of a Bound Atom to the 3D Zero-Point Energy. *Physical Review Letters*, 75(22):4011–4014, Nov. 1995. doi:10.1103/PhysRevLett.75.4011. URL https://link.aps.org/doi/10.1103/PhysRevLett.75.4011. Publisher: American Physical Society. [cited on page 29].

T. Mori, T. N. Ikeda, E. Kaminishi, and M. Ueda. Thermalization and prethermalization in isolated quantum systems: a theoretical overview. *Journal of Physics B: Atomic,*

Molecular and Optical Physics, 51(11):112001, June 2018. ISSN 0953-4075, 1361-6455. doi:10.1088/1361-6455/aabcdf. URL http://arxiv.org/abs/1712.08790. arXiv:1712.08790 [cond-mat, physics:quant-ph]. [cited on page 3].

A. Muni, L. Lachaud, A. Couto, M. Poirier, R. C. Teixeira, J.-M. Raimond, M. Brune, and S. Gleyzes. Optical coherent manipulation of alkaline-earth circular Rydberg states. *Nature Physics*, 18(5):502–505, May 2022. ISSN 1745-2481. doi:10.1038/s41567-022-01519-w. URL https://www.nature.com/articles/s41567-022-01519-w. Publisher: Nature Publishing Group. [cited on page 211].

P. Méhaignerie, C. Sayrin, J.-M. Raimond, M. Brune, and G. Roux. Spin-motion coupling in a circular-Rydberg-state quantum simulator: Case of two atoms. *Physical Review A*, 107(6):063106, June 2023. doi:10.1103/PhysRevA.107.063106. URL https://link.aps.org/doi/10.1103/PhysRevA.107.063106. Publisher: American Physical Society. [cited on pages 114, 115, and 121].

J. Mögerle, K. Brechtelsbauer, A. T. Gea-Caballero, J. Prior, G. Emperauger, G. Bornet, C. Chen, T. Lahaye, A. Browaeys, and H. P. Büchler. Spin-1 Haldane phase in a chain of Rydberg atoms, Oct. 2024. URL http://arxiv.org/abs/2410.21424. arXiv:2410.21424. [cited on pages 110 and 214].

T. L. Nguyen, J. M. Raimond, C. Sayrin, R. Cortiñas, T. Cantat-Moltrecht, F. Assemat, I. Dotsenko, S. Gleyzes, S. Haroche, G. Roux, T. Jolicoeur, and M. Brune. Towards Quantum Simulation with Circular Rydberg Atoms. *Physical Review X*, 8(1):011032, Feb. 2018. ISSN 2160-3308. doi:10.1103/PhysRevX.8.011032. URL https://link.aps.org/doi/10.1103/PhysRevX.8.011032. [cited on page 211].

F. Nogrette, H. Labuhn, S. Ravets, D. Barredo, L. Béguin, A. Vernier, T. Lahaye, and A. Browaeys. Single-Atom Trapping in Holographic 2D Arrays of Microtraps with Arbitrary Geometries. *Physical Review X*, 4(2):021034, May 2014. ISSN 2160-3308. doi:10.1103/PhysRevX.4.021034. URL https://link.aps.org/doi/10.1103/PhysRevX.4.021034. [cited on pages 17, 18, and 72].

G. Pagano, A. Bapat, P. Becker, K. S. Collins, A. De, P. W. Hess, H. B. Kaplan, A. Kyprianidis, W. L. Tan, C. Baldwin, L. T. Brady, A. Deshpande, F. Liu, S. Jordan, A. V. Gorshkov, and C. Monroe. Quantum approximate optimization of the long-range Ising model with a trapped-ion quantum simulator. *Proceedings of the National Academy of Sciences*, 117(41):25396–25401, Oct. 2020. doi:10.1073/pnas.2006373117.

URL https://www.pnas.org/doi/full/10.1073/pnas.2006373117. Publisher: Proceedings of the National Academy of Sciences. [cited on pages 69 and 151].

B. Paredes, A. Widera, V. Murg, O. Mandel, S. Fölling, I. Cirac, G. V. Shlyapnikov, T. W. Hänsch, and I. Bloch. Tonks–Girardeau gas of ultracold atoms in an optical lattice. *Nature*, 429(6989):277–281, May 2004. ISSN 1476-4687. doi:10.1038/nature02530. URL https://www.nature.com/articles/nature02530. Publisher: Nature Publishing Group. [cited on page 151].

D. Peter, S. Müller, S. Wessel, and H. P. Büchler. Anomalous Behavior of Spin Systems with Dipolar Interactions. *Physical Review Letters*, 109(2):025303, July 2012. doi:10.1103/PhysRevLett.109.025303. URL https://link.aps.org/doi/10.1103/PhysRevLett.109.025303. Publisher: American Physical Society. [cited on pages 125, 130, 138, and 177].

L. Pezzè, A. Smerzi, M. K. Oberthaler, R. Schmied, and P. Treutlein. Quantum metrology with nonclassical states of atomic ensembles. *Reviews of Modern Physics*, 90(3):035005, Sept. 2018. ISSN 0034-6861, 1539-0756. doi:10.1103/RevModPhys.90.035005. URL https://link.aps.org/doi/10.1103/RevModPhys.90.035005. [cited on pages 12, 215, and 218].

J. Preskill. Quantum Computing in the NISQ era and beyond. *Quantum*, 2:79, Aug. 2018. doi:10.22331/q-2018-08-06-79. URL https://quantum-journal.org/papers/q-2018-08-06-79/. Publisher: Verein zur Förderung des Open Access Publizierens in den Quantenwissenschaften. [cited on pages 12 and 13].

M. Qiao, G. Emperauger, C. Chen, L. Homeier, S. Hollerith, G. Bornet, R. Martin, B. Gély, L. Klein, D. Barredo, S. Geier, N.-C. Chiu, F. Grusdt, A. Bohrdt, T. Lahaye, and A. Browaeys. Realization of a doped quantum antiferromagnet with dipolar tunnelings in a Rydberg tweezer array, Jan. 2025. URL http://arxiv.org/abs/2501.08233. arXiv:2501.08233 [quant-ph]. [cited on page 188].

M. Qin, C.-M. Chung, H. Shi, E. Vitali, C. Hubig, U. Schollwöck, S. R. White, S. Zhang, and S. C. on the Many-Electron Problem. Absence of Superconductivity in the Pure Two-Dimensional Hubbard Model. *Physical Review X*, 10(3):031016, July 2020. doi:10.1103/PhysRevX.10.031016. URL https://link.aps.org/doi/10.1103/PhysRevX.10.031016. Publisher: American Physical Society. [cited on page 188].

J. M. Raimond, G. Vitrant, and S. Haroche. Spectral line broadening due to the interaction between very excited atoms: 'the dense Rydberg gas'. *Journal of Physics B: Atomic and Molecular Physics*, 14(21):L655, Nov. 1981. ISSN 0022-3700. doi:10.1088/0022-3700/14/21/003. URL https://dx.doi.org/10.1088/0022-3700/14/21/003. [cited on page 89].

S. Ravets, H. Labuhn, D. Barredo, L. Béguin, T. Lahaye, and A. Browaeys. Coherent dipole–dipole coupling between two single Rydberg atoms at an electrically-tuned Förster resonance. *Nature Physics*, 10(12):914–917, Dec. 2014. ISSN 1745-2481. doi:10.1038/nphys3119. URL https://www.nature.com/articles/nphys3119. Publisher: Nature Publishing Group. [cited on page 95].

S. Ravets, H. Labuhn, D. Barredo, T. Lahaye, and A. Browaeys. Measurement of the angular dependence of the dipole-dipole interaction between two individual Rydberg atoms at a Förster resonance. *Physical Review A*, 92(2):020701, Aug. 2015. doi:10.1103/PhysRevA.92.020701. URL https://link.aps.org/doi/10.1103/PhysRevA.92.020701. Publisher: American Physical Society. [cited on pages 91 and 95].

B. W. Reichardt, D. Aasen, R. Chao, A. Chernoguzov, W. v. Dam, J. P. Gaebler, D. Gresh, D. Lucchetti, M. Mills, S. A. Moses, B. Neyenhuis, A. Paetznick, A. Paz, P. E. Siegfried, M. P. d. Silva, K. M. Svore, Z. Wang, and M. Zanner. Demonstration of quantum computation and error correction with a tesseract code, Dec. 2024. URL http://arxiv.org/abs/2409.04628. arXiv:2409.04628 [quant-ph]. [cited on page 14].

P. Richerme, C. Senko, J. Smith, A. Lee, S. Korenblit, and C. Monroe. Experimental performance of a quantum simulator: Optimizing adiabatic evolution and identifying many-body ground states. *Physical Review A*, 88(1):012334, July 2013. doi:10.1103/PhysRevA.88.012334. URL https://link.aps.org/doi/10.1103/PhysRevA.88.012334. Publisher: American Physical Society. [cited on pages 9 and 152].

J. M. Robinson, M. Miklos, Y. M. Tso, C. J. Kennedy, T. Bothwell, D. Kedar, J. K. Thompson, and J. Ye. Direct comparison of two spin-squeezed optical clock ensembles at the 10^{-17} level. *Nature Physics*, 20(2):208–213, Feb. 2024. ISSN 1745-2481. doi:10.1038/s41567-023-02310-1. URL https://www.nature.com/articles/s41567-023-02310-1. Publisher: Nature Publishing Group. [cited on page 12].

T. Roscilde, T. Comparin, and F. Mezzacapo. Entangling Dynamics from Effective Rotor-Spin-Wave Separation in U(1)-Symmetric Quantum Spin Models. *Physical Review Letters*, 131(16):160403, Oct. 2023. doi:10.1103/PhysRevLett.131.160403. URL https://link.aps.org/doi/10.1103/PhysRevLett.131.160403. Publisher: American Physical Society. [cited on page 177].

N. Rossi. *Force sensing with nanowires*. Thesis, University_of_Basel, 2019. URL http://edoc.unibas.ch/diss/DissB_73768. [cited on page 13].

P. Roushan, C. Neill, A. Megrant, Y. Chen, R. Babbush, R. Barends, B. Campbell, Z. Chen, B. Chiaro, A. Dunsworth, A. Fowler, E. Jeffrey, J. Kelly, E. Lucero, J. Mutus, P. J. J. O'Malley, M. Neeley, C. Quintana, D. Sank, A. Vainsencher, J. Wenner, T. White, E. Kapit, H. Neven, and J. Martinis. Chiral ground-state currents of interacting photons in a synthetic magnetic field. *Nature Physics*, 13 (2):146–151, Feb. 2017. ISSN 1745-2481. doi:10.1038/nphys3930. URL https://www.nature.com/articles/nphys3930. Number: 2 Publisher: Nature Publishing Group. [cited on pages 69, 85, and 87].

S. Sachdev. *Quantum Phase Transitions*. Cambridge University Press, Cambridge, 2 edition, 2011. ISBN 978-0-521-51468-2. doi:10.1017/CBO9780511973765. URL https://www.cambridge.org/core/books/quantum-phase-transitions/33C1C81500346005E54C1DE4223E5562. [cited on page 96].

A. W. Sandvik. Quantum spin systems - models and computational methods, 2010. URL https://physics.bu.edu/~sandvik/nccu/l1.pdf. [cited on page 7].

B. Sbierski, M. Bintz, S. Chatterjee, M. Schuler, N. Y. Yao, and L. Pollet. Magnetism in the two-dimensional dipolar XY model. *Physical Review B*, 109(14):144411, Apr. 2024. doi:10.1103/PhysRevB.109.144411. URL https://link.aps.org/doi/10.1103/PhysRevB.109.144411. Publisher: American Physical Society. [cited on pages 130, 135, 138, and 140].

A. Scheie, P. Laurell, B. Lake, S. E. Nagler, M. B. Stone, J.-S. Caux, and D. A. Tennant. Quantum wake dynamics in Heisenberg antiferromagnetic chains. *Nature Communications*, 13(1):5796, Oct. 2022. ISSN 2041-1723. doi:10.1038/s41467-022-33571-8. URL https://www.nature.com/articles/s41467-022-33571-8. Publisher: Nature Publishing Group. [cited on page 173].

N. Schlosser, G. Reymond, I. Protsenko, and P. Grangier. Sub-poissonian loading of single atoms in a microscopic dipole trap. *Nature*, 411(6841):1024–1027, June

2001. ISSN 1476-4687. doi:10.1038/35082512. URL https://www.nature.com/articles/35082512. Number: 6841 Publisher: Nature Publishing Group. [cited on pages 15 and 17].

J. T. Schneider, S. J. Thomson, and L. Sanchez-Palencia. Entanglement spectrum and quantum phase diagram of the long-range XXZ chain. *Physical Review B*, 106(1): 014306, July 2022. doi:10.1103/PhysRevB.106.014306. URL https://link.aps.org/doi/10.1103/PhysRevB.106.014306. Publisher: American Physical Society. [cited on page 151].

P. Scholl. *Quantum simulation of spin models with large arrays of Rydberg atoms*. These de doctorat, université Paris-Saclay, Dec. 2021. URL https://www.theses.fr/2021UPASP130. [cited on pages 9, 18, and 97].

P. Scholl, M. Schuler, H. J. Williams, A. A. Eberharter, D. Barredo, K.-N. Schymik, V. Lienhard, L.-P. Henry, T. C. Lang, T. Lahaye, A. M. Läuchli, and A. Browaeys. Quantum simulation of 2D antiferromagnets with hundreds of Rydberg atoms. *Nature*, 595(7866):233–238, July 2021. ISSN 1476-4687. doi:10.1038/s41586-021-03585-1. URL https://www.nature.com/articles/s41586-021-03585-1. Number: 7866 Publisher: Nature Publishing Group. [cited on page 21].

P. Scholl, A. L. Shaw, R. B.-S. Tsai, R. Finkelstein, J. Choi, and M. Endres. Erasure conversion in a high-fidelity Rydberg quantum simulator. *Nature*, 622(7982):273–278, Oct. 2023. ISSN 1476-4687. doi:10.1038/s41586-023-06516-4. URL https://www.nature.com/articles/s41586-023-06516-4. Publisher: Nature Publishing Group. [cited on pages 12 and 94].

M. Schuler and A. M. Läuchli. Studying Continuous Symmetry Breaking with Exact Diagonalization. URL https://www.cond-mat.de/events/correl16/manuscripts/laeuchli.pdf. [cited on page 141].

A. Schwartz, M. Dressel, G. Grüner, V. Vescoli, L. Degiorgi, and T. Giamarchi. On-chain electrodynamics of metallic TMTSF_2 X salts: Observation of Tomonaga-Luttinger liquid response. *Physical Review B*, 58(3):1261–1271, July 1998. doi:10.1103/PhysRevB.58.1261. URL https://link.aps.org/doi/10.1103/PhysRevB.58.1261. Publisher: American Physical Society. [cited on page 151].

K.-N. Schymik. *Scaling-up the Tweezer Platform - Trapping Arrays of Single Atoms in a Cryogenic Environment*. These de doctorat, université Paris-Saclay, Mar. 2022. URL https://theses.fr/2022UPASP031. [cited on pages 19, 20, 46, and 211].

K.-N. Schymik, V. Lienhard, D. Barredo, P. Scholl, H. Williams, A. Browaeys, and T. Lahaye. Enhanced atom-by-atom assembly of arbitrary tweezer arrays. *Physical Review A*, 102(6):063107, Dec. 2020. doi:10.1103/PhysRevA.102.063107. URL https://link.aps.org/doi/10.1103/PhysRevA.102.063107. Publisher: American Physical Society. [cited on page 20].

G. Semeghini, H. Levine, A. Keesling, S. Ebadi, T. T. Wang, D. Bluvstein, R. Verresen, H. Pichler, M. Kalinowski, R. Samajdar, A. Omran, S. Sachdev, A. Vishwanath, M. Greiner, V. Vuletić, and M. D. Lukin. Probing topological spin liquids on a programmable quantum simulator. *Science*, 374(6572):1242–1247, Dec. 2021. doi:10.1126/science.abi8794. URL https://www.science.org/doi/10.1126/science.abi8794. Publisher: American Association for the Advancement of Science. [cited on pages 9 and 214].

A. L. Shaw, Z. Chen, J. Choi, D. K. Mark, P. Scholl, R. Finkelstein, A. Elben, S. Choi, and M. Endres. Benchmarking highly entangled states on a 60-atom analogue quantum simulator. *Nature*, 628(8006):71–77, Apr. 2024. ISSN 1476-4687. doi:10.1038/s41586-024-07173-x. URL https://www.nature.com/articles/s41586-024-07173-x. Publisher: Nature Publishing Group. [cited on page 12].

J. F. Sherson, C. Weitenberg, M. Endres, M. Cheneau, I. Bloch, and S. Kuhr. Single-atom-resolved fluorescence imaging of an atomic Mott insulator. *Nature*, 467(7311):68–72, Sept. 2010. ISSN 1476-4687. doi:10.1038/nature09378. URL https://www.nature.com/articles/nature09378. Publisher: Nature Publishing Group. [cited on page 8].

S. Shi, B. Xu, K. Zhang, G.-S. Ye, D.-S. Xiang, Y. Liu, J. Wang, D. Su, and L. Li. High-fidelity photonic quantum logic gate based on near-optimal Rydberg single-photon source. *Nature Communications*, 13(1):4454, Aug. 2022. ISSN 2041-1723. doi:10.1038/s41467-022-32083-9. URL https://www.nature.com/articles/s41467-022-32083-9. Publisher: Nature Publishing Group. [cited on page 12].

P. Shor. Fault-tolerant quantum computation. In *Proceedings of 37th Conference on Foundations of Computer Science*, pages 56–65, Oct. 1996. doi:10.1109/SFCS.1996.548464. URL https://ieeexplore.ieee.org/document/548464. ISSN: 0272-5428. [cited on page 13].

B. I. Shraiman and E. D. Siggia. Mobile Vacancies in a Quantum Heisenberg Antiferromagnet. *Physical Review Letters*, 61(4):467–470, July 1988.

doi:10.1103/PhysRevLett.61.467. URL https://link.aps.org/doi/10.1103/PhysRevLett.61.467. Publisher: American Physical Society. [cited on page 206].

A. Signoles, T. Franz, R. Ferracini Alves, M. Gärttner, S. Whitlock, G. Zürn, and M. Weidemüller. Glassy Dynamics in a Disordered Heisenberg Quantum Spin System. *Physical Review X*, 11(1):011011, Jan. 2021. doi:10.1103/PhysRevX.11.011011. URL https://link.aps.org/doi/10.1103/PhysRevX.11.011011. Publisher: American Physical Society. [cited on pages 89 and 95].

M. T. Simons, A. B. Artusio-Glimpse, A. K. Robinson, N. Prajapati, and C. L. Holloway. Rydberg atom-based sensors for radio-frequency electric field metrology, sensing, and communications. *Measurement: Sensors*, 18:100273, Dec. 2021. ISSN 2665-9174. doi:10.1016/j.measen.2021.100273. URL https://www.sciencedirect.com/science/article/pii/S2665917421002361. [cited on page 13].

K. Singh, C. E. Bradley, S. Anand, V. Ramesh, R. White, and H. Bernien. Mid-circuit correction of correlated phase errors using an array of spectator qubits. *Science*, 380(6651):1265–1269, June 2023. doi:10.1126/science.ade5337. URL https://www.science.org/doi/full/10.1126/science.ade5337. Publisher: American Association for the Advancement of Science. [cited on page 211].

K. Slagle, D. Aasen, H. Pichler, R. S. K. Mong, P. Fendley, X. Chen, M. Endres, and J. Alicea. Microscopic characterization of Ising conformal field theory in Rydberg chains. *Physical Review B*, 104(23):235109, Dec. 2021. doi:10.1103/PhysRevB.104.235109. URL https://link.aps.org/doi/10.1103/PhysRevB.104.235109. Publisher: American Physical Society. [cited on page 153].

J. A. Sobota, S.-L. Yang, A. F. Kemper, J. J. Lee, F. T. Schmitt, W. Li, R. G. Moore, J. G. Analytis, I. R. Fisher, P. S. Kirchmann, T. P. Devereaux, and Z.-X. Shen. Direct Optical Coupling to an Unoccupied Dirac Surface State in the Topological Insulator Bi_2 Se_3. *Physical Review Letters*, 111(13):136802, Sept. 2013. doi:10.1103/PhysRevLett.111.136802. URL https://link.aps.org/doi/10.1103/PhysRevLett.111.136802. Publisher: American Physical Society. [cited on page 165].

J. A. Sobota, Y. He, and Z.-X. Shen. Angle-resolved photoemission studies of quantum materials. *Reviews of Modern Physics*, 93(2):025006, May 2021. doi:10.1103/RevModPhys.93.025006. URL https://link.aps.org/doi/10.1103/RevModPhys.93.025006. Publisher: American Physical Society. [cited on page 164].

P. St-Jean, V. Goblot, E. Galopin, A. Lemaître, T. Ozawa, L. Le Gratiet, I. Sagnes, J. Bloch, and A. Amo. Lasing in topological edge states of a one-dimensional lattice. *Nature Photonics*, 11(10):651–656, Oct. 2017. ISSN 1749-4893. doi:10.1038/s41566-017-0006-2. URL https://www.nature.com/articles/s41566-017-0006-2. Publisher: Nature Publishing Group. [cited on pages 8 and 9].

J. Steinhauer, R. Ozeri, N. Katz, and N. Davidson. Excitation Spectrum of a Bose-Einstein Condensate. *Physical Review Letters*, 88(12):120407, Mar. 2002. doi:10.1103/PhysRevLett.88.120407. URL https://link.aps.org/doi/10.1103/PhysRevLett.88.120407. Publisher: American Physical Society. [cited on page 165].

J. Stenger, S. Inouye, A. P. Chikkatur, D. M. Stamper-Kurn, D. E. Pritchard, and W. Ketterle. Bragg Spectroscopy of a Bose-Einstein Condensate. *Physical Review Letters*, 82(23):4569–4573, June 1999. doi:10.1103/PhysRevLett.82.4569. URL https://link.aps.org/doi/10.1103/PhysRevLett.82.4569. Publisher: American Physical Society. [cited on page 164].

T. Sägesser, S. Jain, P. Hrmo, A. Ferk, M. Simoni, Y. Cui, C. Mordini, D. Kienzler, and J. Home. A 3-dimensional scanning trapped-ion probe, Dec. 2024. URL http://arxiv.org/abs/2412.17528. arXiv:2412.17528 [quant-ph]. [cited on page 13].

R. Tao, M. Ammenwerth, F. Gyger, I. Bloch, and J. Zeiher. High-Fidelity Detection of Large-Scale Atom Arrays in an Optical Lattice. *Physical Review Letters*, 133(1): 013401, July 2024. ISSN 0031-9007, 1079-7114. doi:10.1103/PhysRevLett.133.013401. URL https://link.aps.org/doi/10.1103/PhysRevLett.133.013401. [cited on pages 14 and 212].

H. Tasaki. Long-Range Order, "Tower" of States, and Symmetry Breaking in Lattice Quantum Systems. *Journal of Statistical Physics*, 174(4):735–761, Feb. 2019. ISSN 1572-9613. doi:10.1007/s10955-018-2193-8. URL https://doi.org/10.1007/s10955-018-2193-8. [cited on pages 127 and 128].

D. A. Tennant, R. A. Cowley, S. E. Nagler, and A. M. Tsvelik. Measurement of the spin-excitation continuum in one-dimensional KCuF_3 using neutron scattering. *Physical Review B*, 52(18):13368–13380, Nov. 1995. doi:10.1103/PhysRevB.52.13368. URL https://link.aps.org/doi/10.1103/PhysRevB.52.13368. Publisher: American Physical Society. [cited on page 173].

J. D. Thompson. *A quantum interface between single atoms and nanophotonic structures*. PhD thesis, 2014. URL https://dash.harvard.edu/handle/1/13070060. [cited on page 30].

J. D. Thompson, T. G. Tiecke, A. S. Zibrov, V. Vuletić, and M. D. Lukin. Coherence and Raman Sideband Cooling of a Single Atom in an Optical Tweezer. *Physical Review Letters*, 110(13):133001, Mar. 2013. doi:10.1103/PhysRevLett.110.133001. URL https://link.aps.org/doi/10.1103/PhysRevLett.110.133001. Publisher: American Physical Society. [cited on pages 29, 38, 40, 41, and 46].

S.-i. Tomonaga. Remarks on Bloch's Method of Sound Waves applied to Many-Fermion Problems. *Progress of Theoretical Physics*, 5(4):544–569, July 1950. ISSN 0033-068X. doi:10.1143/ptp/5.4.544. URL https://doi.org/10.1143/ptp/5.4.544. [cited on page 150].

D.-A. Trinh, K. V. Adwaith, M. Branco, A. Rouxel, S. Welinski, P. Berger, F. Goldfarb, and F. Bretenaker. Modulation transfer protocol for Rydberg RF receivers. *Applied Physics Letters*, 125(15):154001, Oct. 2024. ISSN 0003-6951, 1077-3118. doi:10.1063/5.0216969. URL https://pubs.aip.org/apl/article/125/15/154001/3315525/Modulation-transfer-protocol-for-Rydberg-RF. [cited on page 13].

D. I. Tsomokos, J. J. García-Ripoll, N. R. Cooper, and J. K. Pachos. Chiral entanglement in triangular lattice models. *Physical Review A*, 77(1):012106, Jan. 2008. doi:10.1103/PhysRevA.77.012106. URL https://link.aps.org/doi/10.1103/PhysRevA.77.012106. Publisher: American Physical Society. [cited on pages 85 and 87].

C. Tuchendler, A. M. Lance, A. Browaeys, Y. R. P. Sortais, and P. Grangier. Energy distribution and cooling of a single atom in an optical tweezer. *Physical Review A*, 78(3):033425, Sept. 2008. doi:10.1103/PhysRevA.78.033425. URL https://link.aps.org/doi/10.1103/PhysRevA.78.033425. Publisher: American Physical Society. [cited on pages 42, 43, 44, and 50].

E. Urban, T. A. Johnson, T. Henage, L. Isenhower, D. D. Yavuz, T. G. Walker, and M. Saffman. Observation of Rydberg blockade between two atoms. *Nature Physics*, 5(2):110–114, Feb. 2009. ISSN 1745-2481. doi:10.1038/nphys1178. URL https://www.nature.com/articles/nphys1178. Publisher: Nature Publishing Group. [cited on page 94].

L. Villa. *Out-of-equilibrium dynamics and quench spectroscopy of ultracold many-body quantum systems*. phdthesis, Institut Polytechnique de Paris, July 2021. URL https://theses.hal.science/tel-03372978. [cited on page 166].

L. Villa, J. Despres, and L. Sanchez-Palencia. Unraveling the excitation spectrum of many-body systems from quantum quenches. *Physical Review A*, 100(6):063632, Dec. 2019. ISSN 2469-9926, 2469-9934. doi:10.1103/PhysRevA.100.063632. URL https://link.aps.org/doi/10.1103/PhysRevA.100.063632. [cited on pages 163, 165, 166, and 168].

L. Villa, J. Despres, S. J. Thomson, and L. Sanchez-Palencia. Local quench spectroscopy of many-body quantum systems. *Physical Review A*, 102(3):033337, Sept. 2020. doi:10.1103/PhysRevA.102.033337. URL https://link.aps.org/doi/10.1103/PhysRevA.102.033337. Publisher: American Physical Society. [cited on pages 163 and 165].

J. Villain, R. Bidaux, J.-P. Carton, and R. Conte. Order as an effect of disorder. *Journal de Physique*, 41(11):1263–1272, Nov. 1980. ISSN 0302-0738, 2777-3396. doi:10.1051/jphys:0198000410110126300. URL http://dx.doi.org/10.1051/jphys:0198000410110126300. Publisher: Société Française de Physique. [cited on page 214].

C. Wang, F.-M. Liu, M.-C. Chen, H. Chen, X.-H. Zhao, C. Ying, Z.-X. Shang, J.-W. Wang, Y.-H. Huo, C.-Z. Peng, X. Zhu, C.-Y. Lu, and J.-W. Pan. Realization of fractional quantum Hall state with interacting photons. *Science*, 384(6695): 579–584, May 2024. doi:10.1126/science.ado3912. URL https://www.science.org/doi/full/10.1126/science.ado3912. Publisher: American Association for the Advancement of Science. [cited on pages 8 and 9].

K. Wang, X. He, R. Guo, P. Xu, C. Sheng, J. Zhuang, Z. Xiong, M. Liu, J. Wang, and M. Zhan. Preparation of a heteronuclear two-atom system in the three-dimensional ground state in an optical tweezer. *Physical Review A*, 100(6):063429, Dec. 2019. doi:10.1103/PhysRevA.100.063429. URL https://link.aps.org/doi/10.1103/PhysRevA.100.063429. Publisher: American Physical Society. [cited on page 211].

S. Weber, C. Tresp, H. Menke, A. Urvoy, O. Firstenberg, H. P. Büchler, and S. Hofferberth. Calculation of Rydberg interaction potentials. *Journal of Physics B: Atomic, Molecular and Optical Physics*, 50(13):133001, June 2017. ISSN 0953-4075.

doi:10.1088/1361-6455/aa743a. URL https://dx.doi.org/10.1088/1361-6455/aa743a. Publisher: IOP Publishing. [cited on pages 16, 57, 90, 94, 102, and 107].

P. Weckesser, K. Srakaew, T. Blatz, D. Wei, D. Adler, S. Agrawal, A. Bohrdt, I. Bloch, and J. Zeiher. Realization of a Rydberg-dressed extended Bose Hubbard model, May 2024. URL http://arxiv.org/abs/2405.20128. arXiv:2405.20128 [cond-mat]. [cited on page 198].

D. Wei, A. Rubio-Abadal, B. Ye, F. Machado, J. Kemp, K. Srakaew, S. Hollerith, J. Rui, S. Gopalakrishnan, N. Y. Yao, I. Bloch, and J. Zeiher. Quantum gas microscopy of Kardar-Parisi-Zhang superdiffusion. *Science*, 376(6594):716–720, May 2022. doi:10.1126/science.abk2397. URL https://www.science.org/doi/10.1126/science.abk2397. Publisher: American Association for the Advancement of Science. [cited on page 10].

G. Wendin. Quantum information processing with superconducting circuits: a review. *Reports on Progress in Physics*, 80(10):106001, Sept. 2017. ISSN 0034-4885. doi:10.1088/1361-6633/aa7e1a. URL https://dx.doi.org/10.1088/1361-6633/aa7e1a. Publisher: IOP Publishing. [cited on page 8].

J. F. Wienand, S. Karch, A. Impertro, C. Schweizer, E. McCulloch, R. Vasseur, S. Gopalakrishnan, M. Aidelsburger, and I. Bloch. Emergence of fluctuating hydrodynamics in chaotic quantum systems. *Nature Physics*, pages 1–6, Aug. 2024. ISSN 1745-2481. doi:10.1038/s41567-024-02611-z. URL https://www.nature.com/articles/s41567-024-02611-z. Publisher: Nature Publishing Group. [cited on page 10].

A. Wietek, M. Schuler, and A. M. Läuchli. Studying Continuous Symmetry Breaking using Energy Level Spectroscopy, Apr. 2017. URL http://arxiv.org/abs/1704.08622. arXiv:1704.08622 [cond-mat, physics:quant-ph]. [cited on page 127].

K. Winkler, G. Thalhammer, F. Lang, R. Grimm, J. Hecker Denschlag, A. J. Daley, A. Kantian, H. P. Büchler, and P. Zoller. Repulsively bound atom pairs in an optical lattice. *Nature*, 441(7095):853–856, June 2006. ISSN 1476-4687. doi:10.1038/nature04918. URL https://www.nature.com/articles/nature04918. Publisher: Nature Publishing Group. [cited on page 198].

H. Wu, R. Richaud, J.-M. Raimond, M. Brune, and S. Gleyzes. Millisecond-Lived Circular Rydberg Atoms in a Room-Temperature Experiment. *Physical Review Letters*, 130(2):023202, Jan. 2023. doi:10.1103/PhysRevLett.130.023202. URL https:

//link.aps.org/doi/10.1103/PhysRevLett.130.023202. Publisher: American Physical Society. [cited on page 211].

T.-Y. Wu, A. Kumar, F. Giraldo, and D. S. Weiss. Stern–Gerlach detection of neutral-atom qubits in a state-dependent optical lattice. *Nature Physics*, 15(6): 538–542, June 2019. ISSN 1745-2481. doi:10.1038/s41567-019-0478-8. URL https://www.nature.com/articles/s41567-019-0478-8. Publisher: Nature Publishing Group. [cited on page 211].

T. Xia, M. Lichtman, K. Maller, A. W. Carr, M. J. Piotrowicz, L. Isenhower, and M. Saffman. Randomized Benchmarking of Single-Qubit Gates in a 2D Array of Neutral-Atom Qubits. *Physical Review Letters*, 114(10):100503, Mar. 2015. doi:10.1103/PhysRevLett.114.100503. URL https://link.aps.org/doi/10.1103/PhysRevLett.114.100503. Publisher: American Physical Society. [cited on page 69].

H. Xu, C.-M. Chung, M. Qin, U. Schollwöck, S. R. White, and S. Zhang. Coexistence of superconductivity with partially filled stripes in the Hubbard model. *Science*, 384(6696):eadh7691, May 2024. doi:10.1126/science.adh7691. URL https://www.science.org/doi/10.1126/science.adh7691. Publisher: American Association for the Advancement of Science. [cited on page 188].

A. Yacoby, H. L. Stormer, N. S. Wingreen, L. N. Pfeiffer, K. W. Baldwin, and K. W. West. Nonuniversal Conductance Quantization in Quantum Wires. *Physical Review Letters*, 77(22):4612–4615, Nov. 1996. doi:10.1103/PhysRevLett.77.4612. URL https://link.aps.org/doi/10.1103/PhysRevLett.77.4612. Publisher: American Physical Society. [cited on page 151].

B. Yang, Y.-Y. Chen, Y.-G. Zheng, H. Sun, H.-N. Dai, X.-W. Guan, Z.-S. Yuan, and J.-W. Pan. Quantum criticality and the Tomonaga-Luttinger liquid in one-dimensional Bose gases. *Physical Review Letters*, 119(16):165701, Oct. 2017. doi:10.1103/PhysRevLett.119.165701. URL https://link.aps.org/doi/10.1103/PhysRevLett.119.165701. Publisher: American Physical Society. [cited on page 151].

T. L. Yang, P. Grišins, Y. T. Chang, Z. H. Zhao, C. Shih, T. Giamarchi, and R. G. Hulet. Measurement of the Dynamical Structure Factor of a 1D Interacting Fermi Gas. *Physical Review Letters*, 121(10):103001, Sept. 2018. doi:10.1103/PhysRevLett.121.103001. URL https://link.aps.org/doi/10.1103/

PhysRevLett.121.103001. Publisher: American Physical Society. [cited on page 151].

S. Yarkoni, E. Raponi, T. Bäck, and S. Schmitt. Quantum annealing for industry applications: introduction and review. *Reports on Progress in Physics*, 85(10): 104001, Sept. 2022. ISSN 0034-4885. doi:10.1088/1361-6633/ac8c54. URL https://dx.doi.org/10.1088/1361-6633/ac8c54. Publisher: IOP Publishing. [cited on page 12].

D. D. Yavuz, P. B. Kulatunga, E. Urban, T. A. Johnson, N. Proite, T. Henage, T. G. Walker, and M. Saffman. Fast Ground State Manipulation of Neutral Atoms in Microscopic Optical Traps. *Physical Review Letters*, 96(6):063001, Feb. 2006. doi:10.1103/PhysRevLett.96.063001. URL https://link.aps.org/doi/10.1103/PhysRevLett.96.063001. Publisher: American Physical Society. [cited on page 69].

Y. Yu, N. R. Hutzler, J. T. Zhang, L. R. Liu, J. D. Hood, T. Rosenband, and K.-K. Ni. Motional-ground-state cooling outside the Lamb-Dicke regime. *Physical Review A*, 97(6):063423, June 2018. doi:10.1103/PhysRevA.97.063423. URL https://link.aps.org/doi/10.1103/PhysRevA.97.063423. Publisher: American Physical Society. [cited on page 46].

J. Yuan, W. Yang, M. Jing, H. Zhang, Y. Jiao, W. Li, L. Zhang, L. Xiao, and S. Jia. Quantum sensing of microwave electric fields based on Rydberg atoms. *Reports on Progress in Physics*, 86(10):106001, Sept. 2023. ISSN 0034-4885. doi:10.1088/1361-6633/acf22f. URL https://dx.doi.org/10.1088/1361-6633/acf22f. Publisher: IOP Publishing. [cited on page 13].

J. Zhang, P. W. Hess, A. Kyprianidis, P. Becker, A. Lee, J. Smith, G. Pagano, I.-D. Potirniche, A. C. Potter, A. Vishwanath, N. Y. Yao, and C. Monroe. Observation of a discrete time crystal. *Nature*, 543(7644):217–220, Mar. 2017. ISSN 1476-4687. doi:10.1038/nature21413. URL https://www.nature.com/articles/nature21413. Publisher: Nature Publishing Group. [cited on page 69].

H.-S. Zhong, H. Wang, Y.-H. Deng, M.-C. Chen, L.-C. Peng, Y.-H. Luo, J. Qin, D. Wu, X. Ding, Y. Hu, P. Hu, X.-Y. Yang, W.-J. Zhang, H. Li, Y. Li, X. Jiang, L. Gan, G. Yang, L. You, Z. Wang, L. Li, N.-L. Liu, C.-Y. Lu, and J.-W. Pan. Quantum computational advantage using photons. *Science*, 370(6523):1460–1463, Dec. 2020. doi:10.1126/science.abe8770. URL https://www.science.org/doi/

10.1126/science.abe8770. Publisher: American Association for the Advancement of Science. [cited on page 12].

Z.-Y. Zhou, G.-X. Su, J. C. Halimeh, R. Ott, H. Sun, P. Hauke, B. Yang, Z.-S. Yuan, J. Berges, and J.-W. Pan. Thermalization dynamics of a gauge theory on a quantum simulator. *Science*, 377(6603):311–314, July 2022. ISSN 0036-8075, 1095-9203. doi:10.1126/science.abl6277. URL https://www.science.org/doi/10.1126/science.abl6277. [cited on page 10].

N. Šibalić, J. D. Pritchard, C. S. Adams, and K. J. Weatherill. ARC: An open-source library for calculating properties of alkali Rydberg atoms. *Computer Physics Communications*, 220:319–331, Nov. 2017. ISSN 0010-4655. doi:10.1016/j.cpc.2017.06.015. URL https://www.sciencedirect.com/science/article/pii/S0010465517301972. [cited on page 66].

List of publications

Experimental papers

- C. Chen, G. Bornet, M. Bintz, G. Emperauger, L. Leclerc, V. S. Liu, P. Scholl, D. Barredo, J. Hauschild, S. Chatterjee, M. Schuler, A. M. Läuchli, M. P. Zaletel, T. Lahaye, N. Y. Yao, and A. Browaeys. **Continuous symmetry breaking in a two-dimensional Rydberg array**. *Nature*, 616(7958):691–695, Apr. 2023a. ISSN 1476-4687. doi:10.1038/s41586-023-05859-2. Number: 7958 Publisher: Nature Publishing Group.

- G. Bornet, G. Emperauger, C. Chen, B. Ye, M. Block, M. Bintz, J. A. Boyd, D. Barredo, T. Comparin, F. Mezzacapo, T. Roscilde, T. Lahaye, N. Y. Yao, and A. Browaeys. **Scalable spin squeezing in a dipolar Rydberg atom array**. *Nature*, pages 1–6, Aug. 2023. ISSN 1476-4687. doi:10.1038/s41586-023-06414-9. Publisher: Nature Publishing Group.

- C. Chen, G. Emperauger, G. Bornet, F. Caleca, B. Gély, M. Bintz, S. Chatterjee, V. Liu, D. Barredo, N. Y. Yao, T. Lahaye, F. Mezzacapo, T. Roscilde, and A. Browaeys. **Spectroscopy of elementary excitations from quench dynamics in a dipolar XY Rydberg simulator**, Nov. 2023b. arXiv:2311.11726.

- G. Bornet, G. Emperauger, C. Chen, F. Machado, S. Chern, L. Leclerc, B. Gély, Y. T. Chew, D. Barredo, T. Lahaye, N. Y. Yao, and A. Browaeys. **Enhancing a Many-Body Dipolar Rydberg Tweezer Array with Arbitrary Local Controls**. *Physical Review Letters*, 132(26):263601, June 2024. doi:10.1103/PhysRevLett.132.263601. Publisher: American Physical Society.

- G. Emperauger, M. Qiao, C. Chen, F. Caleca, S. Bocini, M. Bintz, G. Bornet, R. Martin, B. Gély, L. Klein, D. Barredo, S. Chatterjee, N. Yao, F. Mezzacapo, T. Lahaye, T. Roscilde, and A. Browaeys. **Tomonaga-Luttinger liquid behavior in a Rydberg-encoded spin chain**, Jan. 2025. arXiv:2501.08179.

- M. Qiao, G. Emperauger, C. Chen, L. Homeier, S. Hollerith, G. Bornet, R. Martin, B. Gély, L. Klein, D. Barredo, S. Geier, N.-C. Chiu, F. Grusdt, A. Bohrdt, T. Lahaye, and A. Browaeys. **Realization of a doped quantum**

antiferromagnet with dipolar hopping in a Rydberg tweezer array, Jan. 2025. arXiv:2501.08233.

- G. Emperauger, M. Qiao, G. Bornet, C. Chen, R. Martin, Y. T. Chew, B. Gély, L. Klein, D. Barredo, A. Browaeys., and T. Lahaye **Benchmarking direct and indirect dipolar spin-exchange interactions between two Rydberg atoms**, Mar. 2025. arXiv.2503.15034.

Theory papers (collaborations)

- J. Mögerle, K. Brechtelsbauer, A. T. Gea-Caballero, J. Prior, G. Emperauger, G. Bornet, C. Chen, T. Lahaye, A. Browaeys, and H. P. Büchler. **Spin-1 Haldane phase in a chain of Rydberg atoms**, Oct. 2024. arXiv:2410.21424.

- H. Lange, G. Bornet, G. Emperauger, C. Chen, T. Lahaye, S. Kienle, A. Browaeys, and A. Bohrdt. **Transformer neural networks and quantum simulators: a hybrid approach for simulating strongly correlated systems**. Quantum 9, 1675., Mar. 2025. 10.22331/q-2025-03-26-1675.